HAL
open science

Synthesis of polynitrogen compounds by pressure as the next-generation high energy density materials

Dominique Laniel

To cite this version:

Dominique Laniel. Synthesis of polynitrogen compounds by pressure as the next-generation high energy density materials. Condensed Matter [cond-mat]. Sorbonne Université, 2018. English. NNT : 2018SORUS472 . tel-02315738v2

HAL Id: tel-02315738

https://hal.science/tel-02315738v2

Submitted on 28 Aug 2020

HAL is a multi-disciplinary open access archive for the deposit and dissemination of scientific research documents, whether they are published or not. The documents may come from teaching and research institutions in France or abroad, or from public or private research centers.

L'archive ouverte pluridisciplinaire **HAL**, est destinée au dépôt et à la diffusion de documents scientifiques de niveau recherche, publiés ou non, émanant des établissements d'enseignement et de recherche français ou étrangers, des laboratoires publics ou privés.

Sorbonne Université

Ecole doctorale 397 : Physique et chimie des matériaux

Synthèse de polymères d'azote par pression comme matériaux énergétiques du futur

Par Dominique Laniel

Thèse de doctorat en Science des matériaux

Dirigée par Paul Loubeyre

Présentée et soutenue publiquement le 18 septembre 2018

Devant un jury composé de :

Chrystèle Sanloup	Chercheur CNRS	Présidente
Emmanuel Lacôte	Chercheur CNRS	Rapporteur
Julien Haines	Chercheur CNRS	Rapporteur
Émilie Labarthe	Ingénieure-Chercheure CNES	Examinatrice
Paul Loubeyre	Directeur de recherche CEA	Directeur de thèse
Gunnar Weck	Ingénieur-Chercheur CEA	Encadrant de thèse

“In the end, when it’s over, all that matters is what you’ve done.”
—Alexander the Great

REMERCIEMENTS

Déjà, ces trois belles années de thèse tirent à leur fin. Rien de tout ce qui a été accompli durant cette période n'aurait été possible sans de très nombreux appuis et encouragements.

D'abord, je tiens à remercier mon directeur de thèse Paul Loubeyre. Sa passion et dévouement pour la science, ses bonnes idées, sa persévérance et ses encouragements m'ont guidé tout au long de cette thèse. Paul, ce fut un grand privilège de travailler avec toi, très sincèrement, merci pour tout.

Tout aussi important durant ces années, je remercie chaleureusement mon encadrant Gunnar Weck. Son grand sens de l'humour, sa patience, sa disponibilité, sa rigueur et curiosité scientifique, ses bons conseils et son attention aux détails m'ont été indispensables durant ces trois années. Gunnar, mille mercis.

C’est un grand honneur pour moi que Messieurs Emmanuel Lacôte, Julien Haines, Émilie Labarthe, ainsi que Madame Chrystèle Sanloup aient accepté d’être membres du jury et je remercie Messieurs Emmanuel Lacôte et Julien Haines pour leurs commentaires et leurs corrections.

Merci également à tous les autres membres permanents du LHPS : Ramesh André, Florent Occelli, Thomas Plisson et Agnès Dewaele. Vous avez tous toujours été disponibles pour me donner un coup de main, me conseiller, discuter science ou autres et, au final, rendre ce séjour autant fructueux qu'agréable. Évidemment, je remercie aussi les autres doctorants et apprentis que j'ai côtoyé : Adrien Marizy, Charles Pépin et Églantine Ruaudel; maintenant tous passés à un échelon supérieur. Merci aussi à mon cobureau et thésard Bastien Guigue, toujours disponible pour d'amusantes discussions de physique, sports, politique et autres…

Je tiens à remercier toutes les personnes qui m’ont apporté leur aide sur la ligne ID27 de l’ESRF, soit Gaston Garbarino, Volodymyr Svitlyk et Mohamed Mezouar. Merci également à toutes les personnes qui ont permis que cette thèse se déroule sans problème :

Catherine Cherfils, François Jollet, Laurent Colombet, Muriel Delaveau, Brigitte Flouret et, en particulier, Sandra Boullier.

Ces remerciements ne seraient pas complets sans y inclure ceux qui, de l'autre côté de l'océan, m'ont donné l'énergie et la motivation pour entreprendre, continuer et terminer cette thèse. Amis de la tendre enfance, du primaire, du secondaire et de l'université, un très grand merci. Évidemment, mon frère, ma sœur et tout particulièrement mes parents méritent d'être remerciés. Leur amour inconditionnel – à la fois rassurant, réconfortant et inspirant – même à 5650 km de distance, s'est à tout moment fait sentir. Enfin, à ma compagne, avec qui j'ai partagé mes frustrations, mes espoirs, mes joies et qui a toujours su m'épauler ainsi que m'encourager. Sevgili Başak, çok teşekkür ederim.

RÉSUMÉ DE LA THÈSE

L'exploration spatiale est un des projets les plus ambitieux de l'humanité. Un des éléments le plus critique dans ce domaine est le propergol – carburant de la fusée constituant plus de 90% de la masse totale – qui détermine la charge effective pouvant être transportée. Vu son importance, des matériaux dégageant de plus en plus d'énergie, fait d'éléments abondants, faciles d'extraction ainsi que sans empreinte écologique, sont de plus en plus recherchés. Jusqu'à présent, ceux-ci sont produits par des méthodes de chimie classique typiquement réalisée à pression ambiante. Cependant, l'exploitation du paramètre pression pourrait permettre une rupture technologique en rendant accessible une nouvelle chimie qui donnerait lieu à des matériaux inédits ; soient encore plus puissants et performants. Intervenant directement dans l'équation de l'énergie libre de Gibbs, ce paramètre est idéal pour l'exploration des états thermodynamiques d'un système. Effectivement, des pressions de l'ordre de 100 GPa permettent de transférer une énergie de plus de 10 eV, excédant même l'énergie de cohésion des molécules les plus fortes et permettant de les briser [1]. Plus encore, le transfert d'énergie par la pression promeut la délocalisation électronique, favorisant les structures étendues (polymériques), idéales pour les matériaux énergétiques [2].

L'azote s'impose comme l'élément de choix pour former des matériaux à haute densité d'énergie. En effet, cela s'explique par la différence d'énergie entre la liaison simple N-N (160 kJ/mol) et la liaison triple N≡N (954 kJ/mol), permettant ainsi le stockage d'une forte quantité d'énergie. De plus, produisant du diazote – composant environ 78% de l'atmosphère – comme produit de réaction, c'est un matériau énergétique « vert », c'est-à-dire non dommageable pour l'environnement. Pour ces raisons, un solide composé uniquement de liaisons N-N est perçu comme étant le matériau énergétique ultime [3].

En 1992, des calculs théoriques ont mis en évidence le potentiel de l'approche haute pression pour la synthèse de matériaux énergétiques en prédisant la stabilité de l'azote polymérique cubique gauche (cg-N) au-dessus de 50 GPa [4]. Ce solide est composé d'un réseau tridimensionnel d'atomes d'azote simplement liés et donc idéal d'un point de vue énergétique. Lors de sa décomposition, c'est une énergie de 794 kJ/mol qui est relâchée; soit près de cinq fois plus que le meilleur matériau énergétique conventionnel présentement utilisé.

Vu les propriétés remarquables du solide d'azote polymérique, de nombreuses expériences ont été entreprises afin de le synthétiser en laboratoire [5–9]. En 2004, une équipe y est parvenue en comprimant de l'azote moléculaire jusqu'à 110 GPa, soit plus d'un million de fois la pression atmosphérique, et en le chauffant à plus de 2200 K [10]. Contrairement aux calculs théoriques qui prévoyaient une métastabilité de l'azote polymérique jusqu'aux conditions ambiantes, les expériences ont démontré que ce dernier pouvait seulement être ramené à 42 GPa. Au-dessous de cette pression seuil, le solide cg-N se décompose pour former du N_2 et se faisant libère son énergie emmagasinée

L'utilisation de l'azote polymérique comme matériau énergétique n'est pas possible pour deux raisons. D'abord, il est absolument nécessaire que ce dernier puisse être récupéré aux conditions ambiantes. Ensuite, sa pression de synthèse est beaucoup trop extrême pour être envisageable en industrie, où des pressions maximales de 10 GPa peuvent être atteintes. Peut-on contourner ces deux difficultés pour produire par la pression des matériaux à haute densité d'énergie ?

L'objectif de cette thèse doctorale est la synthèse sous haute pression d'une nouvelle forme, améliorée, d'azote polymérique qui serait métastable aux conditions ambiantes et produite à des pressions moins extrêmes. La méthode choisie pour y parvenir consiste à comprimer de l'azote moléculaire avec un autre élément qui, de par son interaction chimique, puisse perturber suffisamment la molécule N_2 pour induire la rupture de la liaison triple à basse pression, permettant la synthèse d'un réseau polyazoté ainsi qu'une stabilisation jusqu'aux conditions ambiantes.

Le choix de l'élément à mélanger à l'azote repose à la fois sur un raisonnement physique et des calculs théoriques. Du point de vu physique, la précompression chimique a déjà été démontrée comme pouvant être efficace pour perturber puis briser des liaisons covalentes à plus basse pression. Le principe est simple : il suffit d'augmenter la densité électronique de la molécule, comme cela se produit naturellement en augmentant davantage la pression [11]. Pour y parvenir, deux voies sont envisagées. Une première approche est de mélanger l'azote avec un élément

beaucoup plus volumineux qui, simplement par effet géométrique, impose aux atomes d'azote une plus grande proximité et donc une plus forte densité électronique. La deuxième méthode est d'ajouter à l'azote un élément réducteur, tel que les métaux alcalins, qui transfèrerait volontairement une densité électronique à la molécule d'azote. Évidemment, ces deux méthodes ne garantissent en aucun cas qu'une fois la liaison triple de l'azote moléculaire brisée un réseau d'azotes simplement liés se formera, d'où l'importance des calculs théoriques. Ceux-ci, en sondant le paysage énergétique découlant de différents arrangements atomiques, permettent d'obtenir la structure du composé le plus stable à une pression (et concentration) donnée. De plus, ces calculs sont aussi en mesure d'estimer la métastabilité des composés prédits lors du relâchement de la pression. Donc, ayant en tête les principes de la précompression chimique et guidé par les calculs théoriques, les systèmes suivants ont été sélectionnés pour les mesures sous haute pression de cette thèse : N_2 pur, Xe-N_2, H_2-N_2 et Li-N_2.

L'outil expérimental pour atteindre les pressions nécessaires pour dissocier la molécule d'azote est la cellule à enclumes de diamant (CED). Son schéma de principe est assez simple : l'échantillon est confiné par un joint métallique entre deux enclumes de diamant qui se rapprochent l'une de l'autre de façon à comprimer l'échantillon. L'extrémité des enclumes de diamant en contact avec l'échantillon est de très petite taille, soit de l'ordre de la dizaine ou de la centaine de micromètres de diamètre, de sorte qu'une force modérée appliquée sur la base de l'enclume entraîne une pression énorme sur l'échantillon – jusqu'à quelques millions de fois la pression atmosphérique. En plus d'être un des matériaux les plus durs, la grande transparence des diamants sur de larges plages de longueurs d'onde est aussi un de ses plus grands atouts. Effectivement, celle-ci permet une grande variété de techniques de caractérisation par photons. Lors de cette thèse, deux méthodes furent exploitées pour l'étude des échantillons comprimés : la diffraction par rayons X et la spectroscopie Raman. La première permet la résolution structurale des phases produites par pression tandis que la seconde nous informe sur l'évolution des interactions interatomiques.

La première étude expérimentale présentée dans cette thèse porte sur la compression et le chauffage de l'azote pur dans des domaines de pression et température jusqu'à présent jamais explorés. Depuis la synthèse de la phase cg-N, plusieurs études théoriques ont porté sur le diagramme de phase de l'azote au-delà de 110 GPa et 2200 K [12–16]. Ces études, ainsi que leur vérification expérimentale, sont essentielles afin de trouver de nouvelles géométries d'atomes d'azote simplement liés qui pourraient s'avérer plus stable que cg-N et donc plus facile à ramener aux conditions ambiantes. D'après ces calculs, la phase cg-N devrait se transformer une première fois à 188 GPa en une structure orthorhombique présentant des couches d'anneaux N_7 distordus (dite *layered polymeric nitrogen*, ou LP-N) puis à 263 GPa, en

une structure cubique s'apparentant à celle du diamant avec des entités N_{10} [12]. On notera cependant qu'entre 188 et 263 GPa, six phases ont des enthalpies très proches de la LP-N, soit à quelques dizaines de meV de celle-ci. Cette très faible différence d'enthalpie entre ces différents solides signifie que, expérimentalement, presque tous pourraient être produits. Cette affirmation est justifiée par des problèmes bien connus avec les calculs théoriques, y compris le fait que ceux-ci sont effectués à une température nulle, signifiant que le terme température-entropie (-TS) dans l'énergie libre de Gibbs n'est pas pris en compte. Pour des systèmes comme l'azote, où des barrières d'activation importantes doivent être surmontées par un chauffage laser jusqu'à des températures atteignant 3000 K, la contribution du terme température-entropie peut très bien devenir suffisante pour stabiliser une structure autre que celle de plus basse énergie.

Suivant la publication de ces calculs, une étude expérimentale soumit l'azote moléculaire à des conditions de pression et température allant jusqu'à 170 GPa et 2500 K. La phase LP-N (prédite à partir de 188 GPa) fut observée à compter de 125 GPa et 2500 K ainsi que jusqu'aux pressions et températures maximales atteintes dans ce travail [17].

Lors de nos études, des pressions de 250 GPa et des températures de 3300 K ont été obtenues, surpassant largement le domaine P-T précédemment atteint, ce qui a permis la synthèse d'une nouvelle phase d'azote polymérique. Sa structure cristalline ne correspond pas à la phase LP-N ni à la phase N_{10} prédite. Cette maille, ayant plutôt une maille tétragonale ($P4_2bc$) de paramètres de réseau a = 4.261(1) Å et c = 8.120(1) Å à 187 GPa, concorde cependant très bien avec une autre structure prédite, celle-ci constituée d'anneaux N_6 interconnectés formant des bicouches (Figure), qui avait une enthalpie calculée à peine plus élevée que la structure N_{10}. Les mesures de spectroscopie Raman permirent de confirmer la présence de liaisons simples entre atomes d'azote. Cette phase a pu être suivie en décompression jusqu'à 60 GPa, pression à laquelle les diamants de la CED ont cédé et l'échantillon s'est échappé.

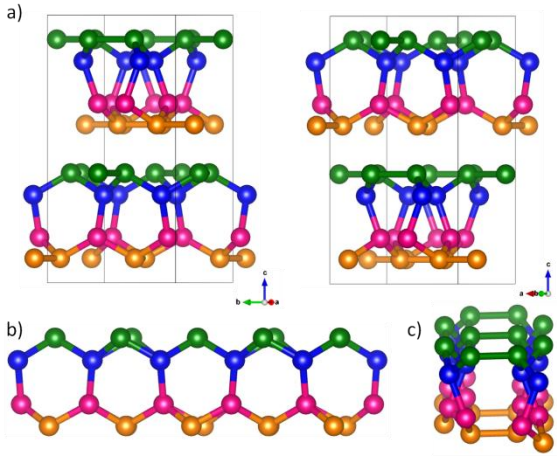

Figure 1 : Structure cristalline du nouveau solide d'azote polymérique. a) La maille du composé, où l'on voit les deux couches d'hexagones interconnectés identiques à une rotation de 90° près. b) et c) Enchaînement d'anneaux N_6. Les atomes de mêmes couleurs sont équivalents.

La deuxième étude porte sur les mélanges Xe-N_2 et avait pour objectifs d'observer directement l'impact d'une précompression chimique dû à la taille des atomes de xénon ainsi que de tenter de synthétiser la structure XeN_6 prédite par les calculs théoriques. Cette phase est la seule prévue stable par les calculs et doit se former à partir de 146 GPa à température nulle ou à 132 GPa à 2500 K. Sa structure est particulière surprenante de par le fait que des liaisons covalentes Xe-N sont attendues, formées grâce à une hybridation des orbitales *5p* du xénon avec les orbitales *2p* de l'azote. Du point de vu énergétique, XeN_6 serait constitué d'hexagones N_6 où les liaisons N-N seraient simples, conférant au composé une énergie libérée comparable aux explosifs modernes lors de sa décomposition [18].

La première étape de cette étude fut la détermination du diagramme de démixtion binaire de Xe-N_2, réalisée en comprimant des échantillons avec 14 concentrations différentes. Ceci permit de découvrir deux solides : un solide riche en xénon, constitué jusqu'à 10% molaire de molécules d'azote et adoptant la structure du xénon pur, ainsi qu'un composé de van der Waals de stoechiométrie $Xe(N_2)_2$ avec une maille cubique (*Fd*-3*m*). Dans ce dernier, les molécules d'azote sont sphériquement désordonnées. Cependant, à 10 GPa le composé $Xe(N_2)_2$ subit une transition de phase martensitique vers une maille tétragonale ($I4_1/amd$) où les molécules d'azote, contraintes par l'interaction quadrupole-quadrupole entre N_2-N_2, s'alignent presque complètement, tel que montré dans la Figure 2. Attestant l'efficacité de la précompression chimique, à 30 GPa les distances intermoléculaires dans $Xe(N_2)_2$ sont de 1.97 Å, soit équivalentes à celles mesurées dans l'azote pur à 80 GPa. En mesurant les modes de vibration des molécules d'azote dans le composé, on observe un

affaiblissement de la liaison intramoléculaire N_2 qui se traduit par la baisse de la fréquence de vibration avec pression (voir sur la Figure 2). Ce phénomène est aussi observé dans l'azote pur à 80 GPa et indique que la proximité des molécules d'azote provoque une redistribution électronique progressive d'intramoléculaire vers intermoléculaire. Cette délocalisation électronique semblait prometteuse pour la rupture de la liaison triple N≡N et la polymérisation du composé $Xe(N_2)_2$.

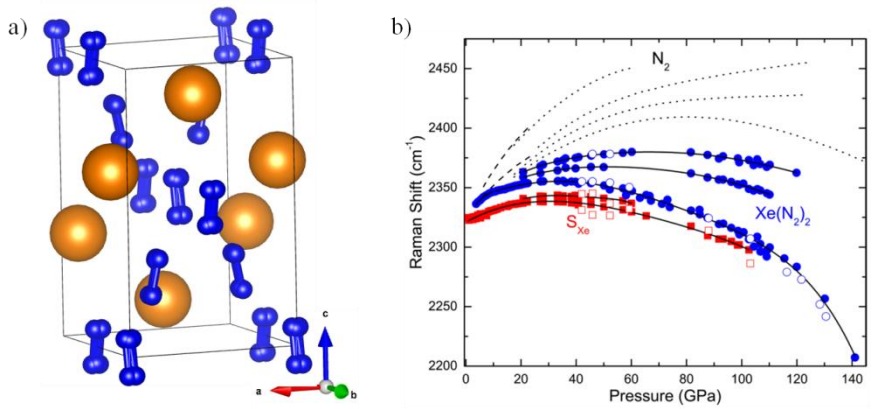

Figure 2 : a) Structure cristalline du composé $Xe(N_2)_2$ dans sa phase haute pression (*I*4₁/*amd*). Les molécules d'azote ont un très léger désordre. Les sphères bleues et orange représentent des atomes d'azote et de xénon, respectivement. b) Évolution en pression des modes de vibration des solides $Xe(N_2)_2$ et S_{Xe} (solide riche en xénon) ainsi que de l'azote pur. Vers 30 GPa, le vibron principal du composé $Xe(N_2)_2$ commence à diminuer avec la pression, signe de l'affaiblissement de la liaison intramoléculaire N_2. Un phénomène semblable est observé dans l'azote pur à 80 GPa.

Le composé $Xe(N_2)_2$ a été comprimé jusqu'à 154 GPa et chauffé à 2000 K sans qu'une transition de phase ne soit observée. En se basant sur le second solide découvert lors de l'étude du diagramme de démixtion binaire — le solide riche en xénon — il a été déduit qu'une importante interaction Xe-N était aussi induite par la pression. Cette interaction, bien qu'affaiblissant aussi la molécule d'azote, viendrait stabiliser l'ensemble de la structure cristalline et empêcher une transition de phase vers une structure polymérique.

Ce n'est qu'en chauffant nos échantillons de Xe-N_2 pour une durée prolongée (environ 1h) à des pressions et températures encore plus élevées qu'une transition de phase a été observée. Les nouvelles raies de diffraction détectées ne correspondent pas avec la structure XeN_6 prédite. Bien que la qualité des données de diffraction ne permette pas la résolution structurelle du nouveau solide, des modes de vibration de basse fréquence pouvant correspondre à des liaisons simples N-N furent détectés. Ce composé, présumé comme étant un composé de xénon polyazoté, a été suivi jusqu'à 23 GPa lors de sa décompression.

La troisième étude porte sur les systèmes N_2-H_2, reconnus comme ayant une riche chimie. Aux conditions ambiantes, sept composés N-H ont déjà été synthétisés, incluant les azanes (familles de composés N_xH_{x+2}) ammoniac (NH_3) et hydrazine (N_2H_4). Les calculs théoriques prévoient une interaction chimique exacerbée entre ces deux éléments et une grande variété de nouveaux arrangements N-H qui serait stabilisés par la pression. Parmi ceux-ci figurent plusieurs matériaux énergétiques tels que de longs azanes, des couches bidimensionnelles d'azotes simplement liés et des espèces anioniques exotiques comme le pentazole ($N_5^-H^+$) [19–23]. Des expériences précédemment réalisées sur des mélanges N_2-H_2 avaient résolu le diagramme de démixtion binaire et découvert deux composés de van der Waals, de stoechiométrie $(N_2)_6(H_2)_7$ et $N_2(H_2)_2$. La structure du premier composé avait été résolue et il avait été observé réagir chimiquement vers 50 GPa pour former du NH_3 ionisé (NH_2^- NH_4^+) [24]. Deux autres séries d'expériences avaient aussi été réalisées sur des poudres de diverses concentrations (allant de 5% à 80% molaire de N_2) jusqu'à 50 GPa. De façon similaire au composé $(N_2)_6(H_2)_7$, une réaction chimique induite par la pression était observée vers 50 GPa mais, interprétée comme produisant de longs azanes hautement énergétiques [25,26]. Sachant que ces poudres doivent respecter le diagramme de démixtion binaire et que $(N_2)_6(H_2)_7$ réagit pour produire de l'ammoniac ionisé, il semblait donc que les azanes longs devraient résulter de la réaction chimique du composé $N_2(H_2)_2$.

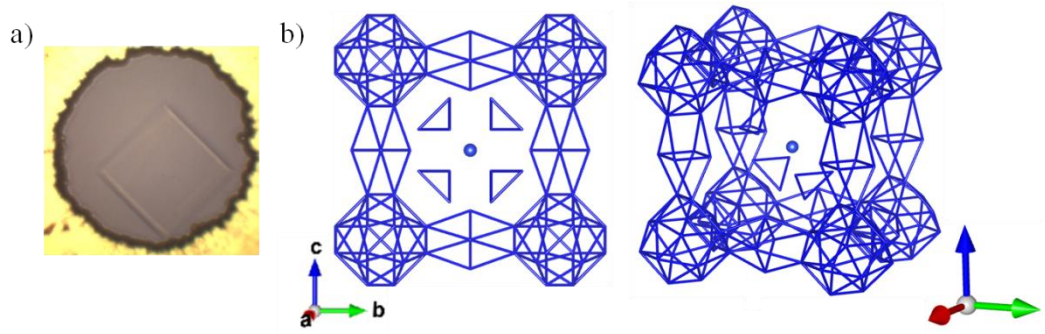

Figure 3 : a) Microphotographe d'un monocristal de $N_2(H_2)_2$. b) Structure cristalline en bâton du solide $N_2(H_2)_2$. Uniquement le sous-réseau d'atomes d'azote est représenté. Une structure en cage, contenant l'hydrogène moléculaire, est clairement visible.

Nous avons étudié l'évolution du composé $N_2(H_2)_2$ sous pression jusqu'à 60 GPa. Sa structure cristalline a pu être résolue par diffraction de rayons X sur monocristal. Totalisant 123 molécules et un volume de 2007.10(1) Å^3 à 7.3 GPa, cette structure complexe est constituée de larges cages formées par un sous-réseau d'atomes d'azote piégeant les molécules d'hydrogène (voir Figure 3). Vers 50 GPa, il a été observé que le solide de $N_2(H_2)_2$ réagit lui aussi chimiquement (voir Figure 4). La signature vibrationnelle du produit de réaction indique que des azanes de différentes longueurs

avaient effectivement été produits. En raison de la stoechiométrie de $N_2(H_2)_2$, identique à celle de l'hydrazine (N_2H_4), la présence de résidus de N_2 ou de H_2 permet d'identifier si des azanes plus courts que celui-ci (consommant plus de H que de N) ou plus longs (consommant plus de N que de H) ont majoritairement été produits. Il s'est avéré que de l'azote moléculaire a pu être détecté; attestant que l'ammoniac (NH_3) était en majorité obtenue comme produit de réaction. Les deux composés de van der Waals réagissant pour produire majoritairement des solides de stoechiométrie NH_3, il est conclu comme étant très improbable que les poudres, composées de ces deux solides, aient comme produits de réaction surtout de très longs azanes.

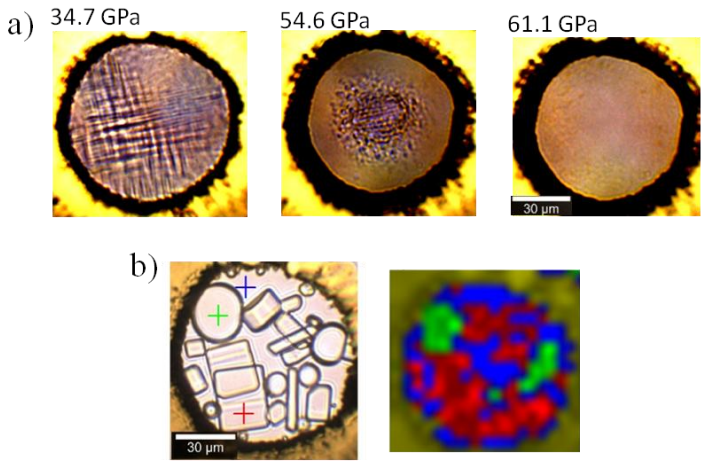

Figure 4 : a) Microphotographes d'un monocristal de $N_2(H_2)_2$ remplissant toute la cavité expérimentale. À partir de 50 GPa, une réaction chimique induite par la pression est amorcée. Le produit de réaction est facile à identifier vu sa couleur jaunâtre. La réaction se complète vers 60 GPa. b) Microphotographe du même échantillon à 1.2 GPa suite à sa décompression. Vers 10 GPa, une nouvelle réaction chimique se produit résultant en la conversion d'ammoniac en hydrazine. À l'équilibre solide-fluide, une cartographie par spectroscopie Raman (droite) permet d'identifier des monocristaux d'hydrazine (rouge), de l'hydrazine liquide (bleu) et des bulles de N_2-H_2 (vert).

Lors de la décompression des produits de réaction du monocristal de $N_2(H_2)_2$ à des pressions sous 10 GPa, une nouvelle transformation chimique est observée. Une cartographie par spectroscopie Raman de l'échantillon, illustrée sur la Figure 4, démontre que la présence d'un seul type d'azane, l'hydrazine, est présent. L'ammoniac établi comme étant stable sous ces conditions, s'est converti en hydrazine, qui lui est métastable. Cet apparent accroc à la thermodynamique, bien que non sans précédent [27], n'est pas encore complètement élucidé.

La quatrième étude effectuée dans le cadre de cette thèse porte sur les mélanges lithium-azote. Étant donné la facilité avec laquelle le lithium donne son unique électron de valence, cette investigation permet de voir l'effet d'une précompression chimique exercée directement par un transfert électronique. Aux

conditions ambiantes, le lithium réagit déjà avec N_2 et permet de briser la liaison covalente triple de l'azote moléculaire pour produire les solides Li_3N et LiN_3, composés des cations Li^+ et des anions N^{3-} et N_3^-, respectivement. L'objectif de cette étude était de produire par pression le composé Li-N le plus riche en azote comportant des entités polyazotés. Ces expériences sont guidées par le fort pouvoir réducteur de Li et par des calculs. Ceux-ci prévoient une riche chimie Li-N à haute densité, avec plus de six stoechiométries permettant des composés stables ($Li_{13}N$, Li_5N, Li_3N_2, LiN, LiN_2 and LiN_5), outre ceux connus aux conditions ambiantes [28–31].

Le composé LiN_5 – le plus riche en azote – est particulièrement intéressant puisqu'il est constitué d'un anion pentazolate (N_5^-), pentagone d'azotes hautement énergétiques. Pour cette raison, la synthèse d'une forme stable de pentazolates aux conditions ambiantes a longtemps été un grand objectif des chimistes. Tout récemment, ceux-ci furent synthétisés et stabilisés grâce à de larges matrices, sous la forme de $(N_5)_6(H_3O)_3(NH_4)_4Cl$ ou ($[Na(H_2O)(N_5)_2]\cdot 2H_2O$ et $[M(H_2O)_4(N_5)_2]\cdot 4H_2O$, M = Mn, Fe, et Co) [32–34]. Bien que constituant un énorme progrès, ces composés sont encore relativement pauvres en azote et donc peu énergétique. Par opposition, le pentazolate dans LiN_5 serait stabilisé uniquement par un atome de lithium et est donc une alternative beaucoup plus attractive que les composés précédemment obtenus. D'après les calculs, un solide de LiN_5 pourrait contenir une énergie de 2.72 kJ/g, et serait donc plus performant que la plupart des matériaux énergétiques communément utilisés [28].

Conformément aux prédictions, nos expériences ont permis la synthèse de quatre stoechiométries différentes de composés Li-N à partir d'un échantillon de lithium pur entouré d'une beaucoup plus grande quantité d'azote moléculaire. Le solide Li_3N, déjà bien connu et caractérisé, est obtenu dès la mise en contact du lithium et de l'azote. À partir de 10 GPa, un solide de stoechiométrie LiN_2 fut produit pour la première fois suite à une chauffe (1200 K). Sa structure cristallographique a pu être déterminée, adoptant une maille hexagonale ($P6_3/mmc$) et est constituée de pernitrures – dimères d'azote de charge négative – d'un ordre de liaison N-N avoisinant 2.5. Dans les zones de l'échantillon plus pauvre en azote, un second composé fut synthétisé, le solide LiN. De maille orthorhombique (*Cmcm*), il comprend lui aussi des pernitrures qui ont, cette fois, un ordre de liaison plus faible approchant 1.5. Au-dessus de 45 GPa, la phase la plus riche en azote prévue par les calculs, le pentazolate de lithium LiN_5 fut obtenue, suivant le chauffage par laser de l'échantillon à des températures de plus de 2500 K. Les structures des composés Li-N découverts lors de cette thèse sont présentés sur la Figure 5.

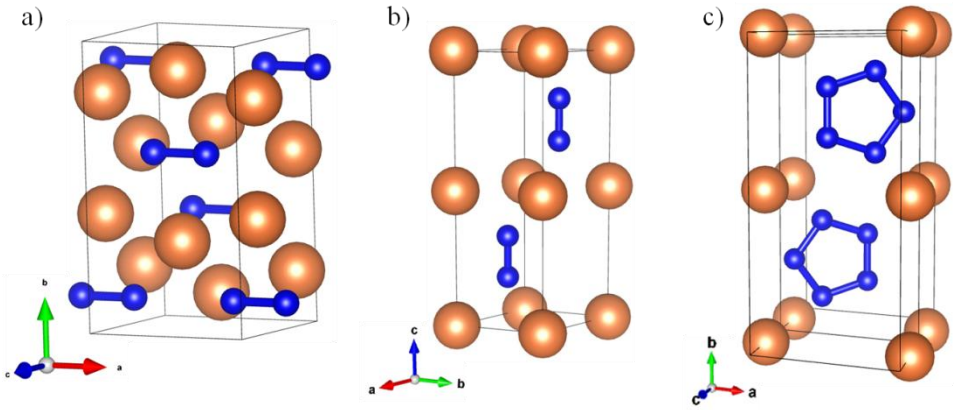

Figure 5 : a) Structure cristalline du solide LiN, contenant des pernitrures. b) Structure cristalline du composé LiN_2, lui aussi formé de pernitrures. c) La structure du solide de LiN_5, tel que proposée dans la littérature [28]**. Les sphères orange et bleues représentent les atomes de lithium et d'azote, respectivement.**

Un résultat important est que le solide de LiN_5 a pu être récupéré aux conditions ambiantes, comme démontré par spectroscopie Raman et spectrométrie de masse. Sa synthèse et sa métastabilité aux conditions ambiantes sont une démonstration du potentiel des synthèses haute pression pour produire des matériaux à haute densité d'énergie qui peuvent rivaliser et même excéder les performances des composés produits par chimie classique.

La recherche faite durant cette thèse est une claire illustration de l'efficacité du paramètre pression pour la synthèse de nouveaux matériaux polyazotés à haute densité d'énergie. Dans chacun des systèmes étudiés, que ce soit l'azote pur ou les mélanges Xe-N_2, N_2-H_2 et Li-N_2, une nouvelle forme d'arrangement N-N simplement lié fut découverte. Dans le cas des mélanges N_2-H_2 et Li-N_2, ces composés ont été produits à des pressions bien en deçà de l'azote polymérique pur, soit 50 et 45 GPa respectivement. La synthèse de LiN_5 et tout particulièrement sa récupération aux conditions ambiantes est une étape importante dans la synthèse de composés énergétiques par pression.

La chimie des hautes pressions est encore à ses débuts comparativement à la chimie classique sous conditions ambiantes. Les outils expérimentaux, et en particulier les géométries d'échantillons, devront certainement encore être améliorés pour permettre plus de flexibilité et une plus grande variété de techniques de caractérisation. Les travaux de cette thèse établissent la chimie des hautes pressions comme une réelle possibilité pour la synthèse de matériaux à haute densité d'énergie avec des

applications aux conditions ambiantes. En particulier, les mélanges à base d'azote et d'hydrogène devraient être revisités en utilisant des pressions élevées combinées à des températures élevées qui pourraient entraîner la formation du pentazole; l'ultime arrangement N_5. Alors que les études étaient jusqu'ici limitées aux composés binaires, des composés ternaires et même quaternaires commencent à être envisagés et fourniront sans aucun doute de nombreuses autres possibilités pour la synthèse de nouveaux matériaux à forte densité d'énergie. Enfin, des méthodes telles que la méchanochimie et la photochimie pourront aussi permettre d'abaisser fortement la pression de synthèse des composés polyazotés.

THESIS SUMMARY

The goal of this thesis is to synthesize novel polynitrogen compounds by pressure as the next-generation high energy density materials (HEDM). To achieve this, the physico-chemical properties of pure nitrogen as well as the xenon-nitrogen, hydrogen-nitrogen and lithium-nitrogen mixtures were studied under extreme pressure and temperature conditions. In the case of the compression of pure nitrogen, a novel polymeric nitrogen solid composed of interconnected chains of N_6 rings was produced at 250 GPa and 3300 K, and then found metastable down to at least 60 GPa. The low pressure Xe-N_2 investigation revealed the formation of a stoichiometric $Xe(N_2)_2$ van der Waals compound. Above 150 GPa and 2500 K a xenon-polynitrogen material was observed and preserved down to 23 GPa. The N_2-H_2 study, focusing on the characterization and high-density behavior of the $N_2(H_2)_2$ van der Waals compound, uncovered its pressure-induced chemical reaction near 50 GPa. The reaction products were determined to be of the azane family (N_xH_{x+2}), with ammonia (NH_3) being the main constituent, disproving results previously reported in the literature. Intriguingly, decompression of the reacted sample resulted, below 10 GPa, in the transformation of ammonia into its thermodynamically less stable counterpart hydrazine (N_2H_4). Lastly, the Li-N_2 system proved to be of great interest due to the large array of anionic nitrogen moieties discovered (N^{3-}, $[N_2]^{\sim 2}$ $[N_2]^{\sim 1}$ and N_5^-), owing to the rich chemistry between these two elements. In particular, lithium pentazolate (LiN_5), containing the elusive energetically-rich pentazolate anion, was synthesized above 45 GPa and 2500 K. Moreover, it could be retained down to ambient conditions. It is the room-condition polynitrogen compound with the largest fraction of nitrogen by weight and the first polynitrogen HEDM produced by high pressure and retrieved down to ambient conditions. These results demonstrate the potential of high pressure for the synthesis of industrially relevant HEDM.

TABLE OF CONTENTS

Remerciements **3**

Résumé de la thèse **5**

Thesis Summary **17**

Introduction **23**

I. The significance of polynitrogen compounds 23

II. The high pressure route: parameters at play 24

II. A. Parameters for metastability *27*

II. B. Low pressure formed polymeric nitrogen arrangements *29*

III. The selected systems for investigations 32

Experimental Techniques in High Pressure Physics **35**

I. Sample preparation, high pressure and high temperature generation 36

I. A. Diamond anvil cells *36*

I. B. Gas loading of mixtures and reactive samples *41*

I. C. Laser-heating *43*

I. D. Pressure measurements *45*

II. Characterisation techniques and data analysis 49

II. A. X-ray diffraction *49*

II. B. Raman Spectroscopy *66*

Nitrogen under extreme conditions: Phase diagram 73

I. The nitrogen molecule 73

II. Solid phases of pure nitrogen 74

II. A. Low pressure phases of pure molecular nitrogen 75
II. B. High pressure phases of pure molecular nitrogen 80
II. C. Polymeric nitrogen phases 82

III. The nitrogen melting curve 85

Novel pure nitrogen polymeric phases 87

I. Introduction 87

II. Article 89

Search for xenon polynitrogen compounds.....115

I. Introduction 115

II. Article 120

III. Chemical reaction in the Xe-N system.....131

Series of chemical transformations in the N_2-H_2 system.....137

I. Introduction 137

II. Article 143

Synthesis of high energy density lithium-nitrogen compounds.....157

I. Introduction 157

II. Articles 161

Conclusions.....209

From theoretical predictions to experiments.....212

High pressure synthesis of polynitrogen compounds: the next steps.....213

Polynitrogen compounds: where to now? 213
Machine learning 215
Development of experimental techniques 216

Annex.....219

I. High pressure investigation of iron and nitrogen: the search for an iron pernitride 219

II. Articles 220

III. Data on the Xe-N solid 239

References 241

INTRODUCTION

I. *THE SIGNIFICANCE OF POLYNITROGEN COMPOUNDS*

On July 20th 1969, a NASA crew landed on the lunar ground, seen at the time as the culminating point of space race. Four days earlier, the Apollo 11 spacecraft had been launched from Kennedy Space Center by the Saturn V rocket. The rocket weighted 2970 tons, representing more than 21 times its payload of 140 tons. Spread across three stages, the first filled with refined kerosene and liquid oxygen (LOX) and the second and third with a mixture of liquid oxygen and liquid hydrogen (LH2), the propellant represented about 93% of the total rocket's mass. Even now, close to 50 years later, the Saturn V rocket still holds the record of the heaviest carried payload sent to low Earth orbit.

Since then, vast improvements were made to space rockets, including the rocket engines redesign, lighter tanks and an overall reusability. Solid propellants were also introduced, but while they have a lower efficiency than their liquid counterparts they are mostly used for their lower cost and greater practicability. These developments improved their overall safety, reliability, performance and cost-effectiveness. Curiously, no significant advancements were realized towards the most critical aspect: a high thrust high specific impulse propellant.[1] Indeed, five decades later, the best high I_{sp} propellant is deemed to be cryogenic LOX/LH2 with a value of about I_{sp} = 450 s (in vacuum), previously employed in the Saturn V rocket. Others, such as liquid fluorine and liquid hydrogen were shown to have a marginally higher but with much greater risks associated. Even now, the propellant represents more than 90% of a rocket's mass

[1] The specific impulse (I_{sp}), typically used to define a propellant's performance, is defined as the total impulse delivered per weight unit of propellant consumed.

and thus higher performance materials would make for dramatic improvements, increasing the carried payload and allowing for faster travel.

In this context, the synthesis of a novel high energy density material could be ground-breaking for spatial applications. Polynitrogens compounds are considered promising since the versatility of nitrogen bonding is particularly well adapted for the chemical storage of energy. This is due to the large energy difference that exists between the triple-bonded N≡N and the single-bonded N-N. Indeed, the triple bonded nitrogen molecule has one of the strongest bonds with an energy of 954 kJ/mol while the single bond is comparatively very weak, with a bond energy of 160 kJ/mol. Transitioning from the single to triple bonded state releases 794 kJ/mol, which is close to five times the energy produced by any conventional energetic material in use today [3]. As such, a solely single-bonded nitrogen solid was deemed having a great potential as the next generation propellant as well as an explosive. Moreover, this compound also makes for *clean* high energy density materials having pure molecular N_2 as its sole decomposition product. However, the low activation barrier towards decomposition renders the synthesis of stable polynitrogen compounds very challenging.

Many new neutral polynitrogen entities are predicted from theoretical calculations, including the N_4, N_6, N_8, N_9, N_{10} and even up to a fullerene-type N_{60} (see review article Ref. [35]). Among those, N_4 is the only neutral nitrogen molecule that was experimentally observed, and has a lifetime of about 1 μs [36]. The synthesis of charged polynitrogen arrangements stabilized by other atoms was more successful and includes N_3^-, N_4^+, N_5^+ and the N_5^- [36–38]. All but N_4^+ are stable in the bulk at ambient conditions. Azides (N_3^-) may be stabilized solely by a single alkali cation while N_5 cation and anion can be secured in large matrices, namely N_5AsF_6 as well as the $(N_5)_6(H_3O)_3(NH_4)_4Cl$ salt and metal pentazolate hydrate complexes ($[Na(H_2O)(N_5)_2]\cdot 2H_2O$ along with $[M(H_2O)_4(N_5)_2]\cdot 4H_2O$, M = Mn, Fe and Co) [32–34,38]. Yet, due to their low nitrogen weight ratio, these compounds are not competitive high energy density materials (HEDM).

The objective of this thesis is the synthesis of novel high energy density polynitrogen compounds by a method alternative to conventional ambient conditions chemistry: high pressure. With its own challenges and difficulties, this method has a great potential to produce previously-unobserved energetic nitrogen phases.

II. *THE HIGH PRESSURE ROUTE: PARAMETERS AT PLAY*

From a thermodynamic point of view, the search for novel phases is done through the exploration of the Gibbs free energy landscape. The Gibbs free energy G is

given by the equation $G = U + pV - TS$, in which U is the system's internal energy, T its temperature, S its entropy, V its volume and p its pressure. Pressure is especially effective since in the multi-megabar range, the pV term can exceed a 10 eV (965 kJ/mol) difference in the Gibbs free energy, larger than the strongest chemical bonds [1]. Not only is pressure very potent to change G, but the way it shapes a material is equally important. To better illustrate this point, let's first consider the case where the energy transferred to a material is provided by increasing temperature. This would first favor a more open structure, such as a bcc, and as temperature continues to go up, it would eventually cause melting, decomposition into elemental species and even ionization. However, the same material's behavior upon the same energy transfer but through pressure is radically different and, for chemistry purposes, much more favorable. Indeed, what is instead observed is an electron delocalization, leading to extended solids and metals. This is commonly attributed to the electron's kinetic energy dependency with density ($\propto \rho^{2/3}$) which increases much faster than the electrostatic potential energy ($\propto \rho^{1/3}$). As such, at high pressure the localized electrons progressively become less stable as the kinetic energy overcomes the electrostatic potential energy, thus eventually leading to extended polymeric solids and metals [2].

The first demonstration of the potential of pressure to help break the strong triple-bond of molecular nitrogen was executed by Haber in 1909. In the particular context of those times, the natural reserves of niter, indispensable as a fertilizer for the efficient growth of crops, were running dangerously low. New sources of fixated nitrogen were thus direly needed to prevent mass famines. By a savvy process, Haber managed to produce ammonia from pure molecular nitrogen and hydrogen by mixing them at pressures and temperatures above 100 bars and 900 K, respectively, in the presence of an osmium catalyst [39]. The tabletop experimental process was later refined and adapted for industrial production with the help of Bosch at the BASF chemical company. Attesting to its efficiency, the process is still widely used today.

In the late 20th century, theoretical calculations performed by Mailhiot *et al*. predicted that under sufficient compression, the electron delocalization would cause pure molecular nitrogen to polymerize and produce a purely single-bonded nitrogen solid [4] at a pressure of 50 GPa. At a first glance, these calculations seem at odds with experiments that had detected the molecular vibrational mode of molecular nitrogen up to 180 GPa [40]. However, this set of experimental data was considered in calculations and an explanation was provided: the molecular state would be metastable at these pressures as a significant activation barrier would exist, impeding the transition towards the polymeric state. The structure of the polymeric compound was calculated to be *cubic gauche* (cg), a highly symmetric cubic lattice ($I2_13$) with a single N-N bond length of 1.40 Å. Its expected low pressure stability suggested that cg-N would perhaps

be metastable down to ambient conditions [4,41]. An energy barrier of 0.86 eV/atom impeding its decomposition to the molecular state was calculated and no mechanical instabilities down to ambient pressure were detected, all of which suggested that cg-N could be retrieved upon complete decompression.

At its expected density at ambient conditions (3.91 g/cc), the properties of cg-N that are the most relevant for propellants (I_{sp}) and explosives (detonation pressure) are compared in Table 1 and 2 to commonly used materials. As it can be seen, it is calculated to have a theoretical I_{sp} of 510 s in vacuum and a detonation pressure of 660 GPa, ten times larger than the best non-nuclear explosive, thus validating its extraordinary properties as a high energy density material.

Table 1: Representative values of I_{sp} for common propellants in vacuum compared to the predicted value for cg-N [42,43].

Compound	Specific impulse (I_{sp}, s)
cg-N	510*
LOX/LH2	457
LOX/Methane	365
N2O4/N2H4	348
LOX/RP-1	331
LOX/Butane	255

* theoretical value

Table 2: Explosive properties of common explosives compared to the predicted values for cg-N. Data from Ref. [44].

Compound	Density (g/cc)	Detonation Pressure (GPa)	Energy*
Nitrocellulose	1.65	21.2	60
HMX	1.91	38.5	100
CL-20	2.04	47.8	121
cg-N	3.91	660	1060

* energy normalized for a HMX value of 100

An experimental group announced in 2004 the synthesis of the single-bonded nitrogen network polymeric nitrogen. X-ray diffraction characterization confirmed its structure to be the one predicted by the simulations and Raman spectroscopy featured the symmetric stretching mode corresponding to a single covalent N-N bond. The minimal synthesis pressure as still found to be above the calculated value of 50 GPa. Indeed, cg-N was observed to form at 110 GPa after laser-heating the sample to

temperatures above 2100 K [10]. Moreover, the compound could not be retrieved down to ambient pressure as it decomposed to its molecular form near 42 GPa following a very weak red-laser illumination. Based on its determined equation of state, a density of 3.91 g/cc was to be expected after the complete pressure release. These results demonstrated high pressure to be a valid approach, if not the only one, to synthesize the ultimate green high energy density polymeric nitrogen. However, this solid is still a ways off before being operative for real-world applications. The most obvious issue is surely the apparent lack of metastability down to ambient conditions. Also, the extreme pressure conditions needed to form it are ways beyond industrial capabilities, which are typically limited below 10 GPa.

The pressure synthesis of novel, improved high energy density polynitrogen compounds is the objective of this thesis. Two obstacles need to be tackled, namely 1) the compound's metastability, ideally down to ambient conditions and 2) to lower the pressure conditions for synthesis, preferably below 10 GPa. Solving these two issues could result in an industrially relevant compound. As described in details below, the chosen strategy is to combine nitrogen with a variety of elements in order to form advantageous chemical precursors, favorable due to their potential for chemical precompression, topochemistry and laser-heating. These precursors have been selected with the guidance of theoretical predictions. The synthesized compounds were thoroughly characterized, mainly by X-ray diffraction as well as Raman spectroscopy measurements. Then, their recovery at ambient pressure was systematically attempted.

II. A. Parameters for metastability

A compound's metastability rests solely on one factor: the height of its energy barrier towards a more stable state. As schematized in Figure 1, pressure changes the energy landscape of a system and often induces a shift in the most stable state. This allows to produce a phase that is not stable at ambient conditions but that is under specific thermodynamical conditions. Retrieving the high pressure phase back to ambient conditions, for example, requires a sufficiently large activation (or energy) barrier blocking the transformation back to the energetically-favored state. Theoretical calculations often calculate a crystal's phonon dispersion curve to ensure its mechanical stability; i.e. that the phase is indeed sitting in an energy minimum [45]. In layman terms, this requires that for a small motion of each of the crystal's atoms, a restoring force dragging the atoms back to their equilibrium position exists. The deeper the energy well, the stronger the restoring force and thus the larger metastability.

Threatening a phase's metastability is anything that can supply enough energy to cross the protective energy barrier, with the most obvious culprit being temperature. Indeed, a temperature of 298 K (25°C) corresponds an energy of 25.7 meV/atom. Thus, under ambient conditions a metastable compound critically needs to have a higher energy barrier than that value. For comparison purposes, it was calculated that for a perfect cg-N crystal to decompose into molecular nitrogen at ambient conditions, an energy of 900 meV/atom is necessary [4]. More detailed calculations, this time accounting for surface effects of pristine a cg-N crystal under air, calculated an energy barrier only 100 meV/atom [41]. As warned by the authors of that calculations, that is still far off considering all of the phenomenon (defects, surface steps, edges, etc) effecting the activation barrier depth of a real-life crystal. These could undoubtedly further lower the energy required for the decomposition of cg-N and explain its experimentally-observed insufficient stability.

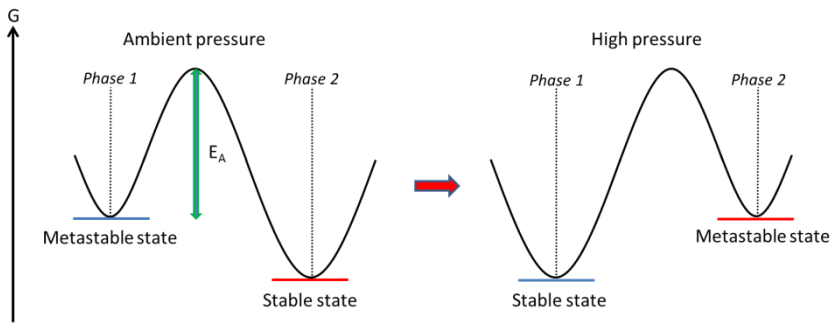

Figure 1: Energy landscape at ambient and high pressure. The activation energy (E_A) is the energy required to access one state from the other, and G is the Gibbs free energy.

A recent density functional theory (DFT) theoretical study using exhaustive datamining on 15097 ambient conditions metastable compounds provide particularly enlightening trends [46]. First, it is shown that, as typically intuited, the greater the cohesive energy of a metastable solid, the larger its activation barrier. As a consequence, elements in the lower rows of the periodic table are progressively worse candidates for high metastability compounds as they tend to form lattices with a lower cohesive energy. Moreover, a direct correlation between the anionic charge and the cohesive energy is found, underlining the importance of electrostatic contributions. Also, nitrogen compounds happen to exhibit the highest energy scale of metastability, explained by their capacity to form very strong covalent and ionic bonds. Additionally, the study looked at the probability distribution of metastability of one, two, three, four and five components compounds along with their activation barrier is calculated. Interestingly, while polymorphs with a larger amount of components have both a lower

activation barrier and a lower propensity to form, compounds resulting from a phase separation have a much higher activation barrier and higher probability to be produced. Finally, it was found that solids which are the Gibbs free energy minimizing state under some thermodynamic condition (pressure, temperature, etc) have a greater probability to be metastable compounds back at normal conditions; in opposition to synthesized solids that were at no point the most stable phase. As drawn in Figure 1, this is typically what is achieved during the pressure synthesis of compound and thus emphasizes the pressure parameter to be a capable method to produce metastable compounds.

II. B. Low pressure formed polymeric nitrogen arrangements

The second objective can now be discussed, namely how to obtain novel polynitrogen phases under less stringent pressure conditions. Two approaches are possible: 1) discovering a new form of polynitrogen compound by mixing nitrogen with another chemical entity and 2) lowering the pressure of synthesis of a known compound by providing extra energy to the system or by choosing an appropriate precursor. These approaches are certainly not mutually exclusive.

II. B. 0. ***New forms of polynitrogen compounds***

This approach, perhaps the most discussed in the literature, is based around an intuition-guided approach revolving around mixing nitrogen with other elements. The interaction of nitrogen with another chemical entity opens up the possibility of new nitrogen arrangements. The energy landscape of the nitrogen mixture system can be explored by structure searching algorithms that may, or may not, reveal new compounds composed of polynitrogen subunits stable under low pressures. Theoretical calculations on this subject have recently exploded in numbers, providing a large variety of polynitrogen arrangements stabilized by other elements. These elements include mostly alkali metals, alkali earth metals, transition metals and even some noble gases [23,47–56]. Experiments are direly needed to confirm or reject these predictions.

While there are no definite rules allowing to predict, before even running calculations or performing the experiments, if a certain nitrogen mixture will produce a polynitrogen network, there is a general guideline. Indeed, at its essence, the objective is to find a chemical entity that will sufficiently perturb the strong nitrogen triple bond so that the N_2 molecule splits apart. This is often accomplished through chemical precompression. The basic idea consists of introducing other chemical entities which,

either by an electron transfer or by the larger volume of their electron cloud, increase the effective average valence electron density of the precompressed nitrogen molecules [11]. The greater the nitrogen electron density, the more favorable are the lower-order bonds and the greater the intramolecular N-N distances. As such, measuring the interatomic (or intramolecular in the cases of H_2 and N_2) distances in the chemically precompressed atoms is typically a good indicator of this phenomenon's effectiveness. Indeed, as a nitrogen molecule shifts from triple- to single-bonded, the N-N bond length increases from about 1.1 to 1.4 Å [57]. Thus, chemical entities that can readily give away electrons, such as atoms with low ionization energies and transition metals, as well as large atomic volume elements are particularly interesting in the context of chemical precompression.

Alkali metal-nitrogen systems provide a good example of the effect of chemical precompression. The alkali metals readily provide a charge transfer of about one electron which enables the formation of an azide (N_3^-), where the nitrogen atoms are bonded through double-bonds. Moreover, larger alkali metals also provide an extra boost in chemical precompression due to their sheer size, bringing closer the nitrogen atoms [31,58,59]. For reasons explained earlier, they also favor the compound metastability since they produce anionic nitrogen entities.

Of course, the mixture needs to be richer in nitrogen than in the perturbing chemical entity so to increase the odds that when the N_2 dimer breaks, N-N bonds are formed instead of bonding nitrogen with another element.

II. B. 1. ***Lowering the synthesis conditions of known polynitrogen compounds***

An alternate approach is to reduce the pressure of synthesis of an already known stable polynitrogen compound by adding extra energy to the compression work. This energy, which would have otherwise been provided by further increasing the pressure, allows overcoming an energetic barrier towards the polynitrogen compound. Laser-heating is the most common and accessible technique, already having been demonstrated on pure nitrogen – and a plethora of other compounds – as the polymeric form was accessed at 110 GPa at 2000 K instead of the amorphous single-bonded type otherwise produced at about 150 GPa [9]. More exotic alternatives include photochemistry, mechanochemistry, the choice of chemical precursors and topochemistry.

Photochemistry – i.e. a chemical reaction induced by the absorption of light – under high pressure was reported on a number of accounts. While it is usually performed by employing highly energetic photons, such as ultraviolet and X-rays

[60,61], a specific, sometimes lower energy, wavelength can be chosen to excite specific molecular levels. For example, N_2-O_2 mixtures above 5 GPa were irradiated by a 1064 nm wavelength photons, corresponding to the energy required to reach the first excited electronic energy level of the O_2 molecule from its ground state. By doing so, a photoinduced chemical reaction was observed and the $NO^+NO_3^-$ compound was produced [62]. More recently, it was demonstrated that a chemical reaction between N_2-H_2 initiated solely by pressure at 47 GPa could also be detected at 10 GPa through near ultraviolet (370 nm) photochemistry. The reaction product was interpreted as azanes (N_xH_{x+2}) of various lengths [25].

High pressure mechanochemistry is generally performed in rotational diamond anvil cells (or in large volume presses such as the ROTOPEC), in which the piston diamond can rotate along the main compression axis. It is reported to reduce the pressure necessary for structural changes (including both chemical reactions and phase transitions) by a factor of 3 to 5. At the nanoscale level, this is interpreted as being due to the strain-induced generation of defects (particularly dislocation pile-ups) that locally produce important stress. These strong defects are thought to allow the barrierless nucleation of the high pressure phases, hence produced at reduced compression [63]. The most notable example of mechanochemistry is perhaps the transformation of rhombohedral boron nitride into the ultra-hard cubic boron nitride at 5.6 GPa instead of 55 GPa under hydrostatic conditions [64].

Another approach is to compress a carefully chosen chemical precursor that may lower the energy barriers impeding the formation a desired compound. This concept is intuitively sound in the case of molecular nitrogen, where a large amount of energy is necessary to break apart the N_2 triple bond. Thus, compressing a nitrogen-rich precursor composed of low bond order N-N entities is more favorable to the formation of an extended nitrogen network than the compression of the same elements mixed with molecular nitrogen. This is exemplified in the case of cesium azide (CsN_3) – in which nitrogen is in the form of a three-membered chain – which was thought to be much more favorable than having Cs and N_2 as reactants in order to produce CsN_5. This strategy was employed to successfully form CsN_5 [49]. Other examples supporting this can be found in theoretical papers. Indeed, it was calculated that the energetically-rich hydronitrogen compound $(NH)_4$, composed of one-dimensional single-bonded nitrogen atoms, could be produced at 36 GPa or 75 GPa depending on whether the compressed precursor was tetrazene (TTZ) or, ammonium azide (AA), respectively [20]. The pressure difference between the two precursors can be explained by the bonding order of their nitrogen atoms. In AA, composed of azides, the bond order is of about 2.5 whereas it is closer to an average of 1.5 in TTZ, made up of (NH_2-N=N-NH_2) molecules.

The topochemical principle provides another set of conditions for a good chemical precursor. This principle states that the preferential reaction pathway in the case of a solid state reaction is the one that minimizes atomic and molecular displacements [65]. As such, the crystalline structure of the reactants often determines the structure of the resulting transformation products. This principle is particularly relevant at high pressures since atomic diffusion is even lower than at ambient conditions. The topochemical effect was demonstrated for both the pressure-induced polymerization of diacetylenes and ethylene [65]. Making good use of this principle can both favor the synthesis of specific geometries of polynitrogens as well as reduce the energy needed for a transformation.

Now having a better handle on the synthesis methods of novel polynitrogen solids from nitrogen-rich mixtures, the eventual means to reduce their formation pressure and the physics behind a compound's metastability, the strategy employed during this Ph.D. thesis can be discussed hereafter.

III. *THE SELECTED SYSTEMS FOR INVESTIGATIONS*

Specific nitrogen systems were chosen for investigation as they seemed promising for the synthesis of improved polynitrogen compounds. Our choices are described below and the questions as well as hopes regarding their outcomes underlined. In all cases, theoretical calculations had been reported in the literature and further had helped guiding our choices.

Pure molecular nitrogen:

At the root of this thesis, it is logical that molecular nitrogen should be the first candidate for an investigation. This would allow the critical acquisition of a reference dataset that will be useful in all subsequent studies as well as to reproduce and reconfirm the established literature data. Of equal importance, significantly overstepping the maximum previously-reported pressure and temperature conditions could allow for the synthesis of a novel form of polymeric nitrogen, as suggested by theoretical calculations. Indeed, a N_{10} diamond-like form of polynitrogen was calculated to be stable above 263 GPa, along with many other arrangements with competitive enthalpies [12]. Could a new single-bonded N-N geometry compound have a greater cohesive energy and thus be easier to retain at ambient conditions? Or perhaps a

discovered novel arrangement could be more accessible by other experimental techniques, such as chemical vapor deposition and laser-shocked syntheses?

Xenon-nitrogen mixture

First among the elements mixed with nitrogen, xenon was a particularly interesting case to observe the effect of chemical precompression based on its very large atomic volume. Would the nitrogen polymerization pressure be reduced proportionally to the percentage of xenon atoms added? Furthermore, knowing that xenon has loosely-bounded valence electrons, would a significant electronic interaction occur between the two elements? If so, would it promote or hinder the formation of an extended network? Moreover, by first determining the Xe-N_2 binary phase diagram, perhaps a van der Waals compound would be discovered and have a structural arrangement facilitating through the topochemical principal a polymerization. Providing further motivation to investigate this system, theoretical calculations have predicted the pressure stabilization of a high energy density polynitrogen-xenon solid. This compound, with a XeN_6 stoichiometry, is expected to form above 145 GPa and is the sole Xe-N compound predicted so far.

Lithium-nitrogen mixture

This mixture would allow to probe the effect of the second parameter in chemical precompression: a gain in electronic density due to an electron transfer. Indeed, the highly reactive lithium atoms were expected to give their sole valence electron to the nitrogen atoms. Would this be more efficient than chemical precompression achieved by the xenon atoms? Moreover, theoretical calculations predicted a large wealth of anionic nitrogen moieties, ranging from N^{3-}, ($[N_2]^{-2}$, $[N_2]^{-4}$), N_3^- and even N_5^- [28,29]. The latter, stabilized as lithium pentazolate (LiN_5), is highly energetic on account of its low N-N bond order and is predicted to be formed below 20 GPa as well as being metastable down to ambient conditions. If the calculations were to hold true, it would be the compound with the largest poly-N over lithium mass ratio (91%) on top of being the first polynitrogen compound produced by pressure. Its experimental confirmation would represent a major breakthrough.

Hydrogen-nitrogen mixture

Though no steric chemical precompression of the hydrogen atoms on the nitrogen atoms is anticipated, theoretical calculations predict many N-H compounds to be produced. These range from azane chains, bi-dimensional polybonded nitrogen layers to anionic species such as the elusive pentazole ($N_5^-H^+$), all expected at pressures below 60 GPa. Furthermore, previous experimental studies are reported in the literature and hint at the synthesis of long, energetically-rich azanes (N_xH_{x+2}) from the compression of N_2-H_2 powders above 50 GPa [25,26]. However, another experimental study has resolved the N_2-H_2 binary phase diagram and determined that these powders would have to be composed of the $(N_2)_6(H_2)_7$ and $N_2(H_2)_2$ van der Waals compounds [24]. Knowing that the compression of a $(N_2)_6(H_2)_7$ single crystal above 50 GPa results in the formation of ionized ammonia, the $N_2(H_2)_2$ compound should be responsible for the synthesis of the long azane chains observed in N_2-H_2 powders. If the structure of the $N_2(H_2)_2$ compound can be determined, perhaps a topochemical effect responsible for the formation of long azanes could be evidenced. The experimental verification of the high pressure behavior of $N_2(H_2)_2$ as well as the possibility to produce other arrangements of hydronitrogen solids motivated the investigation of this system.

To help cross activation barriers, and thus reduce the pressure synthesis of the hypothetical polynitrogen compounds, the various samples, with the exception of N_2-H_2, were laser-heated to typically a few thousands of Kelvin.

The present manuscript is structured as follows. The first two sections describe the high pressure experimental apparatus, the sample preparation methods and the characterization techniques. Next, a whole chapter is devoted to the state of the art on pure molecular nitrogen. Then, following a short introduction, the results obtained during the investigation of pure N_2 as well the Xe-N_2, N_2-H_2 and Li-N_2 mixtures will be presented. Finally, a general discussion on the studies' outcome is made along with an outlook for future work on the synthesis of novel polynitrogen compounds.

EXPERIMENTAL TECHNIQUES IN HIGH PRESSURE PHYSICS

In nature, most of the matter is under pressure and the pressure range is very large. While at the surface of Earth, pressures of about 1086 bars have been measured at the bottom of the Marianna trenches, at its core matter is compressed to 3.6 Mbars, which pales in comparison to the pressure attained in some celestial bodies, reaching $1.6 \bullet 10^{25}$ Mbars in neutron stars. However, only in the last two centuries has man-made high pressure generation been achieved. Accessible first by employing explosives, dynamic pressure studies gained some popularity in the 19th century, period at which the theoretical groundwork was mostly laid out, and in particular Rankine's seminal treatise titled "*On the Thermodynamic Theory of Waves of Finite Longitudinal Disturbance*" in 1857. However, the field of dynamic pressure generation was hindered and slowed down by the lack of high-speed instruments allowing a characterization on the compressed samples, as the shocks could last only between 1 μs to 1 ns. Moreover, even with an ideal setup, the very nature of these experiments does not permit an isothermal compression of matter. Even today, while the diagnostic capabilities have drastically improved and pressures on the order of the Gbar and even the Tbar are attained, the same fundamental difficulties arise.

Parallel to these developments, Percy Williams Bridgman's designed a double anvil press that permitted high static pressures to be obtained. With the large improvements achieved on this first conception, including mostly transparent anvils, a metallic gasket allowing gases to be studied, *in situ* pressure gauges and much more, static pressures of over 1 TPa are now claimed to have been reached. The intrinsically very small dimensions of even the highest-pressure samples (a few cubic micrometers in the Mbar range) is overcome as the latest generation of synchrotrons can produce

tightly focused beams of light of extreme brilliance to probe the sample. Moreover, these allow a plethora of characterization techniques, namely circular and linear polarization (for magnetic studies), high energy resolution inelastic scattering (for dynamical properties), coherence imaging (for sensitive phase contrast images), high energy elastic scattering (for disordered, liquid, amorphous and crystalline systems) and so many more [66]. With so many recent developments granting experimentalists tremendous quantities of tools, it is the golden times of static high pressure physics.

I. *SAMPLE PREPARATION, HIGH PRESSURE AND HIGH TEMPERATURE GENERATION*

The very first anvil cell was produced by Percy Williams Bridgman in early 1930. Although conceptually very basic, this novel apparatus was constituted of a steel structure holding two opposite tungsten carbide anvils between which a sample, typically solid, was positioned [67]. This first device introduced the fundamental principles allowing to generate high pressures. The second breakthrough had to wait until the 1950's to occur, when two groups simultaneously thought of using diamond as anvils [68][69]. The following important developments, giving rise to the traditional apparatus used nowadays, came from the elaboration of a sample cavity, typically constituted of a pierced metallic foil. In the next few sections, each of the vital elements of a diamond anvil cell will be discussed.

I. A. Diamond anvil cells

A diamond anvil cell (DAC) is composed of two main parts: the cylinder and the sliding piston, on both of which are mounted a diamond anvil. By applying a moderate force on the piston, it moves closer to the stationary cylinder thus compressing the sample confined in between the two facing anvils (see Figure 1). Due to the very large ratio between the area of the back and of the very tip (culet) of the diamond, the pressure exerted on the back of the diamond is multiplied at the culet. However, the simplistic formula $P_{culet} = \frac{A_{back}P_{back}}{A_{culet}}$ is not nearly sufficient to calculate the pressure inside the experimental cavity on account of the strain, friction and deformation of the DAC body and of the metallic gasket.

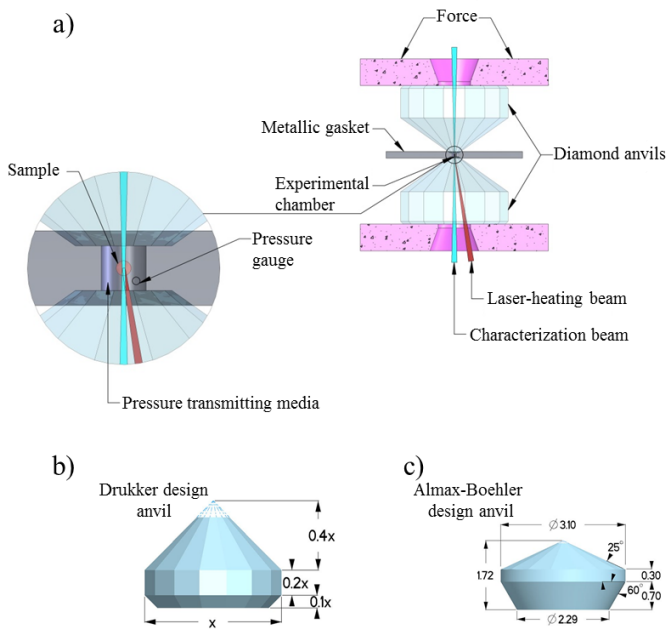

Figure 1: a) Schematic of a diamond anvil cell, equipped with Drukker-type diamond anvils. b) Drukker and c) Almax-Boehler design diamond anvils. The provided values are in millimetres.

There exist two main types of DACs, screw DACs and membrane DACs. As the name suggests it, in screw DACs the piston is screwed into the cylinder while in the membrane DACs, a metallic membrane is inflated by compressed gas and pushes the piston towards the cylinder. The membrane system, improved by Letoullec, Pinceaux and Loubeyre [70] from the initial design of Daniels and Ryschkewitsch [71], is advantageous since it allows a fine control of the pressure applied to the piston and thus to the sample. This is vital for the precise determination of a binary phase diagram as well as for the growth of single crystals. Furthermore, this setup also easily permits a remote regulation of pressure, which is especially useful for synchrotron experiments where opening up the experimental hutch and sample aligning are time consuming as well as for low and high temperature experiments where the cell is in a vacuum chamber. Consequently, this design was used for all experiments presented here. Schematics of this cell are shown in Figure 1 as well as Figure 2.

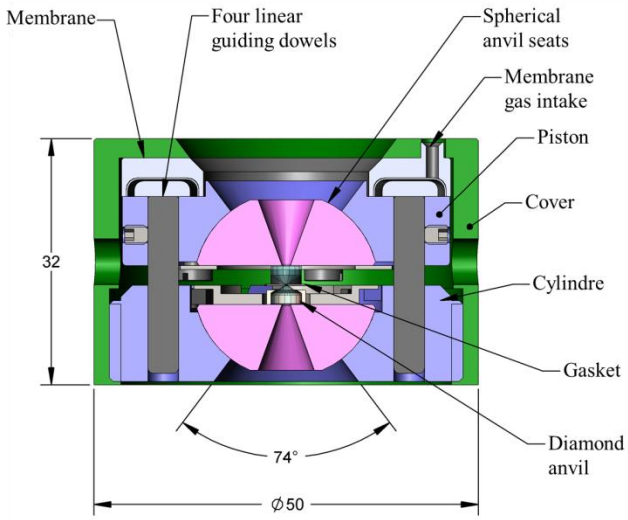

Figure 2 : Complete schematic of a Drukker-type membrane diamond anvil cell.

To achieve very high pressures, the spherical anvil seats on which rest the diamond anvils need to withstand a typical load of ~10 kN. Moreover, a large cell opening is essential for single crystal – and useful for powder – X-ray diffraction experiments, but means less material to back up the diamonds. Thus, a mechanically strong material, namely tungsten carbide boron, boron nitride or titanium diborate, is employed as spherical anvil seats. With the exception of the four tungsten carbide linear guiding dowel, maintaining a perfect alignment of the anvils during a pressure increase, the rest of the cell is typically made of steel (heat-treated Maraging 250). Note that the two different diamond anvil shapes, namely the Drukker and the Almax-Boehler, are used but require slightly different cell geometries (see Figure 1) [72].

I. A. 0. ***Diamond anvils***

Single crystals of diamond are employed in nowadays high pressure cells and have many advantages over tungsten carbide anvils. First, diamond is one of the hardest known materials, achieving a value of 10 on the relative Mohs scale [73]. Second, it has a very high thermal conductivity (2200 W/m·K), reducing the risk of its temperature-induced graphitization (500-900°C at ambient pressure in air) [74]. Third, diamond allows *in-situ* characterization of the compressed sample due to its high transparency to most wavelengths. Its optical properties depend slightly on the concentration of impurities (usually nitrogen atoms, sometime boron) and defects (vacancies). Type I diamonds strongly absorb ultraviolet light above 330 nm and have important absorption bands between 4-6 μm as well as 7-10 μm in the infrared. Diamonds of

higher quality, known as type II, do not strongly absorb in the ultraviolet before 220 nm, have a lower absorption in the 4-6 μm band and are almost completely transparent above 7 μm. Due to their much-improved optical properties in the infrared, they are typically used for infrared absorption spectroscopy measurements. The complete absorption spectra of both types of diamonds can be found in the literature [75].

The maximum pressure that can be achieved using a given diamond anvil mainly depends on its culet size (D). An empirical scale, produced by Ruoff *et al* [76], gives the following relationship:

$$P_{max}(GPa) = 1856\, D(\mu m)^{-1/2}.$$

This formula is plotted in Figure 3. It is regarded as a good rule of thumb for culet diameters between 20 to 300 μm. Indeed, this was recently validated with culets of 20 μm, which allowed reaching a pressure of 398 GPa, easily comparable to the value of 415 GPa given with the above empirical scale [77]. The physics behind this equation is analogous to the Petch relationship as well as to the Griffith criterion: the critical stress for a material found to be inversely proportional to the square root of the characteristic length [78]. In the case of the diamond anvils, the characteristic length translates into the culet size while the pressure within the sample cavity was employed instead of the critical stress to determine the empirical relationship.

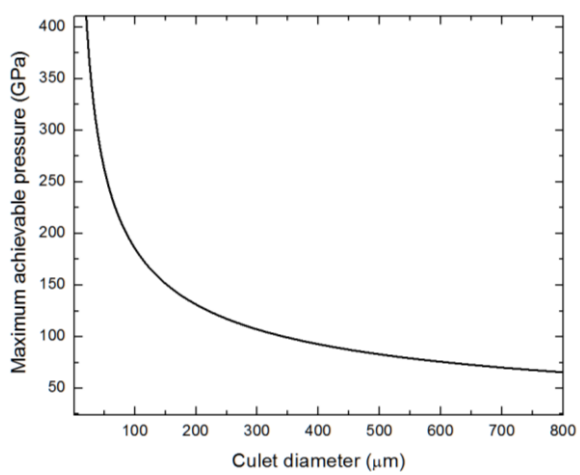

Figure 3: Ruoff's empirical relationship between the maximum achievable pressures with respect to the diamond anvil culet diameter.

However, with focused ion beam machining, new diamond anvils were designed and have allowed even greater pressures to be generated. A tore-shaped anvil has recently been employed to reach pressures nearing 600 GPa on gold [79]. Even the terapascal barrier seems to have been broken using nanocrystalline diamond anvils to

compress gold, however on a very small area of the sample (3 μm in diameter and 1 μm in thickness) [80].

I. A. 1. ***Gasket***

The role of the metallic gasket in a DAC is twofold: 1) contain the sample, thus allowing gases and liquids to be loaded and 2) apply a radial pressure on the sample. Before being employed, the gasket is indented, employing the diamond anvils, to a few tens of gigapascals (~30 GPa) which reduces its thickness and, more importantly, enhances its mechanical properties by strain-hardening it. Only then is the sample cavity pierced, to a size of about 30-70% of the culet's diameter. To do so, an yttrium femtosecond pulsed fiber laser (Amplitude Systèmes) was employed. While a wavelength of 515 nm was typically used, the laser can also emit at 1033 and 344 nm. Coupled with a WS-flex (Optec) motorized piezo-driven scan stages, on which the gasket is mounted, sample cavities of diameter down to 15 μm were accurately drilled. Figure 4 shows an image, obtained by an electron scanning microscope, of a femtosecond laser-made hole in a rhenium gasket.

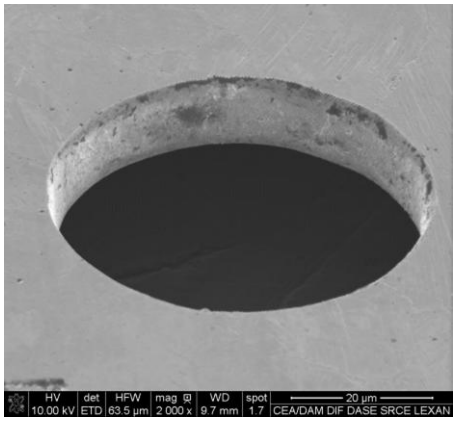

Figure 4: Scanning electron microscope image of a drilled rhenium gasket using a femtosecond pulsed laser.

While gasket materials are partially chosen for their lack of chemical reactivity with most elements, the compression of hydrogen requires extra precautionnary measures. Indeed, due to its size, hydrogen tends to diffuse inside rhenium and stainless steel gaskets. In turn, this weakens the gasket's mechanical properties and slightly changes the sample concentration, as observed in the case of N_2-H_2 mixtures. To prevent this, the sample cavity inner walls were coated with a thin (≈ 2 μm) layer of gold. This was accomplished by filling up and heavily compacting gold (< 1 GPa), using the diamond anvil cell, inside the gasket's hole. Then, all but the gold crown was ablated by

the femtosecond laser. Although, this was not employed during this thesis, a high vacuum metallic coater that allows a thin (a few tens or hundreds of nanometers) coating the inner walls of the experimental chamber can also be used. This technique is useful when much higher pressures are required (> 100 GPa) and therefore the sample cavity is much smaller.

I. A. 2. ***Pressure transmitting medium***

The main role of the pressure transmitting medium is precisely what its name suggets: to transfer the pressure generated from the diamond anvils (and the plastically deforming gasket) in such a fashion that a hydrostatic pressure is applied on the sample. Based solely on hydrostaticity concerns, helium is regarded as the best pressure transmitting media as it solidifies at the highest pressure — 11.5 GPa — and is the solid with the lowest bulk modulus [81,82]. However, other considerations are taken into account when choosing the pressure transmitting media, such as reactivity with the sample, potential destructive diffusion into the diamond anvils, number of diffraction peaks (for X-ray diffraction experiments), Raman modes and infrared absorption as well as the sample chamber dimensions.

In the case of most experiments presented in this thesis, chemical reactions with nitrogen were sought for and therefore nitrogen was the employed pressure transmitting medium as well as acting as a reagent. Solidifying at 2.49 GPa, nitrogen has a low bulk modulus as well as its pressure derivative (K_0=2.69 GPa, K_0'=3.93 and K_0=2.98 GPa and K_0'=3.78 in the δ and ε phases, respectively) making it a fairly good pressure transmitting medium, hydrostatic up to about 13 GPa [75] and quasihydrostatic afterwards, with pressure gradient of about 3 GPa at 44 GPa [83]. Having only a few Raman and infrared active vibrational modes, it however produces many diffraction peaks in the ε phase (rhombohedral, R-3c), which hinder the observation of other solids' diffraction lines [9].

I. B. Gas loading of mixtures and reactive samples

With the objective of synthesizing novel polynitrogen compounds, pure nitrogen or nitrogen gas mixtures (Xe-N_2, H_2-N_2) were typically loaded in the DAC. Due to the very high compressibility of elements that are gases at ambient conditions, their compression from ambient pressure would result in dramatic reduction of the experimental cavity diameter and thus very tiny sample sizes. To avoid this issue, the

gases are loaded into the DAC at high pressures (up to 1400 bars), thus greatly reducing their compressibility and thus the sample cavity shrinkage. Of course, other experiments may also require the loading of gases acting as the pressure transmitting medium.

To reach these high loading pressures, a high pressure gas loading apparatus was used (Sanchez Gas Loading System GLS1500). First, the membrane DAC is left opened in the loading bomb. Two sets of pumps each with an empty volume of 285 cc, one mainly in charge of controlling the DAC membrane pressure and the other of the sample environment pressure, are then filled with the gas or the gas mixture desired to be loaded in the DAC until reaching a pressure of 150-200 bars. Employing a piston-type compression, the gas in the two pumps simultaneously increase in pressure up to 1400 bars on both the DAC's membrane and the loading bomb containing the DAC. In order to seal the DAC, the membrane pressure is further raised an extra ~30 bars. With a camera setup allowing the visualization of the DAC *in-situ*, it can be confirmed that the DAC is closed. Then, the pressure in the loading bomb is brought down to ambient condition while the membrane pump is lowered down in such a was as to keep the sealing pressure constant. The DAC's microvalve can then be sealed, the leftover pressure in the membrane pump released and the DAC disconnected.

When loading gas mixture, its concentration is calculated based on the partial pressure of the two gases corrected with the second order Viriel coefficient, *B(T)*, with *T* being the temperature. The Viriel coefficient takes into account the potential of interaction between the gas particles. The second order expansion of the Viriel equation of state is [84]:

$$\frac{Pv}{RT} = 1 + \frac{B(T)}{v} = 1 + B(T)\left(\frac{P}{RT}\right),$$

where P is the pressure, v the molar volume and R the ideal gas law constant. When determined based on a Lennard-Jones potential, the second order Viriel coefficient *B(T)* can be written as:

$$B(T) = b_0 B^*(T),$$

where $b_0 = -\frac{2}{3}\pi N_a \sigma^3$ and $B^*(T) = \sum_{j=0}^{\infty} \frac{2^{j-3/2}}{j!} \Gamma\left(\frac{2j-1}{4}\right)\left(\frac{k_B T}{\varepsilon}\right)^{-(2j+1)/4}$ [84].

Here, N_a is Avogadro's number, k_B is Boltzmann constant, j is a positive integer and ε as well as σ represent the depth of the potential well and the interatomic distance at which the attractive and repulsive forces are even, respectively.

From the second order Viriel equation of state and a gas partial pressure (P_α, defined as $P_\alpha = x_\alpha P_{mix}$ where P_{mix} is the total pressure of the gas mixture), the concentration of a loaded gas, x_α, can be determined through:

$$x_\alpha = \frac{P_\alpha}{P_{mix}} \left[\frac{\left(1 + \frac{P_{mix} B_{mix}(T)}{RT}\right)}{\left(1 + \frac{P_\alpha B_\alpha(T)}{RT}\right)} \right]$$

where, for a binary gas mixture

$$B_{mix}(T) = \sum_{\alpha=1}^{2} \sum_{\beta=1}^{2} B_{\alpha\beta}(T) x_\alpha x_\beta,$$

in which $B_{\alpha\alpha}(T)$ (and $B_{\beta\beta}(T)$) account for the interaction between same-species particles and $B_{\alpha\beta}(T)$ (as well as $B_{\beta\alpha}(T)$) for the interaction between two different species. As stated above, $B(T) = b_0 B^*(T)$ and thus through b_0 and $B^*(T)$ it contains the crossterms $\varepsilon_{\alpha\beta}$ and $\sigma_{\alpha\beta}$. These can be determined from the Lorentz-Berthelot rule [85], which states that:

$$\sigma_{\alpha\beta} = \frac{\sigma_\alpha + \sigma_\beta}{2} \text{ and } \varepsilon_{\alpha\beta} = \sqrt{\varepsilon_\alpha \varepsilon_\beta}.$$

These values are known for all gases used in this thesis (Xe, H_2 and N_2) [86].

To ensure that the two gases have well blended and form a homogeneous mixture, they are left to mix for over 12 hours before closing the diamond anvil cell.

I. C. Laser-heating

DAC laser-heating allows to reach very high temperatures and pressures that are relevant to planetery sciences and to synthesize novel materials. Two types of high power lasers are typically used: a Nd:YAG laser (λ = 1.064 μm) and a CO_2 laser (λ = 10.6 μm). The emission wavelength of these lasers make each better suited for certain types of materials. Usually, the Nd:YAG laser is employed for opaque and metallic solids whereas the CO_2 laser is more appropriate for transparent or insulating materials, such as oxides and molecular compounds (NH_3, CO_2, H_2O, etc). These continuous wave lasers can generate a beam intensity of up to 100 W which can be focused down to about 10 or 30 μm on the surface of the sample, for the Nd:YAG and CO_2 lasers respectively. Since the temperature is known to decrease dramatically within a few microns into the bulk of the solid [87], even in the case of metals, double-sided laser-heating was typically performed in our experiments to reduce the thermal gradients.

Temperature measurement of the laser-heated samples are achieved by recording the thermal radiation that they produce. Schwarzschild mirrors reflect the heat-produced photons into a spectrometer covering from 400 to 950 nm. A fit of the detected photons to Planck's law is then performed, through the formula:

$$I(\lambda, T) = \frac{2\pi h \epsilon c^2}{\lambda^5 \exp\left(\frac{hc}{\lambda k T} - 1\right)}$$

where T is the temperature, h is Planck's constant, k is Boltzmann's constant, c is the speed of light in vacuum and ε is the sample's emissivity. Using the more general case of a grey body emission, ε is also a fitted parameter. As it can be seen from Figure 5, the thermal emission intensity rapidly decreases with temperature. While temperatures down to 1000 K can still be measured with a typical Si detector, employing a detector sensitive between 1000-1700 nm, such as a InGaAs detector, allows temperatures of 700 K to accurately be measured.

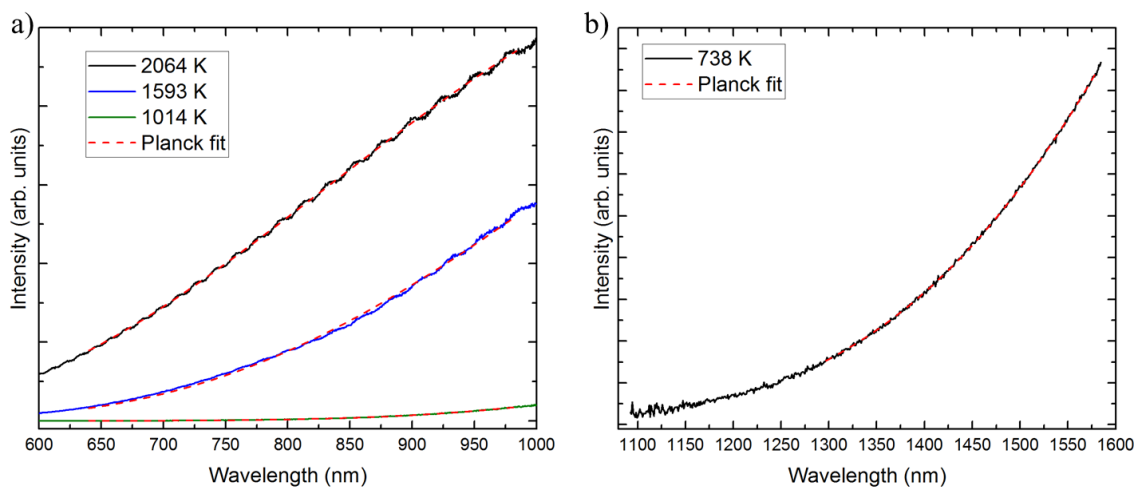

Figure 5: Thermal radiation measured from a tungsten lamp. Spectra at various temperatures, recorded by employing a a) Si (with a single UV-grade fused silica window) and b) InGaAs detector, and fitted using Planck's law, yielding the temperatures shown in the top left of the graph.

I. C. 0. ***Laser-heating nitrogen and nitrogen mixtures***

Three types of samples studied here were laser-heated: pure N_2, Xe-N_2 and Li-N_2 mixtures. In each case, a different element was acting as the laser absorber. Pure nitrogen and xenon have their band gap closing above 160 GPa and 150 GPa, respectively [9,88], and thus become opaque and so good YAG absorbers. In the case of

Li-N_2, pure lithium is a metal and easily heats up under the YAG laser. In the context of this thesis, laser-heating was performed to cross eventual activation barriers impeding a chemical transformation or a phase transition. To make sure that a chemical reaction with the carbon of the diamond anvils did not occur, test runs were performed with a thin layer (~ 200 nm) of a chemical insulator (Al_2O_3, TiO_2) covering the diamond anvil. During these runs, if the same sample behavior was observed, it confirmed that no carbon impurities were taking part.

I. D. Pressure measurements

The accurate determination of pressure in a DAC is a challenge. The main issue resides in the fact that a direct pressure measurement of a sample *inside a DAC* is a complex endeavour that requires the use of specific techniques (ultrasonic measurements, Brillouin scattering, inelastic X-ray scattering) which are not readily available at high pressures (< 75 GPa) and that are very time consuming [89–91]. These methods allow measuring a material's elastic constants which, in turn, can be used to obtain its isothermal bulk modulus (K_T). Through the following relationship, knowledge of the bulk modulus and of the sample's volume (V, typically obtained by X-ray diffraction) can provide the pressure:

$$P(V,T_0) - P(V_0,T_0) = -\int_{V_0}^{V} \frac{K_T(V,T_0)}{V} dV$$

By employing this equation to determine the pressure is considered as a direct measurement and can be used to produce primary pressure gauges. While this method was used for several solids up to high pressures (MgO up to 55 GPa [92], SiC up to 75 GPa [93]), another technique is more commonly employed and allows to obtain primary pressure gauges up to very high pressures. That technique is based on shockwave experiments. During these experiments, a high-speed shockwave is generated through a material, generating high pressures and high temperatures. The Rankine-Hugoniot equations relate a material's pressure (P_{H0}), specific volume (v_{H0}) and internal energy (U_{H0}) before the shockwave as well as right behind the shockfront (P_H, v_H and U_H, respectively) to the shockwave velocity (U_s) and the speed particle velocity inside the compressed region behind the shock front (u_p) [94]:

$$v/v_{H0} = (U_S - u_p)/U_S$$

$$P_H - P_{H0} = u_p U_S / v_{H0}$$

$$U_H - U_{H0} = (P_H + P_{H0})(v_{H0} - v)/2$$

The U_s and u_p parameters can be determined by interferometric velocimetry measurements and thus used to obtain P_H and v_H. However, it must be noted that the values P_H and v_H obtained in this straightforward fashion are actually the pressure and specific volume at the temperature of the Hugoniot. To correct and obtain these parameters down to ambient temperature, a thermodynamic model (typically the Mie-Grüniesen equation of state) which relates the temperature to material's internal energy (see ref. [95]). In this fashion, the cold compression curve $V(P)$ for many simple metals (including Al, Cu, Ta, W, Pt and Au) could be determined [96].

Having these materials' equation of state determined through reliable, direct measurements, the most practical approach is then to calibrate another material's property – one that can conveniently be measured – against these primary pressure gauges. As described below, the most common secondary pressure gauges exploit a material's luminescence, Raman modes (both obtained with optical methods) or its unit cell volume (through X-ray diffraction). Most of these pressure gauges can be loaded along with the studied sample and permit an *in-situ* measurement of the pressure inside the experimental cavity.

I. D. 0. ***Luminescence gauges***

The most popular luminescence gauge is Cr-doped Al_2O_3 – ruby. The introduction of the metallic ion Cr^{3+} creates new energy levels in alumina. Electrons can be excited to these new states by the absorption of photons of a few eV and reemit, upon their de-excitation, photons of mainly two different energy, producing a doublet composed of the R_1 and R_2 peaks.

Due to the modification of the crystalline field by pressure, the energy levels slightly shift during the compression of the ruby (see Figure 6 a)). By calibrating the energy of the photons reemitted against pressure, this fluorescence can afterwards be used to determine the pressure inside the sample cavity. Indeed, the following empirical formula is the most commonly used to relate the measured peak wavelength (λ) and the *in-situ* quasi-hydrostatic pressure (P_H) [96]:

$$P_H = \frac{1920}{9.61}\left[\left(\frac{\lambda}{\lambda_0}\right)^{9.61} - 1\right],$$

where λ_0 is fluorescence wavelength measured at ambient pressure. The uncertainty is established to be of about 0.03 GPa. Furthermore, the ruby fluorescence

gauge also provides qualitative insight about the hydrostaticity conditions in the experimental chamber: as pressure increases and the hydrostaticity decreases, the full width at half maximum of the R_1-R_2 doublet increases (Figure 6 b)). For significantly non-hydrostatic conditions, for example if the R_1 and R_2 lines merge to produce a single peak, the following equation provides a better estimate of the pressure (P_{NH}) [97]:

$$P_{NH} = \frac{1904}{5}\left[\left(\frac{\lambda}{\lambda_0}\right)^5 - 1\right].$$

A ruby of about 3-5 μm is typically loaded along the sample in the experimental cavity.

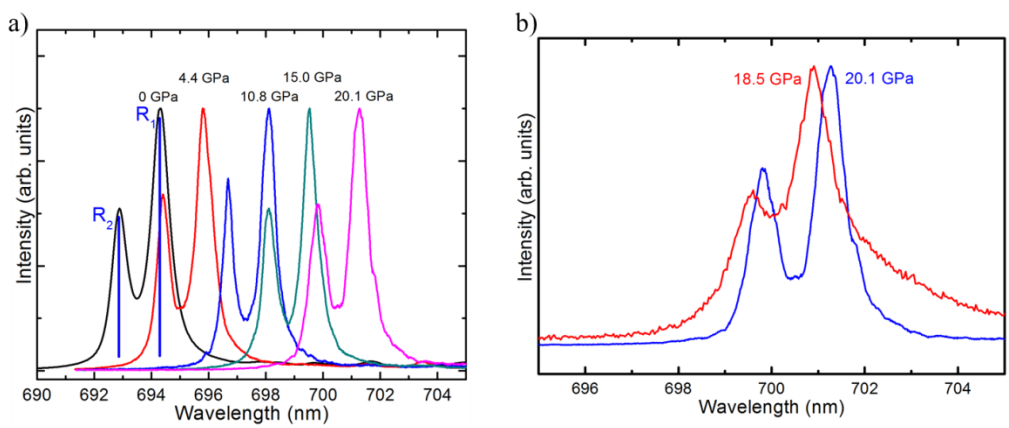

Figure 6: a) Pressure evolution of ruby's fluorescence. b) Fluorescence of a ruby microball under quasi-hydrostatic (blue) and non-hydrostatic (red) pressure conditions. The spectra were obtained from a ruby microball embedded in neon.

I. D. 1. ***X-ray diffraction gauges***

The criteria defining a good X-ray diffraction pressure gauge are the following: a material's high compressibility; chemical inertness; large X-ray scattering power; highly symmetric lattice (few diffraction peaks); well-known equation of state, a simple phase diagram and a weak sensitivity to deviatoric stress. Gold, with a moderate compressibility (167 GPa), 79 electrons, a simple fcc lattice up to pressures of at least a few megabars as well as a very high chemical inertness fills all of the needed characteristics and is thus often used as an X-ray pressure gauge [98]. A small gold chip (≈2 μm) was loaded in the sample chamber for all experiments here requirering an X-ray gauge. The pressure uncertainty with this secondary pressure gauge is less than 1 GPa below 120 GPa [98]. Other gauges are commonly used, such as NaCl, W and Pt.

In the specific case of ultra-high pressure experiments (> 200 GPa), the experimental chamber diameter is often smaller than 15 μm. This generally precludes the use of an *in-situ* pressure gauge such as a ruby or gold microball as its signal, whether its luminescence or diffraction peaks, can overlap with that of the sample and severely hinder its characterization. In such instances, either the rhenium gasket can serve as a pressure gauge, in the case of X-ray diffraction measurements. Indeed, it was demonstrated that if the X-ray diffraction measurements are obtained at the rhenium gasket-sample interface, its diffraction peaks, due to its well-known equation of state, can be employed to determine the pressure in the experimental chamber within about 5% of the actual pressure [99].

I. D. 2. ***Raman gauge***

Dimaond is easily the most employed Raman pressure gauge. Similarly to the rhenium gauge, it is most often employed as a backup gauge or when the experiment does not permit the use of an *in-situ* pressure gauge. The high frequency edge inflexion point of diamond's main vibrational mode (centered at 1333 cm^{-1} under ambient conditions), which shifts under the applied normal stress, was calibrated against lead's equation of state up to 410 GPa (see Figure 7). A pressure uncertainty of only 3 GPa is claimed [100].

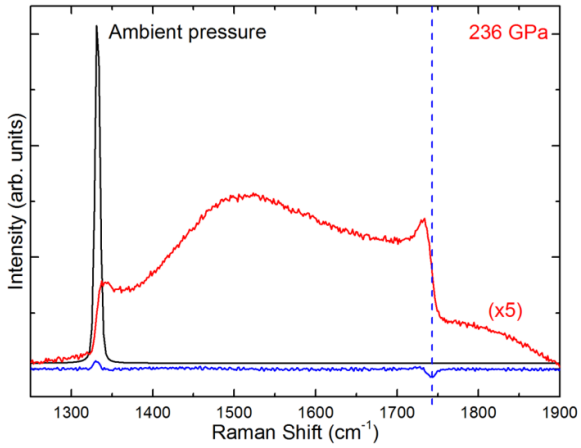

Figure 7: Raman spectra of a diamond anvil at ambient pressure (black) and at 236 GPa (red). The blue line is the first order derivative of the red spectra, and the dashed line marks the inflexion point in the high frequency diamond edge, which gives a pressure of 236 GPa. For visualization purposes, the red spectrum was multiplied by a factor of 5. The red spectrum was obtained from diamond anvils squeezing a Ar-N_2 sample.

II. *CHARACTERISATION TECHNIQUES AND DATA ANALYSIS*

II. A. X-ray diffraction

II. A. 0. ***Theory***

Diffraction is the coherent and elastic scattering of light that occurs to a photon encountering a slit or an obstacle of width similar to its wavelength. In the case of X-rays, having a wavelength on the order of the Angstrom allows it to interact with the atomic structure of matter. When X-rays are diffracted by a periodic lattice, such as a crystal, an interference pattern is formed that is the unique signature of a crystal. This pattern allows determining the crystal's lattice, space group and the position of the atoms constituting it. The formation of this interference pattern is due to the optical path difference traveled by each photon when going through the crystal. The conditions to obtain constructive interferences are given by the Bragg equation:

$$2d_{hkl}sin\theta = n\lambda$$

where λ is the wavelength of the X-ray beam, θ is the incident angle of the X-ray beam with respect to parallel scattering atomic planes separated by a distance d_{hkl} (also called d-spacings), with $h\ k\ l$ being the Miller indices and n is an integer representing the nth order diffraction. Figure 8 schematically illustrates this phenomenon.

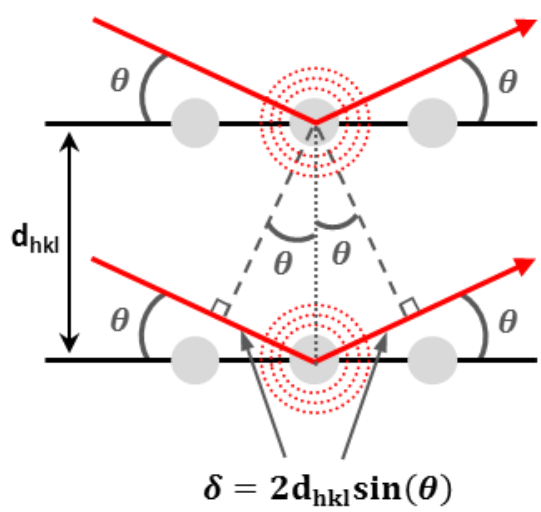

Figure 8: Simple scheme illustrating Bragg's law. Incident X-ray photons, drawn as red arrows, are scattered by the electrons surrounding the atoms. The bottom photon, scattered by a plane of atoms at a distance d_{hkl} from the upper plane, travels a greater distance, denoted as δ. The resulting

interference pattern results from the difference in optical path travelled by upper and bottom photons.

While certainly accurate, Bragg's law is a specific case of a more detailed set of equations – the Laue equations – which contain additional information that can only be accessed in the case of single crystal X-ray diffraction. That information is especially valuable for an unambiguous crystal's space group determination. To derive the Laue equations, one can consider the unit vectors $\boldsymbol{s_0}$ and $\boldsymbol{s}$ which are, respectively, in the direction of the incident and scattered X-ray beams and a pair of atoms, part of a 1D-chain, identified by positions vectors $\mathbf{R_1}$ and $\mathbf{R_2}$, with $\mathbf{a_1} = \mathbf{R_1} - \mathbf{R_2}$. This is schematically represented in Figure 9. The difference in optical path length (DOPL) between the two beams illustrated below is:

$$DOPL = |\boldsymbol{a_1} \cdot \boldsymbol{s} - \boldsymbol{a_1} \cdot \boldsymbol{s_0}|$$

If we set the scattering vector $\boldsymbol{S} = (\boldsymbol{s} - \boldsymbol{s_0})/\lambda$ and, knowing that for constructive interference to occur the DOPL needs to be a multiple of the beam's wavelength, we have:

$$\boldsymbol{a_1} \cdot \boldsymbol{S} = h,$$

where m is an integer. Now taking into account the case of 2D and 3D crystals, an additional equation for each dimension is needed to represent the condition for constructive interference, providing us with the three Laue equations, where $\boldsymbol{a_i}$ are the lattice parameter vectors:

$$\boldsymbol{a_1} \cdot \boldsymbol{S} = h$$

$$\boldsymbol{a_2} \cdot \boldsymbol{S} = k$$

$$\boldsymbol{a_3} \cdot \boldsymbol{S} = l$$

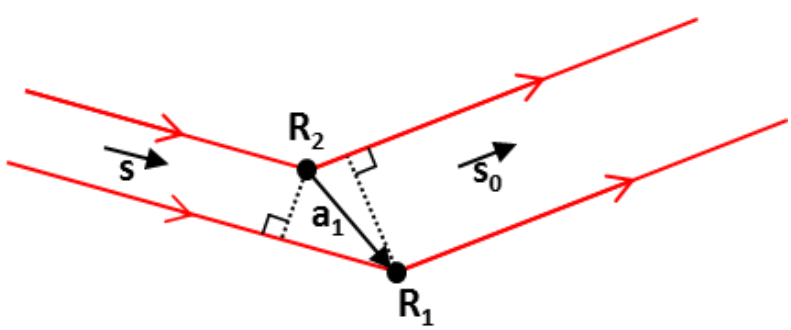

Figure 9: Simple scheme illustrating Laue's law. Incident X-ray photons, drawn as red arrows, are scattered by the electrons surrounding the atoms.

The tip of the scattering vector $\boldsymbol{S_{hkl}}$ allowing for constructive interference defines the reciprocal lattice, as schematically represented below using Ewald's sphere (see Figure 10). As such, it can also be expressed as

$$\boldsymbol{S_{hkl}} = h\boldsymbol{b_1} + k\boldsymbol{b_2} + l\boldsymbol{b_3}$$

where $\boldsymbol{b_1}$, $\boldsymbol{b_2}$ and $\boldsymbol{b_3}$ are the vectors defining the reciprocal lattice and have the following relationship with the real (or direct) space lattice: $(\boldsymbol{a_i} \bullet \boldsymbol{b_j}) = \delta_{ij}$, where δ_{ij} is equal to 1 if $i = j$ and 0 otherwise. The relationship between the Laue equations and Bragg's law can also be evidenced. By considering a plane represented by the Miller indices *hkl*, containing the two non-equivalent vectors $\boldsymbol{a_1}/h$ - $\boldsymbol{a_3}/l$ and $\boldsymbol{a_2}/k$ – $\boldsymbol{a_3}/l$, it can easily be demonstrated that the $\boldsymbol{S_{hkl}}$ scattering vector is perpendicular to this plane. Moreover, the projection of the unit vector $\boldsymbol{a_1}/h$ on the normalized scattering vector perpendicular to the plane yields the interplanar distance:

$$d_{hkl} = \frac{\boldsymbol{a_1}}{h} \cdot \frac{\boldsymbol{S}}{|\boldsymbol{S}|} = \frac{1}{|\boldsymbol{S}|}.$$

Based on Figure 8, we know θ to be defined as the angle between the diffracting plane and the incident as well as scattered beam. Thus, it is readily understood that the angle between $\boldsymbol{s_0}$ and $\boldsymbol{s}$ is of 2θ. Knowing this, based on Figure 10 and the above formula, Bragg's law can be retrieved through simple geometry:

$$\frac{1}{|\boldsymbol{S}|} = {}^{\lambda}/_{2sin\theta} \Rightarrow d_{hkl} = {}^{\lambda}/_{2sin\theta} \Rightarrow 2dsin\theta = \lambda.$$

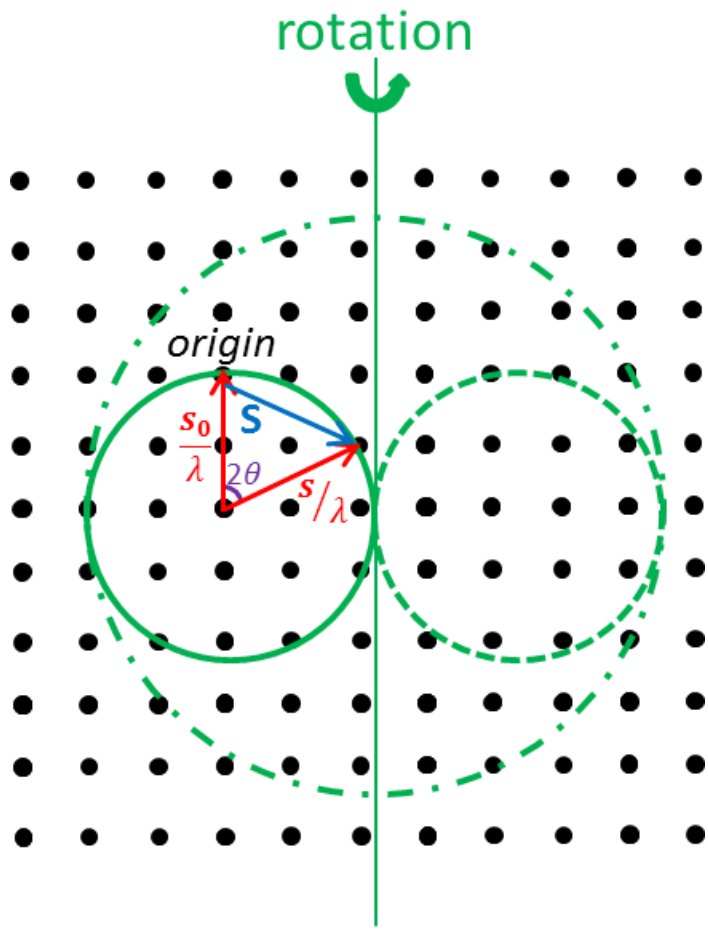

Figure 10: Schematic of the Ewald circle, the 2D equivalent of the Ewald sphere. The dotted green circles illustrate the effect of sample rotation on the nodes of the reciprocal lattice that are probed.

The Ewald sphere geometrically illustrates how Laue equations work. To construct it, one needs to draw on the reciprocal lattice a vector of length $1/\lambda$ parallel to $\boldsymbol{s_0}$ with its tip on the lattice's origin, as illustrated in Figure 10. Then, centered on the *beginning* of that same vector, a sphere of radius $1/\lambda$ is traced. All of the reciprocal lattice nodal points in contact with the *surface* of the sphere will satisfy the Laue conditions and thus produce a diffraction spot. It is observed that the diameter $(2/\lambda)$ of the sphere determines the smallest *d*-spacing that may be measured. Of course, changing the X-ray wavelength allows overcoming this issue and permits a different set of diffraction spots to be observed. Finally, the rotation of the diffracting sample changes the position of the sphere in reciprocal space and grants access to other diffraction spots.

When performing X-ray diffraction experiments, the wavelength of the X-ray beam is known and the diffraction angle is measured. Through the Bragg (and Laue) equation, this allows us in turn to determine the distance between atomic planes. Each constructive interference lines, or simply diffraction lines, help in establishing the relationship between the *d*-spacings, the Miller indices and the crystal's lattice parameters. The most general formula, applicable to crystals of all symmetry, representing this relationship is:

$$\frac{1}{d^2} = \frac{1}{V^2}(T_{11}h^2 + T_{22}k^2 + T_{33}l^2 + 2T_{12}hk + 2T_{23}kl + 2T_{13}hl),$$

where

$$T_{11} = a_2^2 a_3^2 sin^2\alpha,$$

$$T_{22} = a_1^2 a_3^2 sin^2\beta,$$

$$T_{33} = a_1^2 a_2^2 sin^2\gamma$$

$$T_{12} = a_1 a_2 a_3^2 (cos\alpha cos\beta - cos\gamma)$$

$$T_{23} = a_1^2 a_2 a_3 (cos\beta cos\gamma - cos\alpha)$$

$$T_{13} = a_1 a_2^2 a_3 (cos\gamma cos\alpha - cos\beta)$$

$$V = a_1 a_2 a_3 \sqrt{1 - cos^2\alpha - cos^2\beta - cos^2\gamma + 2cos\alpha cos\beta cos\gamma},$$

where a_1, a_2 and a_3 (also more commonly named *a*, *b*, *c*) are the length lattice parameters and α, β, γ are the angular lattice parameters. In the case of a crystal with the cubic symmetry, then $a_1 = a_2 = a_3$ and $\alpha = \beta = \gamma = 90°$ which results in a simplified formula:

$$\frac{1}{d^2} = \frac{h^2 + k^2 + l^2}{a_1^2}.$$

Although Bragg's formula allows determining the whole set of lattice parameters, no information is given on the atomic positions. This information is obtained not from the *d*-spacing values but instead from the relative intensity of the diffraction lines. The intensity is defined by the following formula:

$$I_{hkl} = \frac{I_p K \lambda^3 m_{hkl} P L F_{hkl}^2 v}{V^2}$$

where I_p is the intensity of the incident X-ray beam, K is a correction factor pertaining to the nature of the diffracted beam (X-rays, neutrons or electrons), m_{hkl} is the multiplicity of a diffraction line, v is the diffracting volume, L is a correction factor depending on whether the diffracting sample is a powder or a single crystal, P is the beam polarization and F_{hkl} is the structure factor. The structure factor represents the amplitude and phase of the photons diffraction by a given atomic plane, characterised by their Miller indices. More specifically, it takes into account the parameters relating to the j atoms' in the unit cell: their number of electrons and their thermal displacement – both contained within the atomic scattering factor f_j – as well as their position within the crystalline lattice with regard to their Miller indices. These parameters are linking through the following formula:

$$\boldsymbol{F}(hkl) = F(hkl)\exp(i\alpha_{hkl}) = \sum_{j}^{unit\ cell} f_j \exp\left[2\pi i\left(hx_j + ky_j + lz_j\right)\right].$$

Systematically absent diffraction lines can be understood by the above-defined relationship between the atomic position and their hkl index. Indeed, a face centered cubic crystal, having atoms on the relative positions (0 0 0), (0 ½ ½), (½ 0 ½) and (½ ½ 0), has an non-zero F_{hkl} value only when all hkl indexes are all odd or even. The systematic absence of diffraction lines is vital in determining a crystal's space group. On the other hand, the atomic form factor is representative of an atom's scattering efficiency and at non-zero temperatures, accounts for the thermal motion of the atoms:

$$f_j = \exp\left(-B_j \frac{sin^2\theta}{\lambda^2}\right) \int_0^\infty r\rho(r)G(\theta, r)dr$$

where $G(\theta, r) = \left(\frac{2\sin(4\pi r sin\theta)}{sin\theta/\lambda}\right)$ and B_j is the Debye-Waller term. If the total electronic density was concentrated at $r = 0$ and if thermal effects are neglected, the atomic form factor would be equal to Z, the total amount of electrons carried by an atom. Inserting this result in the above formula for I_{hkl}, we see that the total intensity is proportional to the square of the electron count Z. This explains why low Z atoms, like hydrogen, helium and lithium, are very difficult to detect by X-ray diffraction.

II. A. 1. ***Experimental Setup***

Studying samples in a DAC imposes strict constraints on the sample size. Typical sample sizes are on the order of a few tens of micrometers. In order to have a

sufficiently intense diffraction pattern, the incident photon beam needs to be of very high brilliance. Brilliance is defined as

$$Brilliance = \frac{Photons/second}{(mrad)^2(mm^2\ emission\ area)(0.1\%\ BW)}$$

where BW is bandwidth. The brilliance of a third generation synchrotron light source can be as high as ten orders of magnitude greater than a typical laboratory source [101]. Most of the experiments performed during this thesis were done at ID27 beamline of the European Synchrotron Radiation Facility (ESRF). The X-ray beam at the ID27 beamline is produced by two small-gap undulators and has an oval-shape with its long-axis along the horizontal. By employing a nitrogen-cooled Si(111) monochromator, the X-ray beam energy can range from 6 keV (λ = 2 Å) to 90 keV (λ = 0.14 Å). The X-ray beam is focused by two Kirkpatrick-Baez mirrors and cleaned by two pinholes down to a ~5x5 μm^2 spot on the sample. The diffraction patterns are collected in transmission geometry using a 2D area detector (MAR-CCD) and a CeO_2 reference sample is used to determine the sample-detector distance, the beam's position on the horizontal and vertical axes as well as the tilt and rotation of the detector. The DAC is mounted on motorized translational tables and a goniometer allows the sample rotation about its vertical axis [102]. An *in situ* laser-heating setup composed of two remote controlled Nd:YAG lasers are also set up. The sample temperature during its heating is determined using thermal radiation temperature measurements. The radiation is collected by Schwarzschild objectives — spherical mirrors free of chromatic aberrations — and analyzed over a large wavelength domain (typically 550–900 nm) using a CCD camera mounted on a spectrograph [103]. The beamline's setup is shown and annotated in Figure 11. As specified in a previous section, the detected thermal radiation is fitted by Planck's law, considering a grey body emission.

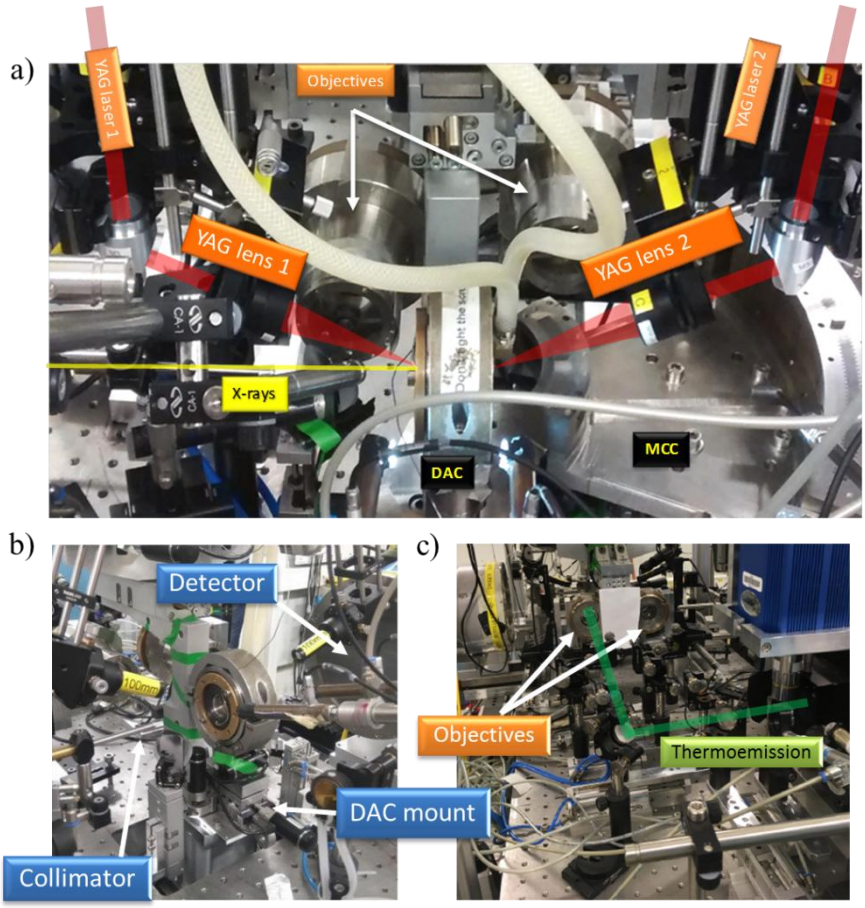

Figure 11: ID27 beamline of the ESRF. a) Photograph of the sample area where the YAG lasers optics, the X-ray beam, the Schwarzschild objectives and the DAC are shown. The MCC, which stands for multi canal collimators are allows to remove a portion of the parasitic Compton scattering, is also shown. It was not used during this thesis. b) Another photograph of the sample area where the detector, collimator and the DAC mount with the motorized translational tables and a goniometer are visible. c) The Schwarzschild objectives along with the thermoemission path and its corresponding optics are shown. Note that same set of optics also serves to produce an image of the sample in the visible.

In all experiments performed for this thesis, the beam's energy was set to 33.17 keV (λ = 0.3738 Å) and angular X-ray diffraction was performed. Depending on the nature of the sample, collection times varied between a few tens of seconds to a few tens of minutes. The DIOPTAS software was employed to visualize and integrate the recorded diffraction patterns [104].

II. A. 2. ***Acquiring and analyzing powder X-ray diffraction data***

Powder X-ray diffraction is performed when the sample is composed of a very large amount of crystallites much smaller than the beam size (ideally on the order of tens of nm) in order to have photons scatter on as many as possible. A perfect powder has crystallites in the same amount in all possible orientations. X-ray diffraction of such a powder produces an X-ray diffraction pattern with perfectly homogeneous diffraction rings (Debye-Scherrer rings). In this fashion, the azimuthally integrated rings' intensity are representative of the atomic positions (through the F_{hkl}). On the other hand, a preferred orientation would produce a bias of the rings' intensity, resulting in some too intense or too weak, and the extracted atomic positions would be incorrect. Thus, only from powders with minimal preferred orientation can it be attempted to resolve the full crystalline structure, whereas only the lattice, which is independent of the diffraction lines' intensity, can be solved with a powder containing a strong crystallite preferential orientation. Different cases are represented and described in Table 1 and Figure 12.

Table 1: Three diffraction images plates obtained at the ESRF ID27 beamline from a laser-heated Li-N_2 sample at 73.2 GPa, showcasing different powder quality. The shadow of one of the laser-heating arms is apparent in the top of each diffraction pattern. See in a section below the description of the Le Bail and Rietveld refinements.

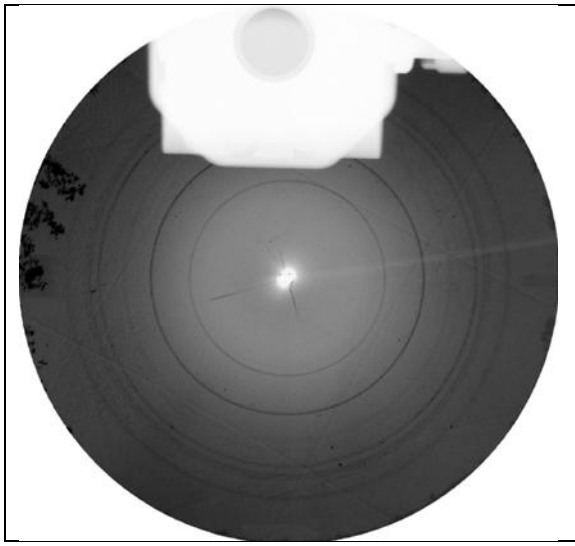	Powder diffraction pattern from the LiN and LiN_2 phases, illustrating the best case scenario for powder quality. Indeed, the powder quality of the two phases is perfect as the rings are continuous and homogeneous. As shown in the integrated powder diffraction pattern (see Figure 12 a)), the peaks of the two phases do not overlap. As such, a Rietveld refinement could be performed and the position of the atoms was accurately determined.

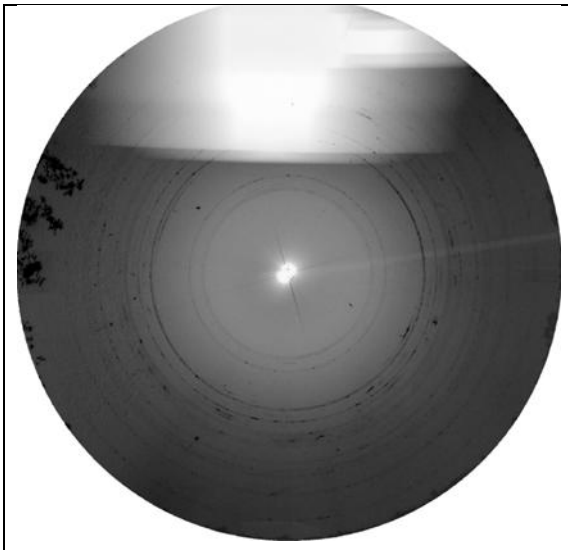	Powder diffraction pattern from the LiN, LiN_2, LiN_5 and ζ-N_2 phases (see Figure 12 b)). The powder quality is good for the Li-N phases but poor for the pure N_2. The presence of four different solids with many overlapping peaks makes it very difficult to determine the previously unknown LiN_5 lattice. While a lattice could be suggested for the LiN_5 solid, obtaining a first guess on the atomic position (with the FOX or similar softwares) failed. This may be due to a wrongly assigned lattice, on account of peaks overlapping with those of the other solids. If it had succeeded, a Rietveld refinement could have been attempted by masking the pure N_2 diffraction spots.
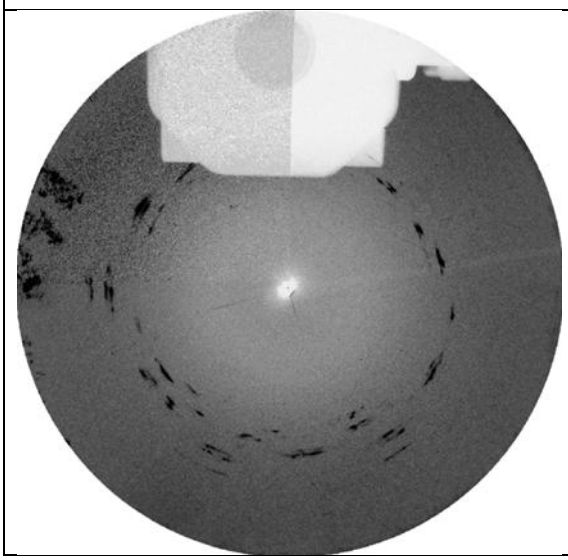	Powder diffraction pattern of pure ζ-N_2. The diffraction powder quality is poor due to a preferential orientation of the N_2 crystallites. While a Le Bail refinement could still be performed, the powder's texture does not allow to draw any information on the atoms' position in the lattice.

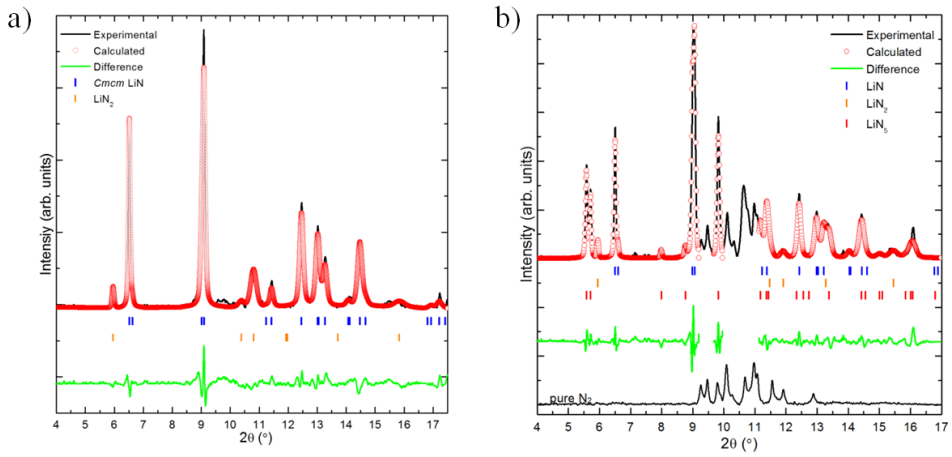

Figure 12: Integrated X-ray diffraction patterns obtained on a laser-heated Li-N_2 sample at 73.2 GPa. The different color tick marks show the position (in 2θ) of the various phases' diffraction lines. a) Rietveld refinement performed on perfect LiN and LiN_2 powders (see Table 1). The exact atomic positions could be obtained. b) Le Bail refinement performed on LiN, LiN_2 and LiN_5 powders. The presence of pure ζ-N_2 (shown at the bottom of the graph) hinder the analysis of the diffraction pattern.

Preferential orientation is one of the weaknesses of powder X-ray diffraction. Other possible issues with this method are the strong overlap of diffraction rings leading to faulty intensities or hidden peaks (see Table 1 and Figure 12), as well as the fact that it prevents the usage of Laue equations leading to the lack of a mean to discriminate between certain space groups. Moreover, powder X-ray diffraction has its diffraction peaks' intensity azimuthally spread, which can make weak peaks hard to differentiate from the background noise. All these difficulties are a direct consequence of the projection of a 3D set of data onto a single dimension. However, as described in more details in a section below, very high pressures are highly prohibitive for single crystal samples. Because of this, most of the X-ray diffraction experiments were performed on powder samples.

To analyse powder X-ray diffraction images, the very first step is to clean the recorded X-ray diffraction images by masking parasitic diffraction spots such as those belonging to the single crystal diamond anvils and gamma rays as well as damaged portions of the detector. Then, the diffraction pattern can be azimuthally integrated to produce a 1D diffractogram (as seen in Figure 12). These two steps can be easily done with a software such as Dioptas [104]. Afterwards, the *d*-spacing position of all diffraction lines belonging to a single phase has to be identified. Then, utilizing a relationship shown in the previous section, the *d*-spacings can be used to find both *hkl* indexes and the lattice parameters. Specialized computer software, such as Dicvol [105],

are ideal to try out a large amount of lattices and provide the user with ones best fitting the observed *d*-spacings. Combined with the Chekcell [106] software, which looks at systematic extinctions of Bragg peaks, space groups are also suggested to the user. To verify the choice of lattice and space group, they can be tested on the same diffraction peaks at a variety of pressure, if that data is available. A Le Bail refinement is also a good validation method. This consists on fitting the experimentally obtained X-ray diffraction pattern by a calculated pattern. In this calculated pattern, the lattice parameters along with the peaks' width parameters are fitted through a standard least-squares method. However, the intensity of each diffraction peaks is adjusted independently; without accounting for the scattering atoms' properties. This is appropriate as the atom's position inside the lattice is not yet determined. A small difference between the experimental and calculated diffraction pattern shows the validity of the Le Bail fit and is a good indicator that the chosen space group and lattice parameters are correct.

Supposing a good enough powder quality (see Table 1), the determination of the position of the atoms in the crystal's lattice can then be attempted. For this, knowledge of the crystal's chemical composition (the atomic species and at the minimum an estimation of its stoichiometry) is essential. Along with the experimental diffractogram, that information can be inputted in specialized structure solving software such as the FOX or EXPO [107,108]. These provide various methods, such as Monte Carlo, simulated annealing, the Patterson method (direct method) that dispense a first guess on the atomic positions. This first iteration can then be refined and validated through a Rietveld refinement, implemented in software such as FULLPROF [109]. The Rietveld refinement is analogous to the Le Bail refinement but takes into account a physical model to fit the peaks' intensity, namely the equation provided earlier for I_{hkl}. As previously described, on top of taking into account experimental parameters, such as the beam polarization, it calculates the effect of a diffraction line's multiplicity, volume of the unit cell and, more importantly, the structure factor which includes an atom's position, site occupancy, thermal parameters, as well as their electronic density. The goal of the Rietveld method is to minimize the function:

$$S_y = \sum_i w_i [y_i(obs) - y_i(calc)]^2$$

with $y_i(obs)$ and $y_i(calc)$ being the intensities of the experimental and calculated diffraction patterns, respectively, of the ith point with a weighting factor of w_i. The quality of the fit is typically asserted by eye, especially through the plotting of the difference between the experimental and calculated curves, although the weighted-profile factor R_{wp} also supplies information on the fit's condition. This parameter is calculated through the following formula:

$$R_{wp} = \sqrt{\frac{\sum_i w_i[y_i(obs) - y_i(calc)]^2}{\sum_i w_i[y_i(obs)]^2}}$$

In most cases, a R_{wp} value below 10% is deemed reasonable. More detailed information on both Le Bail and Rietveld refinements can be found in the literature [110,111].

When the diffracted compound's structure is known and only the lattice parameters are sought for, most of the above-mentioned steps can be skipped. After the azimuthal integration of the diffraction pattern, a simple fitting of the diffraction lines belonging to the known phase as well as assigning to them their (known) *hkl* indices yields the lattice parameters. The XRDA software can be used to perform the lattice parameters determination semi-automatically [112]. As it will be describe shortly after, obtaining a unit cell's lattice parameter evolution with pressure is critical to determine the compound's equation of state.

II. A. 3. ***Acquiring and analyzing single crystal X-ray diffraction data***

Single crystal X-ray diffraction is generally regarded as much more powerful than powder X-ray diffraction. Indeed, while both intrinsically containing the same information, it is distributed in a three dimensional space in the case of single crystal X-ray diffraction whereas it is condensed in a single dimension for powder X-ray diffraction. For this reason, the former does not suffer from peak overlapping, has a higher intensity per diffraction spot and easily allows the determination of the reflection conditions (through Laue's equations), vital for the space group identification. Thus, the complete structural resolution of a complex compound (large unit cell with a high number of atoms) is more accessible from single crystal X-ray diffraction. However, this technique has limited applicability as the growth of the necessary high quality single crystal is not always feasible. In the best case scenario, the solid high pressure phase is bordered by the liquid state. Then, the pressure needs to be slowly increase until a single or several single crystal seeds nucleate. Another approach is to cross the liquid-solid transition line and afterwards slowly cross it back during decompression, reducing the pressure until all but one or a few single crystals are left. However, if the looked-for high pressure phase does not border the melt, it can be attempted to grow a single crystal in the low pressure phase bordering the melt and then increase pressure at a very low rate through the phase transition. This latter method can only potentially preserve the quality of the single crystal if the solid-solid phase transition is of second order phase transition or if it is a displacive (martensitic) phase transition. On top of that, high pressures tend to deteriorate the quality of single crystals due to non-hydrostatic pressure conditions. Moreover, limited reciprocal space coverage on

account of the DAC X-ray opening is another significant issue as it drastically reduces the reciprocal space that can be probed. A thorough discussion of single crystal X-ray diffraction under extreme conditions can be found in Refs. [113,114].

In this thesis, single crystal X-ray diffraction was only performed when investigating the N_2-H_2 system, since it allowed the high pressure growth of a $N_2(H_2)_2$ single crystal from the liquid-solid equilibrium. To preserve a high crystalline quality, the single crystals were kept surrounded in liquid, as seen in Figure 13, which allows perfect hydrostatic conditions. Synchrotron single crystal X-ray diffraction was then performed. An overview of the data acquisition and analysis is provided below. A more detailed procedure can be found elsewhere [115].

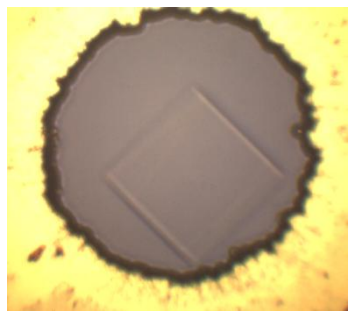

Figure 13: Single crystal of cubic $N_2(H_2)_2$ at the liquid-solid equilibrium pressure.

Before the data acquisition, the single crystal needs to be properly aligned on the X-ray beam. This ensures that during the DAC rotation, the X-ray beam stays on top of the single crystal. The DAC's rotation angle is determined based on its opening — a value of 74° was reached in our experiments. The angular step and measurement time at each increment is determined based on the intensity of the single crystal's diffraction spots and the detector's dynamic range (the lowest and highest intensity reliably measurable by the detector). Basically, the diffraction spots need to be of high enough intensity so that the diffraction spots can be measured but not exceed the detector's saturation limit. The proper angular step and measurement time are readily obtained by knowing the detector's saturation intensity (d_{sat}) and by performing a panoramic acquisition — a continuous acquisition over the full angular range — of the single crystal. The following formula provides the relationship between these parameters:

$$Thr = d_{sat} \frac{t_{step}/\Delta\omega_{step}}{t_{pan}/\Delta\omega_{pan}}$$

where Thr is the threshold intensity of a diffraction spot (on the panoramic scan) that will reach the d_{sat} during the step by step acquisition, t_{step} is the measurement time at a

given angular step $\Delta\omega_{step}$, and t_{pan} is the measurement time for the panoramic acquisition over the full angular range $\Delta\omega_{pan}$. A typical $\Delta\omega_{step}$ is between 0.25 and 1°.

Once the data is collected, a specialized software such as CrysalisPro [116] can be used to process the data up to the structure refinement. First, a peak hunting routine finds all of the recorded diffraction intensities; both diffraction spots and rings. The parasitic diffraction spots and rings such as those belonging to the diamonds and the gasket need to be removed. This can be achieved by pinpointing them in the reciprocal space viewer. Once only the diffraction spots of the sample remain, the software (automatic) indexing routine to determine the unit cell can be launched. When confident with the proposed unit cell, the data reduction and finalization (extraction of the reflection intensities) can be done and will also suggest a space group. The procedures doing this work take into account the background noise, absorption corrections as well as the instrument model, previously determined using a known sample. The final output includes a list of all the diffraction spots' intensities along with their assigned *hkl* value, the unit cell parameters and space group as well as the resolution statistics. Importantly, a R_{int} value, analogous to R_{wp} for powder X-ray diffraction, is provided and represents the data quality. Typically, a R_{int} value lower than 15% is needed to afterwards achieve a reliable structural determination.

Similarly to the powder X-ray diffraction procedure, the structural determination is performed by specialized software, such as Jana2006 [117], which employs a variety of methods (including charge flipping algorithm [118] and direct methods, such as the Patterson method [119]) that utilize the values outputted during the data finalization. Once a first model is obtained, the adjustable parameters can be refined using a least-square minimization routine.

II. A. 4. ***Isothermal equation of states***

The determination of a compound's lattice parameters evolution, and therefore of its volume, with respect to pressure allows to resolve its equation of state. Two isothermal equations of state are commonly used: the Birch-Murnaghan [120]

$$P = \frac{3}{2}K_0\left[\left(\frac{V_0}{V}\right)^{\frac{7}{3}} - \left(\frac{V_0}{V}\right)^{\frac{5}{3}}\right]\left[1 + \frac{3}{4}\left(K_0^{'} - 4\right)\left[\left(\frac{V_0}{V}\right)^{\frac{2}{3}} - 1\right]\right]$$

and the Vinet [121]

$$P = 3K_0\left(\frac{V}{V_0}\right)^{-\frac{2}{3}}\left(1-\left(\frac{V}{V_0}\right)^{\frac{1}{3}}\right)\exp\left[-\frac{3}{2}\left(K_0^{'}-1\right)\left(\left(\frac{V}{V_0}\right)^{\frac{1}{3}}-1\right)\right].$$

In these formulas, K_0 is represents the bulk modulus (incompressibility), K_0' is the bulk modulus pressure derivative and V_0 is the unit cell volume at ambient pressure. While both formulations are adequate for moderate compression, differences are observed at higher compressions. The Vinet equation of state was shown to be preferable for solids with lower bulk modulus whereas the Birch-Murnaghan is better for high bulk modulus materials [122].

The determination a compound's equation of state provides crucial information on the compound's mechanical properties and is therefore of importance for high pressure applications. Furthermore, it can also provide insight on the interatomic chemical bonding within a given material, such as in the case of pernitrides (see the Annex and refs. *54–56*).

II. A. 5. ***X-ray diffraction of pure nitrogen and nitrogen mixtures***

The information provided above is general and commonly applies to all types of samples. However, due to properties unique to nitrogen, such as its inertness, rotational disorder in the solid state and low Z, there are a few tricks and subtleties which have been used in the analysis of diffraction data obtained from nitrogen mixtures.

For starters, in the case of mixtures of N_2 and another inert gas, such as Xe and H_2, there is another method to verify the structure's lattice volume. Since the principal type of interaction between these entities at low to moderate pressures is the van der Waals interaction, they can be assumed to be barely interacting with one another (ideal mixing). As such, their volume is expected to be close to their pure state volume. Combined with the partial or full knowledge of the compound's stoichiometry, for example determined through studying the mixture's binary phase diagram, the lattice's volume should be roughly equal to the sum of the constituent's volume in their pure state. To be more accurate, the volume of the lattice is expected to be slightly inferior as it is thermodynamically favored; often implying a lower volume. Of course, if already confident on the formed compound's lattice, this strategy can be employed to instead determine its stoichiometry. Of course, this does not apply to all nitrogen mixtures, especially if the compound's entropy term is significant or if the mixture's constituents are strongly interacting.

There are also some particularities in performing a structural refinement on compounds made up of N_2 molecules. As discussed in depth in the next section, nitrogen molecules are commonly observed to be rotationally disordered up to 16 GPa [125–127]. This leads to two important issues that hinder the structure determination. First, the molecule's motion results in an effective spread of the electronic density, producing low intensity diffraction peaks that can be tough to detect. The second difficulty is taking into account their preferred orientation during the refinement. To achieve this, several methods were demonstrated. Employed to resolve the complex structure of δ'-N_2 [125], one technique consists in progressively adding molecules with different orientations on a crystallographic site where a N_2 center of mass is known to be sitting. Of course, this needs to be offsetted by changing the molecule's partial occupancy. In this fashion, molecules can be added until the refinement's quality is no longer improved. One of the pitfalls of this procedure is the risk of overfitting your data; i.e. having too many fitting parameters for your dataset. This issue can be alleviated by fixing the N-N bond length if it known, thus removing one fitting parameter per N_2 molecule. Nonetheless, in some cases that is not sufficient. For these cases, another approach that was successfully tested for single crystal X-diffraction data can be attempted. The N_2 molecules were substituted by Si atoms, on the premise that both have the same total number of electrons. Then, the orientational disorder of the molecules was modeled by the introduction of anharmonic anisotropic displacement parameters, typically used for representing the atoms thermal motion. This procedure is perhaps not as accurate as the first method since the atomic form factor of molecular nitrogen and silicon are different due to their difference in electron density geometry. However, the decrease of the number of fitting parameters justifies this approach in cases where the number of independent diffraction spots is limited.

Lastly, when performing Rietveld refinements of a structure composed of a heavy element and nitrogen, the low Z value of nitrogen has to be kept in mind. Indeed, since the structure factor is approximately correlated to the Z^2 of an element, xenon (Z^2 = 2916) or even iron (Z^2 = 676) have a much larger contribution to a compound's diffraction lines' intensity than a nitrogen atom (Z^2 = 49). Thus, refining parameters belonging to a single nitrogen atom can be inconclusive as their variation barely affects the overall fit's quality. For this reason as well for the aforementioned, when possible, considering the N_2 molecule (Z^2 = 196) as a whole instead of two individual atoms in the refinement software is preferred as it reduces the Z^2 gap. For example, this can be done in FULLPROF as it allows whole molecules as an input. This issue is discussed further in the case of Xe-N_2 and Fe-N_2 mixtures.

II. B. Raman Spectroscopy

II. B. 0. *Theory*

Raman spectroscopy is a non-destructive characterization technique based on the inelastic scattering of light by a molecule. It provides an effective tool to obtain information on chemical bonding. Opposite to absorption spectroscopy, where a photon precisely matching the difference between two energy levels — whether they are rotational, vibrational or electronic — is needed, Raman spectroscopy functions with *virtual* energy levels. Upon sample irradiation by an intense monochromatic light source, a very small proportion of photons are absorbed through virtual energy levels and reemitted elastically (Rayleigh scattering), and an even lower amount (about <1/100000) inelastically (Raman scattering). In the case of Raman scattering, the photon either gains or loses energy following its interaction with the sample, in which case anti-Stokes Raman scattering or Stokes Raman scattering, respectively, is said to have occurred. This energy difference originates from the absorption or creation of vibrons or rotons by the incident photon. Figure 14 schematically illustrates these phenomena. As the sample temperature increases and more vibrons as well as rotons are spontaneously generated, anti-Stokes Raman scattering becomes more probable. However, at ambient conditions, it is less probable than Stokes Raman scattering and thus the latter is more conventionally studied. The classical theory, outlined below, explains the phenomenon's processes [128].

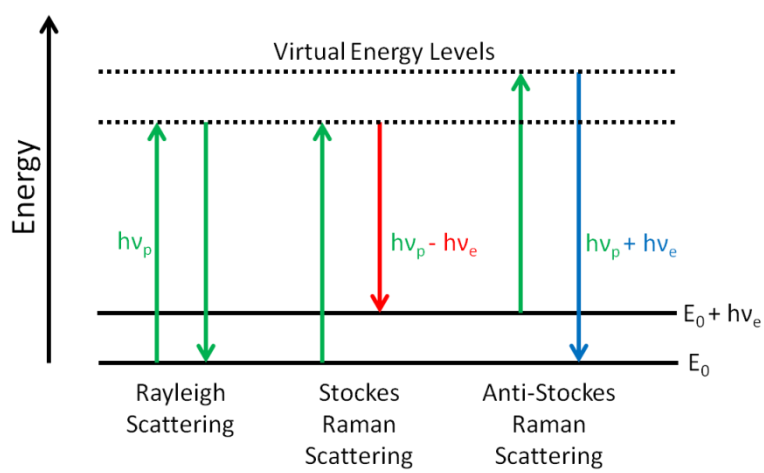

Figure 14: Schematic of the Rayleigh scattering and both types of inelastic scattering: Stockes and anti-Stockes Raman scattering. In case of inelastic scattering, the incident photon of energy $h\nu_p$ gains (anti-Stockes) or loses (Stokes) an energy of $h\nu_e$ through the absorption or creation of vibrons or rotons.

The photons incident on the sample are represented as an electromagnetic field (E) with a frequency w_0 and amplitude E_0:

$$\vec{E} = \overrightarrow{E_0}\cos(\omega_0 t).$$

This electromagnetic field induces an electrical dipole μ_{ind} defined by

$$\overrightarrow{\mu_{ind}} = \alpha\vec{E} = \alpha\overrightarrow{E_0}\cos(\omega_0 t),$$

where α is the molecule's polarizability. At non-zero temperatures, the molecule also vibrates on its own, independently of the oscillating induced dipole. This vibration can be expressed the molecule's displacement q with respect to its equilibrium position q_0 and its resonance frequency, ω_r, such that:

$$q(t) = q_0\cos(\omega_r t).$$

Knowing that the polarizability varies linearly with q for small displacements, a Taylor expansion of α around $q = 0$ yields

$$\alpha = \alpha(q) = \alpha_0 + \left(\frac{\partial\alpha}{\partial q}\right)_{q=0} q + \cdots,$$

where α_0 is the polarizability of the molecule at its equilibrium position. Substituting this result in the formula for the induced electric dipole μ_{ind} gives:

$$\overrightarrow{\mu_{ind}} = \alpha_0\overrightarrow{E_0}\cos(\omega_0 t) + \left(\frac{\partial\alpha}{\partial q}\right)_{q=0}\overrightarrow{E_0}\cos(\omega_0 t)q_0\cos(\omega_r t),$$

and using the trigonometric relation $\cos\theta\cos\varphi = \frac{\cos(\theta-\varphi)+\cos(\theta+\varphi)}{2}$,

$$\overrightarrow{\mu_{ind}} = \alpha_0\overrightarrow{E_0}\cos(\omega_0 t) + \left(\frac{\partial\alpha}{\partial q}\right)_{q=0}\frac{q_0\overrightarrow{E_0}}{2}\{\cos[t(\omega_0 - \omega_r)] + \cos[t(\omega_0 + \omega_r)]\}.$$

This equation readily shows both the elastic and inelastic components of this light-matter interaction. Indeed, the first term corresponds to the elastic Rayleigh scattering while the second and third terms, both part of the Raman scattering, show a loss (red-shift) and gain (blue-shift) of energy, respectively. Correspondingly, these two terms are referred to as Stokes and anti-Stokes Raman scattering.

On the basis that an induced oscillating dipole is a Hertzian dipole (oscillating current, such as found in an antenna), the Raman Stokes' signal intensity is found to be

proportional to the incident photon's wavelength, the intensity of the incident beam as well as the variation of the polarizability with q, such as:

$$I_{Stokes} \propto \left(\frac{\partial \alpha}{\partial q}\right)^2_{q=0} (\omega_0 - \omega_r)^4 E_0^2.$$

Thus, increasing a sample's Stokes Raman signal can only be achieved by either increasing the power of the incident laser or the light's frequency [129]. However, pressure-induced modifications (such as atomic displacements, electronic density redistribution) can impact the $\left(\frac{\partial \alpha}{\partial q}\right)$ term and cause spontaneous intensity changes. Moreover, pressure gradients within the experimental cavity, due to non-hydrostatic conditions, commonly lead to a peak broadening.

The frequency ω_r at which a molecule is vibrating can easily be described by the formula $\omega_r = \frac{1}{2\pi}\sqrt{\frac{K}{\delta}}$, where K is known as the spring constant and δ is the effective mass of the system. While δ is constant with pressure, K tends to increase. Indeed, the spring constant in a molecule, for example N_2, corresponds to the strength of the bond between the nitrogen atoms. As pressure increases, the bond tightens up, similarly to a squeezed spring and the Raman frequencies ω_r goes up. As such, a drop in this value typically indicates a weakening bond.

Raman spectroscopy has the ability to provide a great wealth very quickly. For example, the Raman spectra of phonons is a finger-print of a material's composition and state. Through the vibrational selection rules, obtained by group theory analysis, information about the crystal structure is provided. With pressure the Raman signature of a material changes and allows to study phase transformation, chemical bonding, chemical reactivity. For nitrogen, it is important to remember the Raman frequencies of the three main bonding order: a single bond has a vibrational mode around 800 cm^{-1}, while it is of about 1400 and 2400 cm^{-1} for double and triple bonds, respectively. These can easily be distinguished from one another.

II. B. 1. ***Considerations and limitations for high pressure Raman spectroscopy***

Performing Raman spectroscopy measurements of a sample confined within a diamond anvil cells adds extra constraints as well as difficulties. These are briefly discussed here.

Geometrical constraints: The membrane DAC commonly used in the laboratory has a total body height of 32 mm, allowing for a minimal work distance of 13 mm and 17 mm, when measuring through the cylinder or piston anvil, respectively. The numerical aperture (NA) of the DAC, especially when using Drukker-type diamond anvils, is limited due to the large supporting anvil seats. This issue is lessened by using Almax-Boehler type anvils that allow for a greater DAC opening (up to 70°). Theses constraints restrict the objectives that may be used, as greater magnifications and NAs typically need shorter sample-objective lengths. In turn, this puts a limit on size of the focalized laser beam and on the total amount of light collected by the objective.

Diamond anvil window: In order to reach the sample, the laser beam needs to go through about 1.72 mm of diamond (for the Almax-Boehler type used during this thesis). This causes significant geometric and, at high pressures, chromatic aberrations, which affect the overall signal quality and collection efficiency as well as the depth selectivity. Furthermore, diamond windows produce parasitic back reflections which increase the background level thus decrease the signal-to-noise ratio [130]. Also, color centers in diamond anvils absorb and produce fluorescence proportionally with pressure [131]. This fluorescence tends to decrease along with the excitation laser wavelength. However, knowing that the Raman intensity is proportional to the light frequency at the power of four (${\omega_0}^4$), there is a trade off between the two. Thus, low laser excitation wavelengths (∽488 nm) are usually best at low pressures (< 75 GPa) whereas high wavelengths (∽647 nm) are typically better at higher pressures. Of course, choosing the proper wavelength also needs to account for the probed sample properties, (sensitivity to light, fluorescence, thermal emission, etc), which are prone to be modified with pressure.

Sample heterogeneity: The sample sizes are of a few tens of micrometers or even less at higher pressures. Often, tiny heterogeneities (few cubic micrometers), arise from a pressure-induced chemical reaction or laser-heating. To correctly characterize and understand the physico-chemical phenomena at play, a high spatial resolution (on the order of the micrometer or below) is critical.

II. B. 2. ***Experimental setup***

Confocal Raman spectroscopy measurements were performed using a Alpha300M+ (WITec) system. Figure 15 shows a picture of the confocal Raman microscope with the different parts annotated. A continuous Ar-Kr laser emits the three employed wavelengths: 488 nm, 514 nm and 647 nm. Each is coupled into the microscope with a polarized single-mode optical fiber. This polarized fiber allows only

for the lasers' emission transverse mode (with the electromagnetic oscillations occurring perpendicular to the direction traveled by the light) to carry through, which makes for a very low degradation and dispersion of the laser light. Inside the microscope, the laser is first collimated into a parallel beam and then passed through a laser line filter, removing both the parasitic laser frequencies as well as the luminescence produced by the light's passage into the single-mode fiber. Afterwards, the laser is sent towards the microscope objective by a beamsplitter. While many objectives are mounted on the switching revolver, solely the Olympus x50 objective (NA = 0.35, working distance of 18 mm) was employed during this thesis. This objective allows for a focalized spot size of about 0.6 μm on the sample. The scattered light is then collected with the same objective, passed straight through the beamsplitter and cleaned-up with a long pass Raman filter. Then, being a confocal setup, the light is focused onto a multimode fiber. The core of the fiber serves as the confocal pinhole. The advantage of the confocal setup is that it does not allow light from below or above the focal point to reach the fiber. In turn, this permits a much greater depth resolution and prevents stray light from polluting the signal. On the other end of the multimode collection fiber, the light is dispersed on a diffraction grating and collected by a charge-coupled detector (CCD). Gratings of 600 and 1800 l/mm were employed along with a 2000 by 256 pixel (15x15 μm^2 pixel size) detector which allows a spectral resolution of approximately 7 and 2 cm^{-1} (with the diffraction grating centered at 546 nm), respectively. Finally, the sample is placed on a three-axis piezoelectrical scan stage which permits automated, submicron accuracy displacements.

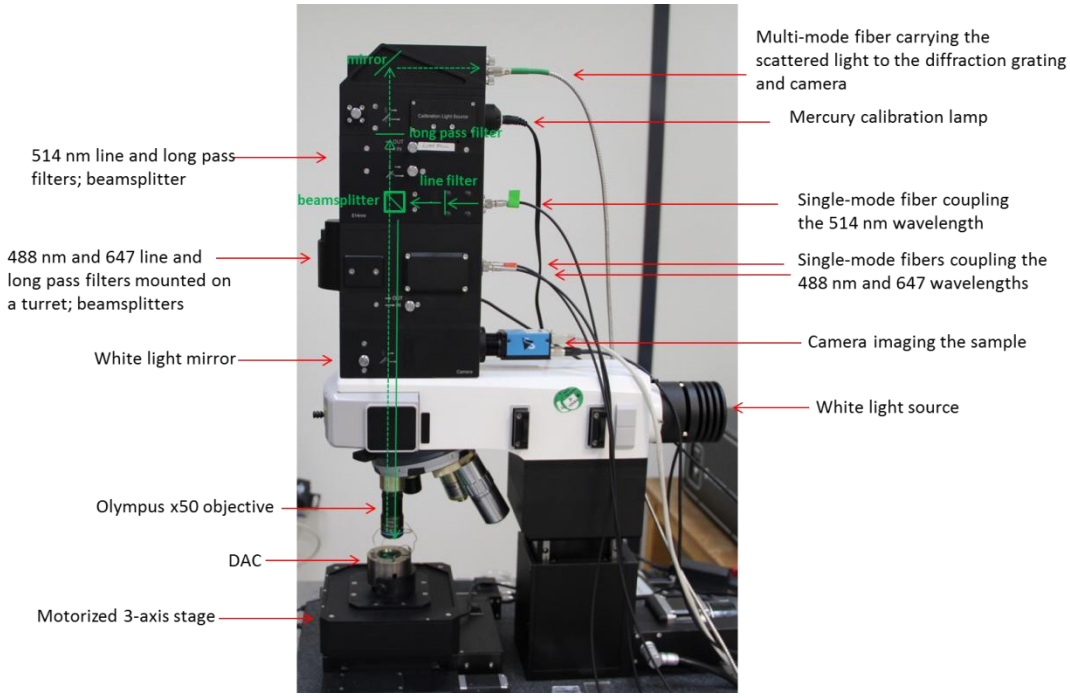

Figure 15: Annotated photo of the WITec confocal Raman setup. In green is drawn the beam path for the 514 nm wavelength.

This whole setup is particularly convenient for high pressure Raman spectroscopy experiments for three main reasons. 1) The very high depth (5 µm) and in-plane (0.6 µm) resolutions. The depth resolution greatly improves the signal quality by reducing the diamond fluorescence while the in-plane resolution allows to resolve the tiniest features. 2) Switching from one of the three wavelengths to another is a matter of a few tens of seconds with little to no alignment optimization. Indeed, the same optical pathway is employed for the three wavelengths, with their corresponding filters all on a rotating mount. For the reasons described earlier, this is tremendously useful for high pressure Raman studies. 3) The piezo-driven motorized stage. These allow for comfortable, easy and quick sample positioning and characterization. Furthermore, they permit precise, long acquisition times and fully automated sample Raman mappings. As detailed in the case of the investigation of N_2-H_2 mixtures, these mappings can be critical to correctly understand the sample behavior (see Figure 16). It is important to note that the in-plane and depth resolutions are not limited by the motors but instead by the size of the laser spot and the optical setup, respectively.

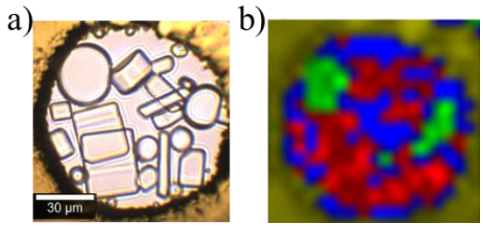

Figure 16: (a) Microphotograph of a 1 : 2 N_2–H_2 mixture at 1.2 GPa, the pressure at which hydrazine is in liquid–solid equilibrium, decompressed from 61.1 GPa. (b) A Raman mapping of the sample. The single crystals with well-defined edges in (b) are hydrazine (red) while bubbles were determined to be a nitrogen– hydrogen liquid mixture (green). Both are in liquid hydrazine (blue).

NITROGEN UNDER EXTREME CONDITIONS: PHASE DIAGRAM

I. *THE NITROGEN MOLECULE*

Nitrogen is the fifth most common element in the Universe and makes up for about 78% of Earth's atmosphere, mostly present in its molecular form N_2. This homonuclear diatomic molecule is strongly bound by a covalent triple bond – the strongest of all known covalent bonds (942 kJ/mol). Attesting to its bond strength, N≡N has an intramolecular distance of 1.098 Å, smaller than its similar-sized periodic table neighbors, namely O=O (1.21 Å), C=C (1.24 Å) as well as isoelectronic C≡O (1.13 Å). As all homoatomic dimers, the N_2 molecule belongs to the symmetry point group $D_{\infty h}$. As such, it possesses a single intrinsic vibrational mode, an A_g symmetrical stretching observed at a frequency of 2744 cm^{-1} in the gas state. This mode is solely observable by Raman spectroscopy as it only induces a change in the molecule's polarizability; not of its dipole moment.

While the N_2 molecule does not have a dipole, its next order-term of the multipole expansion, corresponding to a quadrupole, is non-zero. The following general formula describes the electric potential generated by an electric quadrupole:

$$V_q(\boldsymbol{R}) = \frac{1}{4\pi\epsilon_0|\boldsymbol{R}|^3}\sum_{i,j}\frac{1}{2}Q_{ij}n_i n_j$$

where V is the electric potential, **R** is a vector with its origin in the system of charges, n is a unit vector in that same direction as **R**, Q is the quadrupole moment tensor and ϵ_0 is the electric permittivity. At ambient conditions, molecular nitrogen was measured to

have a quadrupole moment of -4.90 ± 0.3 x 10^{-40} Cm^2 [132], which is average compared to other simple molecules [133]. However, unlike most molecules, N_2 does not have a stronger type of interaction coming into play, such as a dipole moment (CO, NO), a magnetic moment (O_2), hydrogen bonds (H_20, NH_3), etc. Hence, the quadrupole-quadrupole (QQ) interactions are dominant in solid N_2. As deduced from the above formula, the electric potential increases significantly as R gets shorter. The QQ interaction between N_2 molecules thus increases along with pressure. As it will be shown in the following sections, these interactions greatly complexify the ambient temperature solid state structural configuration of the low pressure phases of pure nitrogen, as well as of some nitrogen-rich compounds. Indeed, as the QQ interaction get stronger and stronger, it progressively constrains the rotationally-disordered N_2 molecules and aligns them [134]. Mainly due to this type of interaction, nitrogen adopts six different structures below 20 GPa. At higher pressures, eight other solid phases are known, totaling fourteen, as shown in its phase diagram shown below (Figure 1).

II. *SOLID PHASES OF PURE NITROGEN*

Interestingly, the experimentally observed solid phases of pure molecular nitrogen are troublesome to reproduce with theoretical calculations [13]. At lower pressures, it is mainly due to the difficulty in implementing the QQ interaction [134]. At higher pressures (> 50 GPa), calculations predict the polymeric phase (cg-N) to be stable instead of the molecular phases. Recent work propose the entropy term to be responsible for this discrepancy [135]. Indeed, while the cg-N phase is calculated more stable, a large kinetic barrier – resulting from the strong N_2 triple-bond – impedes the molecular to polymeric transition. To overcome this energy barrier, laser-heating is performed. However, it is suggested that at high temperatures the entropy term of the molecular phases becomes sufficiently large that the polymeric solids are no longer energetically-favored over the former. At 110 GPa and 2000 K, the entropy-temperature term is finally not large enough and the transition to cg-N is observed. As it will be discussed later in this thesis, theoretical calculations seem to be highly predictive for the polymeric phases, perhaps due to their simple physics allowing an accurate modeling, in opposition to the molecular phases.

Based on these considerations, the next sections will be structured in the following fashion: 1) the low pressure molecular phases stabilized by QQ interaction will be presented, 2) the higher pressure molecular phases, deemed favored due to kinetic barriers and the entropy term, will be introduced and, 3) the polymeric phases, predicted by the calculations, will then be examined.

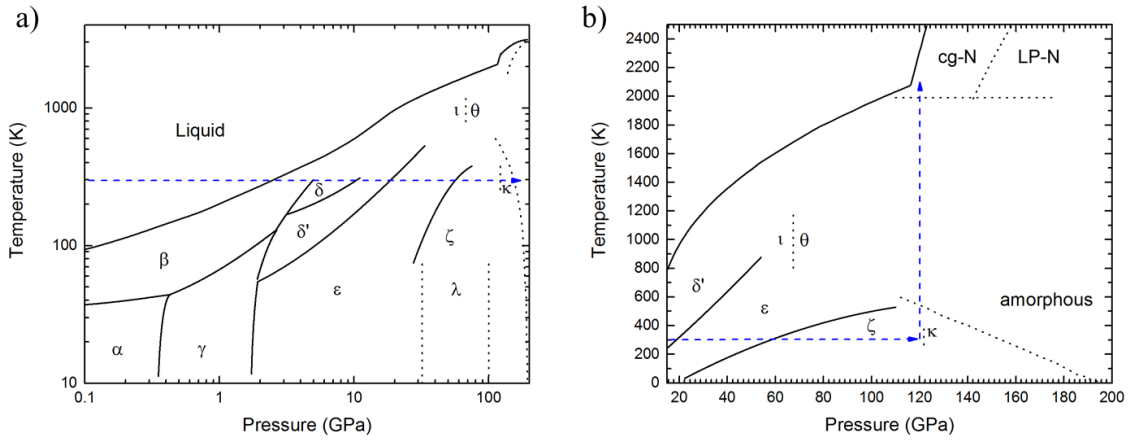

Figure 1: Phase diagram of pure nitrogen with a) logarithmic scales, allowing a clear view of the low pressure-low temperature region and b) linear scales, where the high pressure-high temperature parts can be observed. Data obtained from refs. 2–5. The phase intersected by the dashed blue lines will be discussed.

II. A. Low pressure phases of pure molecular nitrogen

II. A. 0. *The β-N_2 phase*

At ambient temperature, molecular nitrogen solidifies at 2.49 GPa into a hexagonal ($P6_3/mmc$) structure, named β-N_2, with lattice parameters of a = 3.595 Å and c = 5.845 Å [139,140]. In this phase, the position of individual nitrogen atoms is not clearly defined, but merely the center of mass position of each N_2 dimer is, found at the *2d* Wyckoff position (see Figure 2). This is attributed to a static disorder as the molecules are thought to be spherically disordered [139,141]. In the pressure domain of β-N_2, the molecules are still far apart and barely feel the presence of one another, which explain their complete rotational disorder. From Raman spectroscopy studies, a single vibrational mode was revealed, as seen in Figure 3 [141]. This is consistent with the nitrogen molecule's center of mass sitting on a single Wyckoff position and not be close enough to its neighbor so as to be perturbed.

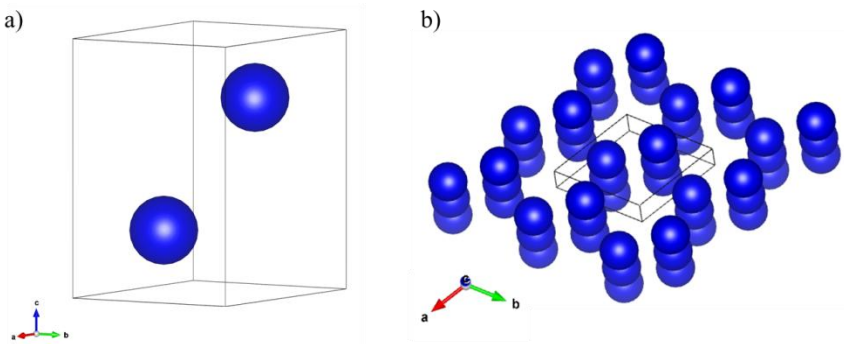

Figure 2: a) The unit cell of *β*-N_2 and b) its extended view. As the N_2 molecules are spherically disordered, they are here represented as single blue spheres.

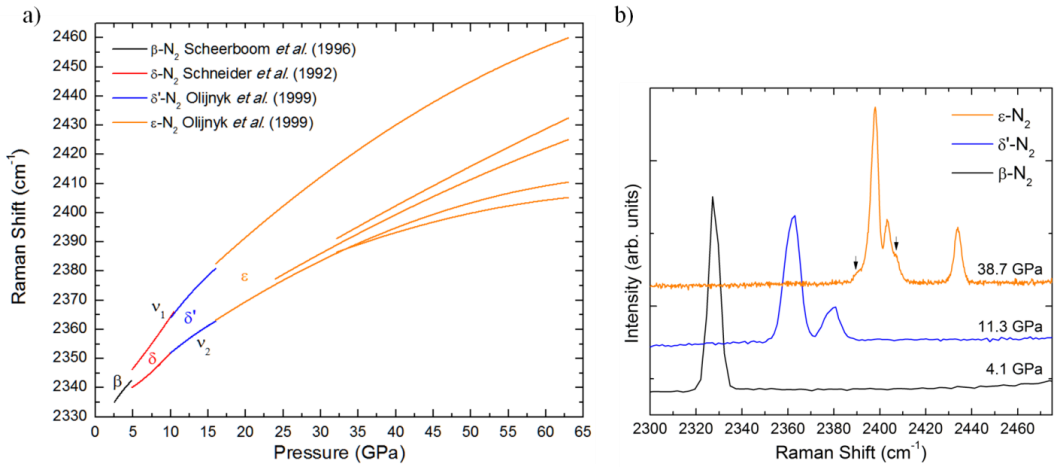

Figure 3: a) Raman mode evolution of the various phases of pure molecular nitrogen up to 62 GPa. The Raman data for the *β* [141], *δ* [142], *δ'* and *ε* phases [143] were obtained from literature. b) Representative spectra of the *β*, *δ* and *ε* phases of pure N_2. The two black arrows pinpoint the weak new peaks arising from the further high pressure splitting of the ν_2 mode. The *ε* phase spectrum was obtained with a diffraction grating of 1800 l/mm while the two others were obtained with a 600 l/mm grating.

II. A. 1. *The δ-N_2 phases*

The *β*→*δ* phase transition is observed at 4.9 GPa [144]. The structure of *δ* is cubic (*Pm*-3*n*) with a lattice parameter of 6.164 Å at 4.9 GPa. Positioned on the *16i* (0.042, 0.042, 0.042) and *48l* (0.239, 0.531, 0.08) Wyckoff sites with an occupancy factor of 25%, the complex arrangement totals 16 nitrogen atoms [125,144]. The odd partial filling of both Wyckoff positions models the rotational disorder of the N_2 molecules. As seen in Figure 4, the molecules are disordered in two different fashions: a disk-like disorder, found on the faces of the cubic unit cell (*48l*) and a spherical

disorder, adopting a bcc arrangement (*16i*). Here, it is thought that the QQ interaction have started to be felt by the N_2 molecules as a portion of the molecules went from completely spherically-disordered to disk-like disordered. Raman spectroscopy measurements revealed two vibrational modes, as shown in Figure 3, that are consistent with the X-ray data. The lowest frequency mode (ν_2) belongs to the disk-like disordered molecules while the highest frequency one (ν_1) is attributed to the spherically-disordered molecules [141,142,145].

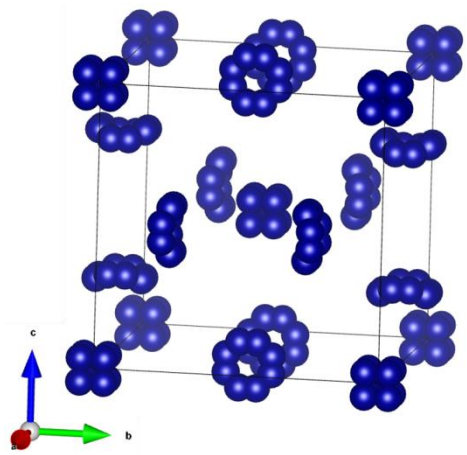

Figure 4: Structure of δ-N_2. The nitrogen atoms are sitting on the *16i* and *48l* Wyckoff positions, are each with a partial occupancy of 0.25, and model the spherical and disk-like rotational disorder, respectively.

II. A. 2. ***The δ'-N_2 phase***

The δ-N_2 phase was first thought to be stable up until it transformed into the ε-N_2 around 16 GPa [83,140]. Indeed, the quality of the best accessible X-ray diffraction patterns did not permit at the time to see new diffraction peaks appearing at 10.5 GPa, although a small, unexplained change in compressibility had been noticed. First suggested by Raman spectroscopy data due the changing gradient of the spherically-disordered N_2 molecule vibron frequency with temperature and then later confirmed by X-ray diffraction experiments, a phase transition from the δ to the δ' phase does occur at 10.5 GPa [125,141,145–148]. An extensive X-ray diffraction single crystal study unambiguously resolved its very complex structure, revealing a tetragonal lattice ($P4_2/ncm$) with a = 8.063 Å and c = 5.685 Å (at 14.5 GPa), containing 16 N atoms on 12 partially occupied Wyckoff positions [125]. The structural arrangement can be understood as being composed of three types of rotationally disordered nitrogen

molecules. Forming a *fcc* sublattice, the first ensemble of molecules are pseudo-spherically disordered, having a preferred rotation plane along the $<\bar{3}\bar{1}\sqrt{2}>$ directions and avoiding the $<01\sqrt{2}>$ directions. The two other types of rotationally-disordered molecules are pseudo disk-like, as they also have preferred and unfavored rotation axes. In total, twelve distinct Wyckoff positions, with occupancies varying from 8% to 33%, were needed to account for this very complex arrangement of nitrogen molecules. The structure is shown in Figure 5. Again, compared to the previous phase, the molecules are more orientated which is attributed to the increase of the QQ interaction.

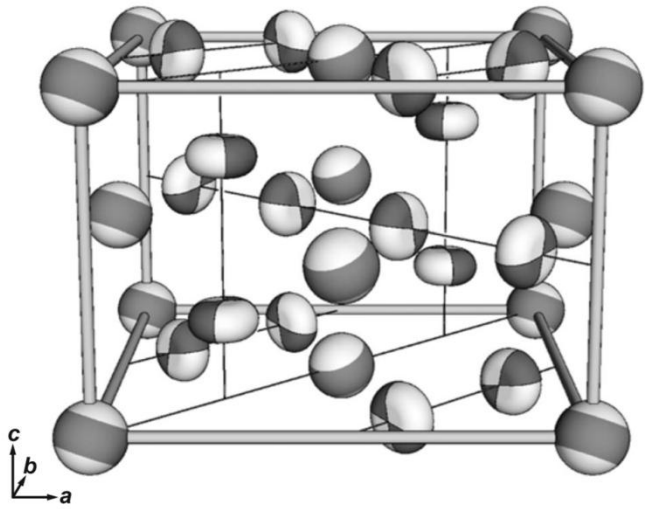

Figure 5: Structure of δ'-N_2 obtained from ref. [125]**. The shaded portions mark the molecules' preferred orientations.**

Regarding the Raman modes of δ'-N_2, still only two vibrational modes, the previously-observed ν_1 and ν_2 stretching modes, are detected and are shown in Figure 3. This comes as a surprise because of the obvious drop in symmetry — compared to the cubic δ-N_2 phase — and since twelve occupied Wyckoff positions allow a greater number of vibrational modes [147]. Indeed, the Raman (and infrared) spectroscopy studies instead predicted a lower-symmetry cubic lattice for δ'-N_2, namely the *Fm*3, *F*432 and *Fm*3*n* space groups, based on the number of recorded vibrational modes. In hindsight, the additional vibrational modes allowed by the $P4_2/ncm$ space group are simply too weak to be measured, even at low temperatures [147]. In any case, these studies also independently came to the conclusion that the $\delta \rightarrow \delta'$ is caused by a partial ordering of the rotating molecules.

II. A. 3. ***The ε-N₂ phase***

At a pressure of about 16 GPa, yet another phase transition occurs. The molecules in the δ'-N_2 structure are thought to finally become fully oriented, distorting the δ'-N_2 lattice through a small displacement as well as a slight extension along the cube diagonal, resulting in the ε-N_2 phase. This new phase adopts a hexagonal lattice ($R\bar{3}c$) with parameters of a = 7.6050 Å and c = 10.6217 Å at 16.3 GPa [83]. The 48 nitrogen atoms are concluded to occupy the *12c* (z = 0.0495) and *36f* (x = 0.2731, y = 0.2127 and z = 0.2828) Wyckoff sites [140]. A drawing of this structure is found in Figure 6. The molecules' arrangement is again attributed to the QQ interaction. Indeed, the molecules adopt a pinwheel configuration, known to minimize the QQ interaction [149]. This interpretation is further supported by theoretical calculations as only by including the QQ interaction, along with a hexadecapole-hexadecapole interaction term, could this structure be found as stable [134]. This slightly differs from the previous low pressure molecular phases where solely the inclusion of the QQ interaction term was sufficient to theoretically obtain the experimentally-observed structures.

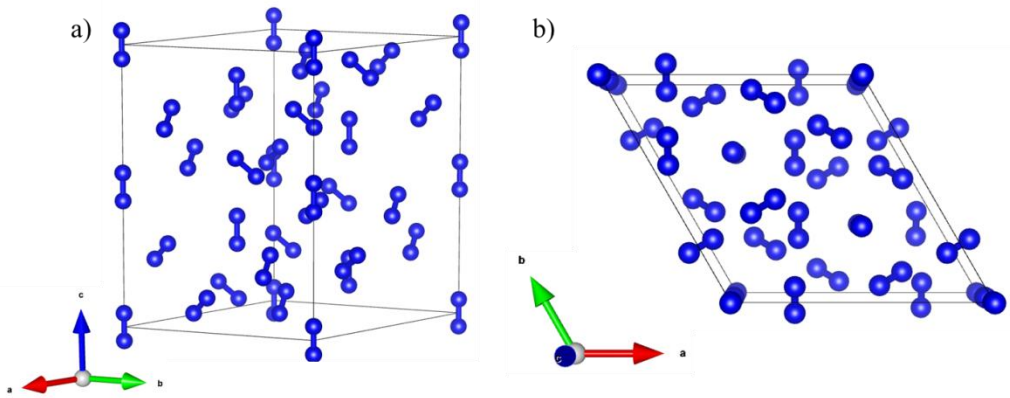

Figure 6: a) Drawing of the structure of the ε-N_2 phase. b) Drawing of the structure of the ε-N_2 phase seen along its *c*-axis, from which the pinwheel arrangement of the N_2 molecules, know to minimize the QQ interaction, is visible.

Raman characterization of the ε-N_2 phase shows at first only the ν_1 and ν_2 modes. However, a small asymmetry of the ν_2 peak progressively becomes a weak shoulder on the high frequency side of the ν_2 mode at 21 GPa. From 30 GPa, the two bands are fully resolved [148]. This doublet is the signature of the A_{1g} and E_{1g} components of the ν_2 peak. Based on group theory calculations, the ε-N_2 structure is precisely expected to have these three measured modes ($\nu_1 + 2\nu_2$) [148]. Thus, when a third and then a fourth ν_2-like modes were measured at higher pressures (see Figure 3), concerns were raised about the structure assigned to the ε-N_2 phase [142,143]. As it stands, it is hypothesized that the previously disk-like molecules are generating the ν_2 peaks and might actually be

still slightly disordered at 16 GPa. Upon further compression, these molecules would completely stop rotating and be ordered, albeit with a fraction oriented differently than the others, thus giving rise to two new ν_2 peaks [143]. This interpretation is further supported the experimental study of a $(N_2)_{11}He$ single crystal by X-ray diffraction. The structure of $(N_2)_{11}He$ was resolved to be strikingly similar to ε-N_2, with the helium atoms substituting nitrogen molecules. However, the N_2 entities were found to still be partially disordered and to only become oriented at 28 GPa, pressure at which its volume is very close to that of pure ε-N_2 around 40 GPa when new Raman modes appear [150]. At 28 GPa, the $(N_2)_{11}He$ solid is said to adopt a hexagonal supercell.

II. B. High pressure phases of pure molecular nitrogen

II. B. 0. *The ζ- and κ-N_2 phases*

The ε-N_2 phase is observed up to about 62 GPa. While calculations predict the cg-N phase to become stable from 56 GPa, experiments reveal that molecular phases are still more stable [13]. It is suggested that these phases are favored by the Gibbs free energy entropy term [135]. For reasons explained later, these high pressure molecular phases are poorly structurally characterized due to the quality of the X-ray diffraction patterns, which progressively degrades with increasing pressure. In any case, the ε phase is found to transform into ζ-N_2 at 62 GPa based on new X-ray diffraction peaks and Raman vibrational modes. It is agreed upon that this new phase is orthorhombic, however the space group, the lattice parameters and even the number of N_2 molecules are still disputed [57,137]. While theoretical calculations based on the reported experimental results have been performed to try and determine the structure, they were ultimately unsuccessful [151].

The study on the $(N_2)_{11}He$ van der Waals compound suggests another explanation for the $\varepsilon \rightarrow \zeta$ phase transition. The $(N_2)_{11}He$ solid does not undergo a phase transition from its hexagonal supercell until 135 GPa, pressure at which it becomes amorphous. Based on the similarities between $(N_2)_{11}He$ and pure nitrogen, it is hypothesized that pure N_2 would also adopt a hexagonal supercell due to the nitrogen molecules finally all becoming orientated at 40 GPa. Because of the poor powder quality, this phase transition would only be noticed by powder X-ray diffraction at 62 GPa [150].

Upon further pressure increase to ~ 115 GPa, a $\zeta \rightarrow \kappa$ transformation was detected based on new diffraction peaks [137]. A monoclinic lattice — without a space group assignment — was attributed to the new phase, with a = 6.918 Å, b = 6.202 Å, c = 2.289 Å and β = 91.774°. Vibrational measurements do suggest both phase transitions: ζ-N_2 based on new Raman modes, shown in Figure 7, and the κ-N_2 phase from five new infrared modes [5,7,9,143,148]. Physical insight on the behavior of the N_2 molecules

under these extreme pressure conditions is this time obtained from the Raman measurements. As it can be seen in Figure 7, the three lowest frequency vibrons are no longer blue shifted with pressure, as typically observed, but instead red shifted. This inversion of pressure shift indicates a weakening of the N_2 intramolecular bond explained by a pressure-induced redistribution of electronic density, transferring part of the triple-bond electron cloud towards intermolecular N_2-N_2 gaps. In effect, this permits an elongation of the N_2 intramolecular bond as well as a decrease of N_2-N_2 distances, both favorable for the later transformation into polymeric nitrogen, in which intra and intermolecular distances are equal [57].

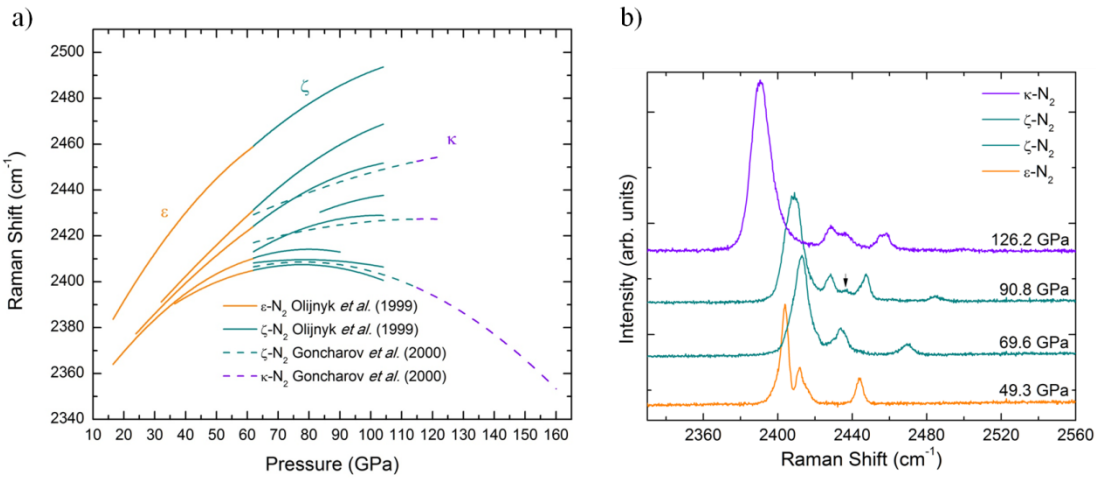

Figure 7: a) High pressure evolution of pure molecular nitrogen Raman modes. Data reproduced from ref. 14 and 18. b) Representative Raman spectra of the *ε*, *ζ* and *κ* phases. The black arrow pinpoints the new peak of the *ζ* phase appearing near 85 GPa. The spectra of the *κ* phase is of better quality than the published experimental data, hence displaying more peaks.

II. B. 1. ***Amorphous molecular nitrogen***

In the *κ* phase, molecular nitrogen was shown to undergo a pressure-induced amorphisation towards a non-molecular phase [6,8,9,137]. The compressed nitrogen samples were shown to progressively become opaque, have a widening followed by a disappearance of both X-ray diffraction peaks and Raman modes. This amorphisation is interpreted as a gradual transition into a non-molecular form of nitrogen: without enough energy to cross the large activation barrier, only local transformations would occur and the lack of sufficient atomic diffusion would prohibit a complete conversion [8]. This hypothesis is supported by a new, very broad, vibrational mode centered about

640 cm^{-1} and thus somewhat close in frequency to the expected single-bonded N-N mode [6,152,153]. Furthermore, electrical and optical measurements determined this amorphous phase to be semiconducting, in stark contrast with the insulating diatomic molecular nitrogen [8].

II. B. 2. ***The ι- and θ-N_2 phases***

The *ι*- and *θ*- N_2 phases are responsible for the poor X-ray diffraction data quality of the *ζ* and *κ* phases. Indeed, the *ι* and *θ* phases are obtained in a similar pressure range as *ζ* and *κ* phases but at higher temperature. As they are metastable down to ambient temperature, they thus prohibit the annealing, or recrystallization from the liquid, of the *ζ* and *κ* phases. Mostly recognized by their vibrational signature, the high pressure-high temperature molecular N_2 phases are ill-characterized by X-ray diffraction [7,154,155]. The *ι*-N_2 phase was observed to be produced between 48-70 GPa above 750 K, and no structural arrangement, lattice parameters or otherwise, are proposed [7,155]. Detected after heating pure N_2 above 600 K at 95 GPa, the *θ* phase is suggested to have an orthorhombic lattice with a = 6.797 Å, b = 7.756 Å and c = 3.761 Å (at 95 GPa). Its diffraction peaks respect the systematic absences of space groups $Pma2$, $Pmn2_1$, $Pmc2_1$, $Pnc2$ and $P2_12_12$ [7]. Interestingly, the stability domain of these two phases seems to strongly depend on the sample's thermodynamic path. For example, in one study the *ι* phase was never observed the despite covering the phase diagram up to 100 GPa and 1800 K [154]. In that same study, it is describe that the *θ* phase can only be obtained from a previously heated and quenched *ζ*-phase. This is explained by large impeding transformational barriers [154,155].

II. C. Polymeric nitrogen phases

II. C. 0. ***The cubic-gauche polymeric nitrogen phase***

From a pressure of 110 GPa, laser-heating a molecular phase of nitrogen, either the *ζ* or *κ* phase, to temperatures above 2000 K finally ruptures the strong triple covalent bond, giving rise to a polymeric network of triply single-bonded nitrogen atoms [10,17,137]. Known as the cubic-gauche polymeric nitrogen (cg-N), it adopts a cubic structure ($I2_13$) with a lattice parameter of a = 3.4542 Å (115.4 GPa). Eight nitrogen atoms, sitting on the *8a* (x = 0.067) Wyckoff sites, are contained within the lattice [10]. This structural arrangement, drawn in Figure 8, matches theoretical calculations performed by Mailhiot *et al*. in 1992 [4].

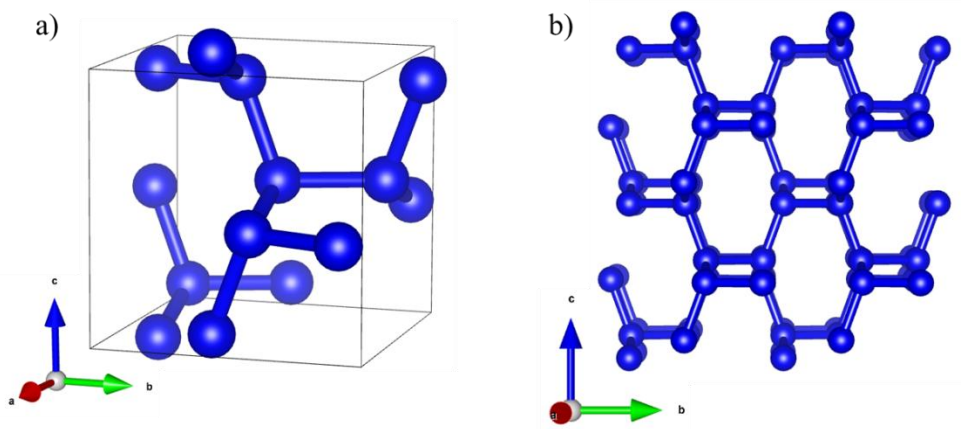

Figure 8: a) The unit cell and b) the extended structure of cubic-gauche polymeric nitrogen are drawn.

Based on group theory analysis, this specific structure should exhibit a total of four vibrational modes, $\Gamma = A + E + 2T$ [152,153]. While the four modes are Raman-active, numerical simulations predict the A mode to be drastically more intense than the three others. In accordance, the experimentally-measured Raman data on cg-N evidenced a single Raman mode, closely matching the calculated A mode, as seen in Figure 9 [153]. The much lower frequency of this vibrational mode compared to the ones of the molecular phase comes as no surprise since the single bond is much weaker than the triple bond. Upon decompression of cg-N at ambient temperature, it was found metastable down to 42 GPa, after which it decomposes back to its molecular form [10]. At temperatures of 60 K however, the polymeric phase was determined metastable at least down to 25 GPa, as a gasket failure prevented further lowering of the pressure.

For the reasons detailed in the introduction, this cg-N is held as the ultimate energetic material and the retrieval to ambient conditions of a similar material would constitute a great accomplishment.

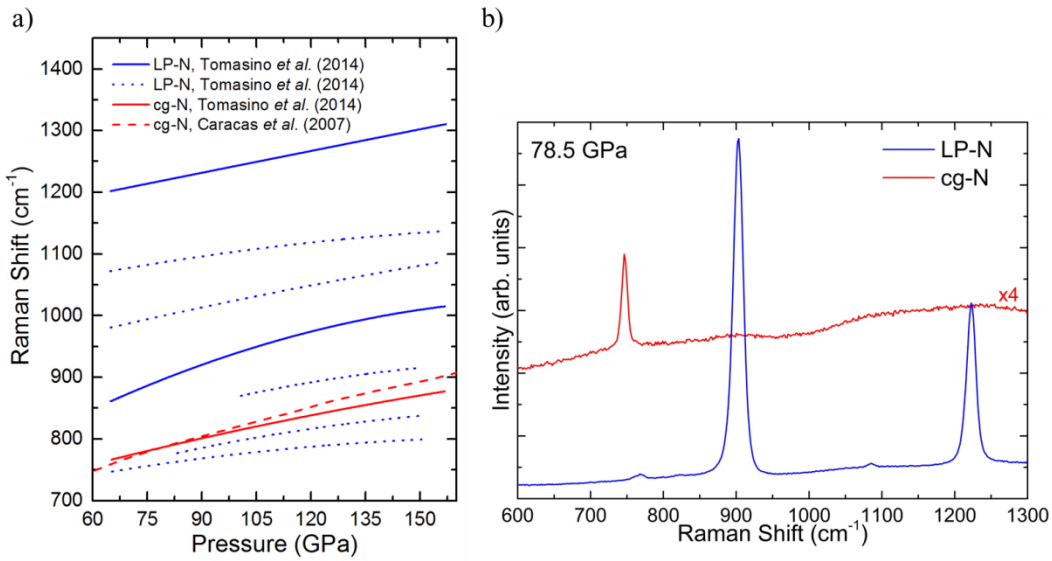

Figure 9: a) Measured Raman modes evolution of both polymeric phases of nitrogen, cg-N (red) and LP-N (blue). The dashed red line corresponds to the theoretically calculated *A* mode of cg-N [153]**, while the dotted blue lines are the much weaker vibrational modes of LP-N** [17]**. b) Raman spectra of both cg-N and LP-N phases following the compression and laser-heating of pure N_2 to 157 GPa and above 2000 K.**

II. C. 1. ***The layered polymeric nitrogen phase***

Direct laser-heating of the optically-darkened κ-N_2 phase above 125 GPa up to 175 GPa results in the synthesis of yet another form of polymeric nitrogen. X-ray diffraction of the new compound revealed diffraction lines that were attributed to the theoretically predicted layered polymeric nitrogen (LP-N) phase, an orthorhombic structure (*Pba*2) with experimentally-determined lattice parameters of a = 4.1602 Å, b = 4.2481 Å and c = 4.3689 Å at 112 GPa [17]. While a Rietveld refinement could not be performed due to the quality of the powder, numerical simulation has predicted the 16 nitrogen atoms on four different *4c* Wyckoff sites: (0.2933, 0.2172, 0.6608), (0.7852, 0.2167, 0.3403), (0.0209, 0.3363, 0.177) and (0.8381, 0.0171, 0.8219) [14]. These atomic positions give rise to 2D layered chains of triply single-bonded nitrogen atoms, as shown in Figure 10. Interestingly, this phase was produced at a lower pressure than expected as calculations had predicted a pressure stability domain between 188-263 GPa [12,14].

With similar interatomic interactions (i.e. single-bonded nitrogen chains), LP-N has Raman modes in the same frequency range as cg-N (see Figure 9). Two very intense modes alongside with five much weaker ones were assigned as the vibrational signature

of LP-N. Based on the compound's X-ray diffraction peaks and Raman modes, it was determined to be metastable down to at least 52 GPa [17].

Intriguingly, the LP-N phase is thought to be produced alongside cg-N and a monoclinic ($C2/c$) polymeric phase, predicted to be metastable under these pressure-temperature conditions [17,156]. However, the latter phase was curiously not detected by Raman spectroscopy.

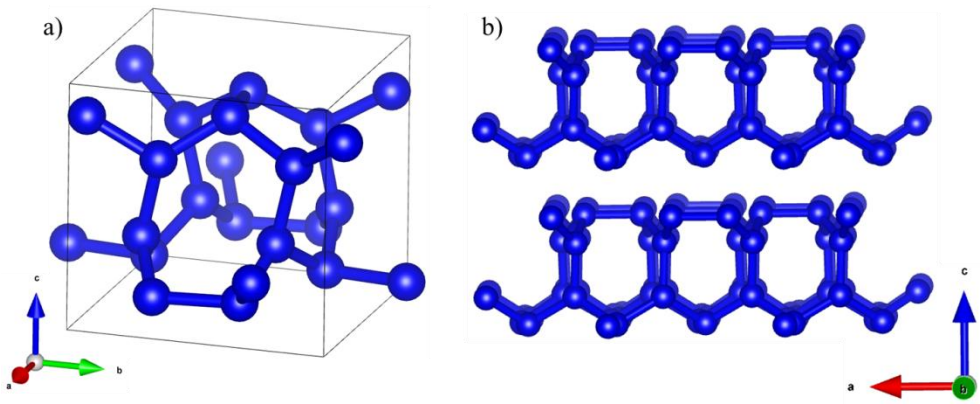

Figure 10: a) The unit cell and b) extended view of the layered polymeric nitrogen phase.

III. *THE NITROGEN MELTING CURVE*

Until very recently, the melting curve of nitrogen was subject to debate. Earlier experimental studies had all observed an intriguing maximum on the melting curve, although there was a disagreement on whether it was at 50 GPa or 70 GPa (see refs [157] and [154,155], respectively). These studies were in agreement with theoretical calculations which explained the melting point maximum by a molecular liquid to polymeric liquid phase transition at 90 GPa [158]. If verified, this polymeric liquid could open up new pathways for retrieving a polymeric form of nitrogen at ambient conditions.

The most recent experimental measurements dispelled these possibilities [136]. Nitrogen was compressed and heated in a novel sample design composed of two boron-doped diamond disks sitting in small pits drilled in the diamond anvils' culet (see Figure 11). This geometry ensured a homogeneous heating and thus melting of the solid nitrogen. The melt was detected by X-ray diffraction, which was also employed to determine the structure of both the solid and the liquid phase. Two major conclusions were drawn from this investigation. First, there is no maximum on the melting curve: it

increases smoothly up to about 116 GPa, after which an isothermal compression of the liquid above 2260 K results in the solidification of the liquid nitrogen into the cg-N phase. Second, the liquid phase from which cg-N was isothermally crystallized is determined to be molecular, and not polymeric. These results are consistent with the theoretical hypothesis, described in section II, that through entropy molecular nitrogen is favored at high temperatures and thus prohibit the formation of polymeric nitrogen up until about 120 GPa. The melting curve shown in Figure 1 was reproduced from ref. [136].

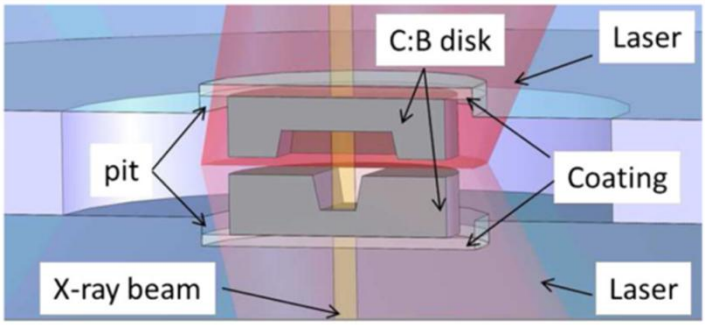

Figure 11: Cross-sectional view drawing of the experimental cavity located between the two diamond anvils a DAC. A small pit is drilled into the diamond anvils by free ion beam machining. The two boron-doped diamond disks are placed in the pits and form a capsule containing the nitrogen sample. The capsule is laser-heated from both sides allowing for a controlled and homogeneous temperature [136]**.**

NOVEL PURE NITROGEN POLYMERIC PHASES

I. *INTRODUCTION*

The multiple experimentally observed phases of pure nitrogen were described in the previous chapter. The highest reported pressure at which pure molecular nitrogen was heated is 175 GPa (3000 K), conditions under which the layered polymeric (LP-N) phase was synthesized [17]. Numerical calculations however have predicted the stable phases of nitrogen up to 800 GPa [12–16]. According to the latest of these simulations, above 100 GPa the following sequence of phases is expected to be cg-$N \xrightarrow[188\ \mathrm{GPa}]{} LP\text{-}N \xrightarrow[263\ \mathrm{GPa}]{} N_{10}$, with this latest phase anticipated to be observed up to 800 GPa [12]. The N_{10} phase is also named the diamondoid nitrogen since its structure contains N_{10} tetracyclic cages also found in its carbon diamond counter part by removing the eight vertex atoms of its unit cell. The structure of diamondoid nitrogen is represented in Figure 1. The N_{10} cage may also be viewed as four interconnected distorted N_6 hexagons. It has a cubic lattice with a = 4.287 Å at 300 GPa and nitrogen atoms on two inequivalent Wyckoff positions, the *12e* (0.3532, 0, 0) and *8c* (0.6745, 0.6745, 0.6745). As with the previously observed cg-N and LP-N phases, all N atoms are sp^3-hybridized and thus each form three single covalent bonds. With the high directionality of covalent bonds, N_{10} is unsurprisingly calculated to be a large band gap insulator (about 3.5 eV at 300 GPa) [12].

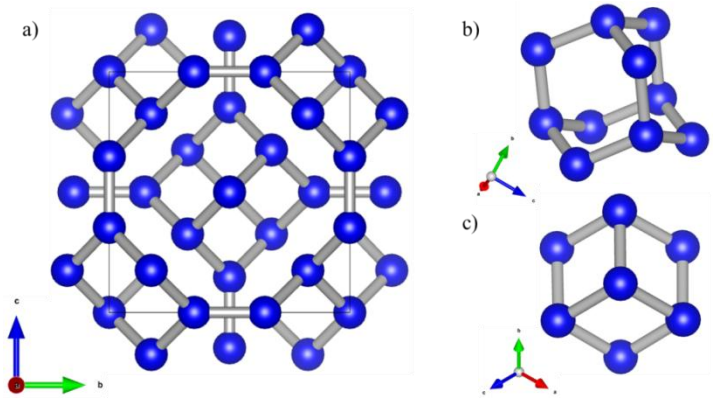

Figure 1: a) Structure of the N_{10} diamondoid compounds. b) N_{10} tetracyclic cage and c) emphasizing one of the four distorted nitrogen hexagons forming the cage.

The above presented sequence of calculated stable nitrogen phases is a simplistic representation of a more complex situation. Indeed, between 188-263 GPa, six other polynitrogen structures have enthalpy energies within a few tens of meV of the LP-N phase [12]. This is illustrated in Figure 2. The very small calculated enthalpy energy difference between these various solids means that experimentally, almost any of those could be produced. This statement is justified by well-known issues with theoretical calculations, including the fact that they are performed at a temperature of absolute zero, meaning that the temperature-entropy (-TS) term in the Gibbs free energy is unaccounted for. For systems like nitrogen, where significant activation barriers need to be overcome through sample laser-heating to temperatures reaching 3000 K, the contribution of the temperature-entropy term may very well become sufficient to stabilize a structure other than the enthalpically-favored. A similar interpretation was provided to justify the experimentally observed stability of WH over that of WH_4, the latter being calculated to have the lowest enthalpy between 15 and 100 GPa [159]. Of course, the choice of the functional – function approximating the exchange-correlation terms in the Hamiltonian – employed by the calculations could also shift the determined enthalpies of a few meV.

As detailed below, pure nitrogen was here compressed up to 250 GPa and laser-heated to 3300 K in order to try and obtain new forms of polymeric nitrogen.

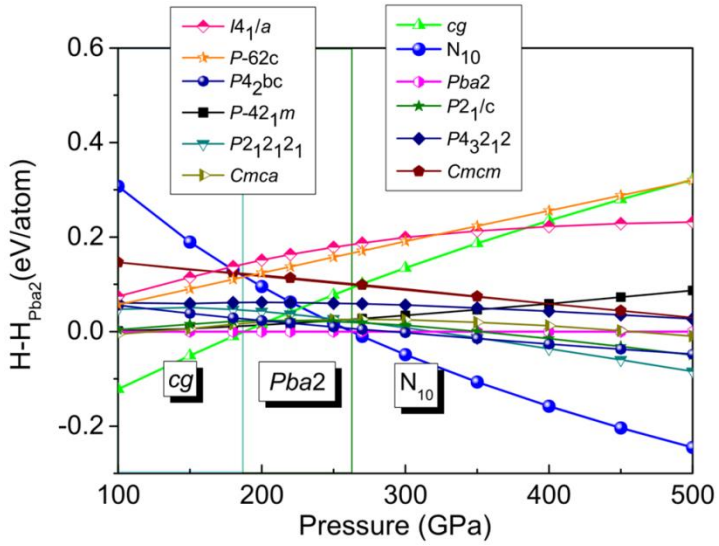

Figure 2: Enthalpy curves of polynitrogen phases between 100 GPa and 500 GPa with respect to the LP-N (*Pba*2) compound. While the cg-N→LP-N-N_{10} sequence is predicted, a large number of phases with similar enthalpy values are predicted between 188 GPa and 263 GPa. The figure was obtained from ref. [12].

II. *ARTICLE*

The many theoretical predictions on the very high pressure and temperature predict novel polynitrogen phases to be synthesized. The experimental verification of these theoretical calculations is critical for a better understanding of the high pressure behavior of nitrogen as well as for the possible discovery of new arrangements poly-N which could inspire the design of an ambient conditions form of nitrogen. In the study titled "The hexagonal layered polymeric nitrogen phase synthesized near 250 GPa" in preparation for submission in Physical Review Letters, pure molecular nitrogen was investigated at 250 GPa to 3000 K.

Upon its compression, Raman spectroscopy and X-ray diffraction measurements on molecular nitrogen were obtained up to 160 and 200 GPa, respectively, pressures at which no more signal could be detected. Shown in Figure 3, these measurements extend the data found in the literature. Interestingly, the detected X-ray diffraction lines of molecular nitrogen seem to closely follow those of κ-N_2 up to about 170 GPa where a distinct shift of slope is noticed. On another sample, this coincided with the complete

disappearance of the Raman modes of molecular N_2, detected to occur between 160 and 170 GPa. A similar behavior was previously observed: Eremets *et al*. had followed the N_2 molecular vibron up to 193 GPa and above 177 GPa, the Raman mode shift with pressure was flat [8]. These datapoints are shown in Figure 3. Simultaneously, they had detected a change in the resistance evolution with pressure. These observations had been explained by the progressive transformation of the molecular solid into a much harder amorphous solid. This interpretation also fits the here-presented X-ray diffraction measurements.

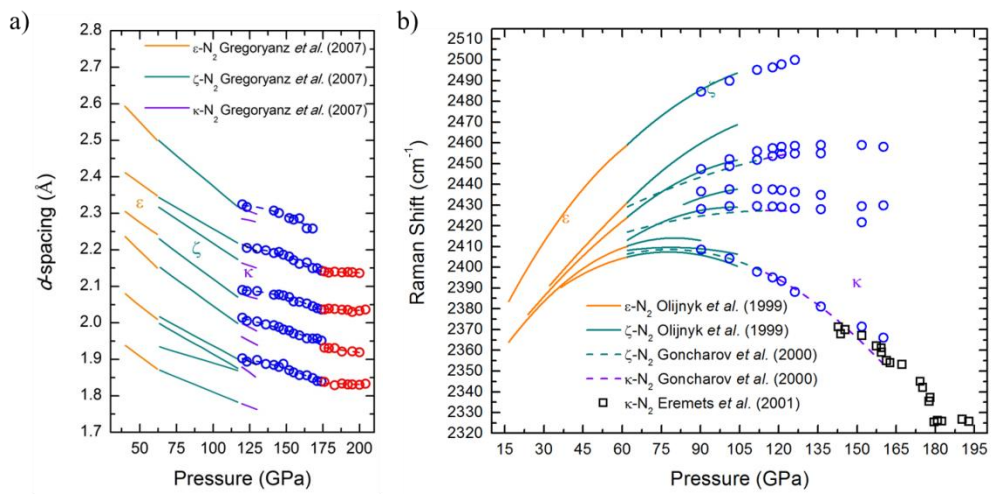

Figure 3: a) X-ray diffraction data obtained on a pure nitrogen sample up to about 200 GPa. The empty blue and red circles are the experimental data collected during this thesis. The shift in the data slope (at the blue and red data point junction) might indicate a structural modification of the κ phase. The full colored lines represent data obtained from Ref [137]**. b) Evolution of the vibrational modes of molecular nitrogen up to 160 GPa. The empty blue circles represent data obtained during this thesis. The full and dashed lines along with the empty black square are from the literature** [8,9,143]**.**

Above 200 GPa, the sample seemed to have become amorphous as neither X-ray diffraction lines nor Raman modes could be detected and completely opaque; in accordance with previous studies [6,8,9,137]. Starting from 209 GPa, the nitrogen sample was laser-heated to moderate temperatures (1200 to 2000 K). As no transformation were observed, the pressure was further increased up to 231 GPa where the sample was heated to 2800 K, and then 3200 K. While no X-ray diffraction signal was detected, the sample progressively became transparent, as shown in Figure 4. Finally, at 244 GPa and 3300 K, new X-ray diffraction peaks were noticed and the sample appeared almost completely transparent. As shown in the paper, the structure of this solid was determined not to match the theoretically predicted N_{10} diamondoid or

the experimentally confirmed cg-N or LP-N phases, but instead a tetragonal ($P4_2bc$) hexagonal layered polymeric (HLP) nitrogen; expected by the calculations to be of slightly higher enthalpy than the N_{10} structure. The structure of HLP-N is drawn in Figure 5. It is composed of layers of interconnected chains of N_6 rings, with the top and bottom layers being identical and simply rotated 90° along the *c*-axis.

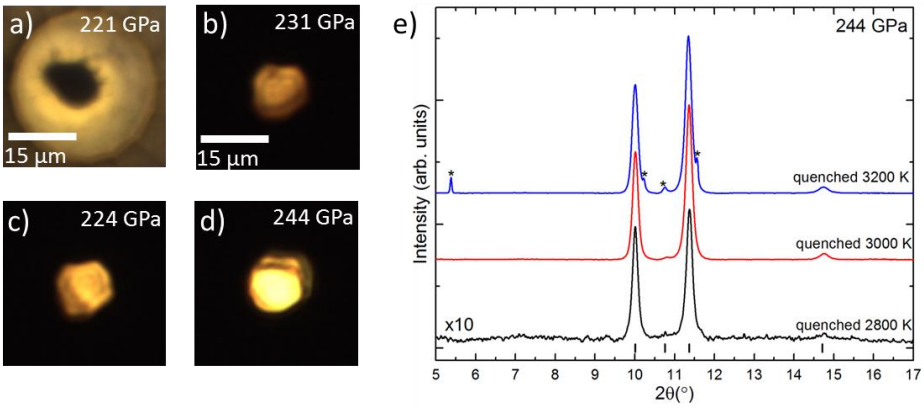

Figure 4: Microphotographs of two pure nitrogen samples. a) Sample 1 at 221 GPa before laser-heating. Sample 2 b) 231 GPa after laser-heating at 2800 K, c) 224 GPa after laser-heating at 2800 K, which caused a pressure decrease and d) following a pressure increase up to 244 GPa and laser-heating at 3300 K. e) X-ray diffraction patterns of sample 2 after its pressure increase up to 244 GPa and subsequent to three laser-heating rounds at increasing temperatures. The diffractogram obtained ensuing the sample quenching from 3200 K shows new diffractions lines attributed to HLP-N. The black tick marks indicate rhenium's diffraction lines.

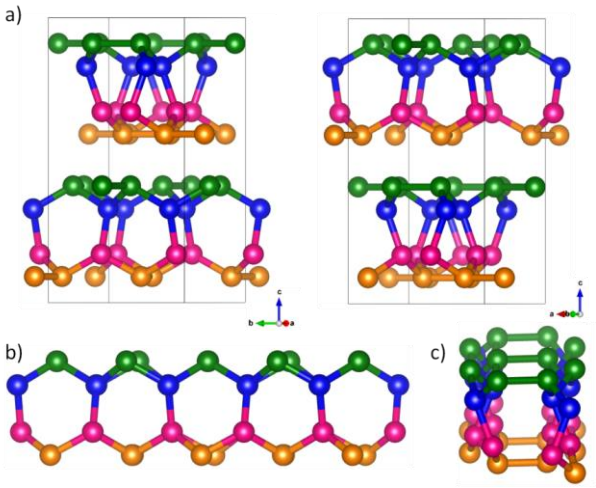

Figure 5: Crystal structure of HLP-N. a) The unit cell, viewed along the *a*- and *b*-axes. The bottom and upper layers are observed to be identical but at 90° rotation with respect to the *c*-axis. b) The N_6 chains viewed from the side and c) from up front.

Theoretical calculations were performed in an attempt to understand why the HLP-N compound was obtained instead of the LP-N phase, which is the enthalpy-minimizing solid at 244 GPa by about 10 meV. As the HLP-N phase is obtained at very high temperatures, it was first hypothesized that it is stabilized through the entropy term of the Gibbs free energy. However, accounting for the -TS term (through the quasi-harmonic approximation) only shifted the energy difference between the two solids by about 1 meV (at 3300 K). Similarly, van der Waals interactions were also added to the calculations and reduced the enthalpy gap between the two phases by about 2 meV. As such, it is thought that the functional employed for these calculations might instead be at fault, or that anharmonic considerations are needed.

The HLP-N compound could be followed during decompression from 244 GPa down to 66 GPa. X-ray diffraction characterization was performed from the maximum pressure down to 176 GPa. In this pressure range, 15 pressure-volume data points were acquired and fitted by a second order Birch-Murnaghan (see Figure 6). Since solids are highly incompressible at these ultra high pressures, the precision on the retrieved bulk modulus is lower. In any case, a value of K_0 = 333(31) GPa (V_0 = 200(4) Å^3) was obtained, which in-line with the other two polymeric nitrogen phases, as LP-N and cg-N are reported to have values of K_0 = 324.2 GPa (K_0' = 6.0) and K_0 = 298 GPa (K_0' = 4), respectively [10,17].

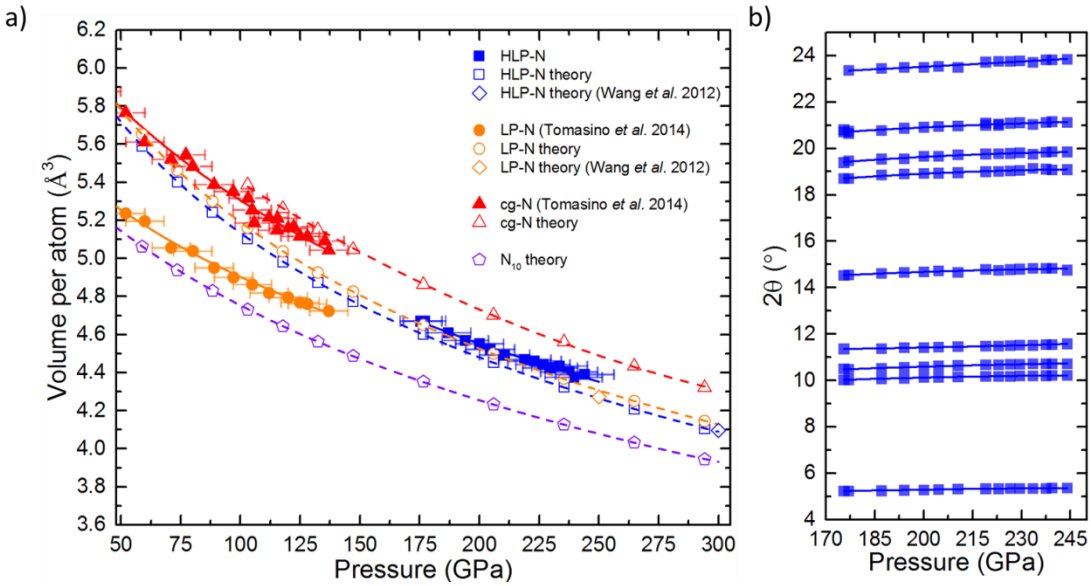

Figure 6: a) Evolution of the volume per atom with respect to pressure for the diamondoid N_{10}, HLP-N, LP-N and cg-N compounds. b) Diffraction lines' position in 2θ of the HLP-N compound from 176 GPa to 244 GPa.

Below 176 GPa, the HLP-N solid was characterized by Raman spectroscopy. As shown in the following manuscript, up to twelve Raman modes were detected, including five lattice modes and seven intramolecular modes with frequencies between 650 and 1300 cm^{-1}. These frequencies are in the range expected from N-N single bonds (700 to 1300 cm^{-1}) [123,124,160,161]. The vibrons were followed down to 66 GPa, pressure at which the diamond anvils ruptured and the nitrogen sample escaped.

The investigation of pure nitrogen at very high pressures and temperatures is a useful reference in the project of obtaining ambient conditions metastable polynitrogen solids. Indeed, this research serves to discover novel, more stable polynitrogen arrangements which, eventually, could be found easier to target through other methods, whether high pressure chemistry by doping nitrogen with selected impurities or by classical chemistry techniques, and secure at ambient conditions. The here-presented synthesis of the HLP-N compound will also contribute to the refinement of the theoretical calculations, which is indispensible in the context of material design.

The hexagonal layered polymeric nitrogen phase synthesized near 250 GPa

D. Laniel[1,2], G. Geneste[1], G. Weck[1], M. Mezouar[3], P. Loubeyre[1]*

[1]CEA, DAM, DIF, F-91297 Arpajon, France.

[2]CNES Launcher Directorate, 52 rue J. Hillairet, 75612 Paris cedex.

[3]European Synchrotron Radiation Facility, 6 Rue Jules Horowitz BP220, F-38043 Grenoble CEDEX, France.

[*] corresponding author: dominique.laniel@cea.fr

Abstract

The nitrogen triple-bond collapses in the 100 GPa pressure range and a rich variety of single-bonded polymeric nitrogen structures unique to this element have been predicted under still higher pressures. Here, we present the synthesis of the hexagonal layered polymeric nitrogen phase (HLP-N) obtained by the sustained laser-heating of pure nitrogen to about 3300 K near 250 GPa in a diamond anvil cell. X-ray diffraction data reveal a tetragonal lattice ($P4_2bc$) that matches the predicted HPL-N structure, which is never given as the most stable structure in theoretical calculations. Complementary calculations are thus performed to investigate which neglected contributions could explain its experimental observation.

Introduction

The complexity of nitrogen was revealed through countless pressure-temperature investigations of its phase diagram, which was found to display a fascinating polymorphism. In total, fourteen distinct solid phases were discovered [1]. These studies were in part motivated by the theoretical prediction that the nitrogen molecule, cemented by one of the strongest known bonds, would break apart at a pressure of approximately 50 GPa [2]. The resulting solid, the cubic-gauche polymeric nitrogen (cg-N), would be solely composed of single-bonded nitrogen atoms forming a three dimensional network. Aside from being fascinating from a theoretical standpoint, cg-N was also predicted to be the ultimate high energy density material. Indeed, due to the very large energy difference that exists between the triple bonded N≡N (954 kJ/mol) and single bonded N-N (160 kJ/mol) configurations, the latter can store a tremendous amount chemical energy which is released upon the decomposition of the single-bonded arrangement towards the molecular phase.

The theoretical prediction was later validated by experiments as cg-N was synthesized, albeit at significantly higher pressures and temperatures than expected (110 GPa and 2000 K) [3]. Unfortunately, this form of polymeric nitrogen could only be retrieved down to about 42 GPa. Since then, much research has been devoted to synthesizing a single-bonded nitrogen arrangement that could be retrieved down to ambient conditions. While recent breakthroughs were achieved in both conventional chemistry [4–6] and high pressure chemistry [7–9], an ideal material has yet to be produced. At the root of it all is the discovery of new polynitrogen geometries that would be better suited for ambient conditions' synthesis.

In that regard, theoretical calculations have rapidly progress. Indeed, a large variety of new single-bonded nitrogen structures was unearthed, including zero-, one-, two-, and three-dimensional motifs [10–16]. As of now, the accepted theoretically calculated sequence of phase transitions is cg-N$\xrightarrow[188\ GPa]{}$ LP-N $\xrightarrow[263\ GPa]{}$ N_{10}, where the LP-N phase is constituted of pseudo N_7 rings chains arranged in layers and the latter is formed of small N_{10} diamondoid clusters [10]. However, this sequence of stable nitrogen phases is a simplistic representation of a more complex situation. Indeed, between 188-263 GPa, six other polynitrogen structures have enthalpies within a few tens of meV of the LP-N phase [10]. The very small calculated enthalpy difference between these various solids means that experimentally, another phase could very well be formed. Above 263 GPa, the N_{10} phase rapidly decreases in enthalpy compared to the other polymeric phases, ensuring that it will eventually be experimentally observed in the 300 GPa regime.

Following these calculations, experiments have extended the pressure-temperature phase diagram of nitrogen to 175 GPa and 3000 K [17]. The LP-N phase was detected when heating pure nitrogen in the 125 GPa – 63 GPa lower than expected by the enthalpy calculations – albeit along with cg-N in significant proportions. At higher pressures, the fraction of produced cg-N was observed to decrease. Moreover, a third polymeric nitrogen phase, *C*2/*c* is claimed to also have been produced as a minority compound. According to calculations, this phase is about 60 meV/atom from the phase with the lowest enthalpy at 130 GPa [16]. This third phase is still subject to controversy [14].

Here, we present the experimental study of pure nitrogen to the most extreme pressure-temperature yet reached by static compression: 244 GPa and 3300 K. A new compound is produced and corresponds to a tetragonal $P4_2bc$ arrangements formed of interconnected chains of nitrogen hexagons. The solid is characterized by both Raman spectroscopy and X-ray diffraction measurements and is found metastable down to a least 66 GPa. Through numerical calculations, further insight is provided on the properties of this new phase.

Results and Discussion

Pure molecular nitrogen samples were loaded at 1400 bars in a diamond anvil cell equipped with diamond culets of 40 to 50 µm and compressed above 200 GPa, pressure at which it is completely opaque, it absorbs the YAG laser and no X-ray diffraction or Raman signature can be detected [18–21]. Beyond pressures of 209 GPa, gently laser-heating the sample to 1200 K was noticed to result in a transformation as it became noticeably partially transparent. Curiously, no X-ray diffraction peaks or vibrational modes appeared. Further compression and laser-heating to 231 GPa and 2800 K increased the solid's transparency but despite obvious modification of its optical properties, still no signature of the converted compound could be distinguished. The nitrogen sample was interpreted to be an amorphous mixture of the various poly-N arrangements. Indeed, in between 188 and 263 GPa, eight possible single bonded phases are predicted by *ab-initio* calculation with enthalpy differences of less than 50 meV [10]. Thus, due to the tiny enthalpy difference between the phases, temperature and pressure gradients within the experimental cavity could plausibly preferentially promote one phase versus another locally, resulting in an indiscriminate blend of sp^3 bonded nitrogen solids. However, at a pressure of 244 GPa, one phase seemingly energetically distanced itself from the others as sample laser-heating to 3300 K resulted in a drastic increase in transparency and the apparition of new diffraction peaks, as illustrated in Fig. 1. While strongly overlapping the powder diffraction lines of the Re gasket, the diffraction spots of the multigrain

new phase could be discerned due to their distinct texture (see Fig. 2). These diffraction spots progressively distanced themselves from those of Re during sample decompression where they were observed down to 176 GPa. The evolution of the new diffraction spots in function of 2θ is shown in the Supplementary Materials.

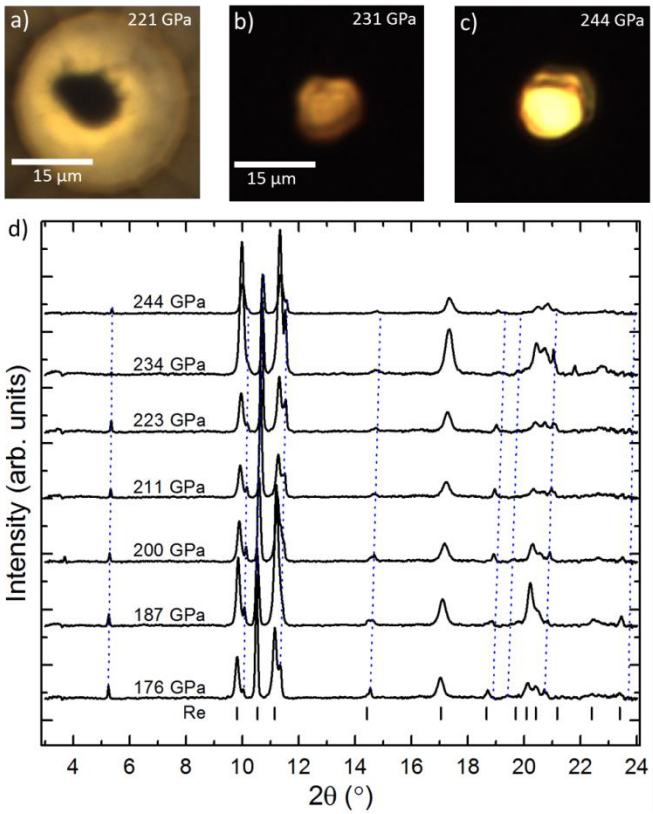

Figure 1: Microphotographs of two pure nitrogen samples. Sample 1 and sample 2 were first laser-heated at pressures of 221 GPa and 209 GPa, respectively. a) Sample 1 at 221 GPa before laser-heating. Sample 2 b) 231 GPa after laser-heating at 2800 K and c) 244 GPa and after laser-heating at 3300 K. d) Integrated X-ray diffraction patterns collected on sample 2 with an X-ray wavelength of λ = 0.3738 Å. The integrated diffraction patterns were obtained at 244 GPa after laser-heating the sample to 3300 K. The transformed sample obtained following its laser-heating was decompressed down to 176 GPa. The Re peaks are marked at 176 GPa by black tick lines. The blue dashed lines follow the nine diffraction lines with pressure. The integrated diffraction patterns are shifted along the *y*-axis for clarity.

At 187 GPa the X-ray diffraction data quality allowed for a Le Bail refinement to be performed (see Fig. 2). However, the newly-observed diffraction spots did not match any of the three previously synthesized polynitrogen phases, which includes the LP-N compound which was previously experimentally formed up to 175 GPa and predicted by the theoretical calculations to have the lowest enthalpy up to 263 GPa [10,17]. Moreover, comparison of the integrated diffraction patterns to the theoretically predicted diamondoid N_{10} cubic (*I*-43*m*) structure, expected to be stable above 263 GPa, did not provide a good fit. However, another predicted structure with a tetragonal ($P4_2bc$) lattice proved to explain exceptionally well all of the new diffraction lines [10]. The Le Bail refinement was performed on the diffractogram recorded at 187 GPa and lattice parameters of a = 4.261(1) Å and c = 8.120(1) Å (V = 147.43 Å^3) were obtained. On account of the orientation of the new phase multigrain, mostly the peaks along the (h0l) direction are discerned. Still, a total of nine diffraction peaks could be followed from 244 GPa down to 176 GPa, as shown in Fig. 1, which is more than sufficient for the accurate determination of a tetragonal lattice.

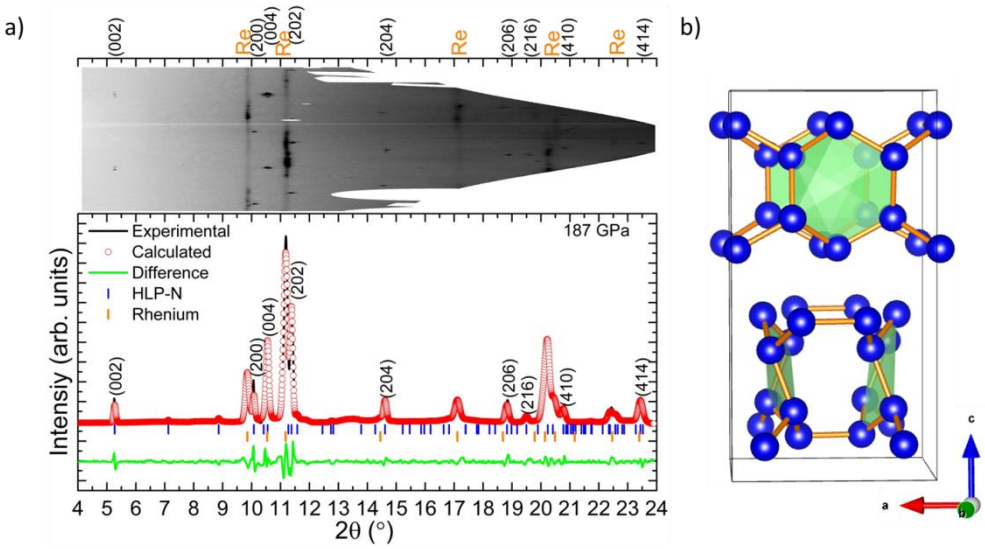

Figure 2: a) Le Bail refinement of an integrated X-ray diffraction pattern recorded at 187 GPa from a sample decompressed from 244 GPa. The (hkl) index of the experimentally observed diffraction peaks are marked. The raw X-ray diffraction pattern is shown above, where the diffraction spots of the multigrain HLP-N sample can be discerned from the Re gasket powder. The reliability factors for the refinement are $\chi^2 = 1.308$, $R_p = 21.6\%$ $R_{wp} = 32.7\%$ and $R_{exp} = 28.6\%$, yielding a goodness of fit of 1.14. An X-ray wavelength of $\lambda = 0.3738$ Å was employed. b) Crystal structure of the HLP-N ($P4_2bc$) compound. For clarity, the inner surface of the N_6 hexagons is filled with a light green plane.

According to the theoretical calculations performed here – and in agreement with the previously reported structure – the tetragonal ($P4_2bc$) lattice contains 32 sp^3-hybridized nitrogen atoms sitting on four distinct *8c* Wyckoff position (see Table S2 in the Supplementary Materials) [10]. As represented in Fig. 2, they are organized into layers stacked in the *c*-axis and made of distorted N_6 hexagons perpendicular to *a*-axis and *b*-axis, successively. The shortest interlayer N-N distance is of 2.02 Å, similar to the shortest intermolecular distance in pure molecular nitrogen at ~100 GPa [22]. Within the hexagons, three different N-N distances are found and vary between 1.30-1.36 Å, with the longest bond length mostly aligned with the *c*-axis. Linking the N_6 rings, two bond lengths are observed at respectively 1.36 Å and 1.38 Å. All of these lengths are characteristic of single bonded nitrogen atoms, as found in cg-N and LP-N [3,17]. Interestingly, the new HLP-N structure is strikingly familiar to the LP-N compound which also contains linked chains quasi-hexagons units arranged in layers.

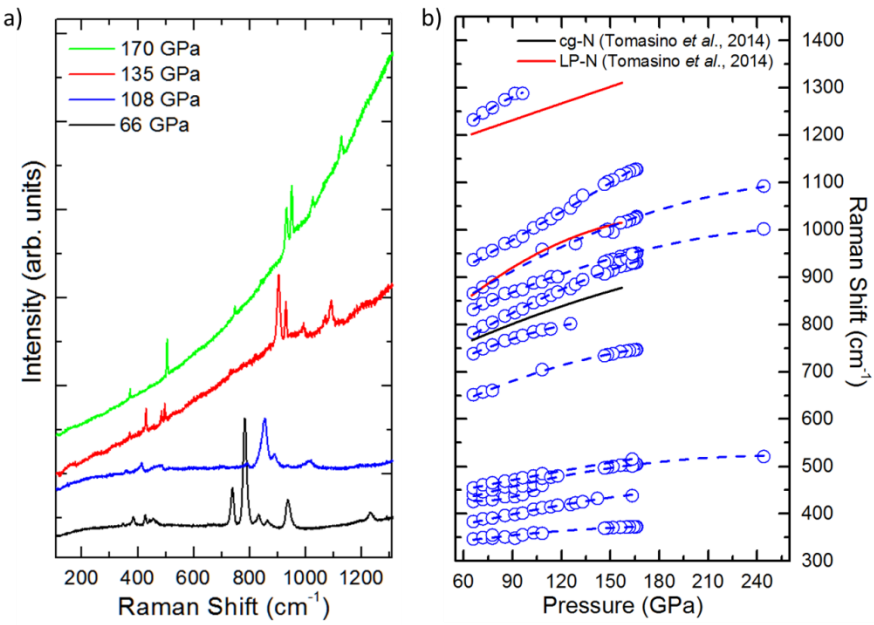

Figure 3: a) Raman spectra obtained from a HLP-N sample during decompression from 170 to 66 GPa, each offsetted for clarity. At 135 GPa, the membrane pressure had been brought to 0.5 bars. In order to further decrease the sample pressure using screws, the membrane pressure was first increased as a precaution to avoid the sample discharge. Unfortunately, this resulted in a broadening of the Raman peak which progressively narrowed on further pressure decrease. b) Raman modes evolution of the HLP-N vibron with pressure. Their continuous and smooth shift with pressure suggests the absence of a phase transition. At 244 GPa, the sample fluorescence only permitted the detection of the three most intense HLP-N modes. The full red and black lines correspond to the LP-N and cg-N Raman modes, respectively, obtained from Ref. 10.

The single-bonded N-N nature of the newly-obtained compound was further confirmed by performing confocal Raman spectroscopy measurements. Indeed, twelve distinct vibrational modes were detected (see Fig. 3) which includes seven at frequencies between 650 and 1300 cm^{-1}, matching the frequency range of other compounds containing single-bonded nitrogen atoms [23–26]. This includes the main Raman modes of cg-N (750-875 cm^{-1}) and LP-N (860-1020 cm^{-1} and 1200-1310 cm^{-1}), measured between 60 and 150 GPa [3,17]. The amount of detected modes do not exceed the 60 Raman modes permitted for the HPL-N structure by group theory analysis ($\Gamma = 12A_1 + 12B_1 + 12B_2 + 24E$).

At the maximum pressure of 244 GPa, the sample presents a strong fluorescence when irradiated with either the 488 or 647.1 nm wavelengths and only the three most intense Raman modes could barely be observed. This fluorescence, perhaps due to poorly transformed portions of the samples, significantly decreases with pressure allowing the detection of lower intensity Raman peaks. The vibrational signature of HLP-N could be followed down during decompression without presenting abrupt changes characteristic of a phase transition. At 66 GPa, one of the diamond anvils failed and freed the nitrogen. Between 244 GPa and 176 GPa, the sample was characterized by X-ray diffraction which explains the gap in between the measurements.

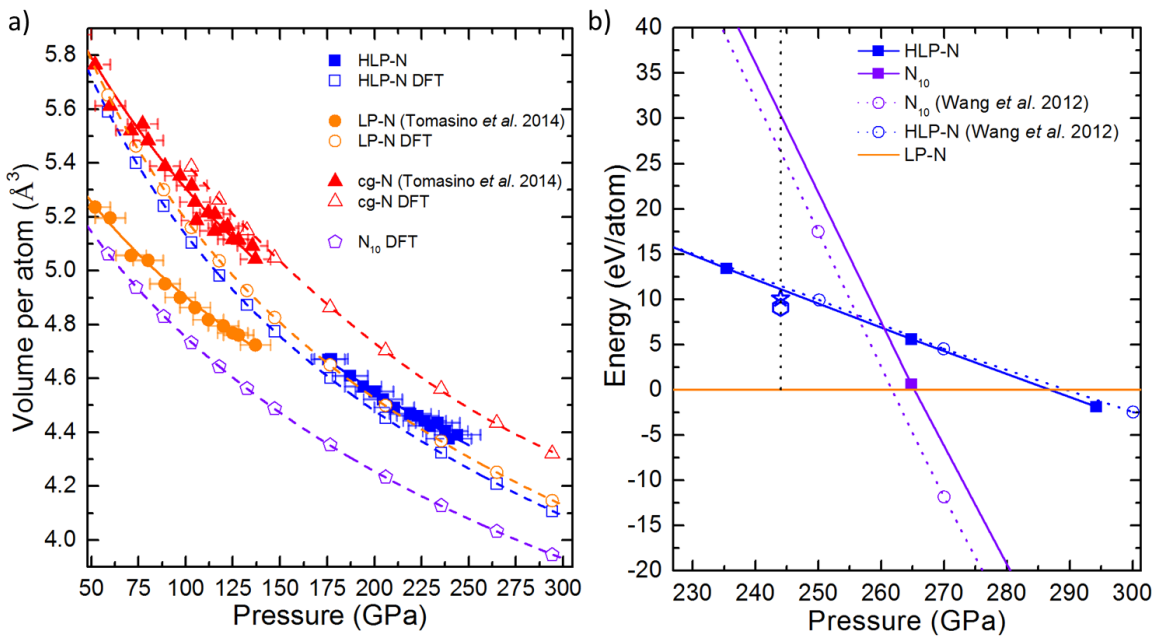

Figure 4: a) Evolution of the volume per atom with respect to pressure for the HLP-N solid as well as for the LP-N and cg-N compounds, obtained from the literature [10]. The pressure uncertainty for the various polymeric phases was determined based on the employed pressure gauges (Re for HLP-N [27], diamond's Raman for the cg-N and LP-N phases [17,28]). An X-ray wavelength of $\lambda = 0.3738$ Å was employed. b) Enthalpy of the LP-N, HLP-N and the N_{10} phases with respect to pressure. The data points are compared with those previously reported [10]. At 244 GPa (dashed vertical line), an enthalpy difference of 11 meV between LP-N and HLP-N is observed. The decrease in the energy difference when accounting for the -TS term (3300 K) and the van der Waals contribution are shown the blue star and hexagon, respectively. The dotted vertical black line marks the pressure at which the HLP-N phase was synthesized (244 GPa).

Based on the X-ray diffraction measurements, the experimental volumes for the HLP-N phase are plotted in Fig. 4 as well as the LP-N and cg-N phases (obtained from the literature [17]) along with their volumes obtained from *ab-initio* calculations. These calculations show the HLP-N to be of higher density than the cg-N and LP-N phase, as commonly observed of phases obtained at greater pressures. Within uncertainty, the experimental and theoretical volumes for the HLP-N and cg-N solids match. Curiously, the experimental LP-N data is at a significantly lower volume than expected by the calculations. Fitting the HLP-N experimental data with a second order Birch-Murnaghan equation of state yields values of V_0 = 200(4) Å^3, K_0 = 333(31) GPa. With the experimental data restricted between 175 and 244 GPa, pressure domain at which the compound is highly incompressible, data points at lower pressure could help increase the precision of these values. In any case, the here-obtained bulk modulus is in-line with those of LP-N and cg-N as they are reported to have values of K_0 = 324.2 GPa (K_0' = 6.0) and K_0 = 298 GPa (K_0' = 4), respectively [3,17].

As alluded to earlier, the HLP-N phase was established by previous theoretical enthalpy calculations to be metastable with respect to the other polynitrogen phases. Indeed, at 244 GPa, the LP-N phase was reported to have an enthalpy 11 meV lower than that of HLP-N. In an attempt to understand the experimental synthesis of the HLP-N solid, further theoretical calculations were performed on the cg-N, LP-N, HLP-N and N_{10} phases. As the enthalpy difference between the LP-N and the HLP-N phases is very small at 244 GPa, the first step was to reproduce the previous enthalpy calculations with a very high convergence rate. As shown in Fig. 4, these calculations perfectly replicate those of Wang *et al.* [10]. Afterwards, two other possibilities were investigated to explain the experimental stabilization of the HLP-N solid. First, the -TS term of Gibbs free energy was taken into account as it is especially relevant due to the very high synthesis temperature. Second, van der Waals interactions were included to better model the

interlayer atomic interactions, shown in Fig 2. Details of the theoretical calculations are provided in the Supplementary Materials.

To include the temperature-entropy term, the phonon dispersion curve of HLP-N and LP-N were first calculated at 244 GPa with the quasi-harmonic approximation (see Supplementary Materials). Computed for the first time, the phonon dispersion curve of HLP-N does not bear any imaginary phonon modes, confirming its dynamical stability. With this additional term, the energy difference between the two phases at 244 GPa and 3300 K only lowered that of the HLP-N phase by about 1 meV with respect to LP-N; bringing the energy difference between the two phases down to 10 meV. Similarly, performing enthalpy calculations with a semi-empirical van der Waals potential reduced the energy difference between the HLP-N and LP-N phases down about 2 meV at 244 GPa. This is illustrated in Fig. 4. In the end, while neither the quasi-harmonic nor the van der Waals considerations could stabilize the HLP-N phase with respect to the LP-N. However, due to the energy marginal difference between the two phases ($\sim$ 10 meV), it is not surprising to find the HLP-N structure experimentally. It is expected that further calculations, perhaps including anharmonic contributions to the phonon bands calculations or by tweaking the employed functional will be able to demonstrate the stability of the here synthesized polynitrogen phase.

Conclusion

In this paper, pure nitrogen was investigated up to the most extreme conditions yet reached through its static compression: 244 GPa and 3300 K. Attesting to the polymorphism of polymeric nitrogen, under these pressure and temperature conditions six phases have an enthalpy within a few meV of the most stable one. Here, one of the phases calculated metastable was demonstrated to be synthesized. Composed of polymeric, interconnected chains of N_6 rings, the HLP-N phase was characterized by Raman spectroscopy and X-ray diffraction. The compound was decompressed down to 66 GPa and its bulk modulus was determined to be of 333(31) GPa. To explain its experimental synthesis, further theoretical calculations were performed. Considering both van der Waals interactions and the entropy-temperature term of Gibbs free energy lowered by 1 to 2 meV the 11 meV energy gap between the HLP-N and LP-N phases at 244 GPa. This result suggests that either anharmonic considerations are needed to correctly predict the high pressure behavior of nitrogen or that the employed functional is not completely adequate.

This is another demonstration of the thermodynamical complexity that is required to accurately model the HP-HT behavior of nitrogen. Indeed, at low pressures including the quadrupole-quadrupole interaction between N_2 molecules is vital to reproduce the experimentally observed phases while at slightly high pressures, entropy is critical to explain the stability of the molecular phases with regards to cg-N [29–31]. Even more recently, the LP-N phase was synthesized at a pressure about 63 GPa lower than expected by the calculations, which has yet to be explained by theory [10,17]. This present study should motivate further theoretical investigation of the system, first to understand the stability of the HLP-N with regards to LP-N and then to interpret how the stability of the HLP-N phase might affect the stability domains of other high pressure phases of nitrogen, notably diamondoid N_{10}.

References

[1] M. Frost, R. T. Howie, P. Dalladay-Simpson, A. F. Goncharov, and E. Gregoryanz, Phys. Rev. B **93**, 024113 (2016).
[2] C. Mailhiot, L. Yang, and A. McMahan, Phys. Rev. B **46**, 14419 (1992).
[3] M. I. Eremets, A. G. Gavriliuk, I. A. Trojan, D. A. Dzivenko, and R. Boehler, Nat. Mater. **3**, 558 (2004).
[4] C. Zhang, C. Sun, B. Hu, C. Yu, and M. Lu, Science **355**, (2017).
[5] Y. Xu, Q. Wang, C. Shen, Q. Lin, P. Wang, and M. Lu, Nature **549**, 78 (2017).
[6] C. Sun, C. Zhang, C. Jiang, C. Yang, Y. Du, Y. Zhao, B. Hu, Z. Zheng, and K. O. Christe, Nat. Commun. **9**, 1269 (2018).
[7] D. Laniel, G. Weck, G. Gaiffe, G. Garbarino, and P. Loubeyre, J. Phys. Chem. Lett. **9**, 1600 (2018).
[8] B. A. Steele, E. Stavrou, J. C. Crowhurst, J. M. Zaug, V. B. Prakapenka, and I. I. Oleynik, Chem. Mater. **29**, 735 (2017).
[9] S. Duwal, Y.-J. Ryu, M. Kim, C.-S. Yoo, S. Bang, K. Kim, and N. H. Hur, J. Chem. Phys. **148**, 134310 (2018).
[10] X. Wang, Y. Wang, M. Miao, X. Zhong, J. Lv, T. Cui, J. Li, L. Chen, C. J. Pickard, and Y. Ma, Phys. Rev. Lett. **109**, 175502 (2012).
[11] C. J. Pickard and R. J. Needs, Phys. Rev. Lett. **102**, 1 (2009).
[12] A. R. Oganov and C. W. Glass, J. Chem. Phys. **124**, 244704 (2006).
[13] Y. Ma, A. Oganov, Z. Li, Y. Xie, and J. Kotakoski, Phys. Rev. Lett. **102**, 065501 (2009).
[14] A. A. Adeleke, M. J. Greschner, A. Majumdar, B. Wan, H. Liu, Z. Li, H. Gou, and Y. Yao, Phys. Rev. B **96**, 1 (2017).
[15] J. Sun, M. Martinez-Canales, D. D. Klug, C. J. Pickard, and R. J. Needs, Phys. Rev. Lett. **111**, 1 (2013).
[16] Y. Yao, J. S. Tse, and K. Tanaka, Phys. Rev. B - Condens. Matter Mater. Phys. **77**, 1 (2008).
[17] D. Tomasino, M. Kim, J. Smith, and C.-S. Yoo, Phys. Rev. Lett. **113**, 205502 (2014).
[18] A. F. Goncharov, E. Gregoryanz, H. K. Mao, Z. Liu, and R. J. Hemley, Phys. Rev. Lett. **85**, 1262 (2000).
[19] E. Gregoryanz, A. Goncharov, R. Hemley, and H. Mao, Phys. Rev. B **64**, 052103 (2001).
[20] E. Gregoryanz, A. F. Goncharov, C. Sanloup, M. Somayazulu, H. K. Mao, and R. J. Hemley, J. Chem. Phys. **126**, 184505 (2007).
[21] M. I. Eremets, R. J. Hemley, H. Mao, and E. Gregoryanz, Nature **411**, 170 (2001).
[22] M. I. Eremets, A. G. Gavriliuk, N. R. Serebryanaya, I. A. Trojan, D. A. Dzivenko, R. Boehler, H. K. Mao, and R. J. Hemley, J. Chem. Phys. **121**, 11296 (2004).
[23] S. Jiang, X. Huang, D. Duan, S. Zheng, F. Li, X. Yang, Q. Zhou, B. Liu, and T. Cui, J. Phys. Chem. C **118**, 3236 (2014).
[24] A. F. Young, J. A. Montoya, C. Sanloup, M. Lazzeri, E. Gregoryanz, and S. Scandolo, Phys. Rev. B **73**, 2 (2006).
[25] E. Gregoryanz, C. Sanloup, M. Somayazulu, J. Badro, G. Fiquet, H. Mao, and R. J. Hemley, Nat. Mater. **3**, 294 (2004).
[26] A. F. Young, C. Sanloup, E. Gregoryanz, S. Scandolo, R. J. Hemley, and H. K. Mao, Phys. Rev. Lett. **96**, 155501 (2006).
[27] S. Anzellini, A. Dewaele, F. Occelli, P. Loubeyre, and M. Mezouar, J. Appl. Phys. **115**, 043511 (2014).
[28] Y. Akahama and H. Kawamura, J. Appl. Phys. **100**, 043516 (2006).
[29] A. Mulder, J. P. J. Michels, and J. A. Schouten, J. Chem. Phys. **105**, 3235 (1996).
[30] A. Erba, L. Maschio, C. Pisani, and S. Casassa, Phys. Rev. B **84**, 012101 (2011).
[31] G. Weck, F. Datchi, G. Garbarino, S. Ninet, J.-A. Queyroux, T. Plisson, M. Mezouar, and P. Loubeyre, Phys. Rev. Lett. **119**, 235701 (2017).

Supplementary Material

The hexagonal layered polymeric nitrogen phase synthesized near 250 GPa

D. Laniel[1,2], G. Geneste[1], G. Weck[1], M. Mezouar[3], P. Loubeyre[1]*

[1]CEA, DAM, DIF, F-91297 Arpajon, France.

[2]CNES Launcher Directorate, 52 rue J. Hillairet, 75612 Paris cedex.

[3]European Synchrotron Radiation Facility, 6 Rue Jules Horowitz BP220, F-38043 Grenoble CEDEX, France.

* Email: dominique.laniel@cea.fr

Experimental Method

Pure molecular nitrogen was loaded at 1400 bars in a membrane diamond anvil cells (DAC) equipped with diamond culets of 40 to 50 µm. A rhenium gasket with a hole diameter between 17-23 µm was employed. On account of the very small experimental cavity, no internal pressure calibrants were put in to prevent parasitic diffraction lines and chemical reactions. Instead, pressure was determined either with the equation of state of rhenium by collecting the X-ray diffraction signal at the edge of the sample cavity or using the high-frequency edge of the diamond anvils first order Raman band, shown to have a 5% and 2% uncertainty in pressure, respectively [1,2].

Angular dispersive powder X-ray diffraction measurements were obtained at the ID27 beamline of the European Synchrotron Research Facility (ESRF). The X-ray beam, of wavelength set at $\lambda = 0.3738$ Å, was focused down to a full width at half maximum of about 2.5 x 2.5 μm^2. A MAR-CCD detector recorded the X-ray diffraction patterns which were then integrated using DIOPTAS and analyzed using the XRDA as well as the FULLPROF softwares [3–5]. Double-sided YAG laser-heating of the nitrogen samples was performed through both openings of the DAC on ID27 and at our laboratory. Temperatures during laser-heating were accurately measured by fitting the sample's thermal radiation to Planck's law. To ensure homogenous temperatures inside the sample cavity, the temperature was measured from both openings of the DAC and verified to be equal. As molecular nitrogen readily absorbs the YAG laser above about 110 GPa, no absorber was required [6].

Confocal Raman spectroscopy measurements were performed using an Alpha300M+ (WITec). Sample excitation was done with a continuous Ar-Kr laser employing the 488 nm line, focused down to less than 1 µm. The Stokes Raman signal was collected in back-scattering geometry by a CCD coupled to a 1800 lines/mm grating, allowing a spectral resolution of approximately 5 cm^{-1}. To avoid a photoinduced decomposition of the novel polynitrogen phase, the laser power was kept below 10 mW on the sample and acquisition times were of 180 s.

Theoretical Calculation Method

Density-functional calculations have been performed with the ABINIT code [7] and the Projector Augmented Wave (PAW) method [8,9], in the framework of the Generalized Gradient Approximation, as formulated by Perdew, Burke and Ernzerhof [10]. First a set of structural optimizations have been performed to obtain the enthalpy and volume as a function of pressure, for different structures proposed in the literature (cg-N, LP-N, HLP-N and the N_{10} diamondoid). The unit cells of these structures contain respectively 16, 32, 20 and 8 atoms. The plane-wave cut-off is set to 30 Hartrees and a dense k-point mesh is used to sample the Brillouin Zone (16x16x16 for LP-N, 12x12x7 for HLP-N, 16x16x16 for N_{10} and 16x16x16 for cg-N). At one selected pressure (294 GPa), we have checked that the structural optimization using a k-point mesh of 24x24x24 (LP-N), 24x24x15 (HLP-N) and 24x24x24 (N_{10}) provides

the same enthalpy (within differences lower than $5x10^{-5}$ meV/atom) as with the previously mentioned k-point meshes [11]. Also, the enthalpy differences (between HLP-N and LP-N as well as between N_{10} and LP-N) obtained after structural optimization between 44 and 294 GPa are equal to those obtained using a plane-wave cut-off of 25 Hartrees within at most 0.4 meV/atom.

Then, we compute the phonon band structure, effective charges and dielectric tensor of two phases (LP-N and HLP-N) at one pressure (300 GPa), using Density Functional Perturbation Theory as implemented in ABINIT [12]. For these calculations, the plane-wave cut-off is set to 25 Hartrees, and the BZ sampling is 16x16x16 for LP-N and 16x16x10 for HLP-N. The phonon modes are computed on a 8x8x8 (resp. 8x8x5) q-point grid for LP-N (resp. HLP-N). They are used to calculate the phonon contribution to the vibrational free energy at 300 and 3300 K. The convergence is checked with respect to the calculation using a 4x4x4 (resp. 4x4x5) q-point grid to be better than 1 meV/atom on the free energy differences between the two phases.

Finally, we have tested the possible influence of dispersive interactions by correcting the PBE functional with the semi-empirical DFT-D3(BJ) scheme of Grimme et al [13,14]. Using this modified PBE functional, we have recomputed the enthalpies and volume as a function of pressure for the four phases, using the same plane-wave cut-off (30 Ha) and k-point meshes as the ones used for the PBE structural optimizations. This scheme is denoted hereafter as "PBe+VdW".

Additional experimental and theoretical data

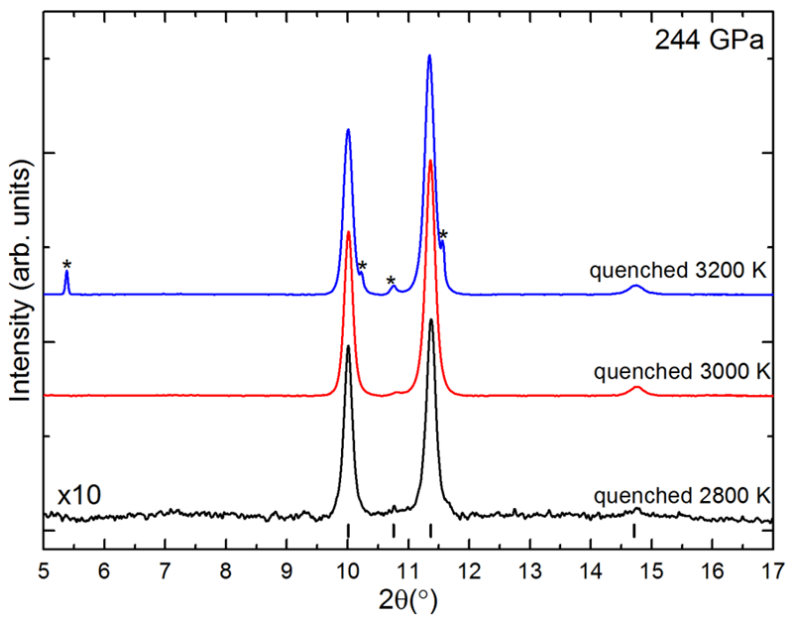

Figure S1: X-ray diffraction patterns of sample 2 at 244 GPa and after rounds of laser-heating at increasing temperatures. The diffractogram obtained ensuing the sample quenching from 3200 K shows new diffractions lines attributed to HLP-N. The black tick marks indicate rhenium's diffraction lines.

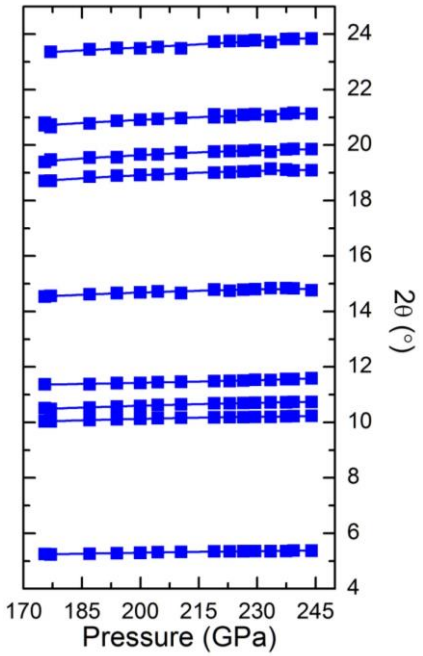

Figure S2: X-ray diffraction lines' position in 2θ of the HLP-N compound from 176 GPa to 244 GPa. An X-ray wavelength of λ = 0.3738 Å was employed.

Table S1: Calculated atomic positions for the HLP-N compound at 294 GPa (*a* = 4.1231 Å and *c* = 7.7296 Å) compared to the previously reported HLP-N lattice at 300 GPa (*a* = 4.1219 Å and *c* = 7.7154 Å) [11].

	Wyckoff site	x	y	z
N1	*8c*	0.8407	0.0296	0.0914
N1 (Wang *et al.)*	*8c*	0.8407	0.0296	0.0911
N2	*8c*	0.1622	0.4681	0.4091
N2 (Wang *et al.*)	*8c*	0.1622	0.4679	0.4095
N3	*8c*	0.3029	0.1934	0.6672
N3 (Wang *et al.*)	*8c*	0.3030	0.1929	0.6696
N4	*8c*	0.1945	0.1963	0.3287
N4 (Wang *et al.*)	*8c*	0.1942	0.1961	0.3287

Table S2: Calculated atomic positions for the HLP-N compound at 235 GPa with lattice parameters *a* = 4.183 Å and *c* = 7.909 Å.

	Wyckoff site	x	y	z
N1	*8c*	0.8401	0.0288	0.0927
N2	*8c*	0.1627	0.4693	0.4075
N3	*8c*	0.3011	0.1958	0.6702
N4	*8c*	0.1967	0.1982	0.3282

Table S3: Position of the HLP-N diffraction peaks with respect to pressure.

P (GPa)	*d*-spacing (Å)	2θ (°)
175.5	4.08261	5.24779
175.5	2.13742	10.03293
175.5	2.04176	10.50427
175.5	1.88762	11.36476
175.5	1.47791	14.53042
175.5	1.15037	18.70057
175.5	1.11	19.38712
175.5	1.08712	19.79916
175.5	1.03977	20.71046
175.5	1.03529	20.80121
177	4.09419	5.23293
177	2.13707	10.03454
177	2.04659	10.47942
177	1.47538	14.55551
177	1.33654	16.077
177	1.15016	18.70391
177	1.1056	19.465
177	1.04344	20.637
177	1.03829	20.74035
177	0.92327	23.35844
187	4.07641	5.25577
187	2.12875	10.07389
187	2.03735	10.52708
187	1.46941	14.61495
187	0.91972	23.44994
187	1.32866	16.173
187	1.14127	18.851
187	1.10112	19.545
187	1.03678	20.771
187	1.88638	11.37226
194	4.06124	5.27542
194	2.1221	10.10554
194	2.0305	10.5627
194	1.87966	11.413
194	1.46499	14.65925
194	1.13849	18.89742
194	1.10055	19.55513
194	1.03205	20.86709
194	0.91794	23.49612
200	4.05123	5.28845

200	2.11698	10.13005
200	2.02583	10.58707
200	1.46273	14.68201
200	1.13716	18.91981
200	1.09459	19.6628
200	1.03007	20.90773
200	0.91831	23.4864
200	1.87835	11.421
204.5	4.0324	5.31317
204.5	2.11346	10.14695
204.5	2.01937	10.62108
204.5	1.45938	14.71599
204.5	1.13648	18.93124
204.5	1.09509	19.65371
204.5	1.02838	20.94258
204.5	0.91648	23.53403
204.5	1.87492	11.442
210.5	4.02225	5.3266
210.5	2.1105	10.1612
210.5	2.01477	10.64537
210.5	1.87247	11.457
210.5	1.46534	14.65581
210.5	1.13513	18.95384
210.5	1.09111	19.726
210.5	1.02743	20.96204
210.5	0.91831	23.48647
219	4.0111	5.3414
219	2.1071	10.17763
219	2.00837	10.67941
219	1.86841	11.482
219	1.4526	14.785
219	1.13242	18.9997
219	1.08942	19.757
219	1.02556	21.00083
219	1.02061	21.10369
219	0.90932	23.722
223	4.00913	5.34403
223	2.10614	10.1823
223	2.008	10.6814
223	1.45706	14.7395
223	1.13144	19.01623
223	1.02295	21.05499
223	1.86695	11.491

223	1.08833	19.777
223	1.0256	21
223	0.90838	23.747
226.5	4.00481	5.34981
226.5	2.10616	10.18221
226.5	2.0056	10.6942
226.5	1.13032	19.03524
226.5	1.02139	21.08742
226.5	0.90815	23.753
226.5	1.86533	11.501
226.5	1.45338	14.777
226.5	1.088	19.783
229.5	3.99986	5.35643
229.5	2.10365	10.19438
229.5	2.00332	10.70638
229.5	1.86054	11.53069
229.5	1.45133	14.79804
229.5	1.12927	19.05317
229.5	1.02039	21.10832
229.5	1.08653	19.81
229.5	0.90732	23.775
233.5	4.0055	5.34889
233.5	2.10349	10.19516
233.5	2.00169	10.71517
233.5	1.86219	11.52046
233.5	1.02389	21.03541
233.5	1.44793	14.833
233.5	1.12437	19.137
233.5	1.08969	19.752
233.5	0.9097	23.712
237.5	3.9993	5.35717
237.5	2.10041	10.21017
237.5	2.00162	10.71551
237.5	1.85633	11.55693
237.5	1.44761	14.83627
237.5	1.1258	19.11248
237.5	1.02004	21.11568
237.5	1.08491	19.84
237.5	0.90578	23.816
239.4	3.98966	5.37013
239.4	2.09892	10.21741
239.4	1.99897	10.72977
239.4	1.85667	11.5548

239.4	1.44828	14.82932
239.4	1.12772	19.07954
239.4	1.01818	21.15474
239.4	1.08393	19.858
239.4	0.90552	23.823
244	3.99151	5.36764
244	2.09631	10.23018
244	1.99913	10.72893
244	1.8517	11.58592
244	1.4549	14.76151
244	1.12752	19.08302
244	1.01979	21.12087
244	0.90511	23.834
244	1.08458	19.846

Table S4: Volume per atom of the HLP-N lattice with respect to pressure.

P (GPa)	Volume/atom ($Å^3$)
175.5	4.67102
177	4.67256
187	4.60982
194	4.56986
200	4.55144
204.5	4.52213
210.5	4.49275
219	4.46861
223	4.46074
226.5	4.44253
229.5	4.42494
233.5	4.43472
237.5	4.40378
239.4	4.37598
244	4.39085

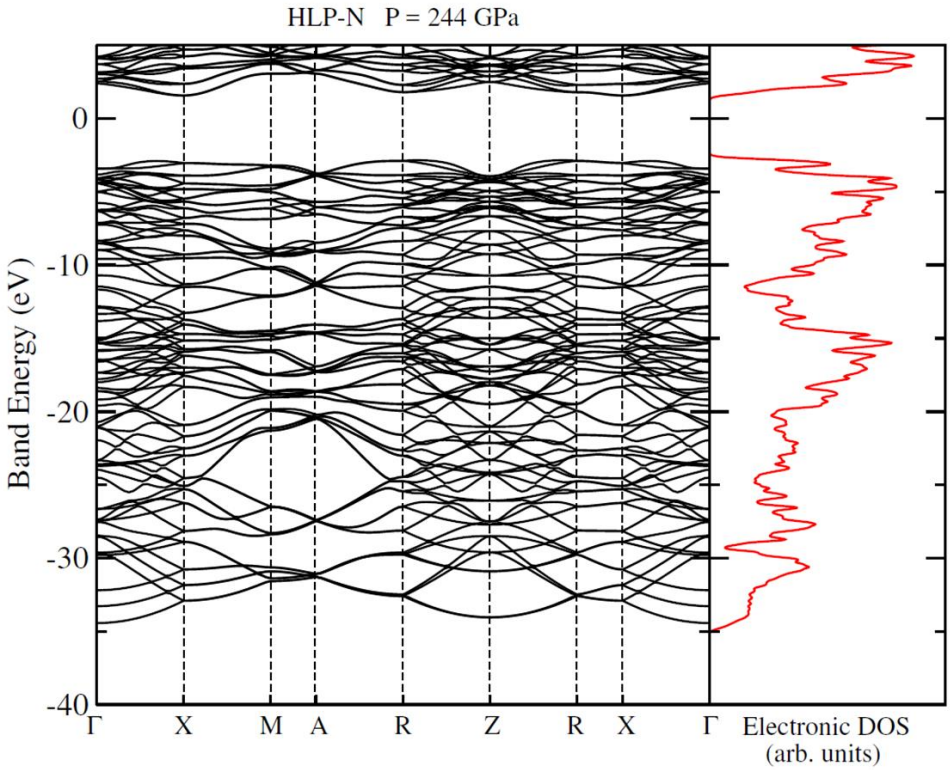

Figure S3: Electronic band structure of the HLP-N phase at 244 GPa along with its electronic density of states (DOS). The Fermi level was set at 0 eV. The band gap is of 3.9 eV.

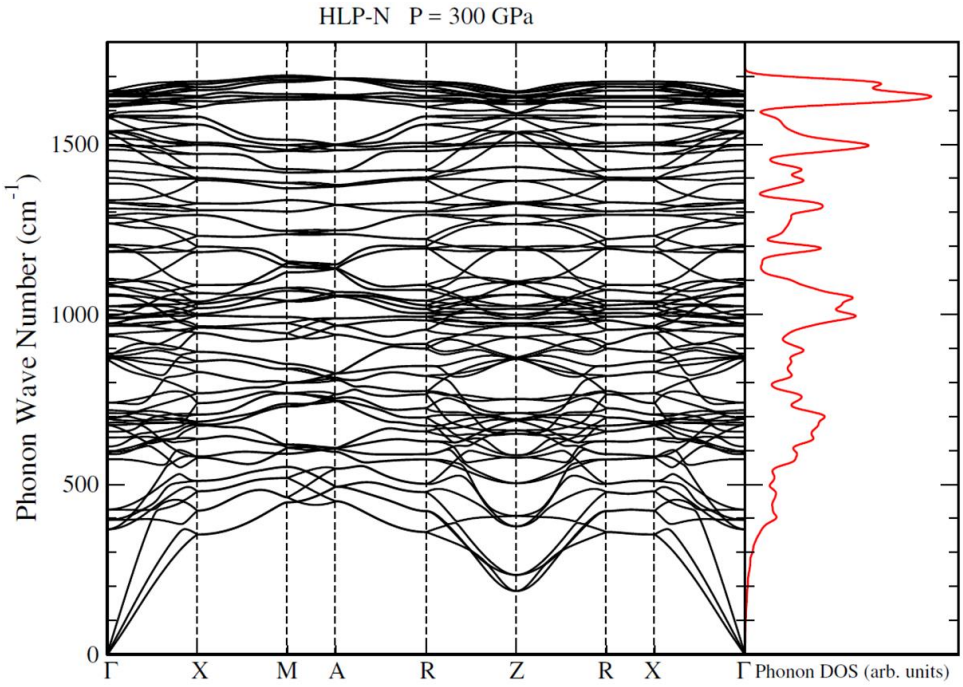

Figure S4: Phonon band structure of the HLP-N phase at 300 GPa along with its DOS. The optical phonons (all but three lowest-frequency modes) at the Γ point are at frequencies between ~370 and ~1600 cm^{-1}.

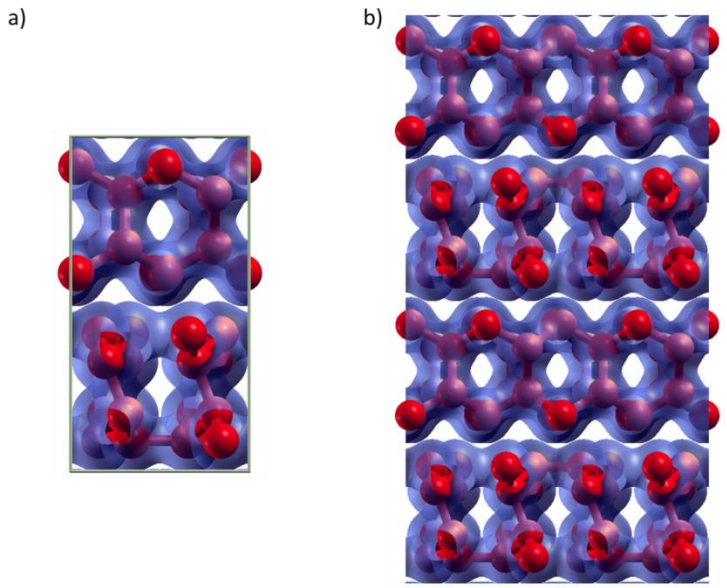

Figure S5: Structure of the HLP-N solid showing the isosurface for the electron density of 1.01 el/Å^3. a) A single lattice and b) four lattices are shown. These drawings show 1) the lack of bonding in the interlayer regions and 2) the significance of accounting for van der Waals interactions.

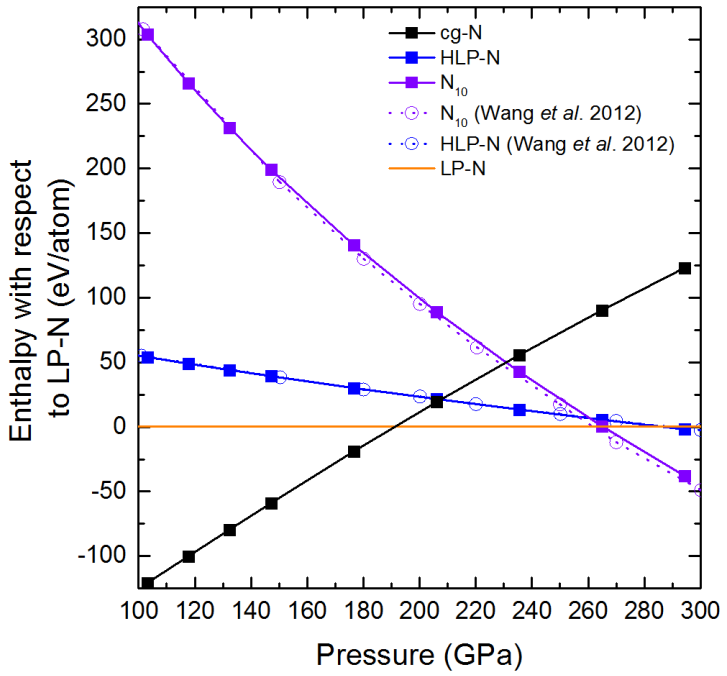

Figure S6: The enthalpy-pressure curve between 100 GPa and 320 GPa.

References

[1] S. Anzellini, A. Dewaele, F. Occelli, P. Loubeyre, and M. Mezouar, J. Appl. Phys. **115**, 043511 (2014).

[2] Y. Akahama and H. Kawamura, J. Phys. Conf. Ser. **215**, 012195 (2010).

[3] S. Desgreniers and K. Lagarec, J. Appl. Crystallogr. **27**, 432 (1994).

[4] C. Prescher and V. B. Prakapenka, High Press. Res. **35**, 223 (2015).

[5] J. Rodriguez-Carvajal, Phys. B Condens. Matter **192**, 55 (1993).

[6] D. Tomasino, M. Kim, J. Smith, and C.-S. Yoo, Phys. Rev. Lett. **113**, 205502 (2014).

[7] X. Gonze, F. Jollet, F. Abreu Araujo, D. Adams, B. Amadon, T. Applencourt, C. Audouze, J.-M. Beuken, J. Bieder, A. Bokhanchuk, E. Bousquet, F. Bruneval, D. Caliste, M. Côté, F. Dahm, F. Da Pieve, M. Delaveau, M. Di Gennaro, B. Dorado, C. Espejo, G. Geneste, L. Genovese, A. Gerossier, M. Giantomassi, Y. Gillet, D. R. Hamann, L. He, G. Jomard, J. Laflamme Janssen, S. Le Roux, A. Levitt, A. Lherbier, F. Liu, I. Lukačević, A. Martin, C. Martins, M. J. T. Oliveira, S. Poncé, Y. Pouillon, T. Rangel, G.-M. Rignanese, A. H. Romero, B. Rousseau, O. Rubel, A. A. Shukri, M. Stankovski, M. Torrent, M. J. Van Setten, B. Van Troeye, M. J. Verstraete, D. Waroquiers, J. Wiktor, B. Xu, A. Zhou, and J. W. Zwanziger, Comput. Phys. Commun. **205**, 106 (2016).

[8] P. E. Blöchl, Phys. Rev. B **50**, 17953 (1994).

[9] M. Torrent, F. Jollet, F. Bottin, G. Zérah, and X. Gonze, Comput. Mater. Sci. **42**, 337 (2008).

[10] J. P. Perdew, K. Burke, and M. Ernzerhof, Phys. Rev. Lett. **77**, 3865 (1996).

[11] X. Wang, Y. Wang, M. Miao, X. Zhong, J. Lv, T. Cui, J. Li, L. Chen, C. J. Pickard, and Y. Ma, Phys. Rev. Lett. **109**, 175502 (2012).

[12] C. Audouze, F. Jollet, M. Torrent, and X. Gonze, Phys. Rev. B - Condens. Matter Mater. Phys. **73**, (2006).

[13] S. Grimme, S. Ehrlich, and L. Goerigk, J. Comput. Chem. **32**, 1456 (2011).

[14] S. Grimme, J. Antony, S. Ehrlich, and H. Krieg, J. Chem. Phys. **132**, 154104 (2010).

SEARCH FOR XENON POLYNITROGEN COMPOUNDS

I. *INTRODUCTION*

Heaviest among the stable noble gases and fifth in the seventh column of the periodic table, xenon is an odorless and colorless gas. It exists in the atmosphere, where it is contained in about one part per million and is retrieved from air by fractional distillation. Due to its scarcity, xenon is one of the most expensive gases.

Part of the noble gases family, it was first thought to be a completely inert gas. However, its electronic structure, providing it with a large number of electrons, makes it a unique case. Indeed, with a radius of 2.16 Å, electrons further away from the xenon nuclei – namely the ones in the *5p* shell – are very loosely bound and susceptible to interact, particularly with a highly electronegative atom [162]. The potential for a chemical reaction with xenon was first demonstrated in 1962 when Neil Bartlett produced the first ever noble gas compound: xenon hexafluoroplatinate ($Xe^+[PtF_6]^-$) [163]. Soon after, this lead to the discovery of the noble gas binary compound XeF_4 by a direct chemical reaction between Xe and F at 400°C in an atmosphere of molecular hydrogen [164]. The compound was thoroughly characterized by a large variety of experimental methods (single crystal X-ray and neutron diffraction, infrared and Raman spectroscopy as well as nuclear magnetic resonance [165]) and its structure was unambiguously determined [166,167]. Its structure is shown in Figure 1. Later, it was understood that by slightly changing the concentrations of xenon and fluorine as well as the reaction temperature, the XeF_2 and XeF_6 compounds could also be produced [168–170]. The structure of XeF_2 is also shown in Fig. 1. On the other hand, that of XeF_6 is poorly known, partially due to its six different crystalline arrangements each with large unit cells [166,171]. After this first syntheses, a plethora of Xe-based compounds were produced, now numbering in the tens [165,172].

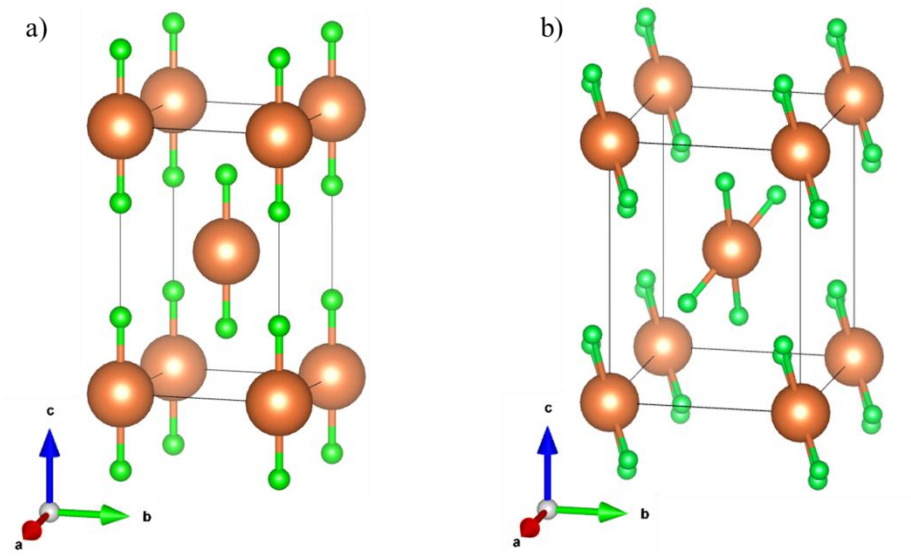

Figure 1: Crystal structure of the xenon fluoride compounds. a) XeF_2 crystallizes in a tetragonal ($I4_1/mmm$) unit cell with Xe and fluorine atoms on the *2a* and *4e* (z = 0.2857 Å) Wyckoff positions with Xe-F bond lengths of 1.997 Å. b) XeF_4 adopts a monoclinic lattice ($P2_1/n$) with the Xe atom on the *2a* Wyckoff position and the F atoms two different *4e* sites, (-0.225, 0.027, -0.306) and (0.242, 0.165, -0.162). The Xe-F bond lengths are of 1.951 and 1.954.

At ambient pressure, the behavior and the properties of xenon are well understood [165]. Its compression to extreme densities however, both as a pure element and in a mixture, unveiled a new exciting chemistry. In the case of elemental xenon, a reorganization of its electronic density was expected to lead to an insulator to metal phase transition, through the pressure-induced indirect overlap of the *5p* valence and *5d* conduction bands. The metallization was first calculated to occur around 200 GPa [173] and was later revised down to 128 GPa [174,175]. These predictions generated a great deal of research activities [88,176–185]. Progressively, the properties of xenon under compression were uncovered. At ambient temperature, xenon solidifies at a pressure of 0.4 GPa and adopts an *fcc* arrangement [186]. The solid undergoes a very sluggish martensitic phase transition from *fcc* to *hcp* starting as early as 3 GPa [183]. Near 70 GPa, the transformation is completed and the hexagonal phase persists at least up to 259 GPa [181,183,187]. The metallization of xenon was observed by absorption and reflection measurements at 134 GPa [88,185], as later confirmed by electrical conductivity data [182].

Having the pressure behavior of pure xenon mapped up allows a better understanding of the changes induced by other atomic species. At low pressure, mixtures of xenon with another hardly reacting entity, such as H_2O, O_2, N_2 and H_2 typically form compounds bound through weak van der Waals interaction. For these types of compounds, it was inferred from studies on metallic alloys that their solid state

solubility is mainly driven by geometrical effects, known as the Hume-Rothery rule [188]. This empirical rule states that if the effective molecular diameter ratio (α) of the two mixed species exceeds about 14%, a poor solid state solubility is to be expected and instead stoichiometric compounds may be formed [189]. In particular, it was demonstrated that a α between 0.76 and 0.84 also allows to form a specific type of compound with the AB_2 stoichiometry coined as Laves phases [190]. Nonetheless, Laves phase compounds were experimentally observed in solids for a broader range of α values (from 0.6 to 0.95) [191]. In the case of xenon-oxygen, -water and -hydrogen mixtures, stoichiometric solids were observed, respectively the $Xe(O_2)_2$, $Xe_4O_{12}H_{12}$ and $Xe(H_2)_8$ compounds [192–194]. As it will be described below, xenon can not only be part of weakly bonded van der Waals compounds but also actively chemically interact with other elements.

Mixtures of xenon with elements found in the Earth are of particular interest as they could provide an answer to a long-standing question in geophysics and planetary sciences: the missing xenon paradox. Based on chondritic meteorites, whose chemical composition is assimilated to that of an undifferentiated Earth, less than 10% of Earth's xenon is accounted for [195]. It is expected that the missing xenon is sequestered in the Earth itself [196]. Numerical calculations support this hypothesis as they predict xenon to form strong covalent bonds with oxygen and intermetallic compounds with iron and nickel - elements constituting a large portion of Earth's chemical entities - under high pressures [156,197–199]. Recent experiments added more weight to this theory as Xe_2O_5, Xe_3O_2, $XeNi_3$ and $Xe(Fe, Fe/Ni)_3$ were synthesized [200–202]. In the case of the Xe-O_2 compounds, both could be produced just below 100 GPa and are favored depending on the Xe/O_2 ratio: Xe_2O_5 and Xe_3O_2 for oxygen-rich and poor mixtures, respectively. Xe_2O_5 adopts a tetragonal (*P*4/*ncc*) configuration with xenon in the 4+ and 6+ valence states, with Xe-O bonds lengths between 1.83-1.98 Å (at 83 GPa). On the other hand, Xe_3O_2 is found in an orthorhombic (*Immm*) arrangement with a xenon atom in the 4+ valence state and a second, non-bonding (valence state of 0). The Xe-O distance was determined to be of 1.99 at 97 GPa and is similar to those found in Xe_2O_5. The two structures are drawn in Figure 2.

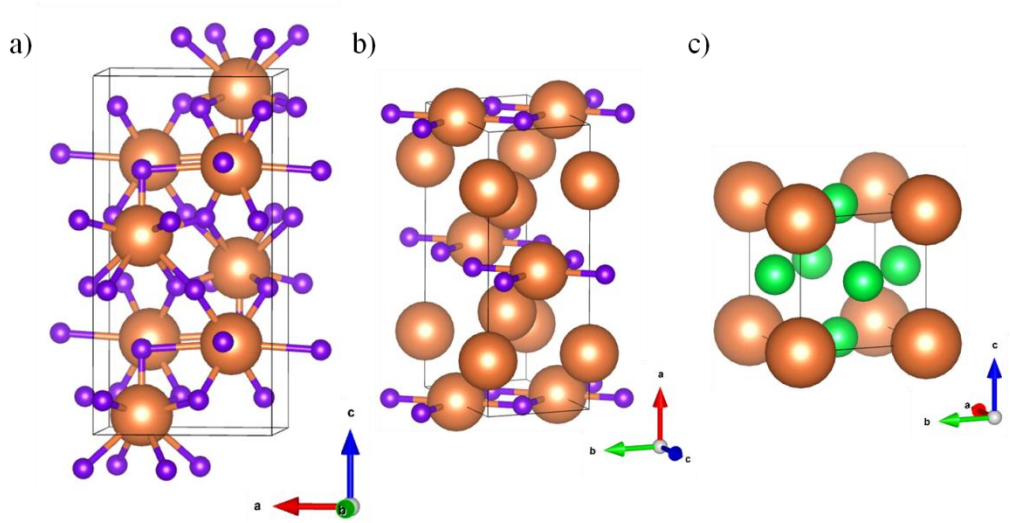

Figure 2: Structures of the a) Xe_2O_5, b) Xe_3O_2 and c) $XeNi_3$ compounds. The orange, purple and green atoms represent xenon, oxygen and nickel, respectively.

The synthesis of $XeNi_3$ was done at 150 GPa by laser-heating pure nickel embedded in xenon [201,202]. A simple cubic (*Pm*-3*m*) structure was observed, isostructural to Cu_3Au. A chemical reaction between xenon and iron was only detected above 210 GPa, also after laser-heating the sample. The resulting X-ray diffraction pattern seemed to indicate the synthesis of two intermetallic Xe-Fe compounds, found in orthorhombic (*Pmmn*) and cubic (*Pm*-3*m*) arrangements, the latter with the same atomic positions as $XeNi_3$ occupied. While the experiments are not conclusive, Xe/Fe ratios of 1:3 are suggested for both solids.

These results demonstrate both the low pressure tendency of xenon to produce van der Waals compound and its the high pressure chemical reactivity. However many questions still remain to be answered. First, what does the binary phase diagram of Xe-N_2 looks like? Similarly to water, hydrogen and oxygen mixtures with xenon, would a van der Waals compound be formed? If one of more compounds are formed, would they be adequate candidates to test out chemical precompression or observe the effect of topochemistry? Would a xenon-nitrogen chemical interaction be observed? Would it lead to the synthesis of a polymeric Xe-N solid? If so, at what pressure? What would be its metastability?

Already, a few tentative answers can be provided. At 5.5 GPa, xenon and molecular nitrogen have an effective molecular diameter ratio of $\alpha = 0.88$. Solely from this value, a solid-state solubility along with the formation of a van der Waals compound could be expected. Such a compound also has been suggested to form in Xe-N_2 mixtures (35). Based on the Raman characterization of samples at 84 and 7.5 mol% of N_2

performed at 408 K, a van der Waals compound with a mole fraction of xenon between 0.4 and 0.7 was hypothesized. A single vibrational mode of this solid was detected near 5 GPa and could be followed up to 13 GPa. Numerical simulations provide further clues on the Xe-N_2 high pressure behavior. Employing first-principle swarm-structure calculations (the CALYPSO method [203]), Peng *et al*. [18] constructed the convex hull diagram of Xe-N_2 by searching for stable compounds at 17 different mixture concentrations. Only at a Xe/N_2 ratio of 1:3 was a compound calculated to have a lower enthalpy than the two separated elements. The XeN_6 compound was calculated to be stable above 146 GPa up to at least 300 GPa at a null temperature. The synthesis pressure of this compound was expected to decrease down to 132 GPa at 2500 K. As drawn in Figure 3, its predicted hexagonal (*R*-3*m*) structure is quite surprising. The N atoms are arranged in a distorted-hexagonal like N_6 chairs while the xenon atoms form twelve covalent bonds with nitrogen atoms. This was thought to be possible by a hybridization of xenon's *5p* and nitrogen's *2p* orbitals, allowing a charge transfer of 2.2 e^- from Xe to six N. Because of this electronic redistribution and by employing its lone electron pair, nitrogen atoms would remarkably be able to form four covalent bonds: two with Xe atoms and two other with N atoms. The N-N bonds would have lengths of 1.35 Å, clearly within the range of single bonds (cg-N has N-N distances of 1.346 Å at 115 GPa [10]). These very energetic bonds would provide the XeN_6 compound with an astounding decomposition energy of 2.4 kJ/g, comparable with modern-day explosives [204]. The solid was calculated dynamically stable above 50 GPa.

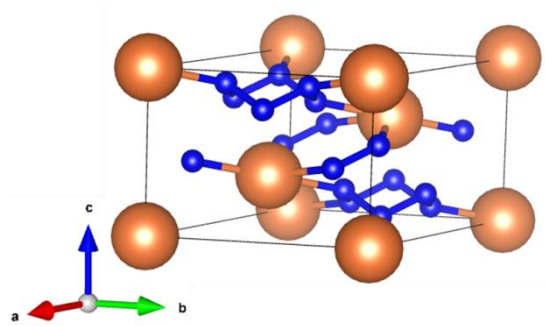

Figure 3: Structure of the XeN_6 compound, where the chaired-shape of the N_6 hexagons is visible. For the sake of clarity, the twelve bonds of Xe were not drawn.

The experimental investigation done during this thesis is detailed below.

II. *ARTICLE*

The starting point of this study was to determine the binary phase diagram of Xe-N_2, shown in Figure 4. This unveiled two new solids: a xenon-rich alloy (S_{Xe}, with less than 10 mol% of N_2) and a van der Waals compound with the $Xe(N_2)_2$ stoichiometry, stable from 4.9 GPa.

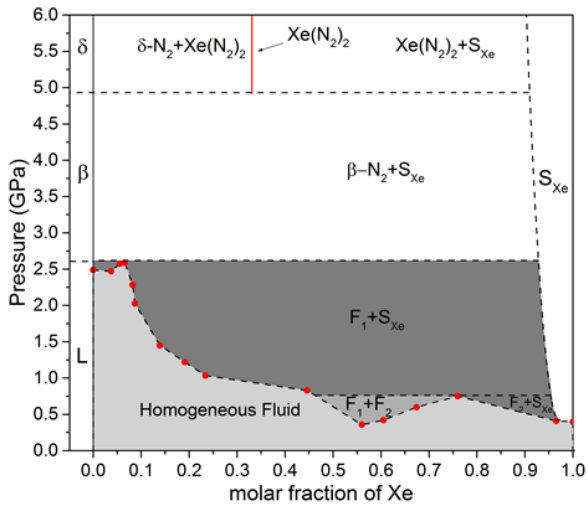

Figure 4: (a) Binary phase diagram of Xe-N_2. Red dots and squares represent experimental data of the liquidus and of the appearance of the $Xe(N_2)_2$ solid. The phases of pure nitrogen are indicated on the left-hand side of the diagram. F_1 and F_2 are nitrogen-rich and xenon-rich fluids, respectively, while S_{Xe} is a xenon-rich solid. The $Xe(N_2)_2$ van der Waals compound is formed at a pressure of 4.9 GPa.

The $Xe(N_2)_2$ solid adopts a cubic lattice (*Fd*-3*m*), corresponding to a $MgCu_2$-type Laves phase (see Figure 5 a)). With a hard-sphere radii ratio of $\alpha = 0.88$, a Xe-N_2 mixture falls into the range where Laves phase have previously been observed. In this cubic form, the nitrogen molecules were found to be completely spherically disordered, seemingly yet unaffected by the quadrupole-quadrupole interaction. However, a martensitic phase transition induced by N_2-N_2 QQ interactions was observed at 10 GPa, inducing an almost complete alignment of the N_2 molecules. Further confirming the role of the QQ interactions in the phase transition, the molecules adopted a slipped-parallel configuration which, as described in the paper, is known to minimize the QQ interaction. The high pressure structure was resolved to be tetragonal ($I4_1/amd$) (see Figure 5 b)). Interestingly, in this configuration, vertical and horizontal 2D planes of nitrogen molecules are formed. Due to the orientation of the N_2 molecules (see Figure 5 c)), this

structure was though to favor their polymerization on account of the topochemical principle.

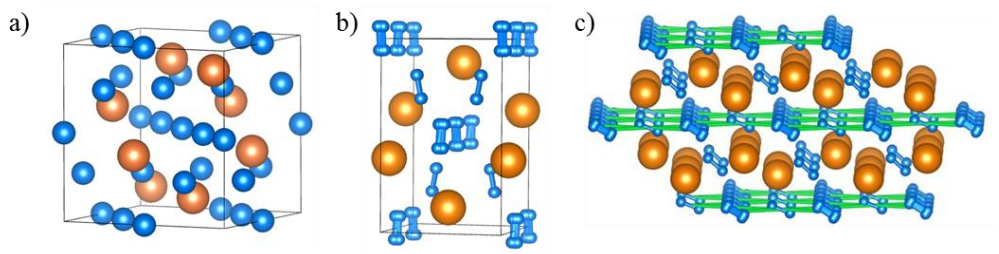

Figure 5: a) Cubic structure of $Xe(N_2)_2$, formed at 4.9 GPa. The nitrogen molecules are spherically disordered are so are drawn as blue spheres. b) Tetragonal structure of $Xe(N_2)_2$, formed at 10 GPa. The cubic to tetragonal phase transition is explained by the almost complete alignment of the N_2 molecules, on account of QQ interaction. c) Tetragonal structure of $Xe(N_2)_2$, with the horizontal N_2 planes evidenced.

Upon further compression, the chemical precompression exerted by the xenon atoms was found to be significant: at only 30 GPa, the nitrogen molecules were behaving as those in the pure compound at about 80 GPa [57]. This was deduced from the close-to identical N_2-N_2 intermolecular distances in $Xe(N_2)_2$ at 30 GPa compared to those in pure N_2 at 80 GPa as well as from the beginning of the $Xe(N_2)_2$ N_2 vibron's red shift (see Figure 6). As explained in the section relating to pure molecular nitrogen, the red shift is indicative of the weakening of the N_2 intramolecular bond due to an electron charge transfer, shifting part of the triple-bond electron cloud towards intermolecular N_2-N_2 gaps. In turn, this causes an increase in the N_2 dimer's length and a shortening of the intermolecular distances. Based on the measurable precompression effect as well as the nitrogen molecule planes favoring topochemistry, a transformation either into the predicted XeN_6 structure or into a polymeric phase not predicted by the calculations, could reasonably be expected. Surprisingly, at no point up to 154 GPa did the N_2 molecules split apart, even after laser-heating the samples up to 2000 K. This is especially unexpected as the N_2 molecule triple-bond, through its vibrons frequency, is known to be weaker than in pure N_2, which polymerizes at 110 GPa and above 2000 K. Thus, the only logical conclusion is that a Xe-N chemical interaction is stabilizing the $Xe(N_2)_2$ compound and impeding a chemical transformation. This hypothesis is supported by further arguments in the following paper.

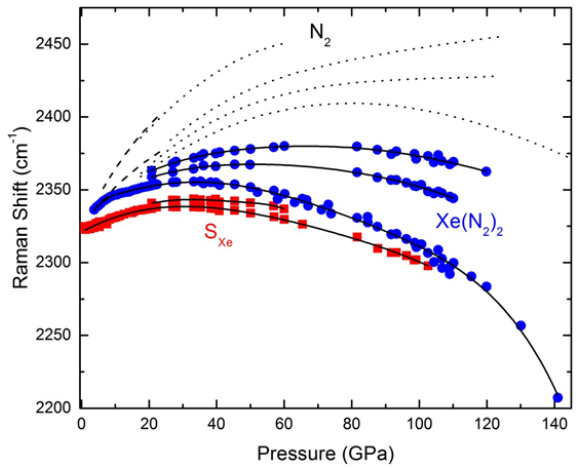

Figure 6: Raman shift of N_2 vibron modes in different solids with respect to pressure. Data were obtained from mixtures with concentrations between 11 and 30 mol % Xe. The red squares and blue circles were obtained from S_{Xe} and $Xe(N_2)_2$, respectively. The black dashed and dotted lines are the pure N_2 vibrational modes taken from references [142] **and** [5], **respectively.**

These results are published in the journal *Physical Review B* in an article titled "$Xe(N_2)_2$ compound up to 150 GPa: Reluctance to the formation of a xenon nitride". Simultaneously to the publication of this paper, R. Howie *et al*. as well as Niwa *et al*. reported similar results in *Scientific Reports* and in the *Journal of Physical Chemistry and Chemical Physics*, respectively [205,206].

This first study of Xe-N_2 mixtures was a clear demonstration of the significant impact of chemical precompression on the N_2 molecules by an atom with a much larger atomic volume. Moreover, the tetragonal structure of the $Xe(N_2)_2$ compound, found above 10 GPa, favored a polymerization of the nitrogen molecules on account of the topochemical principle. Nonetheless, a significant chemical interaction between Xe and N_2 was observed to stabilize the tetragonal structure and prevent the formation of an extended network. If xenon were to have been replaced by a similar-sized element that could have transferred a portion of its electronic density to the nitrogen atoms (an element with a lower ionisation energy), such as an alkali, an alkaline earth or transition metal, perhaps this could have been a sufficient push to break apart the nitrogen molecules and induce polymerization at low pressures (~ 60 GPa).

$Xe(N_2)_2$ compound to 150 GPa: Reluctance to the formation of a xenon nitride

D. Laniel,* G. Weck, and P. Loubeyre
CEA, DAM, DIF, F-91297 Arpajon, France

(Received 13 May 2016; revised manuscript received 27 September 2016; published 16 November 2016)

The Xe-N_2 binary phase diagram was determined at 296 K from the pressure evolution of 14 different concentrations. The properties of Xe-N_2 mixtures were characterized using visual observation, Raman spectroscopy, and powder x-ray diffraction. Above 4.9 GPa, the $Xe(N_2)_2$ van der Waals compound is stable and adopts the $MgCu_2$-type Laves phase structure (Fd-$3m$) with N_2 molecules orientationally disordered. At 10 GPa, this cubic lattice undergoes a martensitic phase transition into a tetragonal ($I4_1/amd$) unit cell. This transition is associated with a partial ordering of the N_2 molecules, possibly due to the growing N_2-N_2 quadrupole-quadrupole interaction with density. No other phase transition was detected up to 154 GPa, even after heating the sample to 2000 K. Above 30 GPa, a softening of the N_2 vibron mode with pressure reveals a weakening of the N_2 intramolecular bond that suggests an electronic redistribution between N_2-N_2 and Xe-N_2 entities. These interactions could explain the great stability of the $Xe(N_2)_2$ compound. However, no xenon nitride was observed.

DOI: 10.1103/PhysRevB.94.174109

I. INTRODUCTION

Pressure is a strong driving force for auto-organization in simple molecular systems. In particular, a new class of molecular solids, i.e., van der Waals compounds, are ubiquitously discovered in molecular mixtures under pressure, whereas they are absent in cryocrystals. Most of the time, their stability can be understood in terms of efficient packing and configuration entropy, similarly to intermetallics or hard-sphere binary compounds [1,2]. N_2 has already been observed to form van der Waals compounds with He [3], Ne [4], and H_2 [5]. However, in nitrogen-based molecular mixtures, efficient packing and configuration entropy considerations solely cannot explain the stability of van der Waals compounds such as $(N_2)_6(Ne)_7$, which has a clathrate-like arrangement of nitrogen molecules [4]. The presence of a strong quadrupole-quadrupole (QQ) interaction between N_2 molecules has to be accounted for.

The noble-gas chemistry of Xe has attracted of lot of interest. At ambient pressure and by relying on specific precursors, xenon can form Xe fluorides [6–8], Xe oxides [9–11], and even Xe nitrides [9,12,13], although the latter have poor thermal stability. Under high pressure, the reactivity of xenon should be greatly enhanced and novel ionic as well as covalent compounds are expected to be formed with many elements [14]. Indeed, XeF_2 [15], Xe hydrides [16], Xe hydrates [17], and Xe oxides [18] have already been observed. The direct interaction of Xe and nitrogen under pressure is predicted to result in a Xe nitride with the XeN_6 stoichiometry [19]. Structurally, XeN_6 is formed by N_6 hexagons and a 12-fold coordination of Xe bonded with nitrogen. Aside from this unusual chemical organization, this Xe nitride should also be a high energy density material. The observation of compounds formation in Xe-N_2 mixtures under pressure is thus promising and of great interest.

In this paper, we demonstrate the existence of a high-pressure van der Waals compound with the $Xe(N_2)_2$ stoichiometry. The binary phase diagram presented here has been determined from the study of 18 Xe-N_2 mixtures with a total of 14 different concentrations. Samples were characterized by synchrotron x-ray diffraction, Raman spectroscopy and visual observation. The remarkable stability of the $Xe(N_2)_2$ compound up to a maximum pressure and temperature of 154 GPa and 2000 K, respectively, could prevent the observation of xenon nitrides predicted under such extreme thermodynamical conditions.

II. Xe-N_2 BINARY PHASE DIAGRAM

Unlike many other rare gas–simple molecule mixtures, Xe-N_2 has not been investigated at low temperatures [20]. At high pressure, the Xe-N_2 phase diagram has been sketched at 408 K from Raman spectroscopy measurements at two concentrations, interestingly suggesting the formation of a stoichiometric compound [21]. Here, we present a detailed determination of the Xe-N_2 binary phase diagram at 296 K. The existence of a stoichiometric compound, $Xe(N_2)_2$, is demonstrated. The experimental procedure is similar to the one used in our previous high-pressure measurements of molecular mixtures [4,22,23]. Membrane diamond anvil cells (DACs), enabling a fine control of pressure to probe structural changes, were equipped with flat anvil culets (500 μm in diameter) and an inox-301 gasket. The cells were then loaded at room temperature in a high-pressure vessel, typically under a pressure of 15 MPa and after sufficient homogenization time (∼12 h). The mixture concentration was estimated from the gases' partial pressures, corrected with the first-order virial coefficients. A ruby microsphere served as a pressure gauge, using the recent quasihydrostatic scale [24]. The uncertainties in pressure and concentration are ±0.05 GPa and ±1 mol %, respectively.

The liquidus phase boundary was determined by visual observation through a microscope apparatus combining pressure measurements. Solid-fluid and fluid-fluid equilibria could easily be observed. The transition points were most finely detected when a single crystal was in equilibrium with the fluid or when a single fluid ball was in equilibrium with another

*dominique.laniel@cea.fr

 ©2016 American Physical Society

fluid. The liquidus line was then delimited by the locus of pressure versus concentration, where the small single crystal or fluid ball was seen to disappear into a homogeneous fluid. As shown in Fig. 1(a), the Xe-N_2 binary phase diagram is of eutectic type with a fluid-fluid phase separation domain. It has two triple points: one corresponding to the equilibrium $F_1 + F_2 + S_{Xe}$, at 0.7 GPa and 76 mol % Xe, and the other resulting from the equilibrium of $F_1 + S_{Xe} + \beta$-N_2 at 2.6 GPa and 7 mol % Xe.

The nature of the equilibrium in the solid phase was inferred from the combination of visual observation, Raman spectroscopy and powder x-ray diffraction. The latter was performed at the ID09 ($\lambda = 0.4117$ Å) and ID27 ($\lambda = 0.3738$ Å) beamlines of the European Synchrotron Radiation Facility (ESRF). From these measurements, the Xe-rich solid (S_{Xe}) is determined to have the fcc structure of pure solid Xe and to contain a significant amount of N_2. Homogeneous solidification of Xe-rich fluid mixtures containing up to 4 mol % N_2 is observed. Furthermore, the N_2 miscibility in the S_{Xe} alloy increases with pressure. From the volume difference between S_{Xe} (formed from the phase separation in a 6.6 mol % Xe mixture, hence at 2.6 GPa) and pure Xe, it is determined that a maximum of 9.7 mol % N_2 can be inserted into the S_{Xe} solid. A change of N_2 solubility from 4 mol % to 9.7 mol % also produces a difference in the N_2 vibron frequency, as seen in Fig. 1(e). On the other hand, no indication of Xe solubility in the N_2 solid is detected; its N_2 vibron modes, phase transitions, and structures all match those measured in pure solid N_2. Above 4.9 GPa, the formation of a stoichiometric compound is detected from both x-ray diffraction and Raman spectroscopy measurements, as seen in Fig. 1(e) with the emergence of a new Raman mode. From the phase separation equilibria at various concentrations and from the volume of the unit cell, as discussed in the next section, its stoichiometry is inferred to be $Xe(N_2)_2$. Even after heating a 30 mol % Xe mixture at 200 °C for over a week, $Xe(N_2)_2$ is still found to coexist with two other solid phases (S_{Xe} and pure N_2). A full recrystallization into the stoichiometric compound seems heavily hindered in the solid state by the diffusion barrier of Xe.

The space filling of hard spheres is used as a guidepost to explain the phase diagram and the formation of compounds in mixtures of molecular systems under pressure [3,23,25]. At 296 K and up to 7 GPa, O_2 and N_2 are highly miscible and form alloys at all concentrations [25]. That is explained by the pronounced orientational disorder of the two molecules in this pressure domain and by their very similar effective pair interactions, inferred from their equations of state [26]. It is thus interesting to compare their binary phase diagram when mixed with Xe. For both mixtures, an AB_2 stoichiometric compound exists, namely $Xe(N_2)_2$ and $Xe(O_2)_2$, and have a Laves phase structure. Their stability can be explained by the relationship between their diameter ratio and by the formation of compounds in hard-sphere mixtures [22]. However, their liquidus line is quite different and a fluid-fluid phase separation is only observed for Xe-N_2 mixtures. On the other hand, the $Xe(O_2)_2$ compound is stable above 3.1 GPa and is apparent on the liquidus line by a peritectic point. In both cases, the solubility of N_2 or O_2 in solid Xe is of a few mol % and increases with pressure, whereas the solubility of Xe in solid N_2 or solid O_2 is less than 1 mol %, if any.

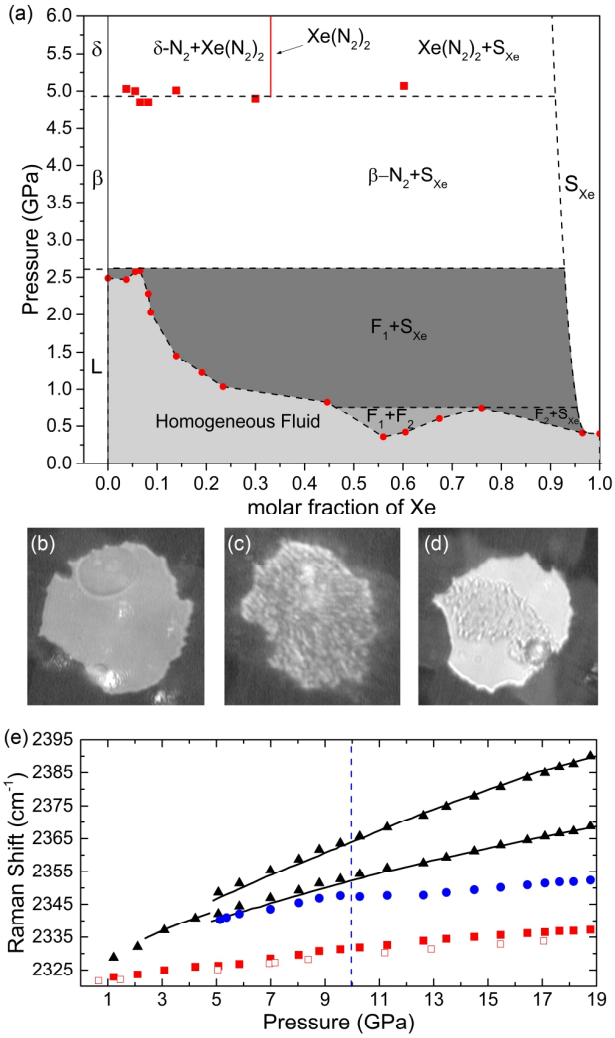

FIG. 1. (a) Binary phase diagram of Xe-N_2. Red dots and squares represent experimental data of the liquidus and of the appearance of the $Xe(N_2)_2$ solid (error bars in concentration and pressure are smaller than the dots' diameter). The phases of pure nitrogen are indicated on the left-hand side of the diagram. F_1 and F_2 are nitrogen-rich and xenon-rich fluids, respectively, while S_{Xe} is a xenon-rich solid. The $Xe(N_2)_2$ van der Waals compound is formed at the same pressure (4.9 GPa) as the $\beta \rightarrow \delta$ phase transition in pure nitrogen. (b) Microphotograph of a 67.4 mol % Xe mixture at 0.7 GPa. An F_1 bubble (top) is seen in the F_2 fluid. (c) Microphotograph of a 6.5 mol % Xe mixture at 3.1 GPa. The fine β-N_2 and S_{Xe} powder result from the brutal phase separation occurring at 2.6 GPa. (d) Microphotograph of a 13.9 mol % Xe mixture at 2.1 GPa. The S_{Xe} solid is observed in the F_1 fluid. (e) Raman frequency shift of N_2 vibron modes in different solids with respect to pressure. The black lines represent the vibrational modes of pure N_2 taken from Scheerboom *et al.* [27]. The black triangles, blue dots, and red squares were obtained from pure N_2, $Xe(N_2)_2$, and S_{Xe}, respectively. The filled symbols were all taken from Xe-N_2 mixtures of 30 mol % Xe. The empty red squares are from a 96 mol % Xe mixture. The Raman shift difference between the empty and filled red squares illustrates the increasing miscibility of N_2 in the xenon-rich solid with pressure. The dashed blue line indicates the phase transition in $Xe(N_2)_2$, which is noticeable by a weak discontinuity in its N_2 vibron frequency.

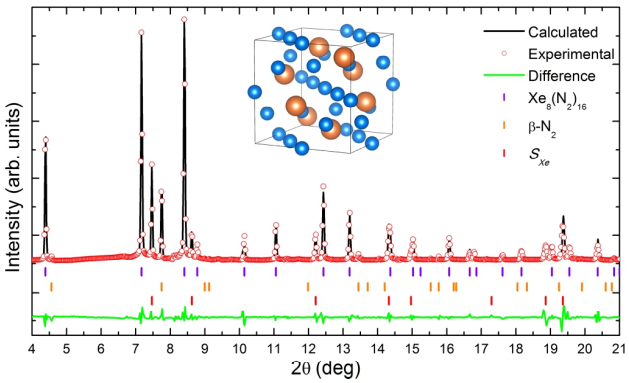

FIG. 2. Powder XRD pattern ($\lambda = 0.4117$ Å) obtained from a 6.6 mol % Xe mixture at 4.2 GPa (decompressed from 5.2 GPa) superimposed with its Le Bail refinement. Even at this concentration, three solid phases (S_{Xe}, β-N_2 and $Xe(N_2)_2$) are observed. A cubic (Fd-$3m$) unit cell with $a = 9.31$ Å fits well the diffraction lines of $Xe(N_2)_2$. The distance between the center of mass of the first-neighbor N_2-N_2 molecules is 3.29 Å, whereas the shortest Xe-N_2 distance is 3.86 Å. (Inset) Drawing of the Laves phase $Xe(N_2)_2$ where the Xe atoms (orange spheres) and the spherically disordered N_2 molecules (blue spheres) occupy the Mg (8a) and Cu (16d) sites, respectively.

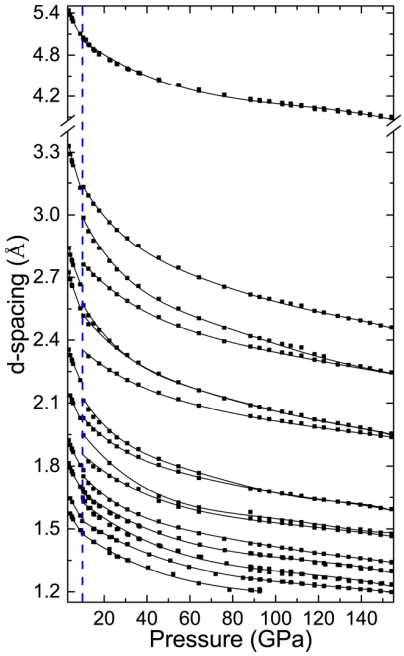

FIG. 3. Evolution of the $Xe(N_2)_2$ compound d-spacings with pressure. The dotted blue line at 10 GPa evidences the d-spacing discontinuities associated with a cubic-to-tetragonal martensitic phase transition.

III. THE $Xe(N_2)_2$ VAN DER WAALS COMPOUND

A. Cubic phase

The $Xe(N_2)_2$ van der Waals compound was characterized from both powder x-ray diffraction and Raman spectroscopy in the solid-solid phase separation observed above 4.9 GPa for various initial concentrations. Integration of the powder x-ray diffraction images was achieved with the FIT2D [28] and DIOPTAS [29] utilities, while the DICVOL [30], CHEKCELL [31], and XRDA [32] programs were used for their analysis. A Le Bail refinement was performed on a powder x-ray diffraction pattern obtained at 4.2 GPa and is shown in Fig. 2. $Xe(N_2)_2$ was found to have a cubic lattice (Fd-$3m$) with a unit cell volume of $V = 806.95$ Å^3. That volume is slightly less (0.5%) than the ideal mixing volume ($8 \times V_{Xe} + 16 \times V_{N_2}$) at the same pressure [33,34], which suggests the $Xe(N_2)_2$ stoichiometry. From considerations of maximization of the packing fraction and configurational entropy in hard-sphere mixtures, the AB_2 Laves phase is predicted stable when the hard-sphere radii ratio α is between 0.76 and 0.84, with 0.816 giving the most efficient packing [35]. Nonetheless, Laves phase compounds were experimentally observed in solids for a broader range of α values (from 0.6 to 0.95) [36]. Although first detected in metallic binary phases, Laves phases are also a common occurrence in van der Waals molecular compounds such as $Xe(O_2)_2$ [22], $CH_4(H_2)_2$ [37], and $Ar(H_2)_2$ [38], under pressure. Indeed, in the $CH_4(H_2)_2$ and $Ar(H_2)_2$ compounds, the molecular constituents are orientationally disordered and so are roughly approximated by hard spheres. At 5.5 GPa, the xenon-nitrogen van der Waals compound has a $\alpha = 0.88$, which nears the predicted range of values for which hard-sphere-like compounds are stable. Among the three possible Laves phases, only the one isomorphous to the $MgCu_2$ structure has a cubic Fd-$3m$ unit cell. Thus, we propose that $Xe_8(N_2)_{16}$ adopts the $MgCu_2$-type Laves phase structure, with the Xe and N_2 entities occupying the Mg (8a) and Cu (16d) sites, respectively. The same structure was attributed to $Xe(O_2)_2$ [22].

$Xe(N_2)_2$ adopts a structure that is understood by representing its constituents as hard spheres. The N_2 molecules are thus thought to be spherically disordered (as drawn in Fig. 2), which is consistent with the low-pressure phases of pure N_2 [39,40]. Attempts to confirm these atomic positions from a Rietveld refinement were unsuccessful, mainly due to preferential orientations of $Xe(N_2)_2$ crystallites.

B. Tetragonal phase

At 10 GPa, $Xe(N_2)_2$ undergoes a phase transition characterized by discontinuities in the d-spacings (Fig. 3) and a weak anomaly on the pressure evolution of the Raman frequency shift [Fig. 1(e)]. The high-pressure phase was found to have the tetragonal $I4_1/amd$ space group with lattice parameters $a = 5.982(1)$ Å and $c = 9.338(1)$ Å [$V = 334.15(3)$ Å^3] at 10.3 GPa. The volume of this new lattice is less (2.1%) than the ideal volume of mixing ($4 \times V_{Xe} + 8 \times V_{N_2}$) at the same pressure, which suggests the same $Xe(N_2)_2$ stoichiometry as the low-pressure phase. The tetragonal structure is obtained by a distortion of the low-pressure cubic lattice: a compression along the a and b axes, compensated by an elongation along the c axis. The martensitic phase transition explains why many of the d-spacings are continuous through the phase transition while only a few new diffraction lines appear, and why the N_2 vibron frequency is only slightly perturbed. The same transformation was previously identified in another $MgCu_2$-type Laves phase, $CaLi_2$ [41]. Furthermore, identifying the distortion process advocates for Xe atoms and N_2 molecules

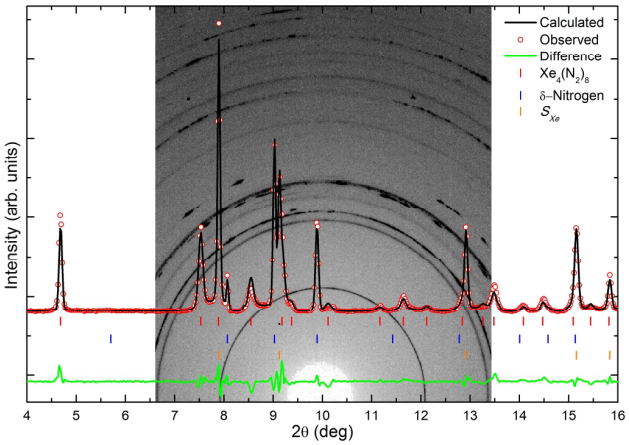

FIG. 4. Rietveld refinement of tetragonal ($I4_1/amd$) $Xe(N_2)_2$ at 10.3 GPa. The image plate corresponding to the refined diffraction pattern is in the background. The diffraction pattern was obtained from a 6.6 mol % Xe mixture with a wavelength of $\lambda = 0.4117$ Å. The $Xe(N_2)_2$ powder is of great quality, whereas the diffraction rings of solid N_2 and S_{Xe} show a nonhomogeneous crystallite distribution. The reliability factors for the refinement are $R_{wp} = 17.2\%$ and $R_{\exp} = 18.1\%$, which yields a satisfactory goodness of fit of 0.95.

center of mass to be on the 4*b* and 8*c* Wyckoff sites, respectively, based on the suggested cubic structure.

A Rietveld refinement of a powder x-ray diffraction pattern obtained at 10.3 GPa (see Fig. 4) was performed using FULLPROF [42]. Although many different positions for the Xe atoms and N_2 molecules center of mass were tested out, those suggested from the martensitic transformation yielded the best results. From there, the rigid body function was used to allow nitrogen molecules to freely explore all orientations about their center of mass. Their state of disorder was determined by adding additional molecules on the same center of mass (and correcting with the appropriate fractional occupancy) to see if it improved the quality of the fit. A partial orientational order gave a better adjustment than the one for isotropically distributed molecules. The intramolecular N_2 bond length was fixed to 1.09 Å, which is a typical value at this pressure [40]. Atomic positions determined from the Rietveld refinement are listed in Table I, and the corresponding crystal structure is drawn in Fig. 5.

While hard-sphere packing considerations mainly explain the stability of $Xe(N_2)_2$ below 10 GPa, the QQ interaction between N_2 molecules also needs to be taken into account. Mostly relevant in the density domain where van der Waals interactions dominate, it increases along with pressures. The QQ interaction tends to reduce the disorder and orient the N_2 molecular axes, as found in pure nitrogen [40,45] as well as in most N_2-based van der Waals compounds [4,40,46]. As seen in Fig. 5, N_2 molecules in $Xe(N_2)_2$ also align themselves in the tetragonal phase.

In the $Xe(N_2)_2$ cubic compound, the spherically disordered nitrogen molecules form four sets of interpenetrating layers of kagome nets. The tetragonal distortion deforms the kagome nets, resulting in N_2 hexagons having two N_2-N_2 distances that are slightly shorter (7%) than the four others [see Fig. 5(b)]. For this specific geometry, we here observe that the QQ interaction favors the slipped-parallel energy-minimizing configuration [47]. Also, the nitrogen molecules are slightly tilted in order to maximize their distance with xenon atoms. Thus, it is clear that QQ interaction plays an important role in the cubic-to-tetragonal phase transition, since (i) it occurs at pressures where van der Waals interactions still dominate, (ii) the molecular disorder is greatly reduced after the phase transition, and (iii) the orientation of the N_2 molecules in the tetragonal phase minimizes the QQ interaction. While quadrupolar orders in a hexagonal plane have been fully studied [48], no theoretical predictions of quadrupolar orders in a kagome lattice have been published, which contrasts with an extensive literature for dipolar orders [49]. The N_2 order observed here could be an experimental solution for this problem that should now motivate further theoretical studies.

C. High-pressure evolution

The pressure evolution of the tetragonal cell of $Xe(N_2)_2$ was followed by x-ray diffraction and Raman spectroscopy up to 154 GPa and 141 GPa, respectively. For these experiments, bevel diamond anvils with a 70 μm culet were used. The diamond anvil cells were loaded in a high-pressure vessel at about 150 MPa after an adequate homogenization time of the mixture. Gold and ruby microspheres placed in the sample chamber were used as pressure gauges [24,50].

Up to the highest measured pressure, no phase transition was observed in the tetragonal lattice. Twelve diffraction lines of $Xe(N_2)_2$ were tracked up to 154 GPa and used to calculate the unit cell volume, shown as a function of pressure in Fig. 6. The data points were fitted by a Vinet equation of state with the following parameters: $B_0 = 4.9(1)$ GPa, $B_0' = 6.0(1)$, and $V_0 = 562.04(2)$ Å^3. The bulk modulus and its derivative are close to the values of pure fcc and hcp xenon, which are $B_0 = 4.887$ GPa, $B_0' = 6.1805$, and $B_0 = 4.887$ GPa, $B_0' = 6.2955$, respectively [43]. The measured volume of $Xe(N_2)_2$ is compared to the ideal mixing volume and is found smaller. Overall, the volume difference grows as a function of pressure, hinting that $Xe(N_2)_2$ is increasingly energetically favored compared to the pure compounds.

TABLE I. Structural parameters of $Xe(N_2)_2$ at 10.3 GPa and 296 K. Space group $I4_1/amd$, $a = b = 5.982(1)$ Å and $c = 9.338(1)$ Å ($V = 334.15(3)$ Å^3).

Atoms	Wyckoff site	x	y	z	Site occupancy	B_{iso}
Xe	4*b*	0	0.25	0.375	1	1.55(3)
N1	32*i*	0.238(2)	0.252(2)	0.809(2)	1/4	0.51(3)
N2	32*i*	0.272(2)	0.229(2)	0.687(2)	1/4	0.51(3)

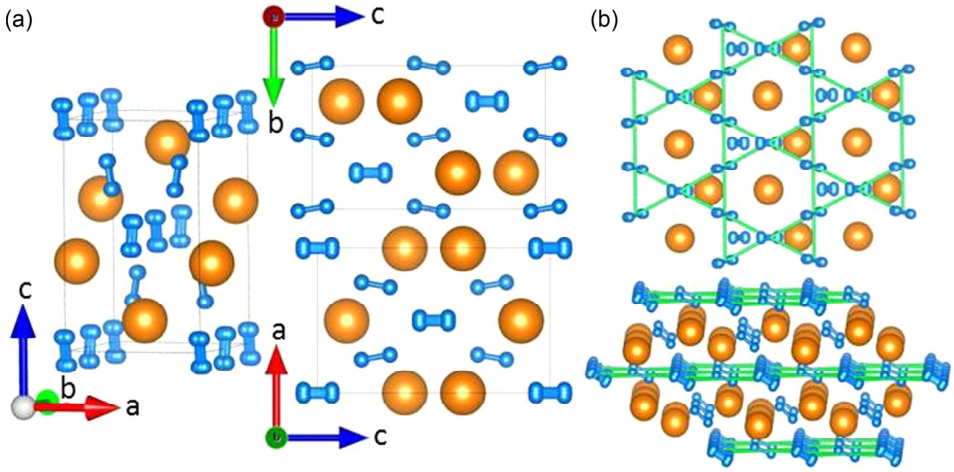

FIG. 5. Tetragonal ($I4_1/amd$) structure of $Xe(N_2)_2$ at 10.3 GPa. Xenon and nitrogen atoms are drawn as orange and blue spheres, respectively. (a) The nitrogen molecules are found only partially disordered after the phase transition. The disorder of the nitrogen molecules is modeled by an overlap of each of the nitrogen molecules with three others: one N_2 center of mass is occupied by a total of four molecules. When taking into account the occupancy of a nitrogen atom (0.25), each N_2 center of mass is effectively occupied by a single molecule, with a slightly varying orientation, representing the N_2 molecule partial disorder. Each Xe atom has four Xe nearest neighbors at distances larger (3.51 Å) than in pure Xe at the same pressure (3.38 Å) [43]. The shortest Xe-N_2 and N_2-N_2 distances (position of the center of mass was used for the N_2 molecules) are of 3.55 Å and 2.99 Å, respectively. (b) Distorted kagome nets in the tetragonal $Xe(N_2)_2$ structure. (Top) Top view of a distorted kagome plane. N_2 hexagons and N_2 triangles forming the distorted kagome lattice have two and one slightly shorter N_2-N_2 distances (7%), respectively. (Bottom) Side view of the kagome planes, which emphasizes the layered arrangement of kagome layer's nets of N_2 molecules and puckered sheets of Xe. N_2 molecules are interpreted to align due to the QQ interaction, known to minimize the energy with the slipped-parallel configuration. The orientation of the molecules was validated with a Rietveld refinement at both 10.3 and 30.0 GPa. Drawings were done using the VESTA software [44].

Raman spectroscopy measurements performed in a 30 mol % Xe mixture to 141 GPa are shown in Figs. 7 and 8. Although $Xe(N_2)_2$ is the dominant compound in the sample chamber, spectra obtained from different regions revealed vibrons corresponding to pure solid N_2 and S_{Xe}. Above 20 GPa and well into the megabar regime, three N_2 vibrational modes of $Xe(N_2)_2$ are clearly observed. The lowest frequency mode is intense, while the two others are weak. With a laser excitation wavelength of 488 nm, sample luminescence is detected from ~40 GPa and amplifies concomitantly with an increase in opacity. By ~60 GPa, the luminescence becomes more important than the Raman signal of the diamond anvils. Between 60.2 and 81.6 GPa, a near-infrared laser excitation wavelength (1064 nm) had to be used and only the strongest $Xe(N_2)_2$ vibration mode could be followed. Above 85 GPa, due to the redshift of the luminescence band with pressure, Raman spectra could again be obtained with the 488 nm laser excitation wavelength. As pressure is further increased, the Raman signal progressively diminishes in intensity and the peaks widen to the point where the strongest vibrational mode can barely be distinguished at 141 GPa. At this pressure, the sample is completely opaque (see inset of Fig. 8). This change in opacity has to be attributed to $Xe(N_2)_2$, since a 11 mol % Xe mixture, constituted only of $Xe(N_2)_2$ and pure N_2 at higher pressures, also becomes dark at similar pressures, while pure N_2 is still transparent at 140 GPa [54]. Decompression of the $Xe(N_2)_2$ compound, laser-heated to 2000 K, displayed a complete reversibility of the sample's opacity as well as of the intensity and frequency of its principal Raman modes (see Fig. 7).

Remarkably, the lowest frequency vibron of $Xe(N_2)_2$ suffers significant softening with compression. Starting from ~30 GPa, it drops below gaseous N_2 vibrational frequency at ~80 GPa and goes down to 2207 cm^{-1} at 141 GPa. The two other N_2 vibrational modes of $Xe(N_2)_2$ follow a trend much more similar to the lowest frequency vibron of pure N_2.

D. Towards a xenon nitride

The vibron mode softening of a molecule under pressure typically indicates a weakening of the intramolecular bonding between its constituents. Observed in Xe-O_2 [43] and pure N_2 [54] systems under pressure, this softening has been ascribed to an electronic density redistribution between the molecular bond and its neighboring atoms. This electronic modification also induces an increased absorption of the visible light. In $Xe(N_2)_2$, the complete darkening and the N_2 bond weakening are interpreted as similar signs of a perturbation of the N_2 intramolecular electronic density due to a growing interaction between N_2-N_2 and Xe-N_2 entities. The N_2-N_2 interaction in $Xe(N_2)_2$ is gauged from observations in pure solid nitrogen under pressure. The lowest vibron frequency in pure nitrogen begins to redshift at ~80 GPa [54], corresponding to intermolecular distances of about 1.93 Å [56]. In $Xe(N_2)_2$, a very similar N_2-N_2 intermolecular distance (1.97 Å) is observed at only 30.0 GPa, pressure at which the N_2 vibron frequency redshifts and hence the N_2 bond weakening is first detected. Thus, we interpret the start of the vibron frequency redshift in $Xe(N_2)_2$ as a pressure-induced electronic redistribution between neighboring N_2 molecules.

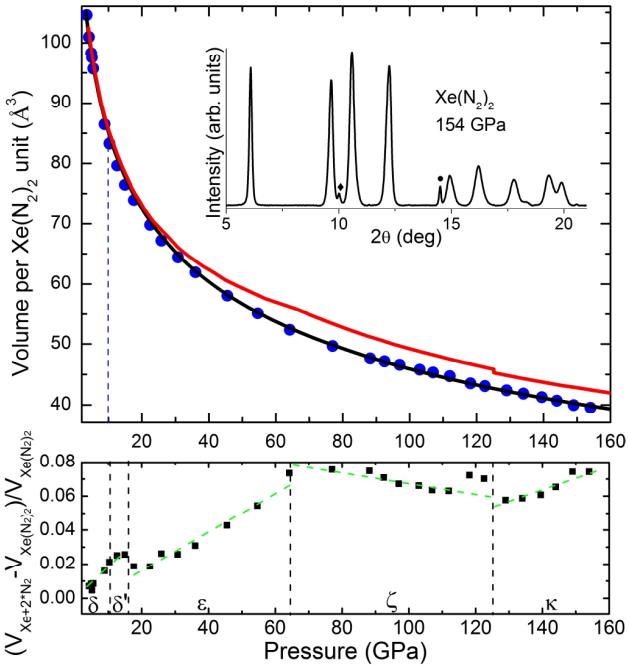

FIG. 6. (Top) Volume of $Xe(N_2)_2$ with respect to pressure. Measurements were made in a 30 mol % Xe mixture. The black line is a Vinet equation of state fit of the data points (blue dots) corresponding to the tetragonal $Xe(N_2)_2$ solid. The red line is the ideal volume of mixing, $V_{Xe} + 2V_{N_2}$, obtained from the equations of states of the pure systems [51–53]. The discontinuity around 125 GPa corresponds to the $\zeta \rightarrow \kappa$ phase transition in pure nitrogen. Literature data were updated with the latest ruby pressure scale [24]. (Inset) Diffraction pattern obtained on a 30 mol % Xe mixture at 154 GPa with a wavelength of $\lambda = 0.3738$ Å. The black lozenge and circle represent diffraction lines from the xenon-rich solid and LiF, respectively. LiF was used as a thermal insulator. (Bottom) Volume difference between the $Xe(N_2)_2$ structure and the ideal volume of mixing, $V_{Xe} + 2V_{N_2}$. The phases of pure nitrogen are indicated and its phase transitions marked by vertical dashed lines.

This interaction is not thought to be dominant at pressures lower than 30 GPa.

In pure N_2, this intermolecular interaction leads to the formation of single-bonded N polymeric phases (cg-N and LP-N) [57,58]. These polymeric phases are obtained at pressures and temperatures above 110 GPa and 2000 K. The $Xe(N_2)_2$ compound was laser-heated to 2000 K at 154 GPa using thin LiF layers on the anvils' culet to thermally insulate the sample from the diamonds. Puzzlingly, no formation of a single-bonded form of nitrogen was observed. Instead, a more complete transformation of the 30 mol % Xe solid into the $Xe(N_2)_2$ compound was detected. Hence, $Xe(N_2)_2$ is the stable phase under such thermodynamic conditions. Moreover, it implies that in this pressure range, electronic contributions other than van der Waals interactions between Xe and N_2 must be taking part in stabilizing the structure.

The Xe-N_2 interaction is gauged by looking at S_{Xe} in which the weakening of the intramolecular N_2 bond is also noticed by a redshift observed above 30 GPa (see Fig. 7). Since the fraction of N_2 molecules is low in S_{Xe} [see

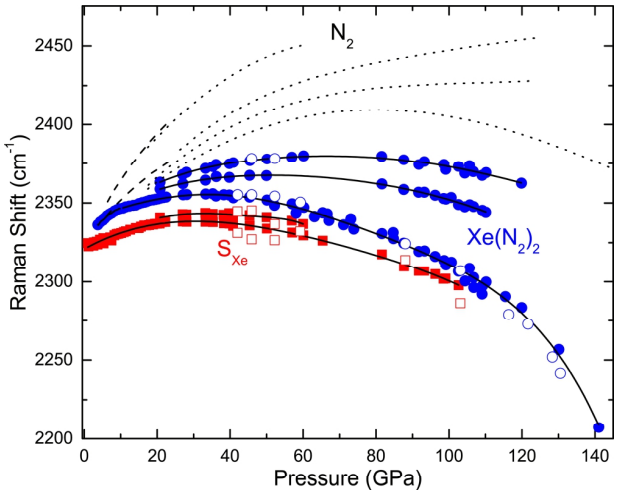

FIG. 7. Raman shift of N_2 vibron modes in different solids with respect to pressure. Data were obtained from mixtures with concentrations between 11 and 30 mol % Xe. The red squares and blue circles were obtained from S_{Xe} and $Xe(N_2)_2$, respectively. The filled symbols represent data points taken during compression, while the empty ones were acquired during sample decompression. The black dashed and dotted lines are the pure N_2 vibrational modes taken from Schneider *et al.* [55] and Goncharov *et al.* [54], respectively. Around 110 GPa, the Raman mode of the S_{Xe} solid is overlapped by the more intense vibrational mode of $Xe(N_2)_2$. Mixtures of 11 mol % Xe, which showed none of the S_{Xe} Raman modes allowed to confirm that the vibron observed above 110 GPa belongs to $Xe(N_2)_2$.

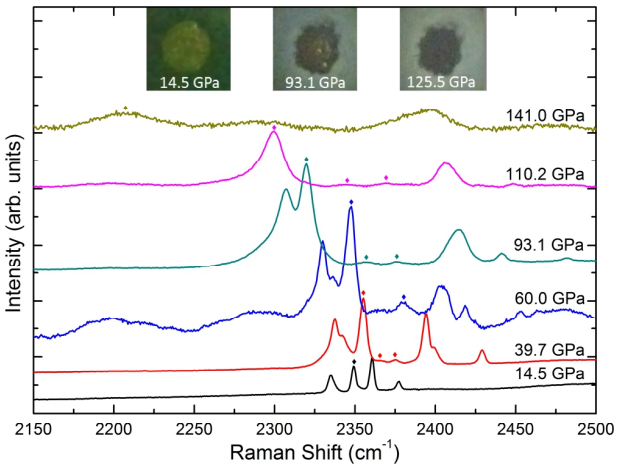

FIG. 8. Raman spectrum of a 30 mol % Xe mixture at selected pressures. An offset on the vertical axis was applied to improve clarity. Lozenges indicate the $Xe(N_2)_2$ vibrational modes. The modes at higher frequency belong to pure solid N_2, while the ones at lower frequency belong to S_{Xe}. The oscillations found in the spectra at 60.0 GPa are caused by the strong fluorescence emanating from the sample. From 100 GPa, the main Raman mode of S_{Xe} is overlapped by the $Xe(N_2)_2$ vibrational mode. At 141 GPa, the $Xe(N_2)_2$ main vibron becomes of lower intensity than the pure N_2 vibrational mode, which is a consequence of the N_2 intramolecular bond weakening. (Inset) Microphotographs of a 30 mol % Xe mixture, illuminated in both transmission and reflection. At 125.5 GPa, the sample becomes completely dark. Light only goes through the ruby ball.

Fig. 1(a)], the interaction between neighboring N_2 is highly unlikely to induce an intramolecular bond weakening. Thus, the weakening is interpreted as due to the Xe-N_2 chemical interaction. When the redshift begins in S_{Xe}, a first-neighbor distance of ~2.82 Å (at 30.0 GPa) is measured between N and Xe atoms. In $Xe(N_2)_2$, the same Xe-N distance is reached at around 65 GPa. Consequently, from this pressure, a Xe-N_2 interaction is also thought to occur in $Xe(N_2)_2$ and increases its stability. This is analogous to the redistribution of electronic density observed in the $Xe(H_2)_8$ compound, which was interpreted to make it stable up to 255 GPa [16].

Recently published numerical simulations of the convex hull of Xe-N_2 compounds predict the synthesis of the XeN_6 xenon nitride from any concentration of Xe-N_2 mixtures when compressed above 146 GPa at ambient temperature or beyond 132 GPa at 2500 K [19]. Under similar pressure-temperature conditions, we here observe the remarkable stability of the $Xe(N_2)_2$ compound. Either the thermodynamical conditions for the formation of XeN_6 were underestimated in the calculations or the $Xe(N_2)_2$ compound is completely modifying the convex hull for the formation of Xe-N compounds. Further theoretical and experimental works are needed to disclose this issue.

IV. CONCLUSION

We have performed a thorough investigation of Xe-N_2 mixtures up to 154 GPa and 2000 K. The binary phase diagram, resolved with 14 different mixture concentrations, is shown to be of eutectic type with two triple points. A Laves phase van der Waals compound with the $Xe(N_2)_2$ stoichiometry is found stable. Its stability is first explained by the efficient packing of a hard-sphere binary mixture. At 10 GPa, cubic $Xe(N_2)_2$ undergoes a martensitic phase transition into a tetragonal structure with a partial ordering of the N_2 molecules that is probably due to the growing influence of the QQ interaction under pressure. As pressure is further increased to 154 GPa, $Xe(N_2)_2$ preserves its crystalline structure, although a redistribution of electronic density occurs between N_2-N_2 and Xe-N_2 entities. This is identified by a significant softening of the N_2 vibrational frequency coupled with a complete sample darkening. The Xe-N_2 interaction could explain the remarkable stability of the $Xe(N_2)_2$ compound under thermodynamical conditions for which the N_2 triple bond should break and the XeN_6 xenon nitride is expected to form. Calculations are now needed to properly map out the electronic density redistribution and identify exactly how $Xe(N_2)_2$ is more stable than a xenon-nitrogen bonded solid in the 150 GPa pressure range.

ACKNOWLEDGMENTS

The authors gratefully acknowledge the Centre National d'Études Spatiales (CNES) for funding the Ph.D. of D.L. The authors also acknowledge the European Synchrotron Radiation Facility (ESRF) for provision of beamtime under proposals HC-1890 as well as HC-2182, and thank G. Garbarino for his technical assistance on the ID09A and ID27 beamlines of the ESRF.

[1] W. Hume-Rothery and R. E. Smallman, *The Structure of Metals and Alloys* (The Institute of Metals, London, 1969).
[2] B. J. Alder, W. E. Alley, and M. Rigby, Physica **73**, 143 (1974).
[3] W. L. Vos, L. W. Finger, R. J. Hemley, J. Z. Hu, H. K. Mao, and J. A. Schouten, Nature (London) **358**, 46 (1992).
[4] T. Plisson, G. Weck, and P. Loubeyre, Phys. Rev. Lett. **113**, 025702 (2014).
[5] D. K. Spaulding, G. Weck, P. Loubeyre, F. Datchi, P. Dumas, and M. Hanfland, Nat. Commun. **5**, 5739 (2014).
[6] J. G. Malm, I. Sheft, and C. L. Chernick, J. Am. Chem. Soc. **85**, 110 (1963).
[7] H. H. Claassen, H. Selig, and J. G. Malm, J. Am. Chem. Soc. **84**, 3593 (1962).
[8] M. A. Tius, Tetrahedron **51**, 6605 (1995).
[9] J. M. Whalen and G. J. Schrobilgen, J. Fluor. Chem. **71**, 225 (1995).
[10] M. V. Ivanova, H. P. A. Mercier, and G. J. Schrobilgen, J. Am. Chem. Soc. **137**, 13398 (2015).
[11] G. J. Schrobilgen and J. M. Whalen, Inorg. Chem. **33**, 5207 (1994).
[12] A. A. A. Emara and G. J. Schrobilgen, J. Chem. Soc., Chem. Commun., 257 (1988).
[13] G. L. Smith, H. P. A. Mercier, and G. J. Schrobilgen, Inorg. Chem. **47**, 4173 (2008).
[14] L. Zhu, H. Liu, C. J. Pickard, G. Zou, and Y. Ma, Nat. Chem. **6**, 644 (2014).
[15] M. Kim, M. Debessai, and C.-S. Yoo, Nat. Chem. **2**, 784 (2010).
[16] M. Somayazulu, P. Dera, A. F. Goncharov, S. A. Gramsch, P. Liermann, W. Yang, Z. Liu, H.-K. Mao, and R. J. Hemley, Nat. Chem. **2**, 50 (2010).
[17] C. Sanloup, S. A. Bonev, M. Hochlaf, and H. E. Maynard-Casely, Phys. Rev. Lett. **110**, 265501 (2013).
[18] A. Dewaele, N. Worth, C. J. Pickard, R. J. Needs, S. Pascarelli, O. Mathon, M. Mezouar, and T. Irifune, Nat. Chem **8**, 784 (2016).
[19] F. Peng, Y. Wang, H. Wang, Y. Zhang, and Y. Ma, Phys. Rev. B **92**, 094104 (2015).
[20] A. I. Prokhvatilov, I. Y. Minchina, and L. D. Yantsevich, *Handbook of Binary Solutions of Cryocrystals* (Begell House, New York, 1996).
[21] M. E. Kooi and J. A. Schouten, Phys. Rev. B **60**, 12635 (1999).
[22] G. Weck, A. Dewaele, and P. Loubeyre, Phys. Rev. B **82**, 014112 (2010).
[23] P. Loubeyre, M. Jean-Louis, R. LeToullec, and L. Charon-Gérard, Phys. Rev. Lett. **70**, 178 (1993).
[24] A. Dewaele, M. Torrent, P. Loubeyre, and M. Mezouar, Phys. Rev. B **78**, 104102 (2008).
[25] D. Sihachakr and P. Loubeyre, Phys. Rev. B **70**, 134105 (2004).
[26] F. H. Ree, *Simple Molecular Systems at Very High Density*, edited by A. Polian, P. Loubeyre, and N. Boccara (Plenum Press, New York, 1989).

[27] M. I. M. Scheerboom and J. A. Schouten, J. Chem. Phys. **105**, 2553 (1996).
[28] A. P. Hammersley, S. O. Svensson, M. Hanfland, A. N. Fitch, and D. Hausermann, High Press. Res. **14**, 235 (1996).
[29] C. Prescher and V. B. Prakapenka, High Press. Res. **35**, 223 (2015).
[30] A. Boultif and D. Louër, J. Appl. Crystallogr. **24**, 987 (1991).
[31] J. Laugier and B. Bochu, LMGP Suite of Programs for the Interpretation of X-ray Experiments, http://www.inpg.fr/LMGP.
[32] S. Desgreniers and K. Lagarec, J. Appl. Crystallogr. **27**, 432 (1994).
[33] A. N. Zisman, I. V. Aleksandrov, and S. M. Stishov, Pis'ma Zh. Eksp. Teor. Fiz. **40**, 253 (1984).
[34] R. L. Mills, B. Olinger, and D. T. Cromer, J. Chem. Phys. **84**, 2837 (1986).
[35] A.-P. Hynninen, L. Filion, and M. Dijkstra, J. Chem. Phys. **131**, 64902 (2009).
[36] J. H. Zhu, C. T. Liu, L. M. Pike, and P. K. Liaw, Metall. Mater. Trans. A **30**, 1449 (1999).
[37] M. Somayazulu, L. W. Finger, R. J. Hemley, and H. Mao, Science **271**, 1400 (1996).
[38] P. Loubeyre, R. Letoullec, and J.-P. Pinceaux, Phys. Rev. Lett. **72**, 1360 (1994).
[39] D. Schiferl, D. T. Cromer, R. R. Ryan, A. C. Larson, R. LeSar, and R. L. Mills, Acta Crystallogr. C **39**, 1151 (1983).
[40] G. W. Stinton, I. Loa, L. F. Lundegaard, and M. I. McMahon, J. Chem. Phys. **131**, 104511 (2009).
[41] J. Feng, N. W. Ashcroft, and R. Hoffmann, Phys. Rev. Lett. **98**, 247002 (2007).
[42] H. M. Rietveld, J. Appl. Crystallogr. **2**, 65 (1969).
[43] A. Dewaele, P. Loubeyre, P. Dumas, and M. Mezouar, Phys. Rev. B **86**, 014103 (2012).
[44] K. Momma and F. Izumi, J. Appl. Crystallogr. **44**, 1272 (2011).
[45] A. Mulder, J. P. J. Michels, and J. A. Schouten, J. Chem. Phys. **105**, 3235 (1996).
[46] S. Ninet, G. Weck, P. Loubeyre, and F. Datchi, Phys. Rev. B **83**, 134107 (2011).
[47] R. G. A. Bone and N. C. Handy, Theor. Chim. Acta **78**, 133 (1990).
[48] S. E. Roosevelt and L. W. Bruch, Phys. Rev. B **41**, 12236 (1990).
[49] J. L. Atwood, Nat. Mater. **1**, 91 (2002).
[50] K. Takemura and A. Dewaele, Phys. Rev. B **78**, 104119 (2008).
[51] H. Cynn, C. S. Yoo, B. Baer, V. Iota-Herbei, A. K. McMahan, M. Nicol, and S. Carlson, Phys. Rev. Lett. **86**, 4552 (2001).
[52] H. Olijnyk, J. Chem. Phys. **93**, 8968 (1990).
[53] E. Gregoryanz, A. F. Goncharov, C. Sanloup, M. Somayazulu, H. K. Mao, and R. J. Hemley, J. Chem. Phys. **126**, 184505 (2007).
[54] A. F. Goncharov, E. Gregoryanz, H. K. Mao, Z. Liu, and R. J. Hemley, Phys. Rev. Lett. **85**, 1262 (2000).
[55] H. Schneider, W. Häfner, A. Wokaun, and H. Olijnyk, J. Chem. Phys. **96**, 8046 (1992).
[56] M. I. Eremets, A. G. Gavriliuk, N. R. Serebryanaya, I. A. Trojan, D. A. Dzivenko, R. Boehler, H. K. Mao, and R. J. Hemley, J. Chem. Phys. **121**, 11296 (2004).
[57] M. I. Eremets, A. G. Gavriliuk, I. A. Trojan, D. A. Dzivenko, and R. Boehler, Nat. Mater. **3**, 558 (2004).
[58] D. Tomasino, M. Kim, J. Smith, and C.-S. Yoo, Phys. Rev. Lett. **113**, 205502 (2014).

III. *CHEMICAL REACTION IN THE XE-N SYSTEM*

In the presented article, the $Xe(N_2)_2$ compound was studied up to 154 GPa and 2000 K. Surprisingly, no chemical reaction was observed under these conditions, even though the N_2 molecule is greatly weakened and that numerical calculations show XeN_6 to be much more stable. The lack of chemical reaction in $Xe(N_2)_2$ was also reported elsewhere, even after heating to 2000 K at 180 GPa [205]. In both cases, the heating of the $Xe(N_2)_2$ compound only served to release some of the strain within the crystal, as deduced from the thinning of the X-ray diffraction peaks. The unsuspected stability of the $Xe(N_2)_2$ compound thus seemed to hinder a possible chemical reaction towards a xenon polynitrogen solid. However, later experiments revealed that while impeding a transformation, it did not completely prohibit it. A few low intensity peaks, later assigned to a xenon polynitrogen compound, were observed after extensive sample laser-heating (> 1 hour at 2500 K). These peaks, marked by asterisks in Figure 7, clearly evidence the new phase to be in minority with respect to $Xe(N_2)_2$. That sample, previously laser-heated at 128 GPa, also has diffraction peaks belonging to cg-N (later confirmed by Raman spectroscopy measurements). The previous laser-heating explains the high powder quality along with the narrow peaks at 148 GPa.

The necessity for prolonged laser-heating to transform the sample indicates a large activation barrier between the two phases causing a low reaction rate. As such, higher temperatures could help increase the reaction rate. Another approach would consist on avoiding having $Xe(N_2)_2$ as a reactant, hoping for a lower energetic barrier between a pure Xe as well as pure N_2 mixture and the new Xe-N phase.

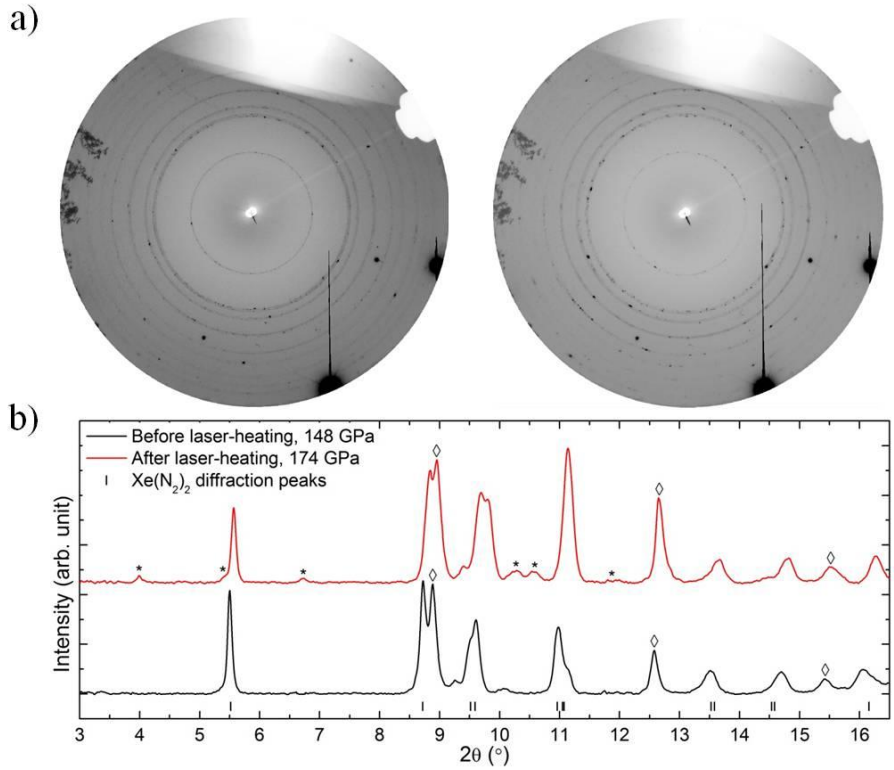

Figure 7: a) Image plates recorded from the X-ray diffraction of a 5 mol% Xe Xe-N_2 sample before (left, 148 GPa) and after (right, 174 GPa) laser-heating. The most intense diffraction spots belong to the diamond anvils. b) Integrated X-ray diffraction patterns before and after laser-heating. The bottom diffractogram shows many peaks consistent with $Xe(N_2)_2$ (shown by tick marks). The upper diffractogram has new peaks appearing after laser-heating that are indicated by asterisks. The lozenges mark cg-N diffraction peaks, arising from a previous sample laser-heating at 128 GPa, also observed from Raman spectroscopy.

It was thus first attempted to circumvent the formation of the van der Waals compound to see if a higher proportion of the sample would transform at high pressures and temperatures. To achieve this, the Xe-N_2 fluid was fast compressed, hoping that xenon's high viscosity would prevent a significant diffusion, necessary to form the $Xe(N_2)_2$ compound. The rapid compression was achieved by closing the microvalve linking the DAC's membrane to the electronic pressure controller, increasing the latter's pressure by about 50 bars and then opening the microvalve. In doing so, the pressure increment was done in a fraction of a second. Figure 8 shows the sample before and after such a compression.

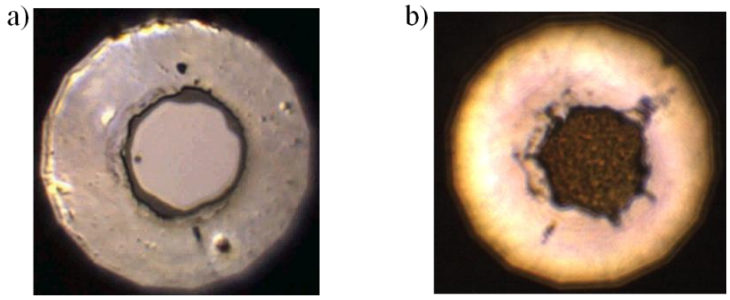

Figure 8: Xe-N_2 sample a) before and b) after its rapid compression. The microvalve was opened with a pressure difference of 50 bars between the membrane and the pressure controller. The sample pressure jumped from 0.6 GPa to 76.3 GPa.

X-ray diffraction measurements validated this approach: after the rapid sample compression, the diffraction peaks of $Xe(N_2)_2$ were not detected but instead, those of pure xenon were observed. Laser-heating this sample at 169 GPa to 2500 K gave rise to new diffraction peaks correlated with the decrease in intensity of those belonging to pure Xe, as seen in Figure 9 a). Unfortunately, the resulting diffraction pattern still contained the $Xe(N_2)_2$ compound as the majority phase. However, the previously observed diffraction peaks belonging to the new Xe-N solid were found to be slightly more intense and better defined. Illustrated in Figure 9 b), these cannot be explained by the theoretically predicted XeN_6, polymeric phases of pure nitrogen (cg-N and LP-N) or pure xenon [10,17,18,187]. The unexplained diffraction lines 2θ position are plotted with pressure in Figure 9 c), down to 70 GPa. Only the peaks observed from multiple samples are shown. The full *d*-spacing table can be found in the Annex section. Depending on the sample preparation and, in particular, if a thin chemically and thermally insulating layer of either LiF or Al_2O_3 was covering the diamond anvils, parasitic diffraction lines were observed. In particular, the Al_2O_3 layer which is amorphous at first, was found to recrystallize in two of its high pressure polymorphs after laser-heating it above 2000 K at pressure exceeding 140 GPa, thus generating many new unwanted diffraction peaks [207]. This was unfortunate as it seemingly provided for the highest fraction of reacted sample along with good powder quality. The various experimental runs are summarized in Table 1. As seen, the lowest temperature to achieve at chemical reaction was 2000 K, using an insulating layer on the diamond anvils. It was also attempted to heat the sample above 3000 K but it very often resulted in the shattering of the diamond anvils. The effect of the sample concentration is discussed further below.

Based on the information gathered from the X-ray diffraction characterization, the new solid has a large lattice as deduced by the low angle diffraction lines, namely at 7.73 Å and 5.36 Å in *d*-spacing. Moreover, a difference in texture between the unassigned diffraction peaks was observed from several, but not all, reacted samples

and would suggests that two new phases, and not just one, have been synthesized along with $Xe(N_2)_2$. This is reminiscent of the high pressure and high temperature xenon-poor Xe_3O_2 and xenon-rich Xe_2O_5 compound formed from Xe-O_2 mixtures [200]. Combined with the presence of intense $Xe(N_2)_2$ diffractions lines, surely overlapping weaker peaks of the new phase, an indexation of the newly produced compound(s) is still ongoing. However, as detailed below, complementary Raman spectroscopy measurements provided further critical information on both the chemical composition of the reacted compound and on its stoichiometry.

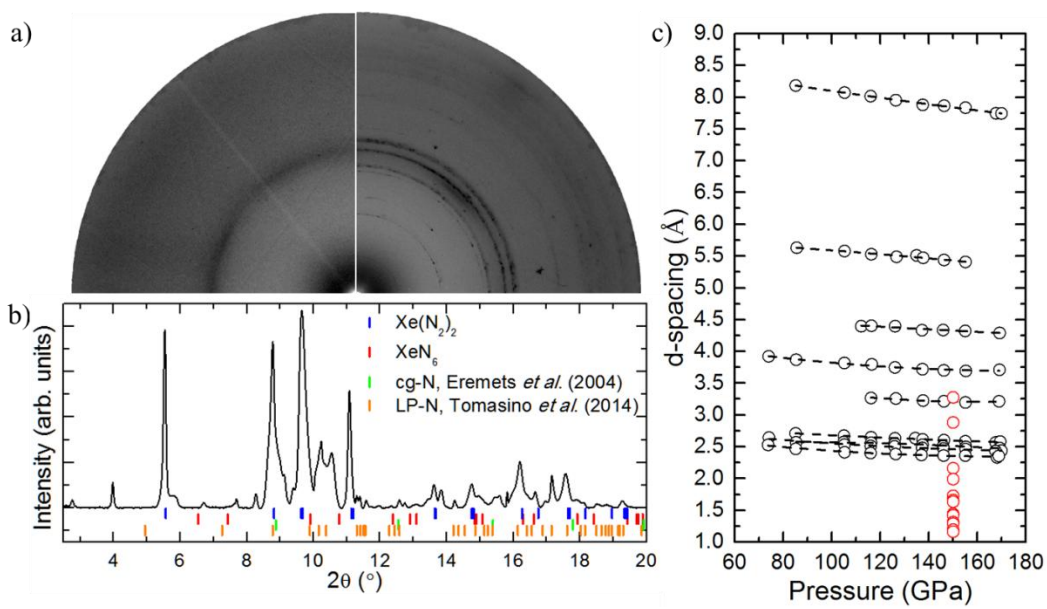

Figure 9: a) Quarter of diffraction image plates obtained on a fast-compressed 19 mol% Xe Xe-N_2 sample without an insulating layer before (left) and after (right) laser-heating to 2800 K at 169 GPa. After laser-heating, very large and diffuse diffraction spots belonging to xenon can still be observed. b) Integrated image plate with tick lines corresponding to $Xe(N_2)_2$, XeN_6, cg-N and LP-N [10,17,18]**, all at 155 GPa. While many diffraction lines are explained by $Xe(N_2)_2$, many new peaks are left unexplained by known phases. c) Pressure evolution of the newly-obtained diffraction lines, drawn as empty black circles. Only those observed from more than one sample were plotted. The empty red circles mark the theoretically calculated diffraction lines for the XeN_6 structure.**

Table 1: Summary of the ten experimental runs performed on Xe-N_2 mixtures at high pressures and temperatures

Run	Concentration (mol % Xe)	Insulating layer	Laser-heating pressure (GPa)	Laser-heating temperature (K)	Chemical reaction
1	33	-	154	2500	No
2	25	LiF	147	2000	Yes
3	25	LiF	143	2500	Yes
4	25	Al_2O_3	146	2500	**Yes**
5	11	Al_2O_3	143	2500	**Yes**
6	20	Al_2O_3	170	2300	**Yes**
7	5	-	148	2500	Yes
8	11	-	163	2500	Yes
9	15	-	205	-	¤
10	19	-	169	2800	**Yes**

* A bolded **Yes** in the Chemical reaction column indicates that a significant amount of the new Xe-N was produced. ¤ The diamond anvils broke during the sample laser-heating.

From two of the reacted samples, Raman spectroscopy measurements were obtained during their decompression between 100 GPa and 23 GPa. Four new Raman modes were detected, including three in the frequency domain of single-bonded nitrogen atoms (700-1300 cm^{-1}) [10,17,123,160,208]. These Raman modes were not observed from samples shown by X-ray diffraction to only be composed of $Xe(N_2)_2$. Their evolution with pressure is shown in Figure 10, along with those of the known polymeric phases of nitrogen: cg-N and LP-N [10,17]. The measured modes are unmistakably different from the established phases, and can thus be regarded as the signature of a novel Xe-N solid with single-bonded nitrogen atoms. Finally, a signature of the poly Xe-N solid, either from Raman or X-ray diffraction measurements, were obtained from mixtures of 5, 11, 15, 19, 20 and 25 mol% Xe. While not necessarily conclusive due to temperature gradient during laser-heating, left-over pure Xe was detected from mixtures of 19 mol% Xe and above and cg-N was produced in samples of 5 and 11 mol% Xe. Presuming this information to be reliable and under the assumption that a single Xe-N compound is produced, its stoichiometry would be between 11 and 19 mol% Xe, thus slightly richer in nitrogen than the theoretically predicted XeN_6 compound (with a Xe/N_2 ratio of 25:75).

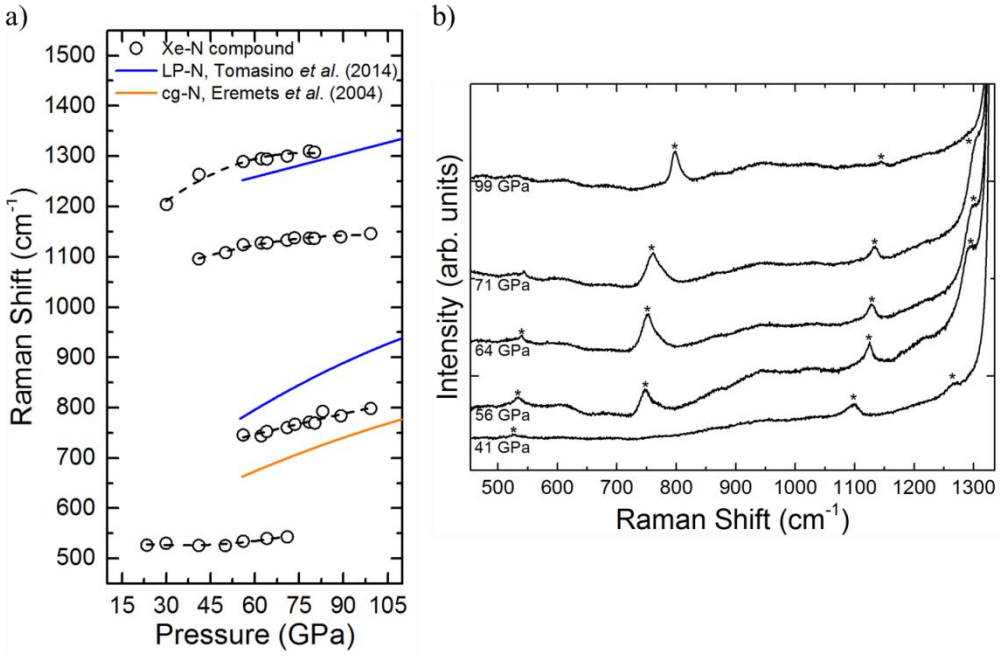

Figure 10: a) Evolution with pressure of the Raman modes of the reacted Xe-N compound along with those of the cg-N and LP-N phases [10,17]**. b) Raman spectra of the reacted Xe-N solid at various pressures, offsetted for clarity. The asterisks mark the detected Raman peaks.**

The comparison between the high pressure studies of Xe-O_2 and Xe-N_2 mixtures is interesting. In the Xe-O_2 system, the XeO, XeO_2 and XeO_3 compounds were calculated as stable at high pressures [198]. While experiments indeed observed a transformation at high pressure, the obtained compounds do not match the structure or stoichiometry of those predicted. Further calculations were able to find the experimentally observed compounds (Xe_2O_5 and Xe_3O_2) only after considering more stoichiometries, searching for larger unit cells and determining the proper functional for xenon oxides [200]. While theoretical calculations on the Xe-N_2 system were performed for many stoichiometries (16), it is possible that the right stoichiometry might have been missed or that, due to limitations on the unit cell size or improper functional choice, the right compound(s) did not come out as stable.

Thus, while further theoretical and experimental studies might be needed to fully resolve the structural characterization of this solid, the results presented here are certainly promising and should be insightful for future work.

SERIES OF CHEMICAL TRANSFORMATIONS IN THE N_2-H_2 SYSTEM

I. *INTRODUCTION*

Composed of a single proton and electron, hydrogen is the lightest of all elements and is by far the most abundant element in the Universe. Gaseous under ambient conditions, its pure stable form is dihydrogen (H_2) constituted of a single covalent bond binding the two atoms together.

In its pure form, H_2 has attracted a significant interest in the field of high pressure physics. In 1935, Wigner and Huntington predicted that at very high pressures, molecular hydrogen would atomize and become metallic [209]. While the metallization pressure was first set to 25 GPa – an incredibly high pressure to achieve at the time of this first prediction – it is now expected around 450 GPa [210]. Only after the forecast of room temperature superconductivity, along with its metastability back to ambient conditions [211], was the intense research for the synthesis of metallic hydrogen initiated. While reports of its metallization have been announced several times, none stood the rigorous scrutiny of the research community [212–215]. Supposing the metastability calculations to hold true and not taking into account the astounding pressure needed to produce it, metallic hydrogen is expected to be an incredible propellant (I_{sp} = 1700 s in vacuum) on account of its high density, moderate molecular recombination energy and low mass of the reaction products [216].

Of special interest here is the particularly rich nitrogen-hydrogen chemistry. At ambient conditions, a wide variety of stable and metastable compounds are known to exist, namely ammonia (NH_3), hydrazine (N_2H_4) – both part of the azane family (N_nH_{2+n}) –, diezene (N_2H_2), triazene (N_3H_3), tetrazene (N_4H_4), hydrogen azide (HN_3) as well as ammonium azide ((NH_4)(N_3)) [217]. With the exception of ammonia, all of these compounds are metastable. Furthermore, hydrazine is the ambient conditions highest energy density compound due to the single bond between its nitrogen atoms and its relatively high density (1.024 g/cm^3 at 2 °C) [218]. While its energy density is not sufficient for it to be considered as a good explosive, the weight of its reaction products allows for a moderate I_{sp} (220 s in vacuum). For its simplicity of use and preparation, it is found on more than 50 satellites' thrusters and is expected to continue to be utilized [219]. The synthesis of longer metastable azanes, thus with a greater concentration of single-bonded N-N atoms, would certainly be of interest as a propellant. By traditional chemical methods, triazane (N_3H_5) is the longest azane to be produced, although it was found highly unstable [217,220].

Pressure opens up another route to produce novel hydronitrogen compounds, including longer azanes. The Haber-Bosch process is an example of the outstanding potential of high pressure to observe nitrogen-hydrogen chemistry. In 1909, the two German scientists first demonstrated in a small-scale setup how the very strong nitrogen molecule could be broken up and chemically react with molecular hydrogen at pressures and temperatures above 25 MPa and 400°C to produce ammonia, through the help of an osmium catalyst. Later, the process was refined and optimized for industrial production, instead opting for the less expensive iron catalyst doped with K_2O, Al_3O_3, SiO_2 and CaO along with lower pressure-temperature requirements [39]. This discovery was of tremendous importance, first of all since the synthesized ammonia, used massively as fertilizer, revolutionized agriculture as well as helped end famines in Europe and secondly, as a demonstration of the role of the pressure parameter to permit the exploration of new chemical interactions.

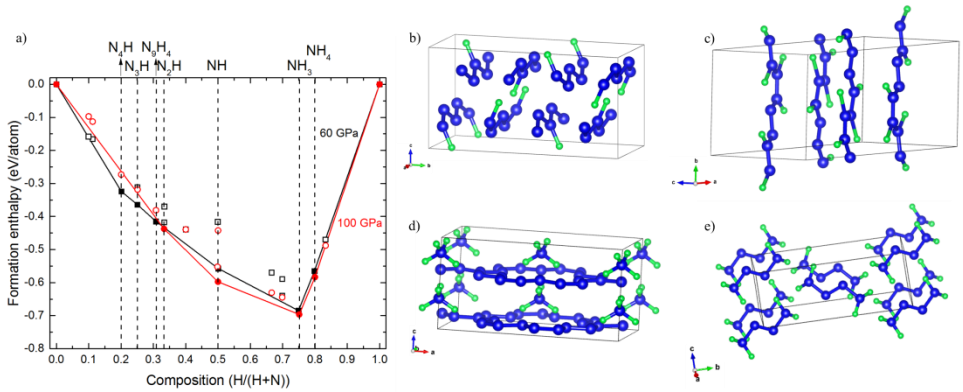

Figure 1: a) Nitrogen-hydrogen enthalpy binary phase diagram, reproducd from Ref. [21]**. N-H compounds predicted on the enthalpy convex hull, of stoichiometry b) N_4H, c) N_3H, d) N_9H_4 and e) NH (tetrazene). The blue and green spheres represent nitrogen and hydrogen atoms, respectively.**

In a little more than a century, the understanding of the hydronitrogen chemistry has drastically improved. Several of the ambient conditions metastable N-H compounds along with pure N_2-H_2 mixtures have been experimentally characterized at high densities [24–26,126,160,208,221–230] while theoretical calculations predicting new pressure-stabilized stoichiometries and phases were performed [19–23]. Of particular interest are the two calculated enthalpy convex hulls, each from a different group, as they nicely summarize what theory expects at any N-H concentration and pressure. While different sets of calculations do not completely agree, they do illustrate similar tendencies. They are shown in Figure 1 and Figure 2. First, they show that ammonia is the sole stable hydronitrogen compound at least up to 15 GPa. While this changes at 30 GPa, NH_3 stays on the enthalpy convex hull up to 470 GPa, pressure at which it decomposes into more stable compounds [21]. However, it is expected undergo an autoionisation between 36-90 GPa with half of the NH_3 molecules losing a hydrogen nucleus (proton) to the other half, thus forming the ionic compound $(NH_2^-)(NH_4^+)$ [21,231]. Second, they both display between 30 and 60 GPa many new intriguing compounds appearing on the convex hull. Indeed, in the first published set of calculations, five solids with stoichiometries of N_4H, N_3H, N_9H_4, NH and NH_4 anticipated stable, as shown in in Figure 1 [21]. These compounds are all constituted of polynitrogen sublattices of different lengths, with the exception of the NH_4 stoichiometry solid, made up of NH_3 and H_2 molecules. Also, the NH stoichiometry compound corresponds to the known ambient conditions metastable N_4H_4 tetrazene, crystallized in a monoclinic $P2_1/c$ lattice. According to the second – and most recent – set of calculations (see Figure 2), two pentazolate (N_5^-) anion-based solids are stable at 60 GPa, one stabilized through an ammonia cation (NH_4^+) and the other solely by an proton (H^+) [23]. These structures are drawn in Figure 2. The authors report these compounds to have a sufficiently low enthalpy such that the previously predicted

compounds no longer appear on the N-H enthalpy convex hull. This assertion is supported by recent theoretical predictions of stable pentazolate arrangements in most alkali-nitrogen mixtures [28,29,47,232] and the experimental synthesis of the CsN_5 [49] and LiN_5 compounds [233]. It is worth noting that hydrazine, although metastable at ambient conditions, never appears on the enthalpy convex hull until slightly over 200 GPa [21].

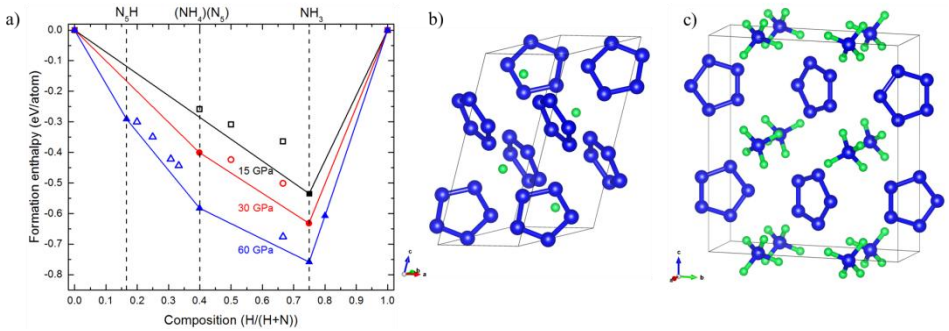

Figure 2: Nitrogen-hydrogen enthalpy binary phase diagram, reproduced from Ref. [23]**. The solids' stoichiometry is a) N_5H and b) N_3H_2. The blue and green spheres represent nitrogen and hydrogen atoms, respectively.**

These predictions may be compared with experiments recently performed on several hydronitrogen compounds. Regarding ammonia, its stability against decomposition up to 183 GPa was demonstrated [225]. Furthermore, the molecules were established to autoionize between 120-150 GPa [225,230], pressures exceeding the value theoretically calculated (between 30-90 GPa). This small discrepancy is attributed to the temperature and entropy contributions which are not accounted for in the enthalpy-based numerical predictions (as they are performed at T = 0 K). Upon decompression, ionized ammonia reverts back to its molecular form around 100 GPa [225,230].

Hydrazine was also the subject of experimental investigations up to 46.5 GPa. After its crystallization in a monoclinic ($P2_1$) solid at 1.2 GPa, it undergoes two structural transformations: at 2.4 GPa into another monoclinic lattice followed by an isostructural phase transition at 18.4 GPa, both ascribed to minor modifications of the intermolecular H-H bonds [160]. Other experiments performed on hydrazine evidenced its metastability at pressures of 3.5 and 5.0 GPa, as a prolonged white X-ray beam irradiation resulted in its dissociation into NH_3 and N_2 [208]. Finally, the last of the ambient conditions' metastable hydronitrogen compound to have been studied under pressure is ammonium azide. While theoretical papers predicted it to transition into an intriguing $(NH)_4$ stoichiometry phase constituted of one-dimensional single-bonded nitrogen chains capped with hydrogen atoms at 36 GPa [20], the experimental results

have shown its behavior to be somewhat less impressive. Indeed, Raman spectroscopy characterizations of the compound up to 71 GPa revealed no polymerization but only subtle structural changes [234–236].

In an attempt to produce some of the exotic predicted hydronitrogen compounds, N_2-H_2 mixtures were also studied at high densities. A preliminary investigation of a 2:1 N_2/H_2 mixture was characterized by Raman spectroscopy up to 83 GPa. At the highest pressure, Raman modes in the frequency domain attributed to single-bonded N-N atoms were detected and followed down to about 35 GPa [227]. Three experimental investigations followed up this first exploratory study. The binary phase diagram of the N_2-H_2 mixtures was determined and is shown in Figure 3 [24]. This study revealed two van der Waals compounds with the $(N_2)_6(H_2)_7$ and $N_2(H_2)_2$ stoichiometry that spontaneously formed at the fluid's solidification near 7 GPa. It was also observed that the two molecular entities, completely miscible in the fluid phase, have a low solubility in the solid phase, with < 2 mol% N_2 in pure H_2 and < 5 mol% H_2 in pure N_2 but. From single crystal X-ray diffraction, the $(N_2)_6(H_2)_7$ compound was structurally resolved and shown to have a rhombohedral unit cell (*R*-3*m*). The 36 N_2 and 42 H_2 molecules are organized in such a way as to produce a cage-like sublattice of nitrogen molecules confining a cluster of rotationally disordered hydrogen molecules. The structure is shown in Figure 3. Further compression of this van der Waals compound near 50 GPa induced a chemical reaction between the two molecular entities. Characterized by optical methods (Raman and infrared absorption), the reaction product was interpreted as ionized ammonia $(NH_4^+)(NH_2^-)$ embedded in amorphous molecular nitrogen. Decompression of the reacted sample below 10 GPa was reported to drive a second chemical reaction, this time with hydrazine as the reaction product. Hydrazine could be retrieved at ambient conditions. Still according to this experimental investigation, the second van der Waals compound, $N_2(H_2)_2$, was suggested to have a cubic structure with a space group of either *Pm*-3*m* or *Pm*-3*n*. Due to its complexity, the compound's structure was not fully resolved. Moreover, it was not studied at pressures higher than 20 GPa. Finally, the hydrogen-doped N_2 solid was compressed close to 150 GPa but no chemical reaction was detected [24].

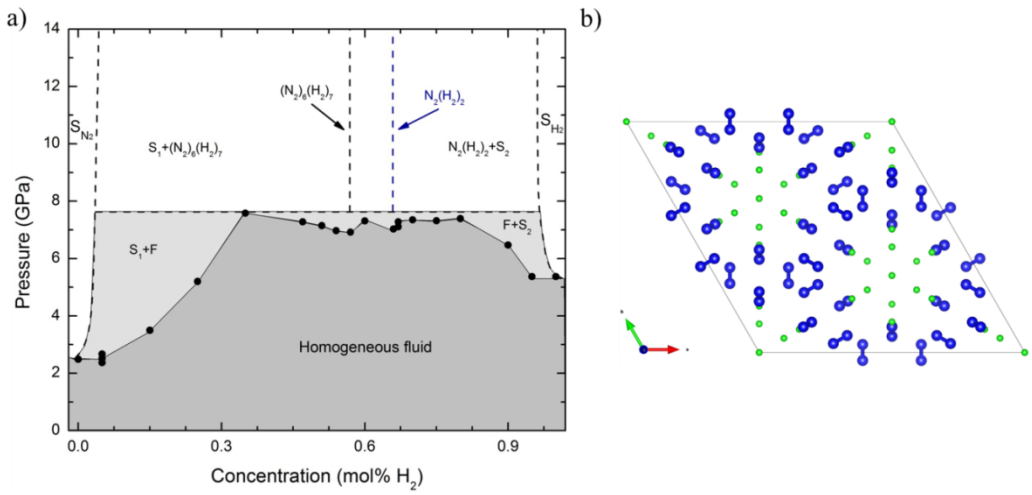

Figure 3: a) Binary phase diagram of N_2-H_2, reproduced from ref. 19. b) Crystal structure of the $(N_2)_6(H_2)_7$ van der Waals compound. The blue and green spheres represent nitrogen and hydrogen atoms, respectively.

These results somewhat contrast with the two other experimental studies that followed. In those, N_2-H_2 powders with concentrations of 5, 10, 20, 50 and 80 mol% N_2 were compressed to 60 GPa and characterized by both X-ray diffraction and Raman spectroscopy [25,26]. While the composition of these powders was reported to differ from the pure compounds, they were not identified. However, based on the known binary phase diagram of N_2-H_2, they are expected to be composed of the H_2-rich, N_2-rich, $N_2(H_2)_2$ or $(N_2)_6(H_2)_7$ solids or a mixture of these, depending of their concentration. In any case, the powders were all found to chemically react near 50 GPa and to all have similar spectroscopic signatures to those obtained from the $(N_2)_6(H_2)_7$ solid. Supported by numerical calculations, the reaction products of the reacted powders were ascribed to azane chains of various lengths (polymers from N_2H_4 to N_6H_8) or tetrazene [25,26]. On decompression, these reaction products were also found to produce hydrazine.

Hereafter we present a study of the $N_2(H_2)_2$ compound under pressure. This investigation mainly aimed at synthesizing novel, possibly energetically-rich hydronitrogen compounds. As the $(N_2)_6(H_2)_7$ and N_2-H_2 powders reportedly did not yield the same reaction products, it was deduced that if solids with N-N single bonds were produced in the powders, they should form from the $N_2(H_2)_2$ van der Waals compound. Indeed, pure N_2 doped with H_2 molecules and $(N_2)_6(H_2)_7$ were shown not to react at least up to 150 GPa and to produce ionized ammonia at 50 GPa, respectively. Secondary objectives were to 1) determine the complex structure of the $N_2(H_2)_2$ compound, 2) validate that the van der Waals compounds composed the N_2-H_2 powders and, 3) supposing a chemical reaction to also occur in the $N_2(H_2)_2$ compound, to provide a better understanding of its reaction products. The achieve the latter point, a

homogeneous $N_2(H_2)_2$ sample (such as a single crystal) was deemed preferable as it provides intrinsic advantages to the determination of the chemical entities formed after a chemical reaction. With a known before reaction stoichiometry, left-over molecular N_2 or H_2 would allow to distinguish if NH_3 or N–H oligomers and polymers were primarily synthesized after the chemical reaction. Moreover, a single crystal would make it easier to resolve the compound's structure. Finally, the objectives 2) and 3) would allow to solve the points of contention between previous experimental studies of N_2-H_2 mixtures [24–26].

II. *ARTICLE*

The results of this study were published in the Journal of Physical Chemistry and Chemical Physics in an article titled "*Pressure-induced chemical reactions in the $N_2(H_2)_2$ compound: from the N_2 and H_2 species to ammonia and back down into hydrazine*". In this article, it is first shown that by single crystal X-ray diffraction, the complex and previously-unsolved crystal structure of the $N_2(H_2)_2$ van der Waals compound was resolved. The difficulties to determine the structure were mainly a) its very large unit cell (2007.10 $Å^3$ at 9.1 GPa), thus containing many atoms, b) a sharp decrease of the X-ray diffraction spots observed intensities as a function of the diffraction angle and c) the very low intensity diffraction spots produced by the H_2 molecules. The structure, shown in Figure 4, contains 41 N_2 molecules and 82 H_2 molecules. Similarly to pure nitrogen and van der Waals compounds containing N_2 (such as $Xe(N_2)_2$ and $(N_2)_6(H_2)_7$), the nitrogen molecules were found to be significantly rotationally disordered. This is interpreted to have resulted in the observed drop of diffraction spots intensity with the diffraction angle. Attempting to employ previously-reported methods to model the rotational disorder, such as adding differently oriented nitrogen molecules on the same N_2 center of mass (while correction for the occupancy) [125], did not succeed as it resulted in an overfitting of the experimental data. Thus, the disorder was modeled by considering the N_2 molecules as Si atoms (the also having 14 electrons) and introducing anharmonic anisotropic displacement parameters (ADP). The ADP is typically used to represent the thermal motion of an atom. In this fashion, the number of fitting parameters was considerably reduced and the center of mass position as well as orientation of the nitrogen molecules (Si atoms) could be resolved. Unfortunately, the position of the hydrogen molecules could not be determined because of the limited X-ray diffraction data.

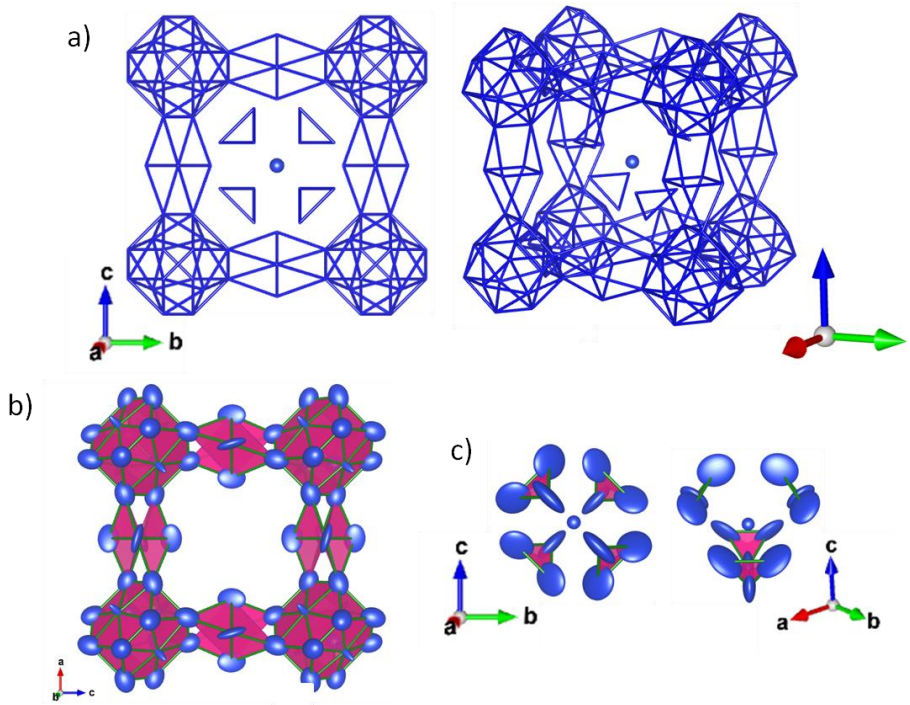

Figure 4: N_2 arrangement of the $N_2(H_2)_2$ compound. (a) A single unit cell in the wireframe representation. The outer scaffold (b) confines the inner portion (c), both of which are drawn with the Si atoms simulating the N_2 molecules. The rotational disorder of the nitrogen molecules (modelled by Si atoms with anharmonic anisotropic displacement parameters) is shown in b) and c).

Given that the structure for the $N_2(H_2)_2$ compound was found, it is tempting to see if it is a good contender for topochemistry. The outer scaffold of the structure, as seen in Figure 4 b), seems to suggest that long polymeric chains could be obtained upon further compression. However, a definite analysis requires the structure evolution with pressure and, more specifically, the knowledge of the N_2 molecules' orientation once the rotational disorder has subsided at higher pressures. Indeed, as found in pure nitrogen, increase the pressure typically forces the molecules to align which can lead to important structural changes (hence the multiple phase transitions in pure N_2). Unfortunately, the $N_2(H_2)_2$ compound was not characterized by X-ray diffraction at higher pressures. The single crystal's quality would have rapidly deteriorated and, especially with the complex arrangement of the compound, would no longer have allowed to resolve the structure.

Instead, the $N_2(H_2)_2$ compound was characterized by Raman spectroscopy up to 55 GPa, pressure at which a chemical reaction spontaneously initiates. This comes somewhat as a surprise since, based on the evolution of the Raman modes with pressure, there is no sign of a chemical interaction between the N_2 and H_2 entities nor of a weakening of the N_2 molecule. Coming back to the high pressure investigations of pure

N_2 and of the $Xe(N_2)_2$ compound, a chemical interaction between N_2-N_2 or Xe-N_2 entities is detected through the sudden redshift of the N_2 vibrons. Moreover, this redshift is also assimilated to a weakening of the N_2 molecule, and still intense laser-heated is required to break apart the N_2 triple bond and overcome the kinetic barrier. However, as shown in Figure 5, the frequency of the N_2 modes in $N_2(H_2)_2$ seems to increase almost linearly with pressure and no heating is necessary for the transformation. A similar phenomenon was observed in the $(N_2)_6(H_2)_7$ compound [24]. This chemical reaction between N_2 and H_2 can not be attributed to a chemical precompression as 1) its unit cell volume is slightly greater (2007.10 Å^3) than the ideal mixing volume at the same pressure (2003.26 Å^3) and 2) there is no sign of charge transfer. While theoretical investigations are needed to provide a mechanism for the sudden chemical reaction, it could be related to hydrogen's high mobility (through quantum tunneling), which allows it to more easily overcome kinetic barriers.

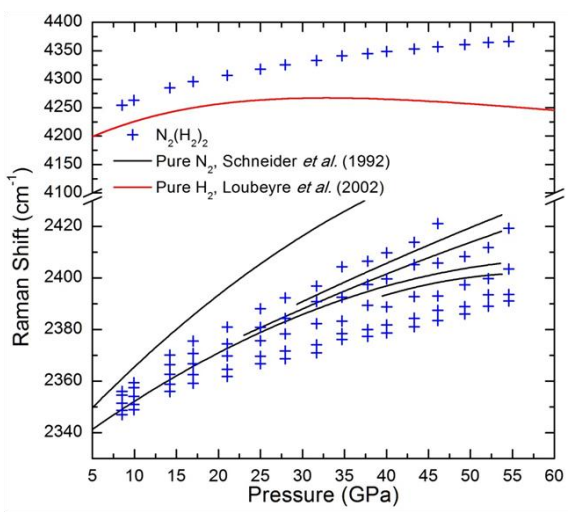

Figure 5: Rama shift of a $N_2(H_2)_2$ single crystal Raman modes with pressure. A single H_2 vibron, blue shifted compared to the pure compound, is observed while five N_2 stretching modes are measured. The pure N_2 and pure H_2 vibrons were obtained from the literature [142,237]**.**

In any case, once the chemical reaction had taken place, left-over molecular nitrogen unmistakably proved the synthesis of a hydrogen-rich reaction product. As the sole vibrational modes measured by Raman spectroscopy could be attributed to the azane family, the main reaction product was asserted to be NH_3. However, longer azanes were determined to also be present as secondary reaction products since the single-bonded N-N Raman mode was detected. This result challenges the previous

experimental studies on N_2-H_2 powders as it is now established that both N_2-H_2 van der Waals compounds produce some form of ammonia. In addition, we have also performed powder X-ray diffraction experiments and showed powders to be composed of both van der Waals compounds. These aspects of our investigation of the N_2-H_2 system are detailed in the following paper.

During the decompression of the ammonia-rich azane mixture, a progressive chemical transformation was observed. Below 10 GPa, the majority of the sample seems to have transformed into hydrazine. As shown in Figure 6, a Raman mapping of the sample at 1.2 GPa reveals no trace of any other form of azane but hydrazine. This is a very surprising result since ammonia is well-known to be energetically-favored with respect to hydrazine, which is metastable at ambient conditions. This is also illustrated in the convex hulls shown in Figure 1 and Figure 2. As concluded in the paper, there is no obvious mechanism for this transformation and a theoretical investigation would be insightful. It is worth noting that the previous studies on the N_2-H_2 mixtures also retrieved hydrazine at ambient conditions [24–26].

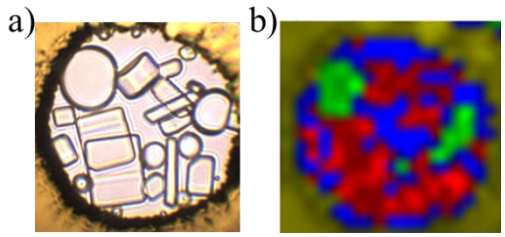

Figure 6: (a) Microphotograph of a 1 : 2 N_2–H_2 mixture at 1.2 GPa, the pressure at which hydrazine is in liquid–solid equilibrium, decompressed from 61.1 GPa. (b) A Raman mapping of the sample. The single crystals with well-defined edges in (b) are hydrazine (red) while bubbles were determined to be a nitrogen– hydrogen liquid mixture (green). Both are in liquid hydrazine (blue).

The results here-shown can hardly be extracted to correct or be compared to the theoretically calculated hydrogen-nitrogen enthalpy convex hull. Indeed, the studied samples have not been provided with enough energy to cross possible activation barriers and thus verify the observed compounds to be the truly thermodynamically-stable compounds. Future experiments should focus on devising a clever sample geometry which would allow for the heating of the N_2-H_2 mixtures to a few thousands of Kelvins. Only then could the true thermodynamically stable nature of hydronitrogens be determined.

The study of the N_2-H_2 system, and in particular of the $N_2(H_2)_2$ van der Waals compound, was critical to provide a better understanding of the reaction product obtaine near 50 GPa. Based on previous experimental and theoretical studies, the $N_2(H_2)_2$ was a promising candidate to synthesize highly effective hydronitrogen energetic materials; ideal for rocket propellants. At the outset of this investigation, topochemistry was suggested as the mechanism responsible for the reported synthesis of long azane chains. While the complex $N_2(H_2)_2$ structure was resolved at low pressure, the rotationally disordered nitrogen molecules prevented to be conclusive with regard to the effect of topochemistry. However, it could unambiguously be shown that reacted $N_2(H_2)_2$ produce mostly ammonia and a minority of longer azanes. The N_2-H_2 system may still be key to the next generation propellant as it has yet to be demonstrated that the disordered azane mixture is the thermodynamically stable high pressure form. As such, laser-heating a hydronitrogen mixture could yield one of the highly energetic compounds predicted by the numerical simulations, such as pentazole.

PCCP

PAPER

View Article Online
View Journal | View Issue

Check for updates

Cite this: *Phys. Chem. Chem. Phys.*, 2018, **20**, 4050

Pressure-induced chemical reactions in the $N_2(H_2)_2$ compound: from the N_2 and H_2 species to ammonia and back down into hydrazine

D. Laniel, *[a] V. Svitlyk,[b] G. Weck[a] and P. Loubeyre[a]

Received 28th November 2017,
Accepted 8th January 2018

DOI: 10.1039/c7cp07989c

rsc.li/pccp

Theory predicts a very rich high pressure chemistry of hydronitrogens with the existence of many N_xH_y compounds. The stability of these phases under pressure is being investigated by the compression of N_2–H_2 mixtures of various compositions. A previous study had disclosed a eutectic-type N_2–H_2 phase diagram with two stoichiometric van der Waals compounds: $(N_2)_6(H_2)_7$ and $N_2(H_2)_2$. The structure and pressure induced chemistry of the $(N_2)_6(H_2)_7$ compound have already been investigated. Here, we determine the structure of the $N_2(H_2)_2$ compound and characterize using Raman spectroscopy measurements the chemical changes under a pressure cycle up to 60 GPa and back to ambient conditions. A $N_2(H_2)_2$ single crystal was grown from a 1 : 2 N_2–H_2 mixture and its crystalline structure was solved using synchrotron X-ray diffraction. Similar to the $(N_2)_6(H_2)_7$ solid, $N_2(H_2)_2$ has a remarkable host–guest structure containing N_2 molecules orientationally disordered with spherical, ellipsoidal and planar shapes. Above 50 GPa, $N_2(H_2)_2$ was found to undergo a chemical reaction. The reaction products were determined to be of the azane family, with NH_3 as the main constituent, along with molecular nitrogen. Upon pressure decrease, the reaction products are found to react in such a way that below 10 GPa, hydrazine is the sole azane detected. Observed down to the opening of the diamond anvil cell, the formation of metastable hydrazine instead of the energetically favorable ammonia is puzzling and remains to be elucidated. That could change the current view of Jovian planets' atmospheres in which ammonia is assumed the only stable hydronitrogen molecule.

I Introduction

Hydronitrogens under ambient conditions display a rich variety of molecules including ammonia (NH_3), hydrazine (N_2H_4), hydrogen azide (HN_3) and ammonium azide $(NH_4)N_3$. Pressure is expected to enhance the diversity of hydronitrogen's chemical associations.[1–6] The high pressure chemistry of hydronitrogen systems has only recently begun to be investigated. A variety of compounds, calculated stable on the formation enthalpy-composition convex hull of the N–H system, are relevant to planetary sciences[7] and as possible metastable high energy density polynitrogen materials.[2–5,8] Indeed, the addition of hydrogen to pure nitrogen provides a natural pathway to break the very strong N_2 triple bond in favor of single N–H bonds along with the very energetic double N=N and single N–N bonds. Mixing the two pure elements at high pressures is predicted to form several novel arrangements including a large variety of long polymeric nitrogen chains and even N_5 rings.[4,5]

Experimentally, studies have characterized the pressure-induced transformations in N_2–H_2 mixtures of various compositions.[9–14] The determination of the N_2–H_2 binary phase diagram demonstrated that only two compounds are formed by compressing N_2–H_2 gas mixtures: the $(N_2)_6(H_2)_7$ and $N_2(H_2)_2$ van der Waals compounds, stable above 7 GPa.[9] Of these two, only $(N_2)_6(H_2)_7$ was structurally resolved and studied at high pressures. A chemical reaction was found to occur near 55 GPa and the reaction products were interpreted to be an amorphous dinitrogen network containing ionized ammonia. In other experiments, N_2–H_2 mixtures of various concentrations (5, 10, 20, 50 and 80 mol% N_2) were studied in the form of powders: fine hundreds of nanometer to a few micrometer-sized crystallites of varying but unknown chemical composition separated by grain bounderies.[10–12] These powders were also found to chemically react above 50 GPa and interestingly were reported to produce amorphous long azane chains (N_nH_{2+n}) or tetrazene across all sample concentrations. In all cases, the formation of hydrazine upon pressure decrease was reported.

It can be safely hypothesized that these powders of various concentrations are made up of the two van der Waals compounds. Thus, a better understanding of these results requires

[a] CEA, DAM, DIF, F-91297 Arpajon, France. E-mail: dominique.laniel@cea.fr
[b] European Synchrotron Radiation Facility, B.P.220, F-38043 Grenoble Cedex, France

This journal is © the Owner Societies 2018

determining the chemical transformations in the previously unstudied van der Waals compound, $N_2(H_2)_2$, at high pressures.

In this paper, the crystal structure of the $N_2(H_2)_2$ compound is presented along with its compression behavior as well as its chemical transformation at 60 GPa. Due to the known stoichiometry of the $N_2(H_2)_2$ compound, left-over molecular N_2 or H_2 after its chemical reaction allowed to distinguish if NH_3 or N–H oligomers and polymers were primarily synthesized. Decompressed to ambient pressure, a further chemical transformation leading to the synthesis of hydrazine, univocally determined as the dominant reaction product, is surprisingly observed.

II Experimental method

N_2–H_2 mixtures with 33 mol% N_2 were loaded at ~20 MPa and room temperature in a membrane diamond anvil cell (DAC) after a sufficient homogenization time (about 12 h). The sample concentration was determined by partial pressures to which a second-order virial correction was applied to account for mixing interactions. The uncertainty in concentrations is below 1 mol%. Membrane DACs were equipped with 300 or 400 μm flat diamond anvil culets and stainless steel gaskets (T301) lined with gold, hence preventing the diffusion of hydrogen into the gasket. Pressure was measured *in situ* using the fluorescence of a ruby microsphere, loaded along with the sample, using a recent ruby pressure calibration.[15]

Confocal Raman spectroscopy was performed up to 61 GPa on $N_2(H_2)_2$ single crystals using an Alpha300M+ instrument (WITec). Sample excitation was done with a continuous Ar–Kr laser using either the 488.0 or 647.1 nm lines with a focused laser spot of less than 1 μm. The Stokes Raman signal was collected in a back-scattering geometry by a CCD coupled to a 1800 l mm^{-1} grating, allowing a spectral resolution of approximately 1.5 cm^{-1}. Automated motorized sample positioning with piezo-driven scan stages of submicron accuracy allowed for precise Raman spectral imaging of the sample.

Single crystal data of the $N_2(H_2)_2$ compound at 9.1 GPa were collected at the European Synchrotron Radiation Facility (ESRF) ID15B High Pressure Beamline, using a wavelength of λ = 0.4111 Å and a beam size of 10 × 10 μm. During collection, the DAC containing the single crystal was oscillated of 74° with a step of 0.25°. Diffraction data were recorded on a flat panel MAR555 direct conversion detector. Experimental intensities were integrated and corrected for absorption with the CrysAlisPro package.[16] Low pressure powder X-ray diffraction experiments were carried out on the ID27 beamline of the ESRF. The monochromatic X-ray beam (λ = 0.3738 Å) was focused down to ~5 μm and a MARCCD detector was used to acquire images. Diffraction images were integrated using Dioptas[17] and analyzed using the XRDA software.[18] Fullprof[19] was used to perform the Le Bail refinement.

III Results and discussion

Structural solution and refinement of the $N_2(H_2)_2$ compound

Cubic $N_2(H_2)_2$ single crystals were grown at 7.3 GPa from 1 : 2 N_2–H_2 mixtures at the fluid–solid equilibrium in accordance with the N_2–H_2 binary phase diagram, shown in Fig. 1. Membrane pressure was increased until the single crystal filled the sample cavity. Using single crystal X-ray diffraction, the crystal structure of $N_2(H_2)_2$ was solved and determined to have a large cubic lattice, with a = 12.6141(2) Å (V = 2007.10(1) Å^3), composed of 41 N_2 molecules and, based on the compound's stoichiometry, 82 H_2 molecules.

The space group and a corresponding structural model of the $N_2(H_2)_2$ compound at 9.1 GPa were obtained using the charge flipping algorithm of Superflip[20] as implemented in the Jana2006 package.[21] The symmetry of $N_2(H_2)_2$ corresponds to a non-centrosymmetric $P\bar{4}3m$ (215) space group and is of the same $m\bar{3}m$ Laue class as previously proposed for this compound.[9] A rapid decrease of the observed intensities as a function of the diffraction angle is observed in the raw experimental data (see Fig. 1b), in accordance with earlier studies.[9]

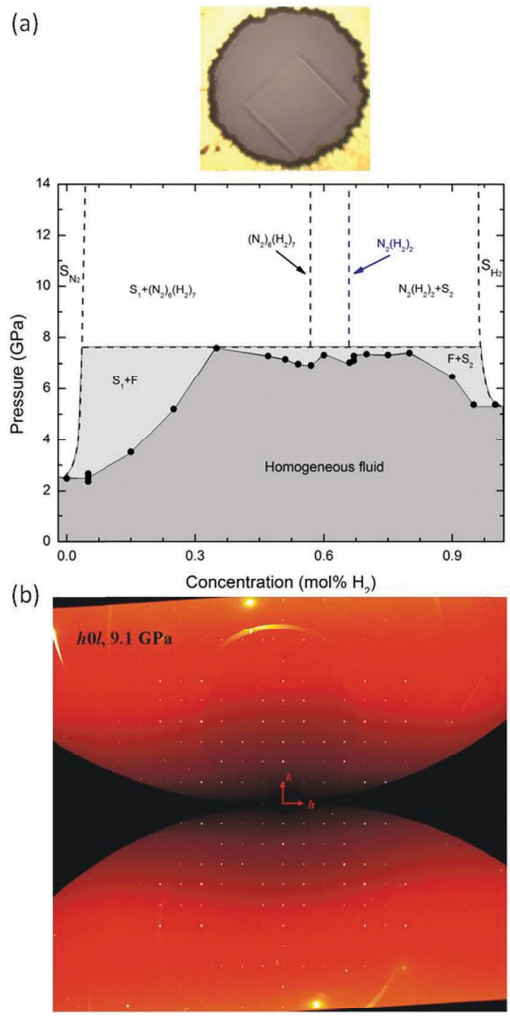

Fig. 1 (a) N_2–H_2 binary phase diagram reproduced from ref. 9. The above is a photomicrograph of a $N_2(H_2)_2$ single crystal in equilibrium with the fluid at 7.3 GPa. The experimental cavity has a diameter of about 100 μm. (b) Experimental $h0l$ slice of the reciprocal space of $N_2(H_2)_2$ at 9.1 GPa and room temperature.

This may indicate a spherical rotational disorder of N_2 molecules, also suggested from the experimental Raman data (see below). Solving for the atomic positions in a partially orientationally disordered system is a complex task that is not directly accounted for in structural solution algorithms. To determine the structure of another partially orientationally disordered molecular system, δ*-N_2, a multisite model to describe disklike molecule was employed.[22] Such an approach was unsuccessfully tested here, probably due to the large amount of nitrogen molecules and thus a low data/parameters ratio. Instead, a successful structural solution using the charge flipping algorithm was obtained by modeling the smeared electron density of nitrogen atom pairs (N_2 molecules, 7 × 2 electrons) by single Si atoms (14 electrons) which allowed determining the center of mass position of the N_2 molecules. Rather high values of the isotropic displacement parameters further confirmed a rotational disorder of the N_2 molecules. Introduction of harmonic anisotropic displacement parameters (ADPs) in the model with Si atoms allowed simulating and determining the preferred rotational disorder of N_2 molecules but still yielded a poor agreement factor (*R*-factor); close to 30% for the model. This indicates that the orientational disorder of the $N_2(H_2)_2$ compound's N_2 molecules should be described by more complex models. Indeed, the introduction of an anharmonic ADP of the 5th order significantly improved the refinement quality and the *R*-factor reached a value of 14%. Structural models with anharmonic ADPs of lower orders resulted in higher *R*-factors, significant residual electron densities in the vicinity of Si atoms and a less stable refinement.

Replacing Si atoms by N_2 molecules further lowered the *R*-factor by 2% but experimental uncertainties in the N–N distances were too high to make reliable crystallographic conclusions. This is due to an intrinsic limit of high pressure experiments where data coverage is significantly reduced due to the limited optical aperture of the DAC. With the current experimental conditions and using the Si-based structure model, the data/parameter ratio was already equal to four. Going from the Si atoms to N_2 molecules brought down this ratio even more and resulted in higher experimental uncertainties. Therefore, the model based on Si atoms was retained (see Tables 1 and 2, Fig. 2).

Only a fraction of H_2 molecules' center of mass (simulated as He atoms) could be reliably located from the residual electron density maps for which this final model resulted in a *R*-factor value of 10.99%. A structural model of $N_2(H_2)_2$ with a center of symmetry ($Pm\bar{3}m$ space group) was tested and resulted in a *R*-factor doubled compared to the non-centrosymmetric structure ($P\bar{4}3m$) and was thus discarded. Summary of the structural refinement and the corresponding structural parameters is presented in Tables 1–3.

The nitrogen molecules' complex arrangement in the $N_2(H_2)_2$ compound is shown in Fig. 2 with the Si atoms simulating the rotational disorder of the N_2 molecules through their ADPs. The structure can be divided between a dense outer N_2 scaffold surrounding an inner, opened-up, portion similarly to the structures of $(N_2)_6(H_2)_7$ and $(N_2)_6Ne_7$,[9,23] albeit constrained by its cubic symmetry. The outer N_2 scaffold, drawn separately in Fig. 2b, has at each of its eight corners a dense subunit made of four quasi-hexagonal rings linked together by four equilateral triangles. The eight corners are connected through twelve units of distorted double trigonal bipyramids, reminiscent of the single trigonal bipyramids found in ε-N.[24] The basis of each bipyramid is an isoceles triangle, with one long and two short edges, at N_2–N_2 center of mass distances of 3.03 Å and 4.29 Å, respectively. The longest edge is shared with an identical second bipyramid. The apex of each bipyramid is part of two quasi-hexagonal rings. Each quasi-hexagonal ring has N_2–N_2 distances alternating between 2.67 Å and 3.23 Å. This ring has at its center a single N_2 molecule, orientated perpendicularly to the plane formed by the $(N_2)_6$ subunit.

The inner portion of the structure is made up of four sets of three nitrogen molecules. Each set has the shape of an equilateral triangle of 3.62 Å per edge, with a N_2 molecule on each vertices adopting a disk-like rotational disorder. Inside this inner cage is a single nitrogen molecule which, in contrast with the others, is spherically disordered. A majority of the hydrogen molecules are expected to be in the free space available in this inner portion. Further details of the crystal structure investigation may be obtained from FIZ Karlsruhe (deposition number CSD-433818).

Since Ar and N_2 have roughly the same van der Waals interaction radius,[25] from hard-sphere packing and entropy considerations[26,27] the 1 : 2 N_2–H_2 mixture was expected to form a AB_2-type Laves phase, analogous to the one found in $Ar(H_2)_2$.[28]

Table 1 Crystal data and structure refinement for $N_2(H_2)_2$ at 9.1 GPa and room temperature

$N_2(H_2)_2$ (Si-based model)	
Space group	$P\bar{4}3m$
Lattice parameters, Å	$a = b = c = 12.6141(2)$
Unit cell volume, Å^3	2007.10(6)
Z	41
Index ranges	$-11 \le h \le 11$, $-4 \le k \le 6$, $-12 \le l \le 13$
Reflns collected	2298
Independent reflns	516 [R_{int} = 0.111]
Data/restraints/par.	516/0/124
R-factors [$I > 3\sigma(I)$]	R = 0.1099, wR = 0.1277
R-factors [all data]	R = 0.1561, wR = 0.1364
Goodness of fit on F^2	7.59[a]
Diff. peak/hole, e Å^{-3}	1.14/−0.46

[a] Value not equal to one (ideal model) reflects the Si- and He-based approximation as well as partial H_2 molecules mapped in the final model; see the text for more details.

Table 2 Atomic and equivalent isotropic displacement (U_{eq}) parameters of $N_2(H_2)_2$ at 9.1 GPa and room temperature

Atom	Site	x/a	y/b	z/c	U_{eq} (Å^2)
N_2 (Si1)	1a	0	0	0	0.133(7)
N_2 (Si2)	4e	0.372(3)	0.372(3)	0.372(3)	0.271(7)
N_2 (Si3)	12i	0.7113(17)	0.1163(19)	0.1163(19)	0.695(13)
N_2 (Si4)	12h	0.5	0.337(2)	0	0.396(15)
N_2 (Si5)	12i	0.5749(9)	0.4251(9)	0.247(2)	0.491(10)
H_2 (He1)	4e	0.216(3)	0.216(3)	0.216(3)	0.061(14)
H_2 (He2)	12i	0.414(3)	0.250(2)	0.250(2)	0.059(11)
H_2 (He3)	12i	0.795(7)	0.071(5)	−0.071(5)	0.13(2)
H_2 (He4)	3d	0.5	0	0	0.09(3)

This journal is © the Owner Societies 2018

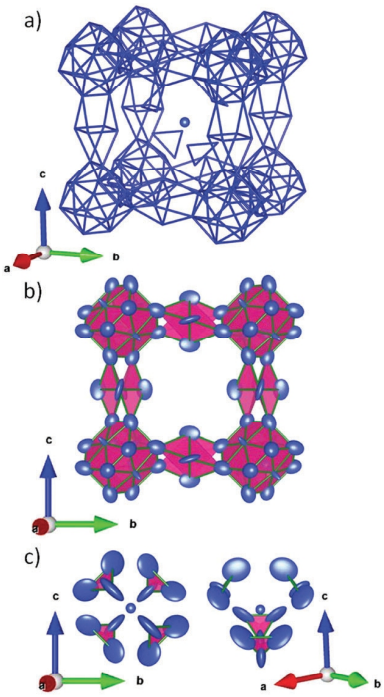

Fig. 2 N_2 arrangement of the $N_2(H_2)_2$ compound. (a) A single unit cell in the wireframe representation. The outer scaffold (b) confines the inner portion (c), both of which are drawn with the Si atoms simulating through their ADPs the rotational disorder of the N_2 molecules. The ADPs are represented by anisotropic displacement ellipsoids shown with a 30% probability.

Here, a AB_2 compound was found but differs from the anticipated structure. This is explained by the presence of an additional type of interaction in the $N_2(H_2)_2$ compound: the quadrupolar–quadrupolar (QQ) interaction between N_2 molecules, not operating in $Ar(H_2)_2$. Indeed, N_2–N_2 QQ interactions are known to result in complex structures, as it was found in other van der Waals compounds formed of N_2 and another molecule or element, such as $Ne_6(H_2)_7$, $(N_2)_6(H_2)_7$ and the high pressure $I4_1/amd$ phase of $Xe(N_2)_2$.[9,23,29] Consequently, understanding the remarkably elaborate structure found in the $N_2(H_2)_2$ compound requires an in-depth discussion of the energy-minimizing QQ interaction that is outside of this paper's scope.

Compression of the $N_2(H_2)_2$ compound and its chemical reaction

Raman spectroscopy was carried out to 54.6 GPa on a $N_2(H_2)_2$ single crystal to investigate changes in bonding during compression. As seen in Fig. 3, one peak of molecular hydrogen is observed through the studied pressure range and is blue-shifted with respect to pure hydrogen, as it is also found in H_2-rare gas mixtures and attributed to the partial suppression of vibrational coupling.[9,28,30,31] Hydrogen roton modes were observed up to the highest pressure, indicating that H_2 molecules remain rotationally free. On the other hand, the nitrogen molecule displays a greater complexity with five distinct vibrational stretching modes in a very short frequency range (between 2346 and 2357 cm^{-1}) even at the lowest pressure. The measured modes follow somewhat closely the ν_2 mode of pure nitrogen, which has a disk-like orientational disorder.[32] This matches well with the fact that all 41 of the N_2 molecules but one were found to have an orientational disorder symmetry lower than spherical.

As pressure is increased, the vibrational peaks of N_2 and H_2 are seen to broaden. This can be explained by the progressive loss of hydrostatic conditions as well as by the strain and deformation of the compressed single crystal (see Fig. 3). At 54.5 GPa, a pressure-induced chemical reaction initiates in the outer region of the single crystal, noticeable from the appearance of a yellowish color and the disappearance of texture. By further increasing the pressure to 61.1 GPa, the $N_2(H_2)_2$ crystal completely reacts, as seen from the photomicrograph in Fig. 3.

Nature and decompression of the reaction products

As the sample entirely turns yellowish under the completion of the chemical reaction, the measured Raman signal, shown in Fig. 4, radically changes. Four intense broad bands emerge at 1100, 1250, 1640 and 3245 cm^{-1}, while the molecular stretching mode of N_2 red shifts and the H_2 mode completely disappears. Raman mapping of the sample showed it to be homogeneous. The full consumption of molecular H_2 with left-over molecular N_2 unequivocally establishes the primary reaction product to have a higher H : N ratio than the single crystal of $N_2(H_2)_2$. Ammonia is the only hydronitrogen which fits this description. This is in good agreement with predictions from the calculated enthalpy-composition convex hull.[4,5] A rough estimate of nitrogen consumption by the reaction products was done by taking the ratio of the integrated area under the N_2 vibron mode before and after the chemical reaction. From this calculation, 86% of nitrogen seems to have been consumed. This value has to be interpreted carefully since it assumes no change in polarizability and orientation of the nitrogen molecules. Nonetheless, a full transformation of a 1 : 2 N_2–H_2 mixture into ammonia would have consumed 67% of N_2 molecules. The difference between the two values could indicate that molecules richer in nitrogen than ammonia have also been produced.

Table 3 Anisotropic displacement (U_{ij}) harmonic parameters of N_2 molecules (Si atoms) in $N_2(H_2)_2$ at 9.1 GPa and room temperature

Atom	U_{11}	U_{22}	U_{33}	U_{12}	U_{13}	U_{23}
N_2 (Si1)	0.133(13)	0.133(13)	0.133(13)	0	0	0
N_2 (Si2)	0.271(12)	0.271(12)	0.271(12)	0.186(11)	0.186(11)	0.186(11)
N_2 (Si3)	0.84(3)	0.62(2)	0.62(2)	0.082(14)	0.082(14)	0.49(2)
N_2 (Si4)	0.177(15)	0.46(2)	0.56(3)	0	−0.189(17)	0
N_2 (Si5)	0.455(16)	0.455(16)	0.561(18)	0.000(16)	0.086(9)	−0.086(9)

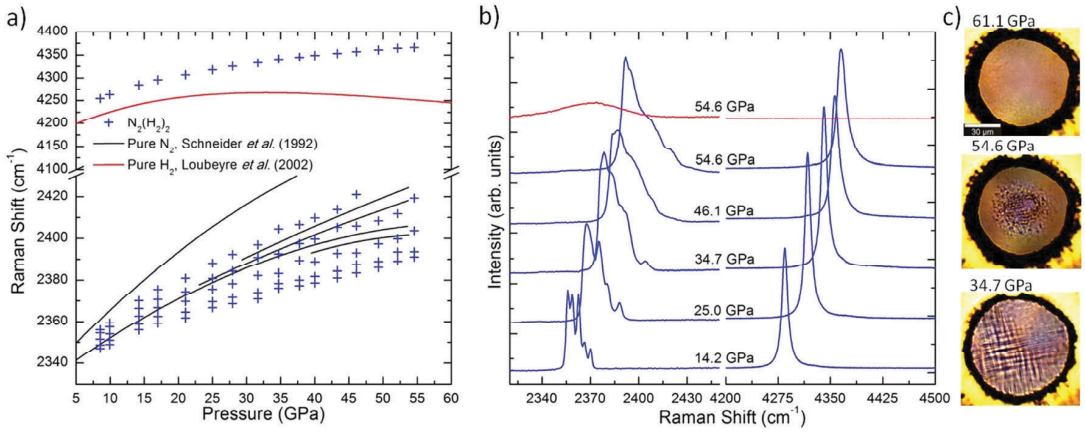

Fig. 3 Compression behavior of a $N_2(H_2)_2$ single crystal. (a) Raman shift as a function of pressure. A single H_2 vibron, blue shifted compared to the pure compound, is observed while the five N_2 stretching modes are measured. The pure N_2 and pure H_2 vibrons were obtained from the literature.[46,47] (b) Raman spectra of $N_2(H_2)_2$ with a *y*-axis offset for each pressure. At 54.6 GPa, a chemical reaction initiates. Two spectra were recorded at that pressure, one on the unreacted region of the $N_2(H_2)_2$ crystal and one on the reacted part (red). The reacted sample is easily distinguished by a new broad band characteristic of amorphous molecular nitrogen as well as the disappearance of the hydrogen vibron. At 61.1 GPa, the reaction is complete, and the crystalline molecular Raman modes of N_2 and H_2 are completely gone. As the transformation progresses, microphotographs (c) show the sample going from transparent to yellowish. The photomicrographs' contrast was modified making the change in color easily visible.

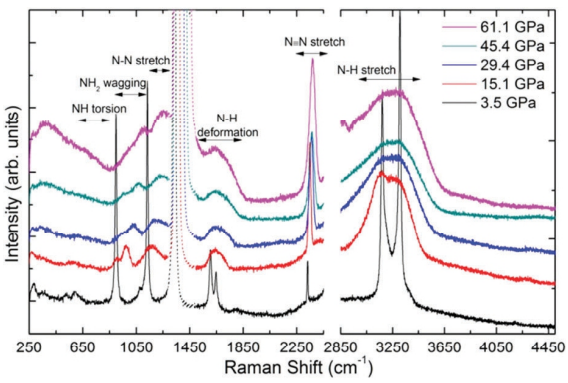

Fig. 4 Raman spectra of the reaction products under decompression. A vertical offset was added for clarity. Below 10 GPa, the Raman modes match those of pure hydrazine. Diamond's first order Raman mode, centered at 1375 cm^{-1}, is distinguished by dashed lines.

Fig. 5 shows the evolution of the broad Raman bands measured from our sample compared with those of molecular NH_3 as well as hydrazine, down to 1.2 GPa. Due to the very wide nature of the measured Raman modes, correctly identifying the right number of peaks present and properly deconvoluting them is prone to imprecision. Therefore, the broad bands' full width at half maximum (FWHM) was plotted along with the peak positions, which were obtained by fitting the bands with the lowest number of pseudo-Voigt allowing a satisfactory fit. In this fashion, it is understood that unidentified peaks might be present in the area defined by each band's FWHM.

The observed high and mid-frequency Raman modes (>3100 and near 1750 cm^{-1}) fit well the modes present in both hydrazine and ammonia: the deformation, antisymmetric and symmetric stretching of NH_2 and antisymmetric bending as well as antisymmetric and symmetric stretching of NH_3,

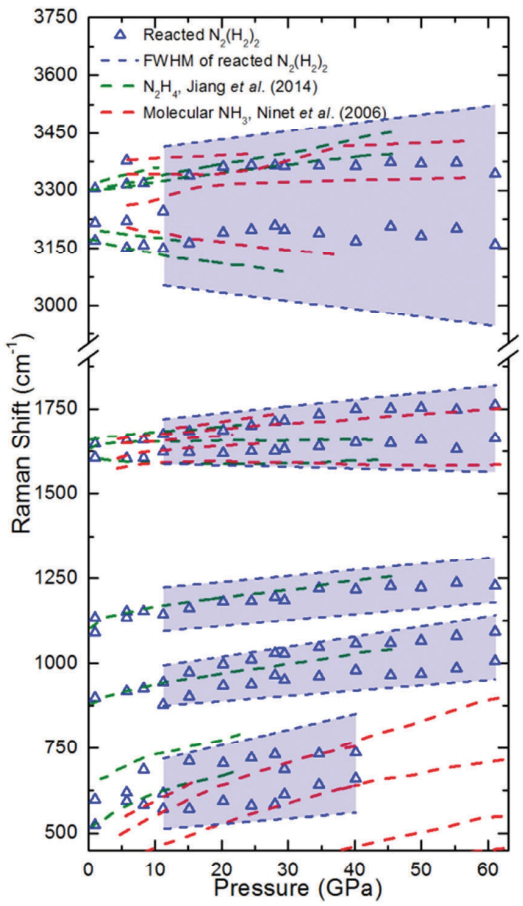

Fig. 5 Raman peaks evolution under decompression of the reacted $N_2(H_2)_2$ single crystal. Due to the very wide nature of these modes, their FWHM was also plotted (blue dashed line) down to 10 GPa, pressure at which hydrazine is observed. The red and green dashed lines represent molecular NH_3 and hydrazine's Raman modes under compression.[33,48]

 This journal is © the Owner Societies 2018

respectively.[33,34] Three more bands are found at lower pressure that match well with the N–N stretch, around 1200 cm^{-1}, the NH_2 wagging at 950 cm^{-1} and the torsion of the two NH_2 units near 600 cm^{-1}, all of which are observed in hydrazine.[33,35,36] Although not plotted in Fig. 5 due to their low intensity, hydrazine is known to have additional (three) NH_2 wagging modes near 880 cm^{-1}, explained either by the ν_6 or ν_{12} modes or their inversion doubling,[33,37] which could explain the second NH_2 wagging mode measured here. The reaction product is therefore clearly very similar to ammonia as well as hydrazine in terms of N–H, and N–N for the latter, bonding order. However, Raman frequency differences between hydrazine and longer similarly single-bonded N–H oligomers are expected to be subtle[10,11] which makes discriminating between the two difficult. The same issues are expected to be encountered using infrared absorption spectroscopy. In any case, a mixture of N_2, NH_3 and other azanes, whether hydrazine, longer azanes or even a combination of both, explains the very broad nature of the measured Raman peaks. Calculated[10] and shown[11] to partially close the bandgap, the synthesis of these molecules could also explain the yellowish color of the sample.

However, the partial or complete ionic character of NH_3, as well as of longer azanes, cannot be ruled out. Ionic NH_3 is predicted stable based on numerical simulations[4] as well as observed as a reaction product of $(N_2)_6(H_2)_7$. This could provide an alternative explanation for the yellowish color of the sample since poorly crystallized ionic compounds are susceptible to defects and therefore to form color centers with the absorption band in the visible region.[38] The presence of other types of hydronitrogens, experimentally observed (such as ammonium azide)[8,39] or theoretically predicted,[2,4–6] as reaction products was considered but did not fit our experimental data.

The mixture of NH_3 along with longer azanes, possibly with an ionic or iono-covalent character, forming a matrix in which nitrogen molecules are embedded also explains the strong red shift and broadness of the N_2 vibron.

Decompression and synthesis of hydrazine

As pressure is decreased, all vibrational modes progressively sharpen and the large N_2 mode drops in intensity. At 10 GPa, a clear transition to hydrazine is observed, concomitantly with the release of molecular hydrogen. Fig. 6 shows the sample at 1.2 GPa when hydrazine is in a liquid–solid equilibrium.[33] Liquid and single crystals of hydrazine are observed along with bubbles of N_2–H_2. At that pressure, a thorough Raman mapping of the sample was performed to detect molecular species other than N_2, H_2 and N_2H_4. No vibrational modes characteristic of other molecules were observed and, more specifically, discriminating low frequency bending and torsional modes of liquid ammonia were not detected.[40] To justify the sample's change in chemical composition, a progressive reaction of ammonia with itself and with nitrogen is thought to occur above 10 GPa and to result in the synthesis of hydrazine. This provides an explanation for the continuous sharpening of all broad bands until they converge to those of pure hydrazine, the consumption of molecular nitrogen as well as the release of molecular hydrogen and the lack of a spectroscopic signature for liquid NH_3.

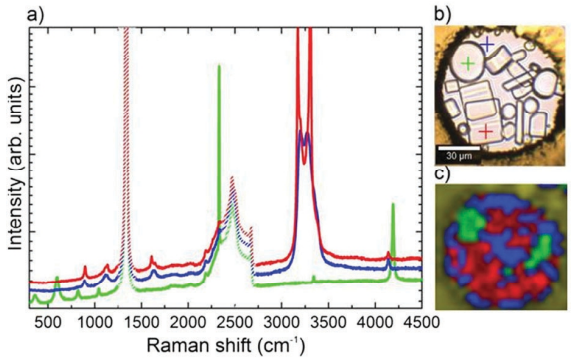

Fig. 6 1 : 2 Raman spectra of a 1 : 2 N_2–H_2 mixture at 1.2 GPa, the pressure at which hydrazine is in liquid–solid equilibrium, decompressed from 61.1 GPa. (a) The black, red and blue spectra correspond to liquid nitrogen–hydrogen in a bubble, liquid hydrazine and a single crystal of hydrazine, respectively. The low intensity of hydrazine's vibrational modes below 2000 cm^{-1} is explained by polarization effects.[49] Diamond's first and second order Raman mode, centered at 1375 and 2500 cm^{-1}, are distinguished by dashed lines. (b) Microphotograph of the sample with the crosses colored so as to match their corresponding Raman spectrum. (c) A Raman mapping of the sample. The single crystals with well-defined edges in (b) are hydrazine (red) while bubbles were determined to be a nitrogen–hydrogen liquid mixture (green). Both are in liquid hydrazine (blue). Intriguingly, this thorough mapping revealed no forms of azanes aside from hydrazine.

This result defies the common knowledge that hydrazine, although metastable under ambient conditions, is not as energetically favorable as ammonia, with a difference in the enthalpy of reaction of 86.5 kJ mol^{-1} (normalized per nitrogen atom) under ambient conditions.[11] Although this difference decreases with pressure, hydrazine still falls above the formation enthalpy-composition convex hull and ammonia is calculated more stable up to at least 100 GPa.[5] Thus, the conversion of ammonia into hydrazine is unexplained and unpredicted by recent numerical simulations. Experimentally, ammonia was previously observed to produce hydrazine in a gas discharge, albeit at very low yields,[41] and hydrazine was retrieved as one of the intermediate reaction products during the thermal decomposition of ammonia, for which the reduced pattern mechanism requires 21 steps. In the present case of a full transformation, the simplest plausible chemical reaction that could take place is the following multi-step chemical reaction: $2NH_3 \rightarrow NH_2^- + NH_4^+ \rightarrow NH_2^- + NH_2^+ + H_2 \rightarrow N_2H_4 + H_2$. However, a literature survey shows that the proposed behaviour of ammonium (NH_4^+) has not been previously observed in ammonium halides up to 40 GPa NH_4X (X = Cl, Br, and I).[42,43] In addition, the proposed interaction between the ions is not detected in pure ammonia, which undergoes self-ionization near 150 GPa but then recombines into NH_3 at 110 GPa during decompression.[44,45] These results suggest that a more complex chemical scheme could occur and so further experimental and theoretical works are needed in order to elucidate this intriguing behaviour.

Comparison to the previous results: insights into the N_2–H_2 system

Previously, the analysis of the pressure-induced chemical reactions in N_2–H_2 powders of various concentrations (5, 10, 20, 50 and 80 mol% N_2) has been hampered by the uncertainty in the structural nature of the starting molecular reagents. Knowing now the crystallographic structure of all compounds present in the N_2–H_2 binary phase diagram, the powders' composition can be determined. A Le Bail refinement (see Fig. 7) of an integrated powder X-ray diffraction pattern obtained on a fast-compressed 1 : 2 N_2–H_2 mixture demonstrates that the $N_2(H_2)_2$ and $(N_2)_6(H_2)_7$ compounds are the powder's main constituents. Although surely present, the H_2-rich alloy's diffraction lines are not observed because of their very low intensity. The $(N_2)_6(H_2)_7$ solid is observed even when the sample concentration is thermodynamically prohibiting it, which is thought to be due to the kinetic effects. Comparison of our powder X-ray diffraction pattern to those obtained from 20 and between 33 to 60 mol% N_2 N_2–H_2 powders (reproduced from ref. 10 and 11, respectively) at 21 GPa is also shown in Fig. 7. These powders can be identified as mixtures of both N_2–H_2 van der Waals compounds.

The N_2–H_2 powders of all concentrations (from 5 to 80 mol% N_2) were reported to react above 50 GPa and produce linear azane chains with spectroscopic signatures very similar to those measured in the reacted $N_2(H_2)_2$ and $(N_2)_6(H_2)_7$ compounds. Moreover, they were also found to further transform into hydrazine below 10 GPa upon pressure release.[10,11] However, the shortest azane – ammonia – was thought not to be part of their reaction products.[10,11] This interpretation is now questioned since it has been demonstrated that these powders are mainly made up of the two N_2–H_2 van der Waals compounds which both chemically react to mainly produce ammonia.[9] Furthermore, the diffusion barriers existing in the solid state at ambient temperature and the thoroughly homogeneous reaction product found in the $N_2(H_2)_2$ single crystal indicate that the chemical reactions occur locally *i.e.* within crystallites. Thus, it is highly probable for powders made up of $N_2(H_2)_2$ and $(N_2)_6(H_2)_7$ to have the same main reaction product as found in the pure van der Waals compounds: ammonia. Incidentally, simulations agree that NH_3 is the most stable compound at 60 GPa and below.[4,5] Note that the N_2-rich N_2–H_2 alloy was demonstrated not to chemically react.[9]

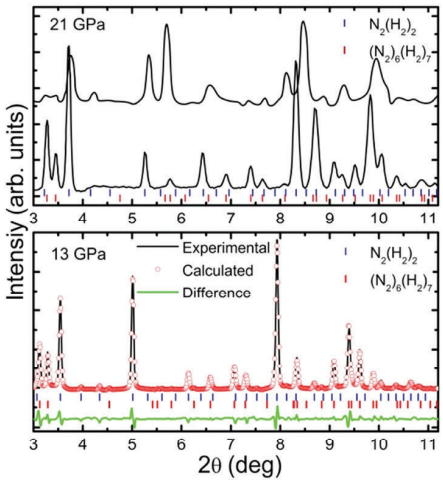

Fig. 7 Diffraction patterns obtained from various N_2–H_2 mixtures. The vertical blue and red ticks correspond to the calculated diffraction lines of the $N_2(H_2)_2$ and $(N_2)_6(H_2)_7$ van der Waals compounds. (Bottom) Le Bail refinement of a fast-compressed 1 : 2 N_2–H_2 powder X-ray diffraction pattern obtained at 13 GPa. Both van der Waals compounds are observed. The diffraction lines of the $N_2(H_2)_2$ compound are properly fitted using a cubic $P\bar{4}3m$ lattice (a = 12.09 Å). A Rietveld refinement could not be performed due to sample texturing. (Top) X-ray diffraction patterns reproduced from ref. 11 (top) and ref. 10 (bottom), obtained from N_2–H_2 mixtures of 20 mol% N_2 and between 33 to 60 mol% N_2, respectively, at 21 GPa. X-ray diffraction lines from both patterns can be properly indexed with the $N_2(H_2)_2$ and $(N_2)_6(H_2)_7$ van der Waals compound, although the top pattern appears to be at a slightly higher pressure. In this same pattern, the hydrogen-rich solid is expected to be present although it is not measured. The three diffraction patterns have different preferential orientation explaining the discrepancy between the observed peaks and their intensity.

IV Conclusion

The structure of the $N_2(H_2)_2$ van der Waals compound, as determined using single crystal X-ray diffraction, has a remarkable host–guest configuration. The complex network of intertwined cages formed of orientationally-disordered nitrogen molecules illustrates the strong driving force of QQ interactions between N_2 molecules for auto-organization. The $N_2(H_2)_2$ compound was studied up to 61.1 GPa, pressure at which a complete chemical transformation is observed. From Raman spectroscopy measurements, the reacted $N_2(H_2)_2$ solid was determined to be constituted of linear azane chains. In agreement with theoretical predictions, ammonia is found to be the main reaction product based on stoichiometric considerations, left-over molecular nitrogen and the measured vibrational modes. Upon decreasing the pressure below 10 GPa, a complete chemical transformation of ammonia into hydrazine is evidenced by the sharpening of the measured vibrational modes, the consumption of molecular nitrogen as well as the release of molecular hydrogen and the lack of a spectroscopic signature for liquid ammonia.

Indeed, NH_3 is accurately predicted to be the most stable compound below 60 GPa,[4,5] yet other compounds are predicted stable on the formation enthalpy-composition convex hull, such as the long-sought pentazolate compound, unlike hydrazine. The dominating transformation of the $N_2(H_2)_2$ molecular compound into hydrazine N_2H_4 through a pressure cycle to 60 GPa now needs to be elucidated. Finally, since N_2–H_2 powders amount to a mixture of the $(N_2)_6(H_2)_7$ and $N_2(H_2)_2$ compounds, which have definite reaction products, a strategy to circumvent them coupled to high temperatures could enable the synthesis of the predicted stable N–H compounds.

Conflicts of interest

There are no conflict of interest to declare.

 This journal is © the Owner Societies 2018

Acknowledgements

The authors gratefully acknowledge the Centre National d'Etudes Spatiales (CNES) and the Natural Sciences and Engineering Research Council of Canada (NSERC) for financially supporting the PhD of D. L. The authors also acknowledge the European Synchrotron Radiation Facility (ESRF) for provision of beamtime on ID15B.

Notes and references

1 Q. J. Liu, W. Zeng, F. S. Liu and Z. T. Liu, *Comput. Theor. Chem.*, 2013, **1014**, 37–42.
2 K. Yin, Y. Wang, H. Liu, F. Peng and L. Zhang, *J. Mater. Chem. A*, 2015, **3**, 4188–4194.
3 A. Hu and F. Zhang, *J. Phys.: Condens. Matter*, 2011, **23**, 22203–22205.
4 G.-R. Qian, C.-H. Hu, A. R. Oganov, Q. Zeng and H.-Y. Zhou, *Sci. Rep.*, 2014, **6**, 25947.
5 B. A. Steele and I. I. Oleynik, *J. Phys. Chem. A*, 2017, **121**, 1808–1813.
6 I. G. Batyrev, *J. Phys. Chem. A*, 2017, **121**, 638–647.
7 *Static Compression of Energetic Materials*, ed. S. M. Peiris and G. J. Piermarini, Springer, 2008.
8 J. C. Crowhurst, J. M. Zaug, H. B. Radousky, B. A. Steele, A. C. Landerville and I. I. Oleynik, *J. Phys. Chem. A*, 2014, **118**, 8695–8700.
9 D. K. Spaulding, G. Weck, P. Loubeyre, F. Datchi, P. Dumas and M. Hanfland, *Nat. Commun.*, 2014, **5**, 5739.
10 H. Wang, M. I. Eremets, I. Troyan, H. Liu, Y. Ma and L. Vereecken, *Sci. Rep.*, 2015, **5**, 13239.
11 A. F. Goncharov, N. Holtgrewe, G. Qian, C. Hu, A. R. Oganov, M. Somayazulu, E. Stavrou, C. J. Pickard, A. Berlie, F. Yen, M. Mahmood, S. S. Lobanov, Z. Konôpkova and V. B. Prakapenka, *J. Chem. Phys.*, 2015, **142**, 214308.
12 J. Ciezak, T. Jenkins and R. Hemley, *AIP Conf. Proc.*, 2009, **1195**, 1291–1294.
13 N. N. Galtsov, A. I. Prokhvatilov and M. A. Strzhemechny, *Low Temp. Phys.*, 2007, **33**, 499.
14 M. Kim and C. S. Yoo, *J. Chem. Phys.*, 2011, **134**, 44519.
15 A. Dewaele, M. Torrent, P. Loubeyre and M. Mezouar, *Phys. Rev. B: Condens. Matter Mater. Phys.*, 2008, **78**, 104102.
16 Rigaku Oxford Diffraction, 2015.
17 C. Prescher and V. B. Prakapenka, *High Pressure Res.*, 2015, **35**, 223.
18 S. Desgreniers and K. Lagarec, *J. Appl. Crystallogr.*, 1994, **27**, 432–434.
19 J. Rodriguez-Carvajal, *Phys. Rev. B: Condens. Matter Mater. Phys.*, 1993, **192**, 55–69.
20 L. Palatinus and G. Chapuis, *J. Appl. Crystallogr.*, 2007, **40**, 786–790.
21 V. Petrícek, M. Dušek and L. Palatinus, *Z. Kristallogr.*, 2014, **229**, 345–352.
22 G. W. Stinton, I. Loa, L. F. Lundegaard and M. I. McMahon, *J. Chem. Phys.*, 2009, **131**, 104511.
23 T. Plisson, G. Weck and P. Loubeyre, *Phys. Rev. Lett.*, 2014, **113**, 25702.
24 H. Olijnyk, *J. Chem. Phys.*, 1990, **93**, 8968.
25 S. S. Batsanov, *Inorg. Mater.*, 2001, **37**, 871–885.
26 W. Hume-Rothery and R. E. Smallman, *The structure of Metals and Alloys*, The Institute of Metals, London, 1969.
27 B. J. Alder, W. E. Alley and M. Rigby, *Physica*, 1974, **73**, 143–155.
28 P. Loubeyre, R. Letoullec and J.-P. Pinceaux, *Phys. Rev. Lett.*, 1994, **72**, 1360–1363.
29 D. Laniel, G. Weck and P. Loubeyre, *Phys. Rev. B*, 2016, **94**, 174109.
30 P. Loubeyre, R. Letoullec and J. P. Pinceaux, *Phys. Rev. B: Condens. Matter Mater. Phys.*, 1992, **45**, 12844–12853.
31 A. K. Kleppe, M. Amboage and A. P. Jephcoat, *Sci. Rep.*, 2014, **4**, 4989.
32 M. I. M. Scheerboom and J. A. Schouten, *J. Chem. Phys.*, 1996, **105**, 2553.
33 S. Jiang, X. Huang, D. Duan, S. Zheng, F. Li, X. Yang, Q. Zhou, B. Liu and T. Cui, *J. Phys. Chem. C*, 2014, **118**, 3236–3243.
34 S. Ninet, Université Pierre et Marie Curie, 2006.
35 M. Pravica, L. Bai and Y. Liu, *Chem. Phys. Lett.*, 2013, **555**, 115–118.
36 R. Chellappa, D. Dattelbaum, L. Daemen and Z. Liu, *J. Phys.: Conf. Ser.*, 2014, **500**, 52008.
37 P. A. Giguère, I. D. Liu and D. Liu, *J. Chem. Phys.*, 1952, **20**, 136.
38 F. W. Patten, *Phys. Rev.*, 1968, **175**, 1216–1227.
39 S. A. Medvedev, T. Palasyuk, I. A. Trojan, P. G. Naumov, J. Evers, T. M. Klapötke and M. I. Eremets, *Vib. Spectrosc.*, 2012, **58**, 188–192.
40 T. Ujike and Y. Tominaga, *J. Raman Spectrosc.*, 2002, **33**, 485–493.
41 P. D. Wall and M. D. Egger, *Nature*, 1971, **232**, 542–545.
42 Y. Ebisuzaki and M. Nicol, *Chem. Phys. Lett.*, 1969, **3**, 480–483.
43 S. Jeon, R. F. Porter and A. L. Ruoff, *J. Raman Spectrosc.*, 1988, **19**, 179–182.
44 T. Palasyuk, I. Troyan, M. Eremets, V. Drozd, S. Medvedev, P. Zaleski-Ejgierd, E. Magos-Palasyuk, H. Wang, S. A. Bonev, D. Dudenko and P. Naumov, *Nat. Commun.*, 2014, **5**, 3460.
45 S. Ninet, F. Datchi, P. Dumas, M. Mezouar, G. Garbarino, A. Mafety, C. J. Pickard, R. J. Needs and A. M. Saitta, *Phys. Rev. B: Condens. Matter Mater. Phys.*, 2014, **89**, 174103.
46 P. Loubeyre, F. Occelli and R. LeToullec, *Nature*, 2002, **416**, 613–617.
47 H. Schneider, W. Häfner, A. Wokaun and H. Olijnyk, *J. Chem. Phys.*, 1992, **96**, 8046.
48 S. Ninet, F. Datchi, A. M. Saitta, M. Lazzeri and B. Canny, *Phys. Rev. B: Condens. Matter Mater. Phys.*, 2006, **74**, 1–11.
49 J. R. Durig, S. F. Bush and E. E. Mercer, *J. Chem. Phys.*, 1966, **44**, 4238–4247.

SYNTHESIS OF HIGH ENERGY DENSITY LITHIUM-NITROGEN COMPOUNDS

I. *INTRODUCTION*

Lithium, third lightest element of the periodic table, assembles under an inert environment into a very ductile, silvery shiny metal. Like other alkali elements, its single valence electron has a very low ionization energy and thus can easily be stripped away. As such, lithium is highly reactive under ambient conditions, readily chemically transforming in contact with air to produce LiOH, LiOH•H_2O, Li_3N and even Li_2CO_3.

Under ambient conditions, lithium is viewed as a simple, prototypical metal adopting a cubic lattice with very weak electron-ion interaction, effectively making it a nearly-free electron material. Under pressure, however, it was shown to completely depart from its straightforward behavior. Its phase diagram is shown in Figure 1. Indeed, the common notion that compact metallic structures (*bcc*, *hcp*, *fcc*) are increasingly favored at high density is disproved in the case of lithium. The ambient conditions *bcc* solid transforms into a *fcc* structure near 7.5 GPa [238,239], but then shifts into a symmetry-lowering *I*-43*d* cubic solid containing 16 atoms at 42 GPa and then into an orthorhombic lattice with 88 atoms around 60 GPa. At higher pressures, the trend continues with two further orthorhombic phase transitions [240]. Near 80 GPa lithium was showed through electrical resistance measurement to become semiconducting [241]. This is understood by a pressure-induced electronic redistribution, where the delocalized electrons are localized in the interstitial positions of the crystal structure, effectively forming a high pressure electride with the electrons behaving as anions [242–244]. This series of phase transition was observed at temperatures below 200 K as at ambient temperature, lithium melts around 40 GPa

[240]. This very curious peculiarity of lithium was hypothesized to be due to zero-point energy quantum effects that would, with pressure, become more important than the crystal's cohesive energy and thus induce a melt [240]. This explanation is still debated in the literature [245–248]. Nevertheless, it reverts back to a solid form at about 100 GPa at ambient temperature. Clearly, lithium is showcases a complex high pressure behavior.

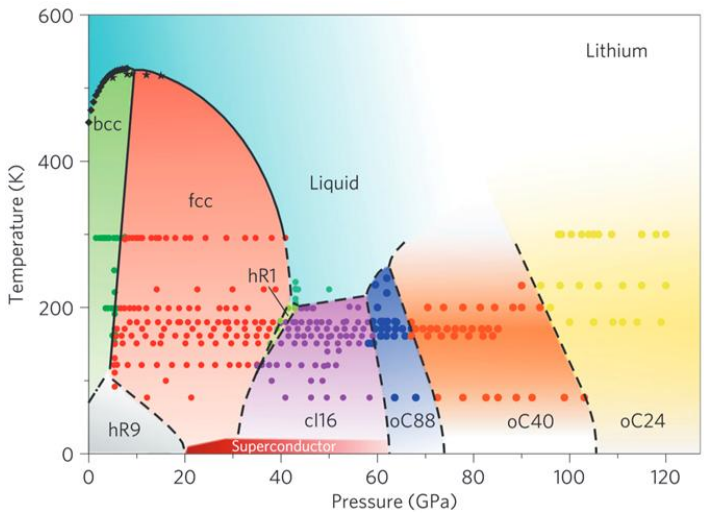

Figure 1: Phase diagram of lithium obtained from the literature [240].

The lithium-nitrogen chemical interaction is also far from being simple. At ambient conditions, two lithium-nitrogen compounds are known: lithium nitride (Li_3N) and lithium azide (LiN_3). Lithium nitride is readily produced by the direct reaction of lithium and nitrogen, enhanced at higher temperatures [249]. Mostly known for its potential in lithium-ion batteries [250–252], it was also considered for hydrogen storing applications [253] and is used for the synthesis of other nitrides [251], such as CrN, TaN and Mo_2N [254]. LiN_3, on the other hand, is found metastable at ambient conditions and is produced by a metathesis reaction from the mixing of sodium azide and lithium sulfate [249]. Containing the energetic azide anion (N_3^-), where the three linear nitrogen atoms form a total of two double bonds, it was initially used as an explosive [255].

Under the application of pressure, the chemical interaction between those two elements is greatly enhanced. For starters, the ambient conditions stable α-Li_3N ($P6_3/mmm$) solid undergoes a structural phase transition into β-Li_3N ($P6_3/mmc$) around 0.6 GPa and goes from transparent red to dark opaque [256]. Above 40 GPa, another structural phase transition results in γ-Li_3N ($Fm3m$), which appears stable up to at least

200 GPa [257]. Under compression, these various phases were characterized solely by X-ray diffraction. Monoclinic ($C2/m$) LiN_3 on the other hand was not observed to undergo any structural modification up to 60 GPa at ambient temperature [258]. More recently, lithium diazenide (Li_2N_2) was obtained from the decomposition of LiN_3 at 9 GPa and 750 K, and retrieved down to ambient conditions where its orthorhombic structure (*Immm*) was resolved [259]. This result hinted that a more complex chemistry could be induced by pressure and that novel stoichiometries were accessible. Indeed, this was later supported by theoretical calculations which unveiled five new stoichiometries stable against decomposition at pressures below 100 GPa: $Li_{13}N$, Li_5N, Li_3N_2, LiN_2 and LiN_5, along with yet undiscovered phases for already known stoichiometries [28–31]. Two independent teams produced enthalpy convex hulls of the Li-N system. Both are shown in Figure 2. Of all the theoretically calculated stable Li-N phases, three stand out as promising high energy density materials and are drawn in Figure 3. The high pressure phase of LiN_2, stable above 58 GPa, is composed of neutral infinite chains of N-N atoms of bond order between one and two, contained in a triclinic (P-1) lattice. With the LiN_3 stoichiometry, a hexagonal ($P6/m$) lattice with planar benzene-like $(N_6)^{2-}$ rings are predicted favorable on the enthalpy convex hull from 44 GPa, as also demonstrated from two other set of independent calculations [29–31]. Here again, the N-N bonds were found to be in between a single and double bond. Stable on the enthalpy convex hull between 10-15 GPa, calculated metastable down to ambient conditions and with the highest N/Li ratio, LiN_5 is the most attractive of these phases [28,29]. Lithium pentazolate is expected to adopt a monoclinic lattice (space group of either $P2_1/c$ or $P2_1$) with planar N_5^- rings having N-N atoms at quasi-equal distances of 1.33-1.34 Å, suggesting a bond order between one and two. The low pressure stability and ambient conditions metastability of LiN_5 is explained by the single electron transfer of lithium to the pentazolate ring, which allows both its aromaticity and the formation of stabilizing ionic bonds. Upon decomposition, an energy of 2.72 kJ/g is expected, which compares to the energy released by modern day explosives (HMX, RDX, TATB) [28].

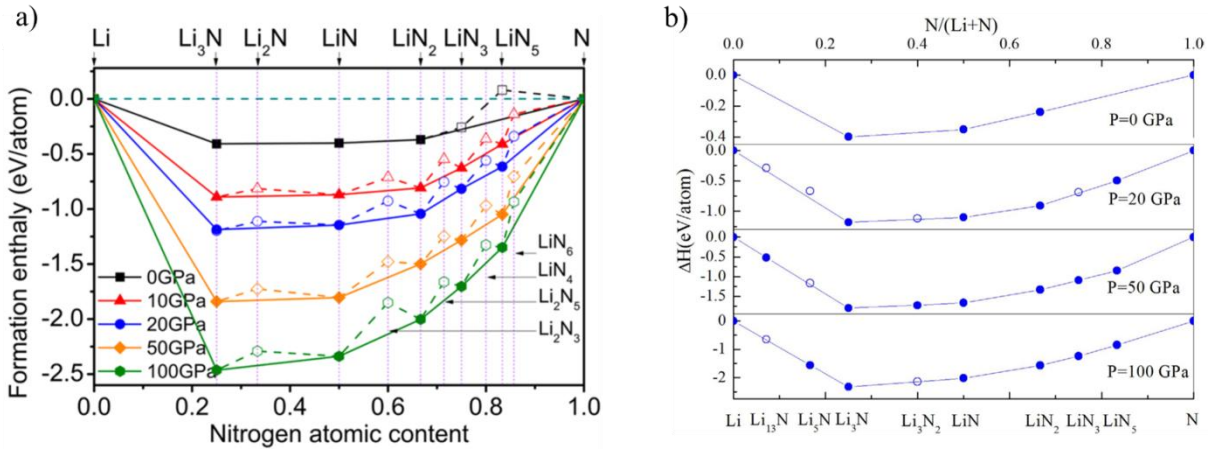

Figure 2: Li-N enthalpy convex hulls obtained from a) ref. [28] **and b) ref.** [29]**.**

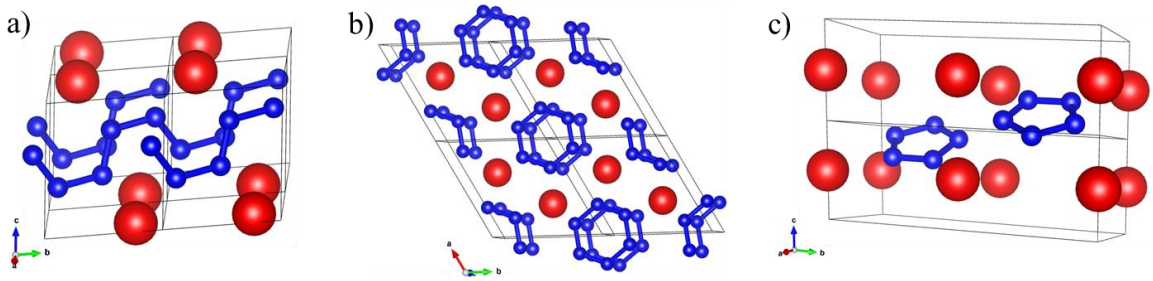

Figure 3: Structures of the high energy density Li-N compounds: a) triclinic LiN_2 (58 GPa), hexagonal LiN_3 (36-44 GPa) and monoclinic LiN_5 (15 GPa) [29]**. In parenthesis are the pressures at which the compounds were calculated to become stable. The blue and red spheres represent the nitrogen and lithium atoms, respectively.**

Due to its potential as a high energy density material, the synthesis of a pentazolate anion is a long-standing goal of chemists. The very first confirmed formation of the N_5 ring was obtained in the mid-1900s in the form of an arylpentazolate ($C_6H_5N_5$) [260]. The chemical isolation of the pentazolate, however, would take more than 50 years to achieve. First detected in the gas phase by mass spectrometry in 2002 [37], it was only recently observed in 2016 as an ion in a liquid solution of tetrahydrofuran (THF, $(CH_2)_4O$), although it proved to be unstable at ambient temperatures and only stable below -40°C [261]. In the past year breakthroughs were realized as the N_5^- anion was produced in both liquid and solid forms at ambient conditions through large stabilizing matrix, namely as a $(N_5)_6(H_3O)_3(NH_4)_4Cl$ salt or as metal pentazolate hydrate complexes

($[Na(H_2O)(N_5)_2]\cdot 2H_2O$ and $[M(H_2O)_4(N_5)_2]\cdot 4H_2O$, M = Mn, Fe, and Co) [33,34,262]. The high pressure approach also appeared as a valuable path to obtain pentazolate-containing solids as the CsN_5 salt could be produced at 60 GPa and, found metastable down to 18 GPa [49]. While of limited practicality due to pressure constraints, the CsN_5 compound has the critical advantage that a single atom was sufficient to stabilize the pentazolate anion.

The first and foremost goal of the study of the lithium-nitrogen system was the synthesis of lithium pentazolate. As described earlier, these types of compounds are heavily sought-for and, if metastable to ambient conditions, would present a great improvement over current pentazolate salts due to its very large N/Li mass ratio of nearly 91%. Moreover, it would definitely establish high pressure as a relevant method to produce ambient conditions metastable polynitrogen compounds. The secondary objective of these investigations was the synthesis and characterization of the other Li-N compounds predicted by the theoretical calculations. From the choice of the loaded sample — small pieces of lithium along with a much greater quantity of nitrogen — many solids with stoichiometries in between that of pure Li and LiN_5 could be formed; each of the stabilized phases being the nitrogen-richest permitted by the free energy convex hull at a given pressure. In addition, the Li-N_2 system provides the opportunity to explore the effects of a chemical precompression achieved through a significant charge transfer. This charge transfer is responsible for the prediction of so many anionic nitrogen moieties, which include N^{3-}, $[N_2]^{-2}$ and $[N_2]^{-1}$, N_3^-, and N_5^-. According to the theoretical simulations discussed in the introduction of this thesis, there is a direct correlation between high metastability and ionic bonds. Retrieving at ambient conditions the anionic nitrogen arrangements is thus probable.

II. *ARTICLES*

Two papers resulted from the investigation of the Li-N_2 system. The first presented here, titled *"Direct reaction of nitrogen and lithium up to 75 GPa: Synthesis of the Li_3N, LiN, LiN_2 and LiN_5 compounds"* and submitted in Inorganic Chemistry, describes the Li-N solids produced upon the compression and laser-heating of pure lithium embedded in a much larger quantity of molecular nitrogen.

Immediately upon loading the Li-N_2 sample, β-Li_3N is observed. This transformation is also reported to occur at ambient conditions; without even the need of heating. As it will be discussed shortly, all of the subsequent chemical reactions require some amount of laser-heating. Of course, this can be attributed to the low

atomic diffusion coefficient in the solid state, and thus highlights the validity of the topochemistry principle. To ensure that β-Li_3N is the most stable Li-N compound while in excess of N_2, it was laser-heated at pressures as low as 3.5 GPa and remained. Laser-heating the sample above 10.5 GPa however results in a chemical reaction and the LiN_2 solid is observed. This solid adopts a hexagonal ($P6_3/mmc$) lattice and contains a charged N_2 dimer (pernitride) (see Figure 4).

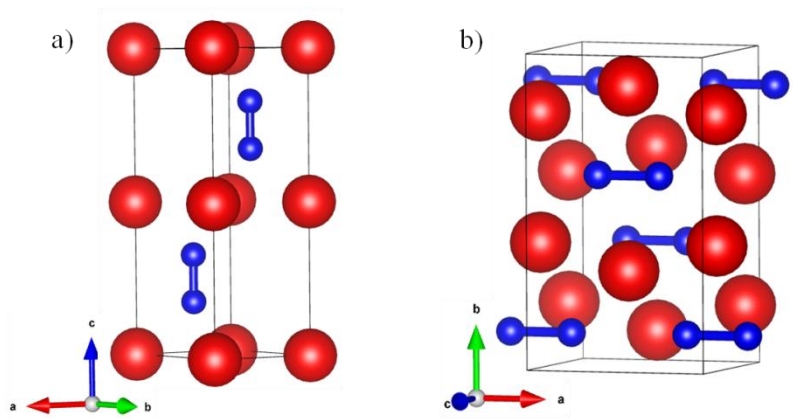

Figure 4: a) Structure of the hexagonal ($P6_3/mmc$) LiN_2 compound. b) Structure of the orthorhombic ($Cmcm$) LiN compound. The blue and red atoms represent the nitrogen and lithium atoms, respectively.

The structure determined matches the theoretically predicted one. As suggested by the compound's stoichiometry, the pernitride was found to have an excess charge close to 1-, based on the N-N bond length determined by X-ray diffraction. These pernitrides, often formed in transition metal-nitrogen compounds (see the study of Fe-N_2 in the Annex), have a noticeable effect on the solid's bulk modulus. The relationship between pernitride and bulk modulus is explained as follows: the *extra* electron(s) transferred to the N_2 dimer fill the N-N antibonding molecular orbitals ($1\pi_g^*$). This filling results in an increased repulsion between the two N atoms, thus leading to a higher bulk modulus [56,263]. Up to the complete filling of the anti-bonding orbitals, the greater the charge density transferred to the N_2 dimer, the larger the bulk modulus. These orbitals are represented in Figure 5. In the case of LiN_2, a single electron fills up the antibonding orbitals. As such, the bulk modulus is not expected to be significantly increased. Indeed, a K_0 = 63(4) GPa and K_0' = 3.9(4), were obtained, as detailed in the article. While it is much larger than those measured in pure Li (11.3 GPa) [238], ε-N_2 (2.98 GPa) [83] as well as LiN_3 (19.1 GPa) [258], it is slightly lower than in β-Li_3N (74 GPa) and γ-Li_3N (78 GPa) [257,264].

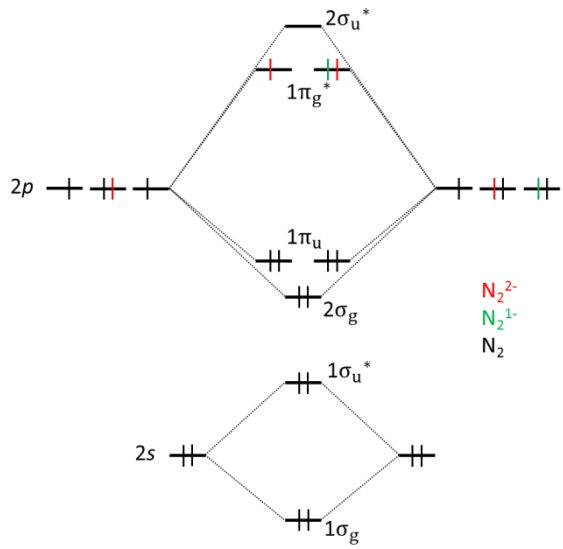

Figure 5: Molecular-orbital diagram of the N_2 molecule as well as of the $[N_2]^{1-}$ and $[N_2]^{2-}$ pernitrides. Figure inspired from Ref. [56].

Above 25.2 GPa, a second new Li-N compound was observed along with LiN_2: LiN. By powder X-ray diffraction, its structure was resolved to be orthorhombic (*Cmcm*) and also contains a pernitride (see Figure 4). This phase was also correctly predicted by the theoretical calculations. Based on the structural determination and the N_2 dimer Raman frequency, a charge transfer of about $2e^-$ was found, as expected from its stoichiometry. According to the explanation described above, the bulk modulus of LiN is expected to be greater than that of LiN_2 as it has an extra electron in the antibonding orbitals. Indeed, values of K_0 = 112(19) GPa and K_0' = 3.2(4) were obtained, with the bulk modulus being almost twice as large as that of LiN_2. Thus far, it is the highest of any known Li-N solid.

Unlike LiN_2, which is the nitrogen-rich stable Li-N compound between about 10 and 45 GPa, LiN is synthesized only when the laser-heated Li_3N piece has insufficient access to molecular nitrogen. Indeed, while LiN_2 forms in the sample regions where there is the most molecular nitrogen, LiN tends to be produced in the bulk of the Li_3N solid. Above 45 GPa, the same observations were made between the nitrogen-richest stable Li-N compound (LiN_5, described below) and LiN. This is shown by Raman mappings in Figure 6. While it is well-known that it is important to have a homogeneous sample temperature during laser-heating, this result highlights the dangers of having a chemically inhomogeneous sample environment. Indeed, during the first set of experiments, as many as five phases could be observed in a single X-ray diffraction pattern, namely pure nitrogen, Li_3N, LiN, LiN_2 and LiN_5. As three of these phases had never been observed before, their determination was arduous. After the nature of the

LiN compound was understood, care was taken to only load into the DAC tiny lithium pieces so that they could be completely transformed. In any case, as shown in the paper, the pressure stability domain of the four observed Li-N phases was resolved through sample laser-heating at regular pressure intervals (∽ 5 GPa).

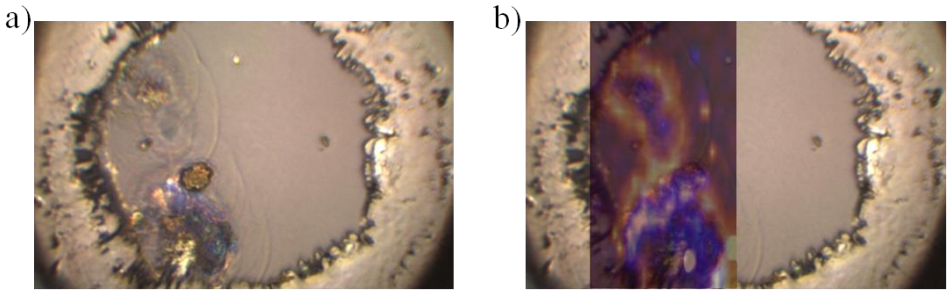

Figure 6: a) Microphotograph of a Li-N_2 sample laser-heated at 60 GPa and decompressed down to 12 GPa. b) The same microphotograph superimposed with the Raman mapping. The yellow to red (weak to strong intensity peaks for LiN_5, respectively) and purple to white (weak to strong intensity peaks for LiN, respectively) portions map where LiN_5 and LiN Raman modes were detected. The LiN_5 is found in the outer regions, further away from the main Li piece and in close contact with molecular N_2.

Published in the Journal of Physical Chemistry Letters, the synthesis of the LiN_5 compound is presented in a paper titled "*High-pressure synthesized lithium pentazolate compound mestastable under ambient conditions*". Upon laser-heating either Li_3N or LiN_2 above 45 GPa, another chemical reaction occurred and the LiN_5 compound was produced. In accordance, new vibrational modes as well as diffraction lines were detected. Unfortunately, the diffraction patterns containing the LiN_5 diffraction lines were always polluted with those of LiN_2, LiN as well as pure N_2. From these diffraction patterns, it was possible to dismiss the structures suggested for LiN_5 by theoretical investigations [28,29]. A monoclinic lattice was suggested based on nine diffraction lines identified on a sample at 73 GPa. Despite many attempts to produce samples with clean diffraction patterns, we were ultimately unsuccessful. Curiously, very thin and small lithium pieces, when laser-heated, tended to form thin, transparent films of LiN_5 (see Figure 7). While these could be identified by Raman spectroscopy, they produced no diffraction signal.

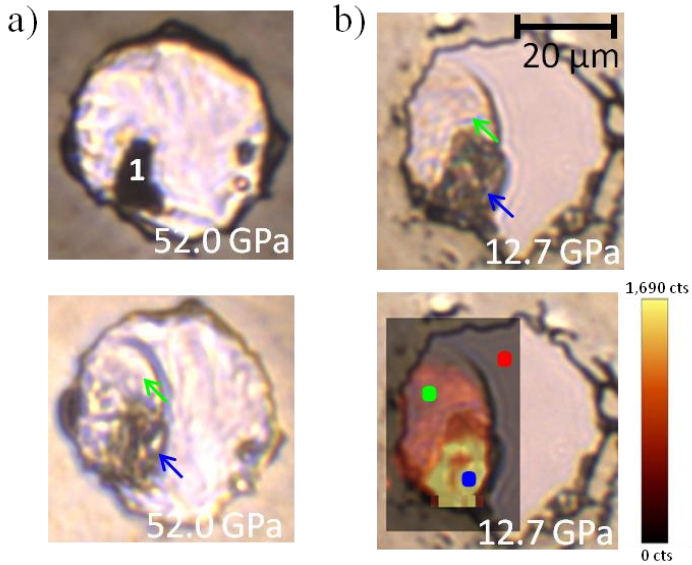

Figure 7: Microphotographs of the chemical transformation of a Li_3N piece embedded in N_2 along with the Raman mapping of the sample chamber to spatially pinpoint the LiN_5 compound. (a) Microphotographs at 52.0 GPa before (top left) and after (bottom left) laser heating. Before heating, the numbers 1 mark the lithium piece. The laser-heated and transformed solid, labeled by a blue arrow, appears translucent and grew in size. A texture change is also observed in the solid nitrogen surrounding the laser-heated lithium piece, identified by a green arrow. (b) Microphotographs of the same sample at 12.7 GPa, with and without the superimposed Raman mapping (top right and bottom right, respectively). At this pressure, pure molecular nitrogen is no longer reticulated as it underwent the ε-N_2 → δ^*-N_2 phase transition. The yellow to red color scale indicates the intensity of the main N_5 stretching Raman mode, from strong to weak, respectively. The textured, transparent area above the main LiN_5 piece is found to have the same N_5 Raman modes.

Other methods to obtain a homogeneous LiN_5 solid were attempted. As the parasitic peaks came from Li-N solids with a lower nitrogen concentration, it was thought that by homogeneously laser-heating the Li_3N piece for a considerable amount of time, thus allowing sufficient nitrogen diffusion, a full transformation into LiN_5 might be obtained. To achieve this, it was tried to load a pure lithium piece positioned on a laser absorber. Unfortunately, due to the difficulty in manipulating pure lithium – which is very sticky – in a glovebox, we were never able to get the wanted sample geometry. A similar approach was attempted with loading LiN_3 instead of pure Li, the former being easier to manipulate and, due to its stoichiometry, does not require as much nitrogen (and thus nitrogen diffusion) to transform into LiN_5. This experiment was done once, and laser-heating the LiN_3 piece resulted in an amorphous solid. However, the sample might have been partially contaminated with water. In another set DAC loading, thinking that the thin transparent LiN_5 solids might be amorphous, there were annealed at 12 GPa. This resulted in its decomposition into LiN_3 and pure N_2.

As described in details in the paper, the Raman modes measured from the LiN_5 samples were clean and perfectly matched the signature modes of an N_5^- ring. Based on these, it was observed that lithium pentazolate was metastable down to ambient conditions (see Figure 8).

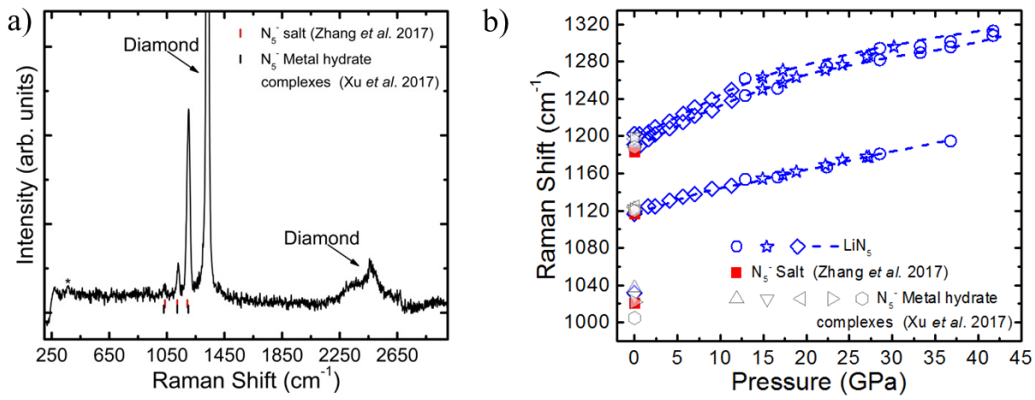

Figure 8: a) Raman spectra of the LiN_5 solid at ambient conditions after opening and closing the DAC in a glove box, allowing molecular nitrogen to be released. The intense first order Raman mode of the diamond anvils is observed near ~1350 cm^{-1} while the large second order mode is detected from 2160 to 2685 cm^{-1}. The tick marks represent the vibrational modes of the pentazolate salt and the $[Mg(H_2O)_6(N_5)_2]\cdot 4H_2O$ pentazolate metal complex.[33,34] **b) Evolution of the LiN_5 Raman mode frequencies with pressure; different symbols correspond to distinct experimental runs. The data obtained in the pentazolate salt and the metal pentazolate hydrate complexes are also reported.**[33,34]

On top of being a great result, the ambient conditions metastability of the LiN_5 compound opened up the possibility of performing other characterization methods. The most definitive technique appropriate for very small sample sizes, flow injection analysis electrospray ionization mass spectrometry, was performed in order to validate the presence of N_5^- rings. This experimental method is described in the Supplementary Materials of the following paper. As LiN_5 decomposed in contact with air, the samples for mass spectrometry were prepared in the glovebox. The LiN_5 was gently scraped off the diamond anvils and placed on a small quartz disk, which was then dropped in methanol. Methanol was chosen as a solvent as it had been demonstrated to properly dissolve N_5^- without decomposing it [34]. This procedure, along with preliminary tests with the mass spectrometer, were performed with LiN_3 samples. These samples also allowed us to optimize the electrospray ionization parameters (given in the paper's Supplementary Materials). Once the procedure was tested and optimized, the methanol solutions containing the pentazolate anion were injected into the mass spectrometer

which was set to detect at a mass/charge (*m/z*) ratio of -70; corresponding to that of N_5^-. From all four N_5^--containing solutions, coming from two separate LiN_5 samples, a weak but an unambiguous peak appeared at the correct *m/z* ratio. A raw spectrum is shown in Figure 9, along with the extracted ion-current time evolution during the methanol-N_5^- solution injection. Hence, the mass spectrometry experiments validated both the presence of the pentazolate anion as well as its metastability down to ambient conditions.

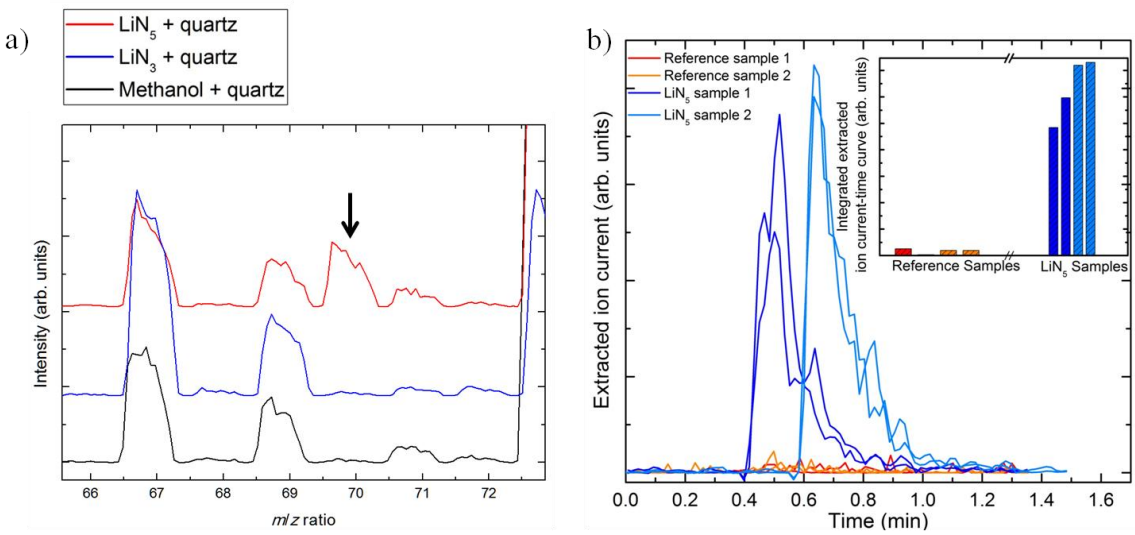

Figure 9: a) Raw mass spectrometry spectra of the solutions containing LiN_5, the LiN_3 calibrant and solely methanol. The arrow marks the peak corresponding to the *m/z* of N_5^-. b) Mass spectrometry results from LiN_5 dissolved in methanol, with the extracted ion current for m/z values between 69.5 and 70.5, measured as a function of time. The LiN_5 samples are injected and measured at 0.4 and 0.58 min, respectively, for samples 1 and 2, while both methanol reference samples were injected at 0.4 min. (Inset) Integrated ion current–time curves shown in the main figure for the two LiN_5 and the two reference samples.

The investigation of the Li-N_2 system proved to be most fruitful. The chemical precompression of the lithium atoms on the nitrogen atoms, achieved through a charge transfer, proved to be very effective. This charge transfer enabled many anionic moieites, namely N^{3-}, $[N_2]^{\sim -2}$ and $[N_2]^{\sim -1}$, N_3^-, and N_5^-, that have a large domain of (meta)stability. Theoretical calculations were most helpful as they adequately predicted the whole of the experimentally observed Li-N compounds.

In particular, the high pressure synthesis of LiN_5 and its demonstrated metastability at ambient conditions is an important result for both the fields of high pressure and of traditional chemistry. It is the first polynitrogen high-energy density material produced by high pressure and retrieved down to ambient conditions. Up to now, it is the room-condition polynitrogen compound with the largest fraction of nitrogen by weight. Furthermore, it is calculated to have the energetic capabilities of modern-day explosives. However, its potential as a propellant is hindered by its lithium atom since it is solid upon decomposition of the lithium pentazolate. Replacing the Li atom with another atom, for example hydrogen, would make for an incredibly powerful material. With LiN_5 as a precursor, both high pressure methods and conventional chemistry could provide means to achieve this.

Direct reaction of nitrogen and lithium up to 75 GPa: Synthesis of the Li_3N, LiN, LiN_2 and LiN_5 compounds

D. Laniel[*,1,2], *G. Weck*[1], *P. Loubeyre*[1]

[1]CEA, DAM, DIF, F-91297 Arpajon, France.

[2]CNES Launcher Directorate, 52 rue J. Hillairet, 75612 Paris cedex

[*]Corresponding author e-mail address: dominique.laniel@cea.fr

Abstract

A wide variety of Li-N compounds are predicted as stable under pressure and associated to various nitrogen anionic moieties. Accordingly, the LiN_5 compound was recently synthesized at 45 GPa by the direct reaction of nitrogen and lithium. In this study, we present an experimental investigation of the Li-N binary phase diagram from ambient pressure up to 73.6 GPa. The samples loaded in the diamond anvil cells were constituted of pure lithium pieces embedded in a much greater quantity of molecular nitrogen and, at incremental pressure steps, were laser-heated to produce the thermodynamically favored solid. The following compounds are observed: Li_3N, LiN_2, LiN as well as LiN_5 and their pressure stability domain is disclosed. Two are synthesized for the first time, namely *Cmcm* LiN and $P6_3/mmc$ LiN_2. Both are structurally resolved and characterized by X-ray diffraction and Raman spectroscopy measurements. Their high bulk modulus is characteristic of charged N_2 dimers.

Introduction

Until recently, only two lithium-nitrogen compounds were known: lithium nitride (Li_3N) and lithium azide (LiN_3). Lithium nitride, containing the N^{3-} anion, is stable at ambient conditions and is readily produced by the direct reaction of lithium and nitrogen, enhanced at high temperatures.[1] Mostly known for its potential in lithium-ion batteries,[2–4] it was also considered for hydrogen storing applications[5] and is used as a precursor for the synthesis of other nitrides,[3] such as CrN, TaN and Mo_2N.[6] On the other hand, LiN_3 is found metastable at ambient conditions and is produced by a metathesis reaction from the mixing of sodium azide and lithium sulfate.[1] It was initially employed as an explosive[7] since it contains the energetic azide anion N_3^-, where the three linear nitrogen atoms form a total of two double bonds.

Under the application of pressure, the chemical interaction between Li and N should be greatly enhanced. In addition to the Li_3N and LiN_3 stoichiometries, six others ($Li_{13}N$, Li_5N, Li_3N_2, LiN, LiN_2 and LiN_5) are predicted stable on the Li-N enthalpy convex hull.[8–11] Owing to lithium's reactivity – prompt to free itself of its single valence electron – the typically inert molecular nitrogen is enticed to break or alter its strong covalent triple bond and form various anionic species. The nitrogen arrangements in the calculated Li-N compounds range from atomic (N^{3-}), charged dimers ($[N_2]^{-2}$, $[N_2]^{-4}$), azides (N_3^-) chains and pentazolate (N_5^-). Of these, lithium pentazolate (LiN_5) is of considerable interest as a high energy

density material since it contained the elusive energetically-rich N_5^- ring expected metastable down to ambient conditions.

So far, the high pressure investigations of Li-N mixtures have mainly focused on the compression of the compounds available at ambient conditions: the stable Li_3N and the metastable LiN_3. Around 0.6 GPa, the ambient conditions' stable α-Li_3N ($P6_3/mmm$) solid undergoes a structural phase transition into β-Li_3N ($P6_3/mmc$) and goes from transparent red to dark opaque.[12] Above 40 GPa, another structural phase transition results in γ-Li_3N ($Fm3m$), which appears stable up to at least 200 GPa.[13] Under compression, X-ray diffraction and X-ray Raman spectroscopy measurements of the various Li_3N phases were reported.[12–14] The monoclinic form ($C2/m$) of LiN_3, stable at ambient conditions, was not observed to undergo any structural modification up to 60 GPa at ambient temperature.[15]

In 2012, another Li-N compound was synthesized: dilithium diazenide (Li_2N_2 or simply LiN), which was obtained from the decomposition of LiN_3 at 9 GPa and 750 K. This solid was solely characterized at ambient conditions where its orthorhombic structure (*Immm*) composed of charged N_2 dimers was solved.[16] This result hinted that, as expected from theoretical calculations, a more complex chemistry could indeed be induced by pressure and that novel stoichiometries are accessible. The very recent synthesis of the elusive LiN_5 compound at 45 GPa, observed metastable down to ambient conditions, confirmed this theoretical picture.[8,9,17]

Here, we present a systematic experimental investigation of the Li-N phase diagram with a sample configuration favoring the synthesis of nitrogen-rich phases. Pure lithium flakes embedded in a much greater quantity of nitrogen were compressed up to 80 GPa as well as laser-heated (up to about 2500 K) at various pressure steps to cross possible activation barriers towards the thermodynamically stable compound. Four Li-N compounds are produced and their pressure stability domain is resolved. Of these, two new solids are produced and characterized by X-ray diffraction and Raman spectroscopy: *Cmcm* LiN and LiN_2. Moreover, complementary data on Li_3N are reported.

Experimental method

Measurements were performed in membrane diamond anvil cells (DAC) equipped with diamond anvils of culets diameter of either 150 µm or 300 µm. A few pure lithium pieces of typically about 10x10x5 μm^3 in size were positioned in the sample chamber under argon gas in a glovebox. The closed sample chamber was then opened up in a high pressure vessel and filled with pure molecular nitrogen (1400 bars). Nitrogen, acting as both a pressure transmitting medium and a reagent, was always largely in excess with respect to lithium. Rhenium was used as gasket material. A small ruby chip or gold micrograin were loaded along with the sample and used to determine the pressure inside the experimental chamber.[18,19] It was always verified by Raman spectroscopy that no water contamination of the sample had occurred during the loading process. To make sure that no chemical reaction occurred with the carbon surface of the diamond anvil, one run was performed with a thin titanium protective layer (200 nm) sputtered on both diamond anvils.[20]

Confocal Raman spectroscopy measurements were performed using an Alpha300M+ (WITec). Sample excitation was done with a continuous Ar-Kr laser employing the 647.1 nm line, focused down to

less than 1 µm. The Stokes Raman signal was collected in back-scattering geometry by a CCD coupled with a 600 lines/mm grating allowing a spectral resolution of approximately 8 cm^{-1}. Automated motorized sample positioning with piezo-driven X-Y scan stages of submicron accuracy allowed for precise Raman mapping of the sample. Raman spectra were typically recorded using 110 mW of laser power and 30 seconds acquisition times.

X-ray diffraction measurements were performed on the ID27 beamline of the ESRF in angular-dispersive mode. The X-ray beam, with $\lambda = 0.3738$ Å, was focused by two Kirkpatrick-Baez mirrors and cleaned by one pinhole to a ~5x5 μm^2 spot on the sample. The sample to detector distance was calibrated using a CeO_2 reference sample. X-ray powder diffraction patterns collected on a MAR-CCD detector were integrated using DIOPTAS and analyzed using the XRDA as well as the FULLPROF softwares.[21–23]

Double-sided laser-heating of the Li-N_2 mixtures was performed at our laboratory and at the ESRF ID27 beamline using YLF lasers. Both pure lithium and the LiN_2 compound absorb the YLF laser and were thus used as absorbers for laser-heating. To promote nitrogen diffusion into the lithium solid, the samples were always laser-heated for several minutes (~ 5 min) above the melting temperature of molecular nitrogen.[24] Below 20 GPa, laser-heating temperatures were limited below ~ 1500 K since going to higher temperatures damaged the samples. Above 20 GPa, the sample were heated to temperatures of ~ 2500 K. If a new phase was detected, the samples were further heated until it was homogeneous or no further transformation was observed. If no reaction took place, pressure was increased after which the sample was laser-heated again. Temperatures were measured by fitting the sample's thermoemission to Planck's law.[25]

Results and discussion

Stability domain of Li-N phases in excess of nitrogen

Twelve independent pressure runs were devoted to investigating the synthesis of the compounds stable on the nitrogen-rich side of the Li-N binary phase diagram up to 73.6 GPa. Four compounds were reproducibly observed, namely Li_3N, LiN, LiN_2 as well as LiN_5 and their respective pressure stability domain determined by X-ray diffraction and Raman spectroscopy measurements associated to laser-heating for selected pressure steps.

Representative sets of integrated X-ray diffraction patterns obtained before and after sample laser-heating are shown in Figure 1, which illustrates the various chemical transformations. Lithium and nitrogen were observed to immediately chemically react to form Li_3N after sample loading, in agreement with the literature.[12] The lowest loading pressure being above the $\alpha \rightarrow \beta$ phase transition in Li_3N (0.6 GPa),[12] a β-Li_3N powder was always first identified. As shown in Figure 1, laser-heating of this powder at 3.5 GPa resulted only in the annealing of β-Li_3N and so no other compound with a larger fraction of nitrogen is stable in this pressure range. At 10.5 GPa, laser-heating Li_3N in excess of nitrogen amounted in the synthesis of the LiN_2 compound. The pressure of stability of LiN_2 is thus in between 3.5 GPa and 10.5 GPa. From 10.5 GPa to 43.2 GPa, laser-heating either the Li_3N or the LiN_2 compounds embedded in excess nitrogen systematically resulted in the formation of LiN_2. This establishes LiN_2 to be the stable Li-N compound with the largest nitrogen of fraction over this pressure range. Above 46.5 GPa up to 73.6

GPa, laser-heating of the Li_3N or the LiN_2 compounds produces the LiN_5 compound. The characterization of LiN_5 is provided elsewhere.[17]

It is interesting to note that from 25.2 GPa and above, the synthesis of the LiN_2 as well as the LiN_5 solids was accompanied with the formation of the LiN compound, as shown in the integrated diffraction patterns of Figure 1. For reasons explained below, LiN was prominently detected in sample regions with low nitrogen concentration and is not observed at 9.0 GPa, contrary to previous investigations.[16] The lattice parameters are the various Li-N phases shown in Figure 1 can be found in Table 1, while their stability domains are summarized in Figure 2.

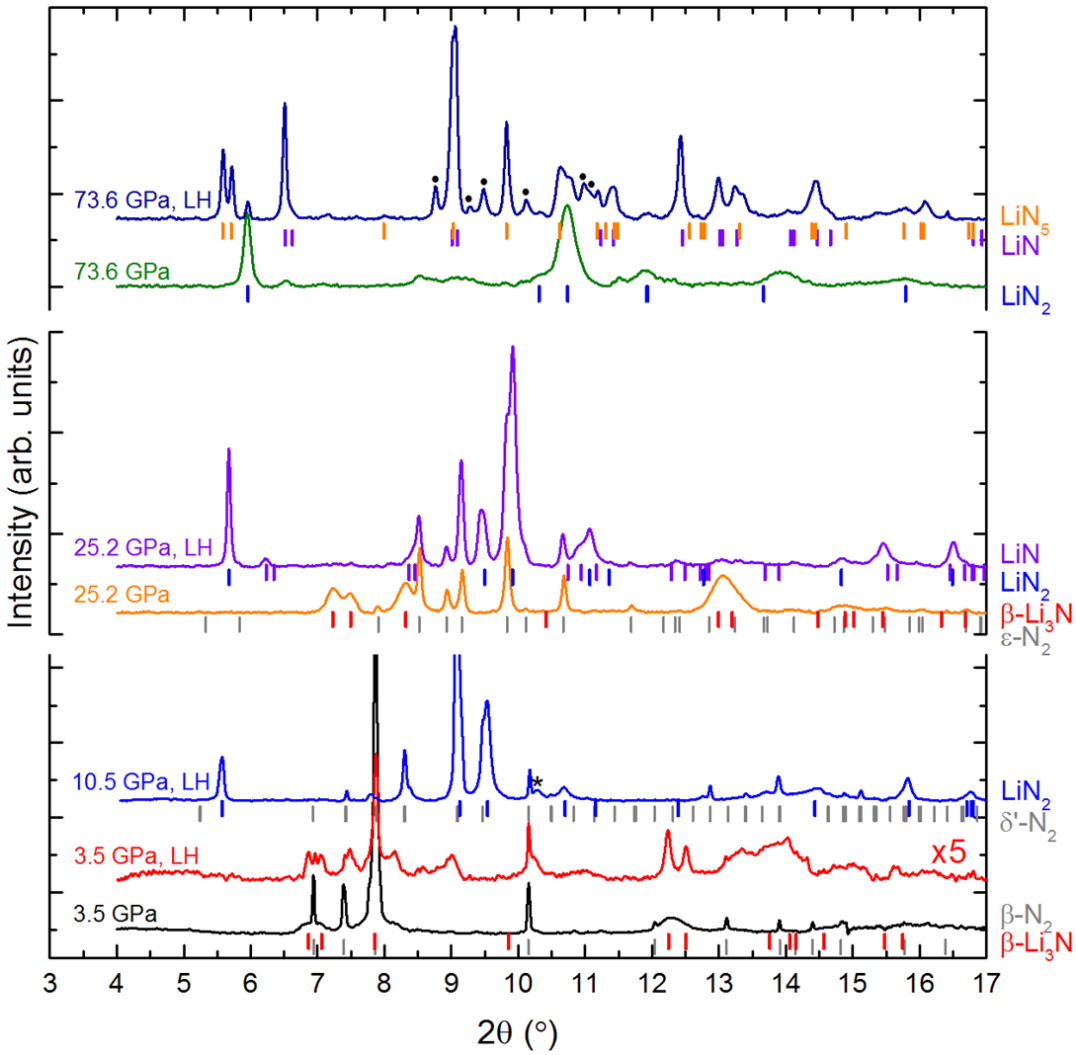

Figure 1: Three sets of integrated X-ray diffraction patterns obtained from two distinct Li-N_2 samples. The first three diffractograms were obtained from a unique sample that was laser-heated (LH) twice: first at 3.5 GPa and then again at 10.5 GPa, resulting in the red and blue diffractograms, respectively. The top four diffractograms were acquired from a second sample, laser-heating once at 25.2 GPa and again at 73.6 GPa. The phases corresponding to the same colored tick marks are indicated on the right of the plot. The asterisk and full circles mark peaks attributed to the rhenium gasket and to ζ-N_2, respectively. The tick marks of ζ-N_2 were not plotted as the compound's lattice is not well established. The lattice parameters of the phases shown in this figure can be found in Table 1.

Table 1: Lattice parameters of the various Li-N compounds shown in Figure 1. The lattice parameters of the *Cmcm* LiN solid at 73.6 GPa are provided in Figure 4.

Compound	Pressure (GPa)	*a* (Å)	*b* (Å)	c (Å)	β (°)
β-Li_3N	3.5	3.506(1)		6.242(1)	
β-Li_3N	25.2	3.306(1)		5.868(1)	
LiN_2	10.5	2.713(1)		7.688(1)	
LiN_2	25.2	2.607(1)		7.553(1)	
LiN_2	73.6	2.401(1)		7.191(1)	
LiN	25.2	7.239(1)	3.924(1)	3.576(1)	
LiN_5	73.6	3.808(1)	3.838(1)	2.410(1)	99.84(4)

Two calculations of the enthalpy convex hulls for the Li-N system provide a complete understanding of i) the experimental observation of the LiN_2 and LiN_5 compounds, ii) the formation of LiN in the region of the heated sample not in contact with the nitrogen reagent, iii) the higher than previously reported synthesis pressure of LiN and iv) the absence of the LiN_3 compound's synthesis.[8,9] Based on these calculations, both the LiN and the LiN_2 compounds are expected to be stable from ambient conditions up to at least 100 GPa. One calculation predicts LiN_3 stable from 49 GPa and LiN_5 from 15 GPa[9] while in the second calculation LiN_3 and LiN_5 sit on the convex hull from 8.5 and 9.9 GPa,[8] respectively. So within the pressure uncertainty of these calculations, it can be expected that both LiN and LiN_2 should become stable on the enthalpy convex hull at very similar pressures; lower than the pressures at which LiN_3 and LiN_5 should be favored. Moreover, LiN_5 should become stable at a pressure very close or lower to that of LiN_3. Here, taking into account the fact that the experiments were performed with lithium embedded largely in excess of nitrogen, thermodynamics will always favor the synthesis of the *nitrogen-richest stable compound* at any given pressure. Henceforth, when laser-heating Li_3N at 10.5 GPa, the formation of LiN_2 is detected as it is thermodynamically preferred over LiN, which was reported to be stable from 9.0 GPa.[16] With the same logic, it is not surprising that LiN_3 was not observed as its pressure stability domain overlaps with that of LiN_5. This explanation justifies why the synthesis of the LiN compound occurs solely in nitrogen-deprived areas of the sample cavity and usually as a minority phase. Thus, the experiments presented here determined that the following series of compounds are to be the stable series of pressure-induced chemical reactions occurring when nitrogen atoms vastly outnumber lithium atoms: Li_3N, LiN_2 and LiN_5. It is important to note that when a mixture of phases is obtained, the phases produced in the bulk of the Li piece are not considered as the nitrogen-richest stable phase on the convex hull. Instead, the nitrogen-richest stable phase on the convex hull at a given pressure is the one observed at the Li-N_2 interface, where the synthesized phases are not significantly dependent on the nitrogen diffusion.

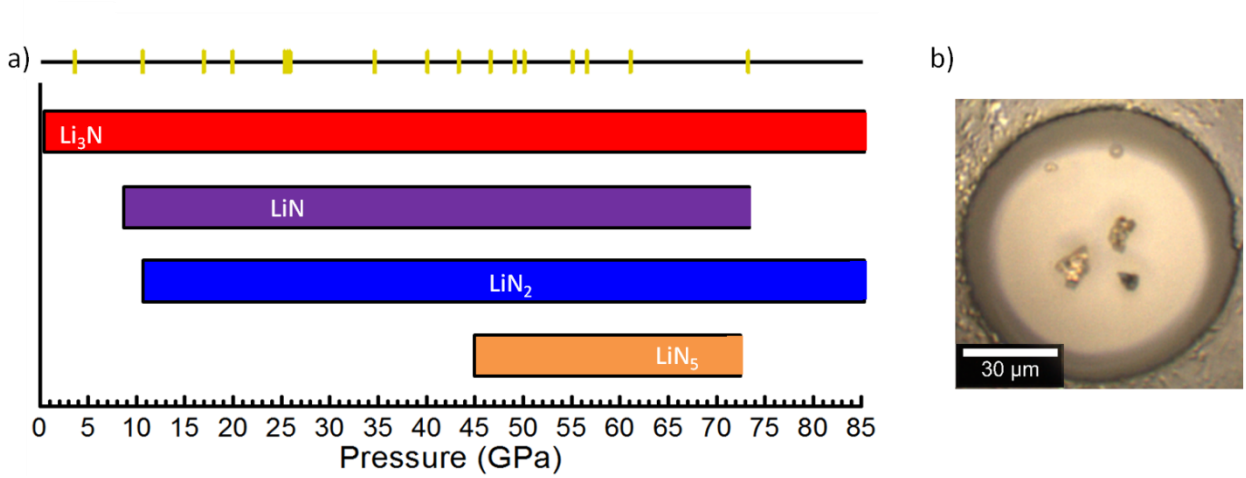

Figure 2: a) Schematic representation of the pressure stability of the Li_3N, LiN, LiN_2 and LiN_5 compounds. The yellow vertical ticks on the horizontal line above the graph indicate the pressure at which laser-heating was performed. An open-ended rectangle means that the compound was not studied above that pressure and thus it is unknown whether or not the phase is still stable. In the case of the Li_3N and LiN compounds, literature data were also used to draw their stability domain.[13,16] b) Microphotograph of a typical Li-N_2 sample after loading. In the center, three small lithium pieces are embedded in a much greater quantity of molecular nitrogen. A small ruby microchip and gold micrograin are visible in the upper portions of the experimental cavity.

In the next sections, Raman spectroscopy measurements and the X-ray diffraction characterization of the Li_3N, LiN and LiN_2 compounds are presented. Experimental data on the lithium pentazolate has previously been reported.[17]

Characterization of the Li-N compounds

Lithium nitride Li_3N

The Li_3N compound has been the subject of extensive X-ray diffraction studies, covering the pressure range of ambient up to 200 GPa.[13,14] However, to the best of our knowledge, only the vibrational modes of α-Li_3N, phase stable up to 0.6 GPa have previously been reported.[26] Here, Raman spectroscopy measurements of β-Li_3N were performed for the first time and are shown up to 39.1 GPa. From its known hexagonal structure ($P6_3/mmc$),[12] group theory predicts a total of five Raman active modes: $\Gamma_{vib} = A_{1g} + 3E_{2g} + E_{1g}$. As seen in Figure 3, four Raman modes – an amount consistent with its structure – could be followed from 3.5 to 39.1 GPa. At the lowest pressure, the four detected vibrational modes of β-Li_3N are close in frequency to those measured from α-Li_3N at ambient conditions.[26] Since the α to β phase transition is of martensitic type, where a simple shift of all Li atoms in α-Li_3N along its *c*-axis results in the β-Li_3N structure,[12] the resemblance in the vibrational mode frequencies is expected. As pressure was increased, the Raman peaks of Li_3N increase smoothly and continuously in frequency. The β → γ phase transition, reported to occur between 35 and 45 GPa, was not detected by the Raman spectroscopy measurements. X-ray diffraction measurements were also performed on the Li_3N samples from 20 to about 62 GPa, reproducing previously published results in terms of structure ($P6_3/mmc$) and equation of state data.[13,14]

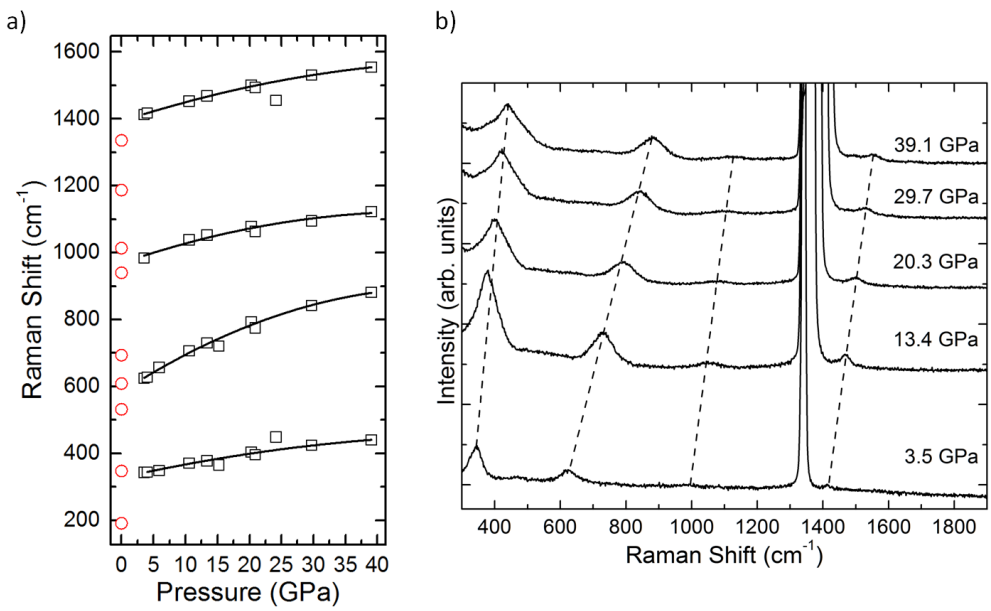

Figure 3: Evolution of β-Li_3N Raman modes with pressure. a) The empty black squares and red circles represent our measurements on β-Li_3N and those of α-Li_3N reproduced from Ref. [26], respectively. The full black lines are guides to the eye. b) Raman spectra of β-Li_3N from 3.5 to 39.1 GPa, offsetted for clarity. The dashed black lines are guides to the eye. The smooth evolution of the detected vibrational modes indicates no phase transition.

Dilithium diazenide LiN

Laser-heating of a Li-N mixture between 25.2 and 73.6 GPa in a nitrogen-deprived environment was observed to result in the synthesis of a novel solid. At 73.6 GPa, the diffraction lines attributed to this new compound were found to be perfectly fitted by an orthorhombic unit cell (*Cmcm* space group), with lattice parameters of a = 3.819(1) Å, b = 6.471(1) Å and c = 3.446(1) Å (V = 85.16(2) $Å^3$). As shown in Figure 4, the good powder quality permitted a Rietveld refinement to be performed and so revealed the atomic positions as well as the compound's stoichiometry. Lithium atoms were determined to occupy two *4c* Wyckoff positions (with y = -0.395(1) and y = -0.811(1)) and the nitrogen atoms were resolved to be sitting on the *8g* sites (x = 0.327(1) and y = -0.612(1)), thus yielding the LiN stoichiometry. In this crystalline arrangement, shown in Figure 4, nitrogen atoms form dimers perfectly aligned along the *a*-axis and may be seen as encircled by four zigzagging Li chains. At 73.6 GPa, the shortest Li-Li distance is 1.986 Å and the N_2 dimers have an intramolecular distance of 1.320 Å. The first shell of Li atoms are at distances varying between 1.792-1.911 Å from an N atom. Regarding the nature of the N-N bond order, it is proposed to be between one and two, albeit much closer to the latter, based on the expected length of a triple (~1.1 Å),[27] double (~1.2-1.3 Å)[16,28,29] and single bond (~1.4 Å).[27] This bond order was expected from the compound's stoichiometry: composed of two lithium atoms that are each susceptible to transfer close to a single electron, a $(N_2)^{\sim 2-}$ charged nitrogen dimer is thus produced. Having an extra electron, nitrogen atoms are no longer compelled to form a triple bond but instead are satisfied with a double bond, as in accordance with diazenide as well as pernitride compounds.[30–36] As previous calculations have shown that lithium atoms do not transfer exactly one electron each,[9] Bader charge calculations could provide a better idea of the charge transferred from the lithium atoms to the nitrogen dimers and thus help narrow down the exact nature of the N_2 bonding in LiN.

The structure proposed for *Cmcm* LiN is very similar to its low pressure phase, *Immm* LiN which was never observed during our experiments.[16] The latter also contains N_2 dimers surrounded by four lithium chains, this time perfectly straight. The N-N bond length measured here and its bond order assignment are in agreement with the values determined from *Immm* LiN where a double bond was suggested for the N_2 dimer, found to have an intramolecular distance of 1.301(3) Å at ambient pressure.[16] The slight increase in N-N distances in *Cmcm* LiN is expected since the lithium atoms in *Cmcm* LiN are forced to become closer to the nitrogen atoms than in *Immm* LiN (between 2.056-2.180 Å) while conserving the same coordination of eight per N_2. In turn, lithium atoms are expected to transfer a larger electronic density to the N pairs, leading to the increase of their intramolecular distance. This phenomenon is observed in other compounds containing charged nitrogen dimers, such as diazenides and pernitrides.[33,36–39]

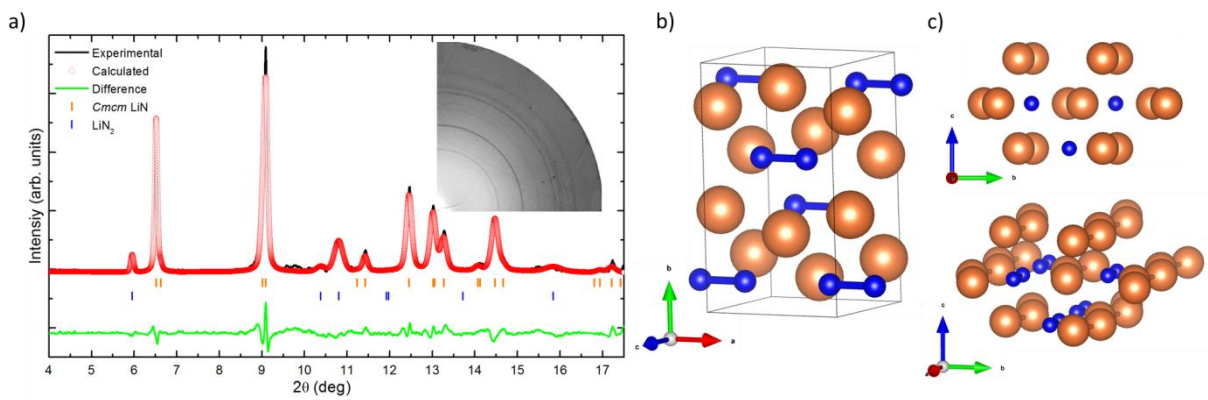

Figure 4: a) Le Bail refinement of an integrated X-ray diffraction pattern obtained from a sample at 73.6 GPa, after laser-heating. The X-ray diffraction pattern, retrieved from the same sample as the one partially composed of LiN_5 in Figure 1, was taken in the bulk of the Li piece, whereas the ones shown in Figure 1 were obtained at its edges, where a mixture of LiN, LiN_2, LiN_5 and pure N_2 is found. The Li_2N_2 compound, with a stoichiometry of LiN, was determined to have an orthorhombic (*Cmcm*) lattice with parameters of a = 3.819(1) Å, b = 6.471(1) Å and c = 3.446(1) Å, giving a volume of V = 85.16(2) Å^3. The reliability factors for the refinement are χ^2 = 1.497, R_p = 22.8%, R_{wp} = 32.5% and R_{exp} = 26.5%. b) Structure of *Cmcm* LiN, c) highlighting the four zigzagging lithium chains surrounding the N_2 dimers.

The synthesis of *Cmcm* LiN is also in agreement with calculations. The LiN stoichiometry appears stable on the enthalpy convex hull from ambient pressure up to 100 GPa.[8,9] The *Cmcm* structure is predicted above 45 GPa but three similar crystalline arrangements are expected more stable at lower pressures. The structure reported here is in perfect agreement with the one proposed by the calculations for *Cmcm* LiN (see Table 2), which anticipate the compound to be metallic, albeit a poor metal as it contains a low electron density at its Fermi energy. This is compatible with a detectable Raman signal, as shown below, particularly since DFT calculations tend to underestimate the electronic gap.

Table 2: Comparison between the experimentally and theoretically obtained atomic positions of the LiN (*Cmcm*) compound. The experimentally determined lattice parameters are of a = 3.819(1) Å, b = 6.471(1) Å and c = 3.446(1) Å (V = 85.16(2) Å^3) at 73.6 GPa, while the theoretically determined lattice parameters are of a = 3.73950 Å, b = 6.36610 Å and c = 3.35050 Å (V = 79.7621 Å^3) at 100 GPa. The theoretical calculations do not provide the lattice parameter of *Cmcm* LiN at a lower pressure.

LiN	Li1 (0,y,0.25)	Li2 (0,y,0.25)	N (x,y,0.25)
Experiment (73.6 GPa)	-0.395(1)	-0.811(1)	x=0.327(1); y=-0.612(1)

Theory (100 GPa)	-0.39946	-0.82072	x=0.33284; y=-0.61220

The structure of the *Cmcm* LiN compound was followed by powder X-ray diffraction between 19.0 and 73.6 GPa. Seven to nine X-ray diffraction lines could be followed in that pressure range and the smooth and continuous 2θ shifts with pressure indicate no obvious structural transition (see Figure 5). The lattice volume evolution with pressure is well fitted by a third order Birch-Murnaghan equation of state with the following parameters: K_0 = 112(19) GPa, K_0' = 3.2(4) and V_0 = 123(2) Å^3. The determined bulk modulus is much larger than those measured in pure Li (11.3 GPa),[40] ε-N_2 (2.98 GPa)[41] as well as β-Li_3N (74 GPa), γ-Li_3N (78 GPa)[13,14] and LiN_3 (19.1 GPa).[15] Similarly with transition metal-nitrides compounds, the low bond order of the N_2 dimer is proposed to be responsible for *Cmcm* LiN high bulk modulus.[36,42,43] This phenomenon is explained by the filling of the N_2 molecular antibonding $1\pi_g$* states which results in both the elongation of the N-N bond and an increased repulsion between the two N atoms, leading to a higher bulk modulus.[38,44] This assumption could be verified by performing crystal orbital Hamilton population (COHP) computations[38,45] as other parameters are also known to come into play, such as the atoms' coordination, the bond's length and the overall iono-covalency of the material.[46]

The *Cmcm* phase was observed as (meta)stable down to 19.0 GPa on decompression. At 14.5 GPa, the decompressed LiN samples produce broad diffraction lines and, combined with the multitude of diffraction lines produced by the δ'-N_2 phase (stable below 16 GPa),[47] the *Cmcm* LiN lattice could no longer be extracted

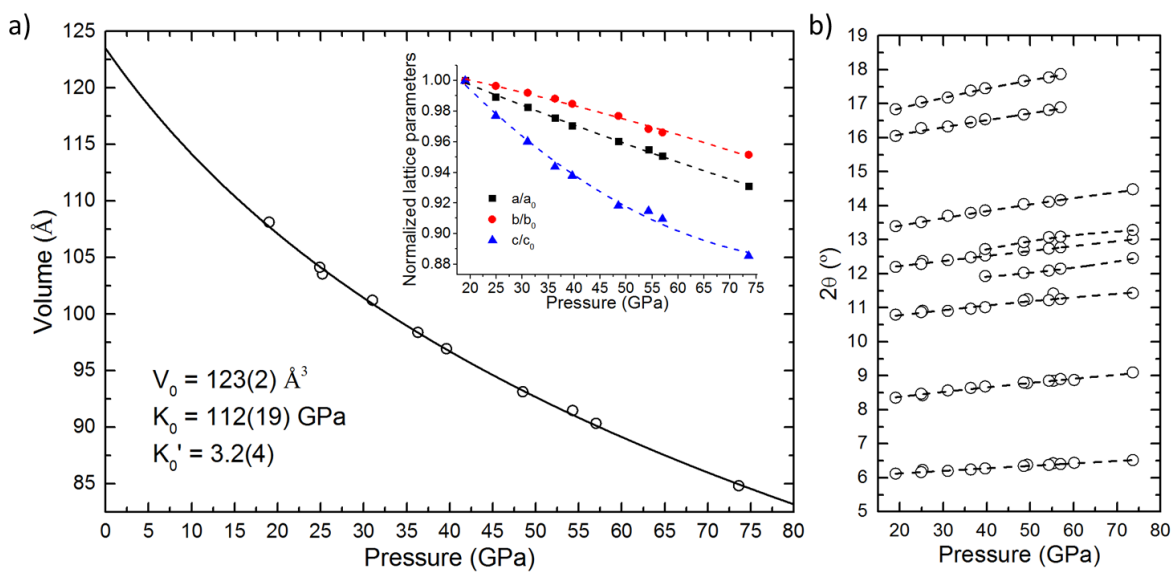

Figure 5: a) Unit cell volume of orthorhombic *Cmcm* LiN as function of pressure. The data points were fitted with a third order Birch-Murnaghan equation of state using V_0 = 123(2) Å^3, K_0 = 112(19) GPa and K_0' = 3.2(4) values, drawn as a full black line. b) Evolution of the LiN compound diffraction lines 2θ values with respect to pressure.

From group theory analysis, *Cmcm* LiN is expected to have twelve Raman active modes as $\Gamma_{vib} = 4A_g + 4B_{1g} + B_{2g} + 3B_{3g}$. Seven of those were detected, including three intense peaks at frequencies between 900 and 1200 cm^{-1} and four much weaker ones, with three of these below 800 cm^{-1} and the other near 1670 cm^{-1} (see Figure 6). The three principal vibrons are at frequencies typically assigned to the

stretching mode of N_2 molecules with a bond order between one and two, as a triple-, double- and single-bonded nitrogen dimers usually have a frequency of 2400 cm^{-1}, 1300-1550 cm^{-1} and 700-850 cm^{-1}, respectively, at ambient conditions.[16,28,29,32,38,48–50] This N-N bond order is consistent with the assignment proposed based on the crystalline structure of *Cmcm* LiN. Upon the decompression of the *Cmcm* LiN compound produced from sample laser-heating above 45 GPa, a decrease in the vibrational modes' intensity along with a broadening is observed from 33.3 GPa. As seen from Figure 6, at 22.4 GPa the vibrational modes become difficult to identify. By 16.7 GPa, they are completely gone. As the LiN stoichiometry (in the *Immm* arrangement) was reported stable down to ambient conditions,[16] a chemical decomposition of LiN is deemed improbable. This is further supported by the lack of appearance of new Raman modes indicative of another Li-N compound. Hence, to explain this phenomenon a sluggish structural phase transition from *Cmcm* towards one of the predicted low pressure structures of LiN is proposed. Indeed, these other phases were calculated to be better metals than *Cmcm*, which could account for the progressive disappearance of the Raman modes. This corroborates with the X-ray diffraction investigations from which the *Cmcm* lattice could no longer be observed below 19.0 GPa, and no new unidentified peaks were detected. This could indicate that, perhaps due to the dragging phase transition, the new phase is poorly crystallize or even amorphous.

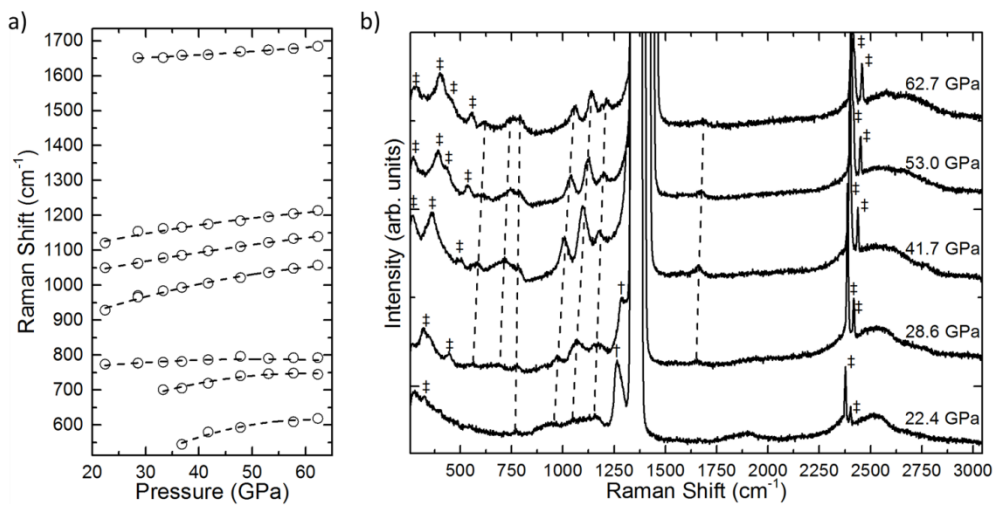

Figure 6: a) Evolution of the main Raman modes of the LiN compound with pressure. b) Cascade of selected spectra, where the ‡ and † symbols marks peaks from pure N_2 and LiN_5, respectively. The intense mode around 1350 cm^{-1} as well as the broad peak at 2550 cm^{-1} are diamond's the first and second order Raman modes. The dashed black lines are guides to the eye.

Lithium diazenide LiN_2

When heating the β-Li_3N compound at pressures above 10.5 GPa, new diffraction lines appear and the laser-heated portion of the solid visually changes from dark opaque to shiny white (see Figure 7). The diffraction lines of the synthesized compound are best fitted by a hexagonal ($P6_3/mmc$) structure with lattice parameters of a = 2.631(1) Å and c = 7.615(1) Å at 21.2 GPa. As shown in Figure 7, a Rietveld refinement could be performed on an integrated X-ray diffraction pattern. The Li and N atoms were resolved to sit on the 2a and 4f (z = 0.827(1)) Wyckoff positions, respectively, thus corresponding to a LiN_2 stoichiometry. Similarly to the LiN compound, the nitrogen atoms are arranged in pairs, forming N_2

dimers parallel to the *c*-axis. The structure adopted by LiN_2 is akin to the NiAs-type structure, where the N_2 molecule center of mass and the Li atom occupy the position of the As anion and Ni cation, respectively. The lithium atoms as well as the N_2 dimers are in a six-fold coordination, with the former in an octahedral site while the latter are in a trigonal prismatic coordination due to the *hcp* packing.

The N-N atoms forming the nitrogen dimers are at a distance of 1.197 Å. Comparison to N-N distances in compounds with dimers of known bond order allows the assignment of a double-bond, albeit this time closer to the triple-bond rather than the single-bond. Again, this was expected based on purely stoichiometric considerations: with a single lithium atom per nitrogen pair, an electron charge transfer of about one is expected, yielding $(N_2)^{\sim 1-}$, which corresponds to a bond order close to 2.5. In turn, this provides an explanation for the shorter N-N distance in LiN_2 compared to LiN. Again, Bader charge calculations are encouraged to finely pinpoint the bond order.

The determined hexagonal LiN_2 structure matches the one theoretically predicted for this stoichiometry (see Table 3).[8,9] According to these calculations, hexagonal LiN_2 is expected to be a good metal; i.e. with a significant electronic density at the Fermi energy. This is in agreement with the optical properties of the synthesized LiN_2 compound as well as its lack of measurable Raman activity.

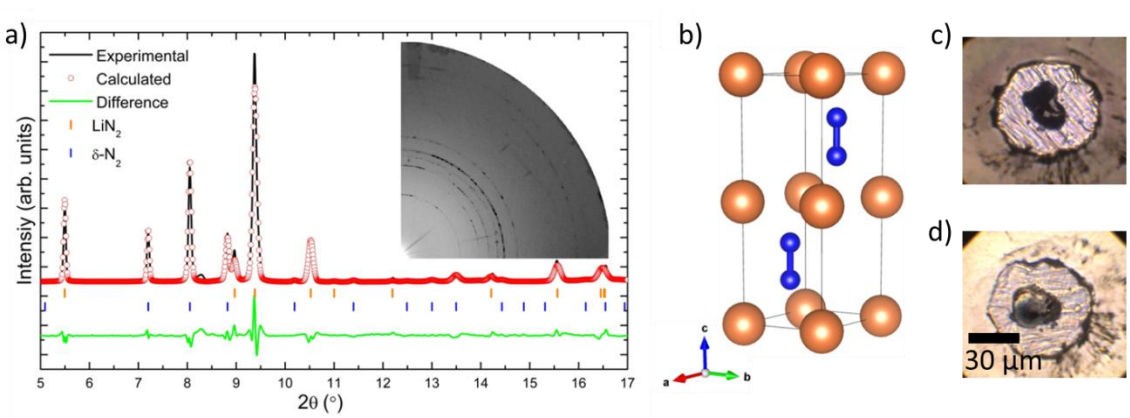

Figure 7: Crystallographic determination of the LiN_2 compound. (a) Rietveld refinement of an integrated X-ray diffraction pattern of LiN_2 synthesized at 20 GPa and decompressed down to 9.6 GPa. The reliability factors for the refinement are $\chi^2 = 3.77$, $R_p = 21.4\%$, $R_{wp} = 32.5\%$, $R_{exp} = 16.8\%$, $R_{Bragg} = 5.41\%$ and $R_f = 8.94\%$. (Inset) The image plate used for the Rietveld refinement. (b) Crystallographic structure of hexagonal $P6_3/mmc$ LiN_2. Microphotographs of a Li_3N sample before c) and after d) laser-heating. After laser-heating, LiN_2 is produced. Its visual properties are different from those of Li_3N, as it is mostly shiny white.

Table 3: Comparison between the experimentally and theoretically obtained structural parameters of the LiN_2 ($P6_3/mmc$) compound. The Wyckoff position of the Li atom (*2a*) does not have free parameters and was thus not included in the table. The N atom is on the *4f* Wyckoff site.

LiN_2	*a* (Å)	*c* (Å)	*V* (Å)	N (-1/3, 2/3, z)
Experiment (21.2 GPa)	2.631(1)	7.615(1)	45.64(2)	0.827(1)
Theory (20 GPa)	2.64010	7.62530	46.0287	0.82630

The diffraction lines belonging to the hexagonal LiN_2 lattice could be followed from 4.6 GPa up to 82.5 GPa. As shown in Figure 8, the evolution of the unit cell volume with pressure was fitted with a third order Birch-Murnaghan equation of state. The ambient pressure bulk modulus along with its

pressure derivative was determined to be of K_0 = 63(4) GPa and K_0' = 3.9(4), respectively, with a fitted ambient conditions volume of V_0 = 57(2) Å^3. This volume is in good agreement with the theoretical volume of hexagonal LiN_2, calculated to be of 57.72 Å^3 at ambient pressure.[9] The obtained K_0 is much larger than the one measured in the pure phases but about half of the bulk modulus of *Cmcm* LiN. The difference between the two phases may originate from the higher bond order of the N_2 molecules and the shorter N-N bond length found in LiN_2. This implies a lower electron density in antibonding states and thus less Coulomb repulsion between the nitrogen atoms. Again, the numerical computation of COHP would have to be performed to validate this interpretation.

According to theoretical calculations, hexagonal LiN_2 was expected to undergo a phase transition into a (*P*-1) monoclinic lattice with extended nitrogen chains at 60 GPa.[8,9] No sign of such a phase transition was noticed up to 83 GPa.

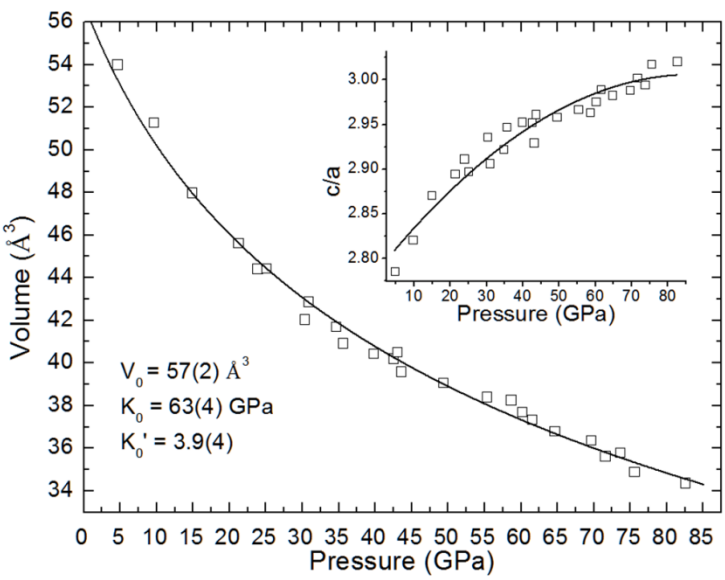

Figure 8: Unit cell volume of hexagonal LiN_2 in function of pressure. The data points were fitted with a third order Birch-Murnaghan equation of state using V_0 = 57(2) Å^3, K_0 = 63(4) GPa and K_0' = 3.9(4) values, drawn as a full black line. (Inset) The *c*/*a* evolution of the LiN_2 hexagonal lattice with pressure. The *c*-axis is found to be less compressible than the *a*-axis.

Conclusion

The nitrogen-rich portion of the Li-N binary phase diagram at high pressure was investigated by compressing lithium pieces embedded in a much greater quantity of nitrogen. A total of four compounds with different stoichiometries were synthesized, namely Li_3N, LiN, LiN_2 and LiN_5. The stability domain of each solid was determined. The high pressure phases *Cmcm* LiN and $P6_3/mmc$ LiN_2 were characterized for the first time. As with other compounds containing charged nitrogen dimers, a correlation between a low N_2 bond order and a low compressibility was established. Interestingly, the Li-N chemistry seems to be dictated by lithium's electronic charge transfer. Indeed, a direct correlation between the extra charge per nitrogen atom (dependant on the compound's stoichiometry) and the number of bonded nitrogen

atoms is found. In the Li_3N solid, there is an extra 3 e^- per N atom which results in an atomic arrangement of nitrogen. For the LiN and LiN_2 solids, where there is a 1 e^- per N and 0.5 e^- per N charged dimers are instead preferred. At still lower charge per nitrogen, the lithium atoms are found to stabilize a N_3^- chain in LiN_3 (-1/3 e^- per N). Finally, at a 0.2 e^- per N atom, the pentazolate anion is formed in LiN_5. These results suggest that, in the case of the Li-N_2 system, longer nitrogen arrangements are favored by a small electron density transfer.The discovery of various stable compounds in Li-N system under pressure illustrates that nitrogen rich nitrides in metal-N systems is a particularly compelling class of materials to be explored at high pressure.

Acknowledgements

The authors gratefully acknowledge the Centre National d'Études Spatiales (CNES) and the Natural Sciences and Engineering Research Council of Canada (NSERC) for financially supporting the Ph.D. of D.L. The authors also acknowledge the European Synchrotron Radiation Facility (ESRF) for provision of beamtime at the ID27 beamline under proposal HC-3387. We wish to thank G. Garbarino, V. Svitlyk, and M. Mezouar for their help with the X-ray diffraction experiments.

References

(1) Dönges, E. Alkali Metals. In *Handbook of preparative inorgative chemistry*; Brauer, G., Ed.; Academic Press: London, 1963; Vol. 1, p 984.

(2) Rabenau, A. Lithium Nitride and Related Materials Case Study of the Use of Modern Solid State Research Techniques. *Solid State Ionics* **1982**, *6* (4), 277–293.

(3) Shodai, T.; Okada, S.; Tobishima, S.; Yamaki, J. Anode Performance of a New Layered Nitride Li3_ CoxN (x = 0.2-0.6). *J. Power Sources* **1997**, *68*, 515–518.

(4) Sun, Y.; Li, Y.; Sun, J.; Li, Y.; Pei, A.; Cui, Y. Stabilized Li3N for Efficient Battery Cathode Prelithiation. *Energy Storage Mater.* **2017**, *6*, 119–124.

(5) Chen, P.; Xiong, Z.; Luo, J.; Lin, J.; Lee Tan, K. Interaction of Hydrogen with Metal Nitrides and Imides. *Nature* **2002**, *420* (6913), 302–304.

(6) O'Loughlin, J. L.; Wallace, C. H.; Knox, M. S.; Kaner, R. B. Rapid Solid-State Synthesis of Tantalum, Chromium, and Molybdenum Nitrides. *Inorg. Chem.* **2001**, *40* (10), 2240–2245.

(7) Fair, H. D.; Walker, R. F. *Energetic Materials*; Plenum Press: New York, 1977.

(8) Peng, F.; Yao, Y.; Liu, H.; Ma, Y. Crystalline LiN5 Predicted from First-Principles as a Possible High-Energy Material. *J. Phys. Chem. Lett.* **2015**, *6*, 2363–2366.

(9) Shen, Y.; Oganov, A. R.; Qian, G.; Dong, H.; Zhu, Q.; Zhou, Z. Novel Lithium-Nitrogen Compounds at Ambient and High Pressures. *Sci. Rep.* **2015**, *5* (14204), 1–8.

(10) Prasad, D. L. V. K.; Ashcroft, N. W.; Hoffmann, R. Evolving Structural Diversity and Metallicity in Compressed Lithium Azide. *J. Phys. Chem. C* **2013**, *117*, 20838–20846.

(11) Zhang, M.; Yan, H.; Wei, Q.; Wang, H.; Wu, Z. Novel High-Pressure Phase with Pseudo-Benzene N6 Molecule of LiN3. *EPL* **2013**, *101* (101), 26004.

(12) Beister, H.; Haag, S.; Kniep, R.; Strössner, K.; Syassen, K. Phase Transformations of Lithium Nitride under Pressure. *Angew. Chem. Int. Ed. Engl.* **1988**, *27* (8), 1101–1103.

(13) Lazicki, A.; Maddox, B.; Evans, W. J.; Yoo, C. S.; McMahan, A. K.; Pickett, W. E.; Scalettar, R. T.; Hu, M. Y.; Chow, P. New Cubic Phase of Li3N: Stability of the N3- Ion to 200 GPa. *Phys. Rev. Lett.* **2005**, *95*, 165503.

(14) Ho, A. C.; Granger, M. K.; Ruoff, A. L.; Van Camp, P. E.; Van Doren, V. E. Experimental and Theoretical Study of Li3N at High Pressure. *Phys. Rev. B* **1999**, *59* (9), 6083–6086.

(15) Medvedev, S. A.; Trojan, I. A.; Eremets, M. I.; Palasyuk, T.; Klapötke, T. M.; Evers, J. Phase Stability of Lithium Azide at Pressures up to 60 GPa. *J. Phys. Condens. Matter* **2009**, *21* (19), 195404.

(16) Schneider, S. B.; Frankovsky, R.; Schnick, W. Lithium Diazenide High-Pressure Synthesis and Characterization of the Alkali Diazenide Li2N2. *Angew. Chem. Int. Ed.* **2012**, *51*, 1873–1875.

(17) Laniel, D.; Weck, G.; Gaiffe, G.; Garbarino, G.; Loubeyre, P. High-Pressure Synthesized Lithium Pentazolate Compound Metastable under Ambient Conditions. *J. Phys. Chem. Lett.* **2018**, *9*, 1600–1604.

(18) Takemura, K.; Dewaele, A. Isothermal Equation of State for Gold with a He-Pressure Medium. *Phys. Rev. B* **2008**, *78*, 104119.

(19) Dewaele, A.; Torrent, M.; Loubeyre, P.; Mezouar, M. Compression Curves of Transition Metals in the Mbar Range: Experiments and Projector Augmented-Wave Calculations. *Phys. Rev. B* **2008**, *78* (10), 104102.

(20) Ohta, K.; Ichimaru, K.; Einaga, M.; Kawaguchi, S.; Shimizu, K.; Matsuoka, T.; Hirao, N.; Ohishi, Y. Phase Boundary of Hot Dense Fluid Hydrogen. *Nat. Sci. Reports* **2015**, *5*, 16560.

(21) Desgreniers, S.; Lagarec, K. XRDA : A Program for Energy-Dispersive X-Ray Diffraction Analysis on a PC. *J. Appl. Crystallogr.* **1994**, *27* (3), 432–434.

(22) Prescher, C.; Prakapenka, V. B. DIOPTAS : A Program for Reduction of Two-Dimensional X-Ray Diffraction Data and Data Exploration. *High Press. Res.* **2015**, *35* (3), 223–230.

(23) Rodriguez-Carvajal, J. Recent Advances in Magnetic Structure Determination Neutron Powder Diffraction. *Phys. B Condens. Matter* **1993**, *192* (1), 55–69.

(24) Weck, G.; Datchi, F.; Garbarino, G.; Ninet, S.; Queyroux, J.-A.; Plisson, T.; Mezouar, M.; Loubeyre, P. Melting Curve and Liquid Structure of Nitrogen Probed by X-Ray Diffraction to 120 GPa. *Phys. Rev. Lett.* **2017**, *119*, 235701.

(25) Benedetti, L. R.; Loubeyre, P. Temperature Gradients, Wavelength-Dependent Emissivity, and Accuracy of High and Very-High Temperatures Measured in the Laser-Heated Diamond Cell. *High Press. Res.* **2004**, *24* (4), 423–445.

(26) Chandrasekhar, H.; Bhattacharya, G.; Migoni, R.; Bilz, H. Infrared and Raman Spectra and Lattice Dynamics of the Superionic Conductor Li3N. *Phys. Rev. B* **1978**, *17* (2), 884–893.

(27) Eremets, M. I.; Gavriliuk, A. G.; Serebryanaya, N. R.; Trojan, I. A.; Dzivenko, D. A.; Boehler, R.; Mao, H. K.; Hemley, R. J. Structural Transformation of Molecular Nitrogen to a Single-Bonded Atomic State at High Pressures. *J. Chem. Phys.* **2004**, *121* (22), 11296–11300.

(28) Schneider, S. B.; Frankovsky, R.; Schnick, W. Synthesis of Alkaline Earth Diazenides MAEN2 (MAE = Ca, Sr, Ba) by Controlled Thermal Decomposition of Azides under High Pressure. *Inorg. Chem.* **2012**, *51* (4), 2366–2373.

(29) Auffermann, G.; Prots, Y.; Kniep., R. SrN and SrN 2 : Diazenides by Synthesis Under. *Angew. Chemie Int. Ed.* **2001**, *40* (3), 547–549.

(30) Young, A. F.; Sanloup, C.; Gregoryanz, E.; Scandolo, S.; Hemley, R. J.; Mao, H. K. Synthesis of Novel Transition Metal Nitrides IrN2 and OsN2. *Phys. Rev. Lett.* **2006**, *96*, 155501.

(31) Crowhurst, J. C.; Goncharov, A. F.; Sadigh, B.; Evans, C. L.; Morrall, P. G.; Ferreira, J. L.; Nelson, A. J. Synthesis and Characterization of the Nitrides of Platinum and Iridium. *Science* **2006**, *311*.

(32) Crowhurst, J. C.; Goncharov, A. F.; Sadigh, B.; Zaug, J. M.; Aberg, D.; Meng, Y.; Prakapenka, V. B. Synthesis and Characterization of Nitrides of Iridium and Palladium. *J. Mater. Res.* **2008**, *23* (01), 1–5.

(33) Niwa, K.; Dzivenko, D.; Suzuki, K.; Riedel, R.; Troyan, I.; Eremets, M.; Hasegawa, M. High Pressure Synthesis of Marcasite-Type Rhodium Pernitride. *Inorg. Chem.* **2014**, *53* (2), 697–699.

(34) Niwa, K.; Suzuki, K.; Muto, S.; Tatsumi, K.; Soda, K.; Kikegawa, T.; Hasegawa, M. Discovery of the Last Remaining Binary Platinum-Group Pernitride RuN2. *Chem. Eur. J.* **2014**, *20* (43), 13885–13888.

(35) Niwa, K.; Terabe, T.; Kato, D.; Takayama, S.; Kato, M.; Soda, K.; Hasegawa, M. Highly Coordinated Iron and Cobalt Nitrides Synthesized at High Pressures and High Temperatures. *Inorg. Chem.* **2017**, *56*, 6410–6418.

(36) Bhadram, V. S.; Kim, D. Y.; Strobel, T. A. High-Pressure Synthesis and Characterization of Incompressible Titanium Pernitride. *Chem. Mater.* **2016**, *28* (6), 1616–1620.

(37) Laniel, D.; Dewaele, A.; Garbarino, G. High Pressure and High Temperature Synthesis of the Iron Pernitride FeN 2. *Inorg. Chem.* **2018**, *57* (11), 6245–6251.

(38) Wessel, M.; Dronskowski, R. Nature of N-N Bonding within High-Pressure Noble-Metal Pernitrides and the Prediction of Lanthanum Pernitride. *J. Am. Chem. Soc.* **2010**, *132*, 2421–2429.

(39) Niwa, K.; Ogasawara, H.; Hasegawa, M. Pyrite Form of Group-14 Element Pernitrides Synthesized at High Pressure and High Temperature. *Dalt. Trans.* **2017**, *46*, 9750–9754.

(40) Hanfland, M.; Loa, I.; Syassen, K.; Schwarz, U.; Takemura, K. Equation of State of Lithium to 21 GPa. *Solid State Commun.* **1999**, *112*, 123–127.

(41) Olijnyk, H. High Pressure X-Ray Diffraction Studies on Solid N2 up to 43.9 GPa. *J. Chem. Phys.* **1990**, *93* (12), 8968.

(42) Laniel, D.; Dewaele, A.; Anzellini, S.; Guignot, N. Study of the Iron Nitride FeN into the Megabar Regime. *J. Alloys Compd.* **2018**, *733*, 53–58.

(43) Gregoryanz, E.; Sanloup, C.; Somayazulu, M.; Badro, J.; Fiquet, G.; Mao, H.; Hemley, R. J. Synthesis and Characterization of a Binary Noble Metal Nitride. *Nat. Mater.* **2004**, *3* (5), 294–297.

(44) Zhang, M.; Cheng, K.; Yan, H.; Wei, Q.; Zheng, B. Electronic Bonding Analyses and Mechanical Strengths of Incompressible Tetragonal Transition Metal Dinitrides TMN2 (TM = Ti, Zr, and Hf). *Sci. Rep.* **2016**, *6* (1), 36911.

(45) Dronskowski, R.; Blöchl, P. E. Crystal Orbital Hamilton Populations (COHP). Energy-Resolved Visualization of Chemical Bonding in Solids Based on Density-Functional Calculations. *J. Phys. Chem.* **1993**, *97*, 8617–8624.

(46) Xu, B.; Wang, Q.; Tian, Y. Bulk Modulus for Polar Covalent Crystals. *Sci. Rep.* **2013**, *3* (1), 3068.

(47) Stinton, G. W.; Loa, I.; Lundegaard, L. F.; McMahon, M. I. The Crystal Structures of δ and δ Nitrogen. *J. Chem. Phys.* **2009**, *131* (10), 104511.

(48) Eremets, M. I.; Gavriliuk, A. G.; Trojan, I. A.; Dzivenko, D. A.; Boehler, R. Single-Bonded Cubic Form of Nitrogen. *Nat. Mater.* **2004**, *3*, 558–563.

(49) Schneider, H.; Häfner, W.; Wokaun, A.; Olijnyk, H. Room Temperature Raman Scattering Studies of External and Internal Modes of Solid Nitrogen at Pressures 8≤P≤54 GPa. *J. Chem. Phys.* **1992**, *96* (11), 8046.

(50) Young, A. F.; Montoya, J. A.; Sanloup, C.; Lazzeri, M.; Gregoryanz, E.; Scandolo, S. Interstitial Dinitrogen Makes PtN2 an Insulating Hard Solid. *Phys. Rev. B* **2006**, *73* (15), 2–5.

THE JOURNAL OF PHYSICAL CHEMISTRY Letters

Letter

Cite This: J. Phys. Chem. Lett. 2018, 9, 1600−1604

pubs.acs.org/JPCL

High-Pressure Synthesized Lithium Pentazolate Compound Metastable under Ambient Conditions

D. Laniel,[†] G. Weck,[†] G. Gaiffe,[†] G. Garbarino,[‡] and P. Loubeyre*,[†]

[†]CEA, DAM, DIF, F-91297 Arpajon, France

[‡]European Synchrotron Radiation Facility, 6 Rue Jules Horowitz BP220, F-38043 Grenoble CEDEX, France

Supporting Information

ABSTRACT: Polynitrogen compounds have been actively pursued driven by their potential as ultra-high-performing propellants or explosives. Despite remarkable breakthroughs over the past two decades, the two figures of merit for a compelling material, namely a large fraction of nitrogen by weight and a bulk stability under ambient conditions, have not yet been achieved. We report the synthesis of a lithium pentazolate solid by compressing and laser-heating lithium embedded in molecular N_2 around 45 GPa along with its recovery under ambient conditions. The observation by Raman spectroscopy of vibrational modes unique to the cyclo-N_5^- anion is the signature of the formation of LiN_5. Mass spectroscopy experiments confirm the presence of the pentazolate anion in the recovered compound. A monoclinic lattice is obtained from X-ray diffraction measurements and the volume of the LiN_5 compound under pressure is in good agreement with the theoretical calculations.

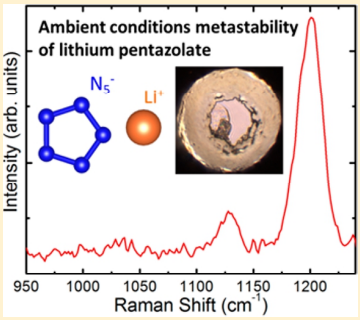

Nitrogen is unique in chemistry due to dinitrogen's triple bond being one of the strongest and its homonuclear single-bond energy being significantly less than one-third of its triple-bond or one-half of its double-bond energy. So, polynitrogens clearly are the potential top performers for storing chemical energy. Great efforts in inorganic chemistry have been devoted to stabilizing at ambient conditions higher than N_2 elemental nitrogen molecular units as building blocks for energetic materials. For the whole 20th century, only N_3^- was known, but over the past two decades other homoatomic units have been discovered, such as N_4, N_5^+, and N_5^-.[1−3] Recently, N_5^- was stabilized at ambient conditions in two types of compounds: a $(N_5)_6(H_3O)_3(NH_4)_4Cl$ salt and metal pentazolate hydrate complexes ($[Na(H_2O)(N_5)_2]\cdot 2H_2O$ and $[M(H_2O)_4(N_5)_2]\cdot 4H_2O$, M = Mn, Fe, and Co),[4−6] yet because of their low nitrogen weight ratio, these compounds are not competitive high energy density materials (HEDMs). Ideally, solely a metal cation, NH_4^+ or H^+ would be used to stabilize the N_5^- anion.

The application of pressure opens another route to stabilize polynitrogen solids with high N content. High pressure breaks the triply bonded dinitrogen molecule and various non-molecular crystalline phases of dense nitrogen have been reported.[7−9] Synthesized at 110 GPa, cubic gauche polymeric nitrogen (cg-N), a network of exclusively sp^3, single-bonded nitrogen atoms, represents the ultimate HEDM polynitrogen compound.[10] Unfortunately, cg-N reverts back to the molecular N_2 solid at 42 GPa.[7] Recent theoretical works have shown that the addition of a carefully chosen element into the nitrogen system should facilitate the pressure synthesis of polynitrogen as well as its recovery under ambient conditions.[11−19] In particular, alkali metals single-handedly allow pentazolate salts to form under pressure.[20−23] This is achieved by the transfer of an electron from these highly electropositive elements to the N_5 rings, enabling both N_5^- aromacity and their stabilization through an ionic bond. The synthesis of a NaN_5 compound was suggested upon comparison of theory and experiments,[21,24] but the first experimental confirmation came recently with the CsN_5 compound, produced at 60 GPa and metastable down to 18 GPa.[20] Interestingly, calculations predict an improved structure stability for lithium pentazolate: thermodynamically stable against decomposition above 20 GPa and mechanically stable under ambient conditions.[23,25] This solid would release an enormous amount of energy (2.72 kJ/g) upon reverting to its molecular N_2 state.[22]

Two compounds in the Li−N system, lithium nitride (Li_3N) and lithium azide (LiN_3), are known to be stable under ambient conditions and have been studied under pressure.[26−28] Below 10 GPa, Li_2N_2 was synthesized from LiN_3 and was recovered upon complete pressure release.[29] Several other Li−N solids are predicted to be stable under pressure, among which LiN_5 has the highest nitrogen fraction, but none so far have been discovered. The aim of this study was to search for the LiN_5 compound. The method here employed was to compress in a diamond anvil cell (DAC) micrometer-sized pure lithium pieces surrounded by a larger volume of molecular nitrogen, used as both a pressure-transmitting medium and reagent. Laser heating of the reactive mixture at high pressure, using pure lithium as a YLF laser absorber, helps in overcoming kinetic barriers. Five different experiments were performed with

Received: February 19, 2018
Accepted: March 13, 2018
Published: March 13, 2018

 © XXXX American Chemical Society

DOI: 10.1021/acs.jpclett.8b00540
J. Phys. Chem. Lett. 2018, 9, 1600−1604

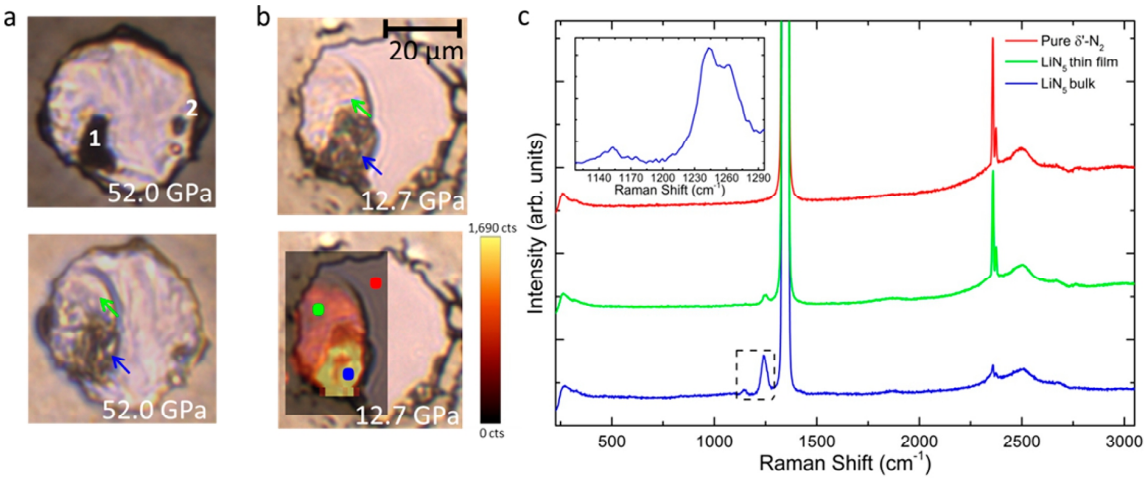

Figure 1. Microphotographs of the chemical transformation of a Li piece embedded in N_2 along with the Raman mapping of the sample chamber to spatially pinpoint the LiN_5 compound. (a) Microphotographs at 52.0 GPa before (top left) and after (bottom left) laser heating. Before heating, the numbers 1 and 2 mark the lithium piece and the pressure gauges; the ruby (below) and gold (above) microspheres. The laser-heated and transformed solid, labeled by a blue arrow, appears translucent and grew in size. A texture change is also observed in the solid nitrogen surrounding the laser-heated lithium piece, identified by a green arrow. (b) Microphotographs of the same sample at 12.7 GPa, with and without the superimposed Raman mapping (top right and bottom right, respectively). At this pressure, pure molecular nitrogen is no longer reticulated as it underwent the ε-N_2 → δ^*-N_2 phase transition. The yellow to red color scale indicates the intensity of the main N_5^- stretching Raman mode, from strong to weak, respectively. The textured, transparent area above the main LiN_5 piece is found to have the same N_5^- Raman modes. (c) Raman spectra of the different regions, color-coded according to the colored dots in the bottom right microphotograph. The spectra were obtained at 12.7 GPa. (Inset) Raman spectrum of the bulk LiN_5 obtained with a higher resolution diffraction grating (1800 lines/mm), allowing us to resolve both breathing modes of the N_5^- anion.

reproducible results. Under a few bars of N_2, lithium transforms into Li_3N (see Supporting Information, Figure S3). This insulating $3Li^+{\cdot}N^{3-}$ ionic compound was observed to form on the surface of the lithium piece, measured from both Raman spectroscopy as well as X-ray diffraction, and acted as a barrier preventing lithium diffusion into the diamond anvils. Above 45 GPa, laser heating of the lithium−nitrogen compound (either Li_3N or LiN_2, see discussion in the Supporting Information) embedded in large amounts of molecular nitrogen produced large flashes of light characteristic of changes in chemical bonding and favored the synthesis of a richer nitrogen compound stable on the Li−N enthalpy convex hull. As seen in Figure 1a, the visual observation of the sample showed clear transformations. First, the lithium piece significantly gained in size, pointing to an increase in its the nitrogen concentration. Second, the opaque lithium sample was converted to a translucent compound, suggestive of a modification in interatomic interactions. This is understood by metallic Li transforming into an insulator/semiconductor solid. Third, molecular nitrogen surrounding the lithium piece changed in texture (labeled by a green arrow in Figure 1b), becoming somewhat smoother compared with the reticulated ε-N_2 solid. Sample decompression below 16.8 GPa, pressure at which molecular nitrogen transitions from ε-N_2 to δ'-N_2 and is no longer reticulated, clearly showed this area to be of a different texture (see Figure 1b), suggesting it to no longer be solely composed of pure nitrogen.

Raman spectra of the compound synthesized above 45 GPa, as shown in Figure 1c, display new vibrational modes in the visually transformed solid: a doublet with peaks at 1239.6 and 1251.0 cm^{-1} as well as a single peak at 1148.9 cm^{-1}. These peaks can also be found, yet with lower intensity, in the textured area around the heated sample, confirming that the compound formation is favorable in a nitrogen-rich environment. These vibrational modes are clearly distinct from those of lithium nitride (Li_3N)[26] and azide (LiN_3),[28] as seen in Figure 2a, as well as of pure nitrogen, which has vibrational modes above 2300cm^{-1}.[8] On the contrary, they match those of the planar pentazolate anion, which has three Raman modes ascribed to antisymmetric breathing, symmetric breathing, and antisymmetric breathing and deformation stretching modes.[13,20,21] These have been calculated at high pressure for the theoretically predicted compounds HN_5, NaN_5, RbN_5 and, in the case of CsN_5, measured.[13,20,21,30] The pressure evolution of these Raman modes is compared in Figure 2a with those measured from the synthesized Li−N compound. The similarity in the number of vibrational modes, their frequencies, as well as their relative intensities is remarkable, suggesting the synthesis of a LiN_5 compound.[13,20] Small frequency differences observed between the values in the different pentazolate compounds can be attributed to crystal field effects. Moreover, the stability of the LiN_5 compound has recently been predicted by two independent sets of theoretical calculations above 20 GPa.[22,23] The transparency of the laser-heated sample fits the theoretically predicted large band-gap insulator nature of the LiN_5 compound, intrinsic to its ionic interactions.[22,23] Finally, a chemical reaction with the carbon of the diamond anvils can be ruled out since the same Raman modes (and X-ray diffraction lines) were measured in a run where the diamond anvils were chemically insulated from the sample by a thin (∼200 nm) Ti layer. Details of this run are provided in the Supporting Information.

The Raman modes of LiN_5 confined in the DAC were followed down to a pressure of 0.5 GPa. Upon decompression, the LiN_5 solid became increasingly sensitive to the heat generated by the Raman excitation laser (648 nm) and, below 5.7 GPa, a few milliwatts of laser power along with long exposures (>30s) were employed. To check if the solid was

DOI: 10.1021/acs.jpclett.8b00540
J. Phys. Chem. Lett. 2018, 9, 1600−1604

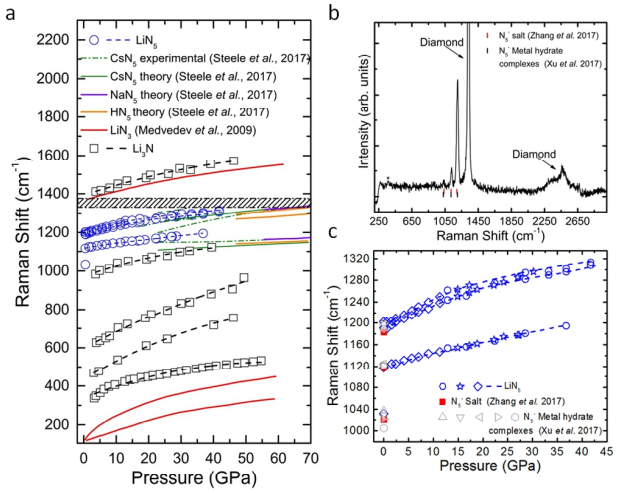

Figure 2. LiN_5 Raman modes from over 40 GPa down to ambient conditions. (a) Evolution of the LiN_5 compound Raman breathing and stretching modes during decompression, along with those of Li_3N and LiN_3.[28] The dashed lines are guides to the eye. The shaded gray area indicates the frequency domain of the intense Raman mode of the diamond anvils. (b) Raman spectra of the LiN_5 solid under ambient conditions after opening and closing the DAC in a glovebox, allowing molecular nitrogen to be released. The intense first-order Raman mode of the diamond anvils is observed near ~1350 cm^{-1}, while the large second-order mode is detected from 2160 to 2685 cm^{-1}. The tick marks represent the vibrational modes of the pentazolate salt and the $[Mg(H_2O)_6(N_5)_2]\cdot 4H_2O$ pentazolate metal complex.[4,5] The asterisk marks a faint lattice mode of the LiN_5 compound. (c) Enlargement of the evolution of the LiN_5 Raman mode frequencies with pressure; different symbols correspond to distinct experimental runs. The data obtained in the pentazolate salt and the metal pentazolate hydrate complexes are also reported.[4,5] Not shown in this Figure, these other compounds have additional Raman modes at lower frequencies that are very weak in intensity.

stable at ambient pressure, the DAC was opened in a glovebox under an argon atmosphere, releasing gaseous molecular N_2, and was then hand-closed. As shown in Figure 2b, under room conditions the breathing and stretching N_5^- Raman modes could still be measured, along with a newly observed low-intensity peak at 1035 cm^{-1}. The comparison of all the modes detected from the LiN_5 compound under ambient conditions with those from the $(N_5)_6(H_3O)_3(NH_4)_4Cl$ salt and the various metal pentazolate hydrate complexes, as seen from Figure 2c, gives a perfect match and thus confirms the synthesis of the pentazolate anion.[4−6] Furthermore, a faint low frequency peak (364 cm^{-1}) was observed from one of the samples retrieved at ambient conditions, with molecular nitrogen released. This mode could be attributed to a lattice mode of LiN_5, as that frequency matches well with the intense Raman mode expected and measured from other high-pressure synthesized pentazolate compounds.[13,20,31] This weak peak was not observed from many other samples as most heated Li pieces resulted in amorphous and poorly crystallized LiN_5 solids, thus with undetectable (or barely detectable) lattice modes. This is corroborated by the lack of X-ray diffraction signal from these samples, as detailed below. Moreover, the LiN_5 Raman modes were always measured in concert with those of pure N_2, as the former is necessarily produced in a nitrogen-rich area. Since solid nitrogen also has measurable lattice modes above 16 GPa and, because of the much greater quantity of nitrogen over that of LiN_5, they could overlap and prohibit the detection of those from LiN_5. Exposing the LiN_5 compound to air provoked its decomposition because its Raman signal could no longer be detected.

Mass spectroscopy measurements were performed to provide further evidence of the synthesis and retrievability under ambient conditions of the pentazolate anion. The very small quantities as well as the reactivity to air of LiN_5 constrained the selection of a suitable technique. Flow injection analysis (FIA) electrospray ionization mass spectrometry (ESI−MS) was deemed appropriate and was employed. Methanol was chosen as the solvent since it had previously been shown to readily dissolve the pentazolate anion.[5] The data were analyzed following procedures specifically designed for FIA with extremely small sample quantities injected along with unknown impurities.[32] In such cases, the ion current integrated over the sought-for m/z ratio with respect to time (before, during, and after sample injection) is plotted. Two LiN_5 samples recovered under ambient conditions were dissolved in methanol and injected in the mass spectrometer. Figure 3 shows the extracted

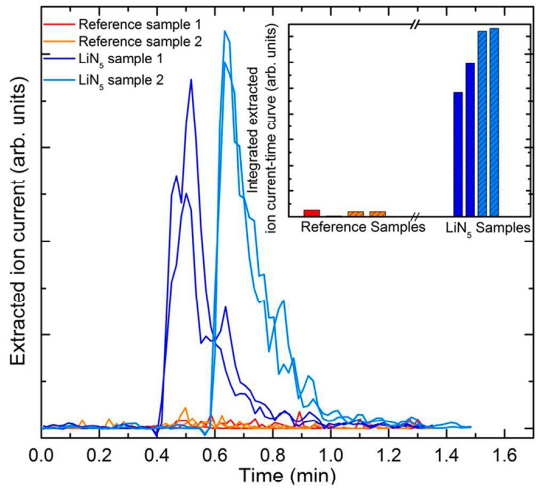

Figure 3. Mass spectrometry results from LiN_5 dissolved in methanol, with the extracted ion current for m/z values between 69.5 and 70.5, measured as a function of time. The LiN_5 samples are injected and measured at 0.4 and 0.58 min, respectively, for samples 1 and 2, while both methanol reference samples were injected at 0.4 min. (Inset) Integrated ion current−time curves shown in the main figure for the two LiN_5 and the two reference samples.

ion current measured for mass/charge ratio m/z values characteristic of the N_5^- anion (between 69.5 and 70.5) as a function of time for the injected methanol-dissolved LiN_5 sample as well as for two methanol reference samples. The sharp intensity increase observed after the sample injection matches the signature expected from a N_5^- anion. A thorough literature and mass data screen did not reveal other possible candidates, arising from a hypothetical sample contamination upon its manipulation, which could account for the measured ion current at that mass/charge ratio. The observed peak is also not present when the same mass spectroscopy measurements were performed on LiN_3 samples. (See the raw mass spectra in Figure S2 of the Supporting Information.)

Structural investigation of the LiN_5 compound was performed in three runs using powder X-ray diffraction. A pure LiN_5 phase could never be synthesized, independent of

DOI: 10.1021/acs.jpclett.8b00540
J. Phys. Chem. Lett. 2018, 9, 1600−1604

the duration of the sample's laser heating. A mixture of three distinct Li−N compounds, identifiable thanks to the comparison of X-ray diffraction spectra obtained in different locations of the sample cavity, was always observed. As shown in Figure 4, the three compounds are hexagonal LiN_2[22,23] (see Figure S4 for a Rietveld refinement), LiN_5, and a third phase also obtained during sample laser-heating above 45 GPa. The diffraction lines of the third phase, obtained with barely any other phases, are well explained by an orthorhombic unit cell ($Pca2_1$), yet with an unknown stoichiometry LiN_x (see Supporting Information and Figure S5 for its Le Bail refinement). The LiN_5 compound's set of X-ray diffraction lines could be recognized by observing a strong correlation between a mapping of its total X-ray diffraction intensity and a mapping of the total intensity of the N_5 stretching Raman modes, as shown in Figure 4b,c, respectively. The lithium pentazolate phase was always formed at the interface with nitrogen, where the Li−N system is in excess of nitrogen. A maximum of nine diffraction lines could be unambiguously attributed to the LiN_5 compound. The four different structures predicted for LiN_5 were tested out but did not satisfactorily match the detected diffraction lines.[22,23] The best fit was achieved with a monoclinic ($P2$, space group number 3) unit cell of lattice parameters a = 3.808(1) Å, b = 3.838(1) Å, c = 2.410(1) Å, and β = 99.84(1)°, yielding a volume of V = 34.70(4) Å^3 at 73.6 GPa. This volume is only slightly lower than that of the theoretically predicted volume per LiN_5 formula unit at 80 GPa (35.84 Å^3),[23] suggesting the supposed 1:5 Li/N ratio to hold true in the synthesized phase. Despite the good powder quality of the LiN_5 solid, a Rietveld refinement to resolve the atomic positions could not be performed due to the diffraction lines' overlapping.

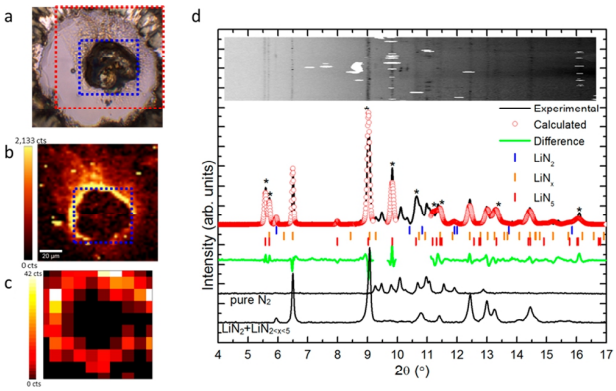

Figure 4. (a) Microphotograph of the decompressed Li−N sample at 6.4 GPa after laser heating at higher pressure. The diamond anvils were protected with a thin Ti layer. The dashed red and blue squares delimit the area probed during the Raman and X-ray diffraction mappings, respectively. (b) Raman mapping of the laser-heated lithium piece where the yellow to red scale represents the intensity, from strong to weak, of the main LiN_5 vibrons. Again, the blue square delimits the area probed during the X-ray diffraction mapping. (c) X-ray diffraction mapping of the same sample, where the yellow to red scale represents the intensity, from strong to weak, of the most intense peak characteristic of the LiN_5 solid's structure (the two lowest angle peaks). Spatial correspondence of the LiN_5 compound is found between the Raman and X-ray diffraction mappings. (d) Integrated powder diffraction pattern of another sample at 73 GPa, obtained with a wavelength of λ = 0.3738 Å, fitted with a Le Bail refinement. The diffraction lines attributed to the LiN_5 compound are adequately explained with a monoclinic ($P2$) lattice. Two regions of the diffraction patterns were not taken into account because the presence of pure nitrogen's diffraction lines prevents reliable fitting. The diffraction pattern of pure ζ-nitrogen is shown below. Because the structure of ζ-N_2 is not well known and contains many diffraction lines,[33] it was not included in the Le Bail fit. To allow a clear identification of the peaks belonging to the LiN_5 compound (marked by asterisks), the integrated X-ray diffraction pattern containing both LiN_2 and LiN_x is also shown below, with its Le Bail fit provided in the Supporting Information. The peak at ∼9° is too wide to be solely explained by the LiN_x compound and contains a contribution from the LiN_5 compound, as also seen from the X-ray diffraction image (above). From this image, pure nitrogen's diffraction signal can easily be identified from its spotty texture.

The here-synthesized LiN_5 compound is the first polynitrogen high-energy density material produced by high pressure and retrieved down to ambient conditions. Up to now, it is the room-condition polynitrogen compound with the largest fraction of nitrogen by weight. Furthermore, it is calculated to have the energetic capabilities of modern-day explosives. Obtaining a significant volume of the LiN_5 solid should motivate further research in methods reducing the pressure of synthesis, such as sample doping and photochemistry.[34,35]

■ ASSOCIATED CONTENT

Supporting Information

The Supporting Information is available free of charge on the ACS Publications website at DOI: 10.1021/acs.jpclett.8b00540.

Details of the sample loading; Raman spectroscopy, mass spectrometry, X-ray diffraction setups and measurements; vibrational and structural insight into the other synthesized Li−N phases. (PDF)

■ AUTHOR INFORMATION

Corresponding Author

*E-mail: paul.loubeyre@cea.fr.

ORCID

D. Laniel: 0000-0002-6889-9820

P. Loubeyre: 0000-0002-1778-3510

Notes

The authors declare no competing financial interest.

■ ACKNOWLEDGMENTS

We acknowledge financial support of the Centre National d'Etudes Spatiales (CNES) and the Natural Sciences and Engineering Research Council of Canada (NSERC) for the Ph.D. of D.L. We also acknowledge the European Synchrotron Radiation Facility (ESRF) for provision of beamtime on ID27. Guy Jacob and Emmanuel Lacôte are thanked for fruitful discussions and their chemical insights. We are grateful to Maxime Bridoux for help in designing the mass spectrometry measurements.

■ REFERENCES

(1) Cacace, F.; de Petris, G.; Troiani, A. Experimental Detection of Tetranitrogen. *Science* **2002**, *295*, 480−481.

(2) Vij, A.; Pavlovich, J. G.; Wilson, W. W.; Vij, V.; Christe, K. O. Experimental Detection of the Pentaazacyclopentadienide (Pentazolate) Anion, Cyclo-N5-. *Angew. Chem., Int. Ed.* **2002**, *41*, 3051−3054.

(3) Christe, K. O.; Wilson, W. W.; Sheehy, J. A.; Boatz, J. A. N5+: A Novel Homoleptic Polynitrogen Ion as a High Energy Density Material. *Angew. Chem., Int. Ed.* **1999**, *38*, 2004−2009.

DOI: 10.1021/acs.jpclett.8b00540
J. Phys. Chem. Lett. 2018, 9, 1600−1604

(4) Xu, Y.; Wang, Q.; Shen, C.; Lin, Q.; Wang, P.; Lu, M. A Series of Energetic Metal Pentazolate Hydrates. *Nature* **2017**, *549*, 78−81.
(5) Zhang, C.; Sun, C.; Hu, B.; Yu, C.; Lu, M. Synthesis and Characterization of the Pentazolate Anion Cyclo-N $\overline{5}$ in (N5)6-(H3O)3(NH4)4Cl. *Science* **2017**, *355*, 374−376.
(6) Zhang, C.; Yang, C.; Hu, B.; Yu, C.; Zheng, Z.; Sun, C. A Symmetric Co(N5)2(H2O)4 4H2O High-Nitrogen Compound Formed by cobalt(II) Cation Trapping of a Cyclo-N5− Anion. *Angew. Chem., Int. Ed.* **2017**, *56*, 4512−4514.
(7) Eremets, M. I.; Gavriliuk, A. G.; Trojan, I. A.; Dzivenko, D. A.; Boehler, R. Single-Bonded Cubic Form of Nitrogen. *Nat. Mater.* **2004**, *3*, 558−563.
(8) Goncharov, A. F.; Gregoryanz, E.; Mao, H. K.; Liu, Z.; Hemley, R. J. Optical Evidence for a Nonmolecular Phase of Nitrogen above 150 GPa. *Phys. Rev. Lett.* **2000**, *85*, 1262−1265.
(9) Tomasino, D.; Kim, M.; Smith, J.; Yoo, C.-S. Pressure-Induced Symmetry-Lowering Transition in Dense Nitrogen to Layered Polymeric Nitrogen (LP-N) with Colossal Raman Intensity. *Phys. Rev. Lett.* **2014**, *113*, 205502.
(10) Christe, K. O. Recent Advances in the Chemistry of N5+, N5− and High-Oxygen Compounds. *Propellants, Explos., Pyrotech.* **2007**, *32*, 194−204.
(11) Peng, F.; Wang, Y.; Wang, H.; Zhang, Y.; Ma, Y. Stable Xenon Nitride at High Pressures. *Phys. Rev. B: Condens. Matter Mater. Phys.* **2015**, *92*, 94104.
(12) Qian, G.-R.; Niu, H.; Hu, C.-H.; Oganov, A. R.; Zeng, Q.; Zhou, H.-Y. Diverse Chemistry of Stable Hydronitrogens, and Implications for Planetary and Materials Sciences. *Sci. Rep.* **2016**, *6*, 25947.
(13) Steele, B. A.; Oleynik, I. I. Pentazole and Ammonium Pentazolate: Crystalline Hydro-Nitrogens at High Pressure. *J. Phys. Chem. A* **2017**, *121*, 1808−1813.
(14) Wei, S.; Li, D.; Liu, Z.; Li, X.; Tian, F.; Duan, D.; Liu, B.; Cui, T. Alkaline-Earth Metal (Mg) Polynitrides at High Pressure as Possible High-Energy Materials. *Phys. Chem. Chem. Phys.* **2017**, *19*, 9246−9252.
(15) Raza, Z.; Pickard, C. J.; Pinilla, C.; Saitta, A. M. High Energy Density Mixed Polymeric Phase from Carbon Monoxide and Nitrogen. *Phys. Rev. Lett.* **2013**, *111*, 235501.
(16) Wei, S.; Li, D.; Liu, Z.; Wang, W.; Tian, F.; Bao, K.; Duan, D.; Liu, B.; Cui, T. A Novel Polymerization of Nitrogen in Beryllium Tetranitride at High Pressure. *J. Phys. Chem. C* **2017**, *121*, 9766−9772.
(17) Li, D.; Tian, F.; Lv, Y. Z.; Wei, S.; Duan, D.; Liu, B.; Cui, T. Stability of Sulfur Nitrides: A First-Principles Study. *J. Phys. Chem. C* **2017**, *121*, 1515−1520.
(18) Raza, Z.; Errea, I.; Oganov, A. R.; Saitta, A. M. Novel Superconducting Skutterudite-Type Phosphorus Nitride at High Pressure from First-Principles Calculations. *Sci. Rep.* **2015**, *4*, 5889.
(19) Li, Y.; Hao, J.; Liu, H.; Lu, S.; Tse, J. S. High-Energy Density and Superhard Nitrogen-Rich B-N Compounds. *Phys. Rev. Lett.* **2015**, *115*, 105502.
(20) Steele, B. A.; Stavrou, E.; Crowhurst, J. C.; Zaug, J. M.; Prakapenka, V. B.; Oleynik, I. I. High-Pressure Synthesis of a Pentazolate Salt. *Chem. Mater.* **2017**, *29*, 735−741.
(21) Steele, B. A.; Oleynik, I. I. Sodium Pentazolate: A Nitrogen Rich High Energy Density Material. *Chem. Phys. Lett.* **2016**, *643*, 21−26.
(22) Peng, F.; Yao, Y.; Liu, H.; Ma, Y. Crystalline LiN5 Predicted from First-Principles as a Possible High-Energy Material. *J. Phys. Chem. Lett.* **2015**, *6*, 2363−2366.
(23) Shen, Y.; Oganov, A. R.; Qian, G.; Zhang, J.; Dong, H.; Zhu, Q.; Zhou, Z. Novel Lithium-Nitrogen Compounds at Ambient and High Pressures. *Sci. Rep.* **2015**, *5*, 1−8.
(24) Eremets, M. I.; Popov, M. Y.; Trojan, I. A.; Denisov, V. N.; Boehler, R.; Hemley, R. J. Polymerization of Nitrogen in Sodium Azide. *J. Chem. Phys.* **2004**, *120*, 10618−10623.
(25) Peng, F.; Yao, Y.; Liu, H.; Ma, Y. Crystalline LiN5 Predicted from First-Principles as a Possible High-Energy Material. *J. Phys. Chem. Lett.* **2015**, *6*, 2363−2366.
(26) Kress, W.; Grimm, H.; Press, W.; Lefebvre, J. Lattice Vibrations in Lithium Nitride, Li3N. *Phys. Rev. B: Condens. Matter Mater. Phys.* **1980**, *22*, 4620−4625.
(27) Lazicki, A.; Maddox, B.; Evans, W. J.; Yoo, C. S.; McMahan, A. K.; Pickett, W. E.; Scalettar, R. T.; Hu, M. Y.; Chow, P. New Cubic Phase of Li3N: Stability of the N3- Ion to 200 GPa. *Phys. Rev. Lett.* **2005**, *95*, 165503.
(28) Medvedev, S. A.; Trojan, I. A.; Eremets, M. I.; Palasyuk, T.; Klapötke, T. M.; Evers, J. Phase Stability of Lithium Azide at Pressures up to 60 GPa. *J. Phys.: Condens. Matter* **2009**, *21*, 195404.
(29) Schneider, S. B.; Frankovsky, R.; Schnick, W. Lithium Diazenide High-Pressure Synthesis and Characterization of the Alkali Diazenide Li2N2. *Angew. Chem., Int. Ed.* **2012**, *51*, 1873−1875.
(30) Williams, A. S.; Steele, B. A.; Oleynik, I. I. Novel Rubidium Poly-Nitrogen Materials at High Pressure. *J. Chem. Phys.* **2017**, *147*, 234701.
(31) Steele, B. A.; Landerville, A. C.; Oleynik, I. I. Density Functional Theory Investigation of Sodium Azide at High Pressure. *J. Phys. Conf. Ser.* **2014**, *500*, 162005.
(32) Cordeau, E.; Arnaudguilhem, C.; Bouyssiere, B.; Hagège, A.; Martinez, J.; Subra, G.; Cantel, S.; Enjalbal, C. Investigation of Elemental Mass Spectrometry in Pharmacology for Peptide Quantitation at Femtomolar Levels. *PLoS One* **2016**, *11*, e0157943.
(33) Gregoryanz, E.; Goncharov, A. F.; Sanloup, C.; Somayazulu, M.; Mao, H. K.; Hemley, R. J. High P-T Transformations of Nitrogen to 170 GPa. *J. Chem. Phys.* **2007**, *126*, 184505.
(34) Dewaele, A.; Loubeyre, P.; Dumas, P.; Mezouar, M. Oxygen Impurities Reduce the Metallization Pressure of Xenon. *Phys. Rev. B: Condens. Matter Mater. Phys.* **2012**, *86*, 14103.
(35) Goncharov, A. F.; Holtgrewe, N.; Qian, G.; Hu, C.; Oganov, A. R.; Somayazulu, M.; Stavrou, E.; Pickard, C. J.; Berlie, A.; Yen, F.; et al. Backbone N X H Compounds at High Pressures. *J. Chem. Phys.* **2015**, *142*, 214308.

DOI: 10.1021/acs.jpclett.8b00540
J. Phys. Chem. Lett. 2018, 9, 1600−1604

Supplementary Material

A High-Pressure Synthesized Lithium Pentazolate Compound Metastable at Ambient Conditions

D. Laniel[1], G. Weck[1], G. Gaiffe[1], G. Garbarino[2], P. Loubeyre[1] *

[1]CEA, DAM, DIF, F-91297 Arpajon, France.

[2]European Synchrotron Radiation Facility, 6 Rue Jules Horowitz BP220, F-38043 Grenoble CEDEX, France.

* Email: paul.loubeyre@cea.fr

Materials and Methods

Figures S1-S7

Tables S1

Experimental method

A few pure lithium flakes of typically about 10x10x5 μm^3 in size were positioned on one of the diamond anvils, with culet diameter of 150 to 300 μm, in a glovebox under argon gas. Rhenium was used as the gasket material. A small ruby chip or gold micrograin was with the sample and used to determine the pressure inside the experimental chamber.[1,2] The diamond anvil cell (DAC) sample chamber was then loaded with pure molecular nitrogen (1400 bars) in a high pressure vessel. Pure nitrogen, acting as both a pressure transmitting medium and a reagent, was always largely in excess with respect to lithium. It was verified by Raman spectroscopy that no water contamination of the lithium sample had occurred during the loading process.

In one run, titanium was sputtered as a thin layer (200 nm) on both diamond anvils to act as a chemical insulator.[3] The same Raman modes and X-ray diffraction patterns were measured, confirming the formation of the LiN_5 compound.

Raman Spectroscopy

Confocal Raman spectroscopy measurements were performed using an Alpha300M+ (WITec). Sample excitation was done with a continuous Ar-Kr laser employing the 647.1 nm line, focused down to less than 1 μm. The Stokes Raman signal was collected in back-scattering geometry by a CCD coupled, unless state otherwise, to a 600 lines/mm grating,

allowing a spectral resolution of approximately 8 cm^{-1}. Automated motorized sample positioning with piezo-driven X-Y scan stages of submicron accuracy allowed for precise Raman mapping of the sample. A laser power of about 60 mW (measured before entering the DAC) was typically used, except upon decompressing LiN_5 down to low pressures (< 20 GPa), for which it was reduced down to 10 mW in order not to damage or melt the LiN_5 compound. Typical acquisition times were of 30 seconds with 60 mW and 4 minutes with 10 mW of laser power.

Mass spectrometry

Flow injection analysis (FIA) electrospray ionization mass spectrometry (ESI-MS) was performed on a TSQ Quantum Access MAX mass spectrometer (Thermo Scientific). The instrument was run in the negative ion mode with the capillary voltage at -2500 V. All samples were dissolved in 50 μL of methanol, which were injected 15 μL at a time in the 10 μL injection loop and then carried into mass spectrometer through a continuous flow of 200 μL/min of methanol. In order to fine tune the experimental parameters and the sample preparation method, initial tests were performed on dehydrated LiN_3 samples, prepared in the argon-filled glovebox. At first, a macroscopic quantity of LiN_3 was dissolved in 50 μL of methanol and ran through the mass spectrometer, which gave an intense signal. Then, a microscopic LiN_3 sample (~ 20x20x5 μm^3), closer in size to the LiN_5 samples, was put on a small quartz plate which was subsequently dropped in a bottle containing 50 μL of methanol. While the measured signal was significantly weaker, the N_3^- mass was unambiguously recorded at 42.5 Da. For the LiN_5 measurements, the DAC was carefully opened up in the glovebox, releasing left-over pressure and gaseous N_2, and the heterogeneous sample containing the LiN_5 compound was picked up from the diamond anvils and put on a quartz plate, which was then dropped in a bottle containing 50 μL of methanol. Reference samples were made up of a quartz plate submerged in 50 μL of methanol. Correspondingly to its

expected mass/charge ratio, the signal of the N_5^- was recorded at 70 Da. All quartz plates that were used had previously been washed in ethanol for over an hour using an ultrasonic cleaner.

Figure S1 compares the signal obtained from the macroscopic LiN_3 sample and the microscopic LiN_3 sample as well as the DAC-prepared sample containing some amount of the LiN_5 compound. The extracted ion current obtained for the N_3^- mass, recorded from the microscopic LiN_3 sample, is about eight times the one measured for the N_5^--containing sample. This can be explained by the larger size of the LiN_3 sample and its purity. Indeed, the laser heated samples, as shown in Fig. 4d, were always made up of a mixture of phases. Moreover, the other Li-N phases compete with LiN_5 for ionization within the mass spectrometer, which could further reduce the recorded N_5^- signal.

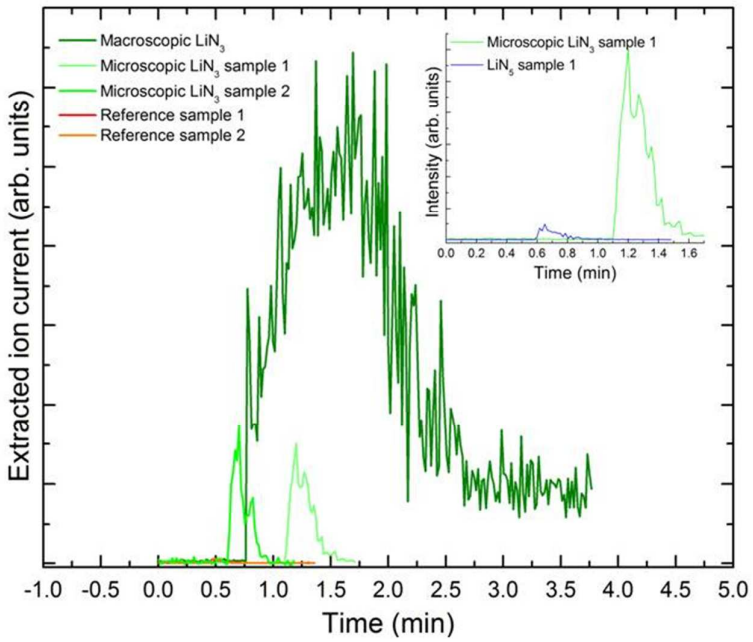

Figure S1. Mass spectrometry calibration measurements on LiN_3. The extracted ion current for *m/z* between 42-43, corresponding to N_3^-, as a function of time and for different sample injection times. The macroscopic LiN_3 sample produced a very strong signal and does not go back to its baseline within the measurement time. This is due to parts of N_3^- anions getting trapped in the MS capillaries. Using a continuous flow (800 μL/min) of methanol, 30 minutes

were needed to remove the left-over N_3^-. The signal recorded from the microscopic LiN_3 samples was unsurprisingly much weaker and did go back to its baseline. (Inset) Comparison of the intensity measured from the microscopic LiN_3 sample and the LiN_5-containing sample. In part due to its greater quantity, the N_3^- signal is about six times stronger than that of N_5^-.

Figure S2 shows the raw spectra for the methanol reference sample, LiN_3 and the LiN_5 sample, all with an identically-prepared small quartz plate. While the spectra are undoubtedly polluted with contaminants, probably picked up from the glove box manipulations, it is noted that all three of them contain the same parasitic peaks, observed at similar intensities. However, there is indubitably a peak appearing at the m/z ratio corresponding to LiN_5 when injecting the LiN_5 sample, peak that is not apparent in the LiN_3 and reference (solely methanol) samples. Four sets of LiN_5 samples, produced from two separate diamond anvil cell experiments, were tested out. The results presented in Fig. 3 of the manuscript are the (time) integrated averages of these samples, shown along with the reference samples. These averages clearly show the presence of a peak corresponding to the *m*/*z* ratio of the N_5^- ion. Of course, we also clearly see from the spectra shown in Fig. S2 the strong peak of the N_3^- ion from the LiN_3 sample, marked by an arrow.

Luckily, the N_5^- anion has a very unique mass/charge ratio. Upon looking-up common databases such as massbank.jp and mzcloud.org, no plausible, common or less common, compounds that could be in the glovebox or in the diamond anvil cell are found, even with high tolerances (± 1 m/z) on the search parameters.

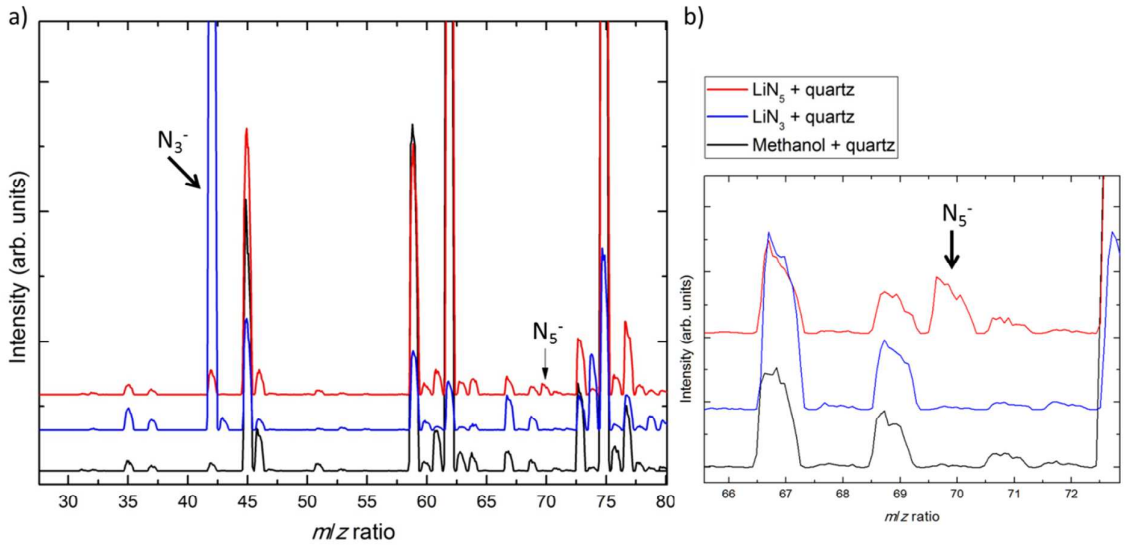

Figure S2. Raw mass spectrometry spectra. The reference (methanol), LiN_3 and LiN_5 samples were all prepared with quartz plates. a) The black, blue and red spectra were acquired during the injection of the reference, LiN_3 and LiN_5 samples, respectively. b) Enlargement of the 65-73.5 *m/z* ratio zone. Upon the injection of the LiN_5 sample, a peak appears in the region of interest (a *m*/*z* of 70).

<u>X-ray diffraction</u>

X-ray diffraction measurements were performed on the ID27 beamline of the ESRF in angular-dispersive mode. The X-ray beam, with $\lambda = 0.3738$ Å, was focused by two Kirkpatrick-Baez mirrors and cleaned by one pinhole to a ~5x5 μm^2 spot on the sample. The sample to detector distance was calibrated using a CeO_2 reference sample. X-ray powder diffraction patterns collected on a MAR-CCD detector were integrated using DIOPTAS and analyzed using the XRDA as well as the FULLPROF softwares.[4–6]

Laser-heating

The double-sided sample laser-heating was performed at the ESRF ID27 beamline and at our laboratory, using either YLF lasers. Pure lithium or LiN_2, both metals, were used as YLF laser absorbers. Temperature was not accurately determined because the synthesis of LiN_5 produces very large and brief emissions of light which perturb the pyrometric measurements. Still it was estimated that temperatures above 1200 K were needed to initiate the chemical reaction.

Other observed Li-N phases

While the full data on these phases will be presented elsewhere, more information on the synthesized Li-N phases are given below to support our claims.

Li_3N

Li_3N, typically produced by burning lithium under an atmosphere of N_2,[7] was found to be produced spontaneously from pure lithium and molecular nitrogen under pressure. The Raman spectra, measured at pressures as low as 4 GPa (see Fig. S2), show peaks characteristic of Li_3N.[8,9] However, a complete transformation does not occur as the sample does not become translucent upon undergoing the $\beta \rightarrow \gamma$ phase transition, as observed in pure β-Li_3N.[7,10–12] Therefore Li_3N is thought to form on the surface of the pure Li piece; at the pure Li/pure N_2 interface. This protecting Li_3N layer prevents the diffusion of lithium, otherwise known to corrode and break diamond anvils at about 20 GPa.[13]

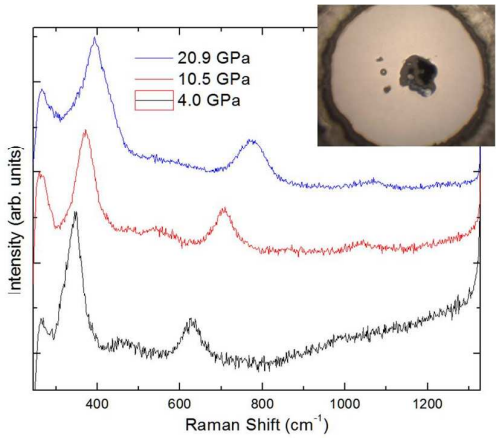

Figure S3. Raman spectra of Li_3N at various pressures. Raman modes measured after loading the sample and increasing the pressure on the pure lithium embedded in pure molecular nitrogen. The measured modes all belong to Li_3N, as neither pure N_2 nor pure metallic Li have measurable vibrational modes in this frequency range, below 16 GPa.[14] The spectra at 20.9 GPa has a slightly larger peak at about 400 cm^{-1}, due to the overlapping ε-N_2 lattice modes.[15] (Inset) Microphotograph of the Li_3N sample at 4.0 GPa.

LiN_2

Laser-heating the Li_3N-covered lithium sample between 20 and 45 GPa was found to produce a previously unreported phase. The lattice was determined to be hexagonal and adopt the $P6_3/mmc$ space group. This assignment matches perfectly a theoretically predicted phase with the LiN_2 stoichiometry.[16,17] Table S1 shows the LiN_2 compound crystallographic parameters at 9.6 GPa, including the position of both Li and N atoms. The Rietveld refinement shown in Fig. S3a validates the crystal structure described above, which is drawn in Fig. S3b. The lattice parameters of LiN_2 could be obtained from 4.6 to 82.5 GPa.

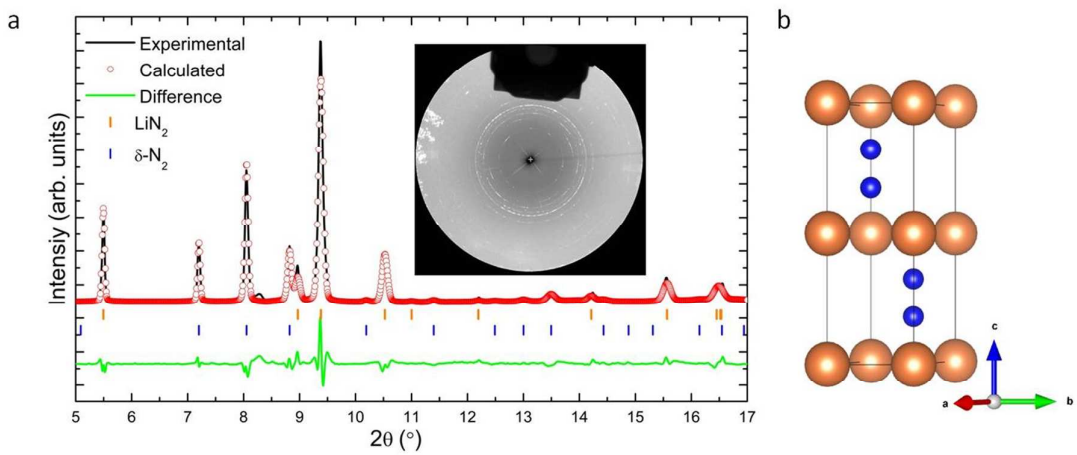

Figure S4. Crystallographic determination of the LiN_2 compound. (a) Rietveld refinement of an integrated X-ray diffraction pattern of LiN_2 synthesized at 20 GPa and decompressed down to 9.6 GPa. (Inset) The image plate used for the Rietveld refinement. (b) Crystallographic structure of hexagonal $P6_3/mmc$ LiN_2. Li and N atoms are shown as blue and orange spheres, respectively.

Table S1. Structural parameters of LiN_2 synthesized at 20 GPa and decompressed down to 9.6 GPa and 296 K. Space group $P6_3/mmc$, $a = b = 2.760(1)$ Å, $c = 7.798(1)$ Å and $V = 51.44(3)$ Å^3.

Atoms	Wyckoff site	*x*	*y*	*z*	Site occupancy
Li	2*a*	0	0	0.5	1
N	4*f*	1/3	2/3	0.673	1

The sample was opaque, absorbed the heating laser and no Raman signal could be measured from it; all of which are consistent with the predicted metallic nature of this compound.

LiN_x

While the orthorhombic LiN_x compound was sometimes measured in small amounts by X-ray diffraction after laser-heating at 25.2 GPa, it was always produced in significant quantities upon laser-heating the samples above 45 GPa. By an X-ray diffraction characterization, it was found fairly homogeneously across the sample albeit on its edges where it was mixed with LiN_5 and therefore of slightly weaker intensity. The LiN_x compound is interpreted as being of intermediate stoichiometry, between that of LiN_2 and LiN_5. Indeed, LiN_x was found favored in regions of the lithium sample in contact with a lower nitrogen quantity, whereas LiN_5 is definitely found in the high-nitrogen concentration regions. Figure S4 shows a Le Bail refinement of its orthorhombic ($Pca/2_1$) unit cell at 73.6 GPa. The sample had previously been laser-heated at 20.0 GPa, producing LiN_2, and laser-heated again at 73.6 GPa. The data quality did not allow to determine the content of its lattice. Its unit cell parameters were followed down to 14.5 GPa. The diffraction lines associated with the LiN_x compound were checked against all predicted Li-N solids but no match could be made.

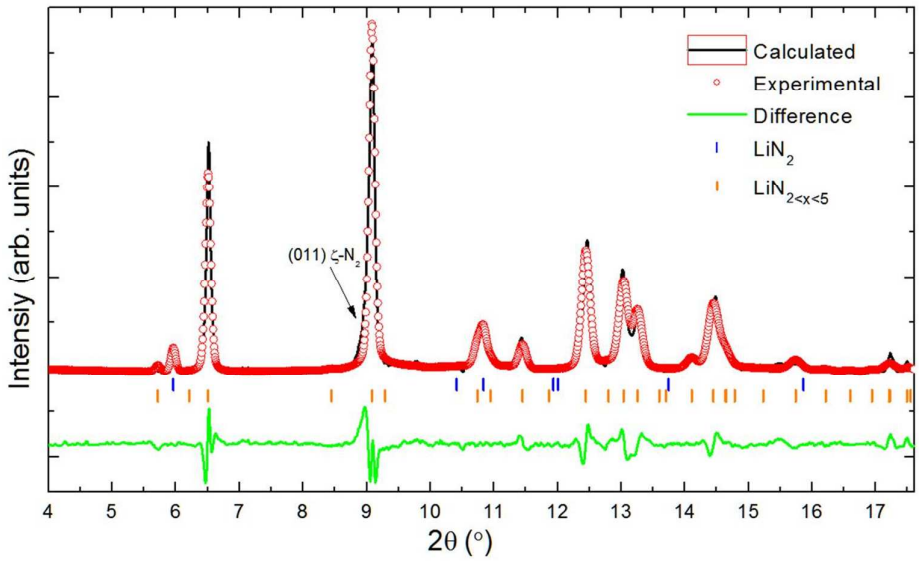

Figure S5. Le Bail refinement of an integrated X-ray diffraction pattern obtained from a sample at 73.6 GPa, after laser-heating. The Li-N compound with a stoichiometry LiN_x was determined to have an orthorhombic ($Pca2_1$) lattice with parameters of a = 6.898(1) Å, b = 3.748(1) Å and c = 3.238(1) Å, giving a volume of V = 83.71(2) Å^3. An arrow indicates a diffraction lines attributed to ζ-N_2, recognizable on the image plate by its distinct texture.[18]

LiN_5

Despite many attempts, a clean diffraction pattern containing solely the diffraction lines of the LiN_5 compound could not be obtained. This can be explained by a number of reasons. First, due to molecular nitrogen concentration and temperature gradients across the sample during laser-heating, the synthesis of a variety of Li-N phases is possible. This results in the observed sample heterogeneity. Second, the focused X-ray beam probes a 10 μm^2 sample region over which it is difficult to isolate a pure LiN_5 phase. In order to improve sample homogeneity, very small lithium pieces were loaded in the DAC, increasing the amount of lithium in contact with molecular nitrogen. Unfortunately, these samples produced mostly thin films of LiN_5, which were either poorly crystalized or too fine to provide a

sufficient X-ray diffraction signal. Obviously, Raman spectroscopy, with a less-than micron probed area, of poor sensitivity towards metallic phases (like LiN_2) and with very clear, non-overlapping characteristic vibrational modes, did not as much suffer from the lack of chemical homogeneity.

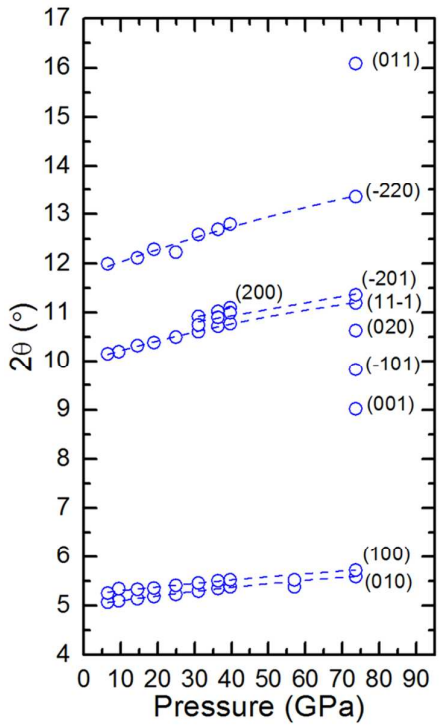

Figure S6. Evolution of the LiN_5 diffraction lines with pressure. Blue dashed lines are guides for the eye. The (*hkl*) assignment, corresponding to a monoclinic (*P*2) lattice is given for each peak.

As shown in Fig. S5, the diffraction lines characteristic of LiN_5 were followed from 73.6 GPa down to 6.4 GPa, through multiple samples. Other diffraction lines belonging to the LiN_5 compound were hidden by the diffraction peaks of the other phases such as LiN_2, LiN_x, Li_3N as well as pure nitrogen. From one sample, studied uniquely at 73.6 GPa by X-ray diffraction, a higher quality diffraction pattern was obtained and nine diffraction lines allowed

the suggestion of a unit cell for the LiN_5 compound. This diffraction pattern is shown in Fig. 4d.

Experimental run with titanium-covered diamond anvils

The diamond anvils were coated with a layer of about 200 nm in thickness. The lithium sample was gently positioned directly on top of the Ti layer on the anvil. The sample was compressed up to 59.8 GPa, pressure at which it was laser-heated. The sample was then brought to the synchrotron where X-ray diffraction was performed. Figure S7a shows an X-ray diffraction pattern, where the two main peaks of LiN_5 are distinctly visible and identified. As always, LiN_x and LiN_2 along with pure N_2 peaks are also observed. The sample was decompressed down to 48.5 GPa, after which Raman spectroscopy measurements were performed. A spectrum at 16.7 GPa is provided in Fig. S7b. The three vibrational modes of the pentazolate anion are observed. Microphotographs of the sample are shown in Fig. 4 of the main paper.

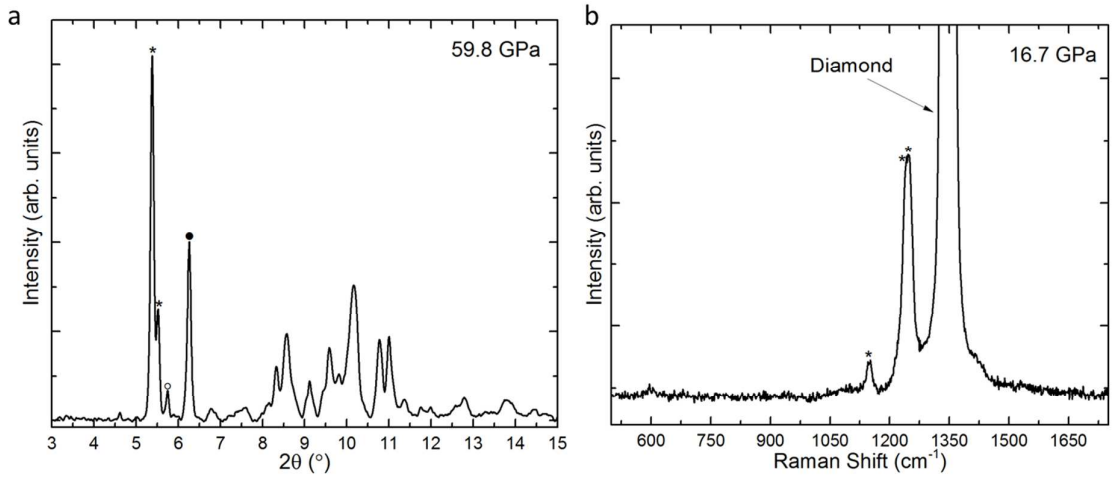

Figure S7. a) X-ray diffraction pattern of a Li-N sample laser-heated at 59.8 GPa with diamonds coated with a thin Ti layer. After laser-heating, new diffraction peaks were

observed. The peaks marked with an asterisk belong to LiN_5 while the empty and full circles correspond to LiN_2 and LiN_x, respectively. b) Raman spectrum of the sample after its decompression down to 16.7 GPa. The three signature Raman modes of LiN_5 are visible.

References

(1) Takemura, K.; Dewaele, A. Isothermal Equation of State for Gold with a He-Pressure Medium. *Phys. Rev. B* **2008**, *78*, 104119.

(2) Dewaele, A.; Torrent, M.; Loubeyre, P.; Mezouar, M. Compression Curves of Transition Metals in the Mbar Range: Experiments and Projector Augmented-Wave Calculations. *Phys. Rev. B* **2008**, *78*, 104102.

(3) Ohta, K.; Ichimaru, K.; Einaga, M.; Kawaguchi, S.; Shimizu, K.; Matsuoka, T.; Hirao, N.; Ohishi, Y. Phase Boundary of Hot Dense Fluid Hydrogen. *Nat. Sci. Reports* **2015**, *5*, 16560.

(4) Desgreniers, S.; Lagarec, K. XRDA : A Program for Energy-Dispersive X-Ray Diffraction Analysis on a PC. *J. Appl. Crystallogr.* **1994**, *27*, 432–434.

(5) Prescher, C.; Prakapenka, V. B. DIOPTAS : A Program for Reduction of Two-Dimensional X-Ray Diffraction Data and Data Exploration. *High Press. Res.* **2015**, *35*, 223–230.

(6) Rodriguez-Carvajal, J. Recent Advances in Magnetic Structure Determination Neutron Powder Diffraction. *Phys. B Condens. Matter* **1993**, *192*, 55–69.

(7) Dönges, E. Alkali Metals. In *Handbook of preparative inorgative chemistry*; Brauer, G., Ed.; Academic Press: London, 1963; Vol. 1, p 984.

(8) Kress, W.; Grimm, H.; Press, W.; Lefebvre, J. Lattice Vibrations in Lithium Nitride, Li3N. *Phys. Rev. B* **1980**, *22*, 4620–4625.

(9) Chandrasekhar, H.; Bhattacharya, G.; Migoni, R.; Bilz, H. Infrared and Raman Spectra and Lattice Dynamics of the Superionic Conductor Li3N. *Phys. Rev. B* **1978**, *17*, 884–

893.

(10) Ho, A. C.; Granger, M. K.; Ruoff, A. L.; Van Camp, P. E.; Van Doren, V. E. Experimental and Theoretical Study of Li3N at High Pressure. *Phys. Rev. B* **1999**, *59*, 6083–6086.

(11) Lazicki, A.; Maddox, B.; Evans, W. J.; Yoo, C. S.; McMahan, A. K.; Pickett, W. E.; Scalettar, R. T.; Hu, M. Y.; Chow, P. New Cubic Phase of Li3N: Stability of the N3- Ion to 200 GPa. *Phys. Rev. Lett.* **2005**, *95*, 165503.

(12) Beister, H.; Haag, S.; Kniep, R.; Strössner, K.; Syassen, K. Phase Transformations of Lithium Nitride under Pressure. *Angew. Chem. Int. Ed. Engl.* **1988**, *27*, 1101–1103.

(13) Hanfland, M.; Loa, I.; Syassen, K.; Schwarz, U.; Takemura, K. Equation of State of Lithium to 21 GPa. *Solid State Commun.* **1999**, *112*, 123–127.

(14) Scheerboom, M. I. M.; Schouten, J. A. Orientational Behavior of Solid Nitrogen at High Pressures Investigated by Vibrational Raman Spectroscopy. *J. Chem. Phys.* **1996**, *105*, 2553–2560.

(15) Goncharov, A. F.; Gregoryanz, E.; Mao, H. K.; Liu, Z.; Hemley, R. J. Optical Evidence for a Nonmolecular Phase of Nitrogen above 150 GPa. *Phys. Rev. Lett.* **2000**, *85*, 1262–1265.

(16) Peng, F.; Yao, Y.; Liu, H.; Ma, Y. Crystalline LiN5 Predicted from First-Principles as a Possible High-Energy Material. *J. Phys. Chem. Lett.* **2015**, *6*, 2363–2366.

(17) Shen, Y.; Oganov, A. R.; Qian, G.; Dong, H.; Zhu, Q.; Zhou, Z. Novel Lithium-Nitrogen Compounds at Ambient and High Pressures. *Sci. Rep.* **2015**, *5*, 1–8.

(18) Gregoryanz, E.; Goncharov, A. F.; Sanloup, C.; Somayazulu, M.; Mao, H. K.; Hemley,

R. J. High P-T Transformations of Nitrogen to 170 GPa. *J. Chem. Phys.* **2007**, *126*, 184505.

CONCLUSIONS

Polynitrogen compounds are seen as top performers to store chemical energy and would be the ultimate high energy density materials (HEDM), if recoverable at ambient conditions. Over the past decade, after many attempts testing various thermodynamical compression and decompression paths, it is now recognized that polymeric nitrogen is not recoverable at ambient pressure after its high pressure synthesis. The aim of this thesis was to search for polynitrogen compounds produced under pressure which could approach the properties of polymeric nitrogen but be obtained at less stringent conditions and recoverable at ambient pressure. The crux of our strategy was to mix nitrogen to another element. Doing so, various effects can be tuned such as chemical pre-compression, electron density transfer, topochemistry, change of concentration, etc. Mixtures best covering the range of these effects were selected for investigation. As such, the N_2-Xe, N_2-H_2 and N_2-Li systems were studied. We discuss below the efficiency of these various physicochemical effects offered by the addition of one element to nitrogen. Then, some future studies and ideas to progress will be presented.

Exploring the phase diagram of pure nitrogen is useful to gain insights on the behavior and chemical reactivity of the nitrogen molecule under pressure. At pressures below 100 GPa, pure nitrogen solid presents a rich polymorphism with the lower pressure structures (< 50 GPa) governed by the quadrupole-quadrupole (QQ) van der Waals interaction. Similarly, the binary phase diagrams of N_2 with H_2 and N_2 with Xe show stoichiometric compounds of which the structure is driven by the QQ interaction. Specifically, in the case of N_2-H_2 mixtures remarkable clathrate host- guest structures have been discovered. In the Xe-N_2 system, the cubic to tetragonal martensitic phase transition in $Xe(N_2)_2$ is similar to the $\beta \rightarrow \delta$ phase transition in pure solid nitrogen. Two such phases were known so far, cg-N at 110 GPa and LP-N at 125 GPa. In fact, many forms of polynitrogens are expected to exist at sufficient pressure, one of which was discovered in this thesis. Pure molecular nitrogen compressed to 244 GPa and laser-heated to a temperature of 3300 K resulted in the synthesis of a novel form of polymeric nitrogen (HLP-N) composed of sp^3 bonded N atoms forming layers of linked nitrogen

hexagons. In Xe-N_2, it is only around 150 GPa that a polymeric Xe-N compound is produced, based on new diffraction lines as well as low frequency Raman modes. Compression of a $N_2(H_2)_2$ single crystal resulted in a chemical reaction near 50 GPa. The reaction products were determined to be mainly composed of NH_3, accompanied with a lower proportion of longer azanes, considered as promising high energy density entities. Last but not least, the LiN_5 solid was produced from Li-N_2 above 45 GPa. Unlike the other novel polynitrogen forms, lithium pentazolate did not decompose during pressure release and was retained down to ambient conditions. Both N_2-H_2 and Li-N_2 systems are clear demonstrations that mixing nitrogen with an interacting element (i.e. not noble gases) is an adequate pathway for the synthesis of polynitrogen compounds at pressures lower than for pure N_2. This is in accordance with theoretical calculations [23,47,56,48–55] as well as recent experimental work, as in the case of the high pressure synthesis of CsN_5, N_8 and $ReN_8{\cdot}xN_2$ from CsN_3-N_2, hydrazinium azide and Re-N_2, respectively [48,266,267]. Moreover, as it will be justified below, the ambient conditions metastability of a compound might not be as critical as initially supposed.

Two of the studied systems, Xe-N_2 and Li-N_2, relied on the chemical precompression effect to observe novel polynitrogen geometries. In both mixtures, interesting results were obtained. In the case of xenon-nitrogen mixtures, it was found that $Xe(N_2)_2$ has N_2-N_2 distances that, at only 30 GPa, match the intermolecular length found in pure N_2 at about 80 GPa [127]. This intermolecular closeness was also felt in the N_2 stretching modes of $Xe(N_2)_2$ as a distinct redshift was detected starting at that pressure. In analogy with pure nitrogen, it is generally accepted that the redshift measured indicates the weakening of the N_2 triple bond due to a redistribution of electronic density, with electrons shifting from the covalent bond to the intermolecular zone. However, is the bond really weakened? If so, is it actually significant? Based on the formula describing the Raman modes frequencies,[1] a decrease in ω_r is undoubtedly the sign of a bond weakening as the mass at play do not change. However, even in $Xe(N_2)_2$ where the bond frequency goes down to 2200 cm^{-1} (2330 cm^{-1} at ambient conditions in pure N_2), it is still very far from even a N=N double bond which has a Raman frequency of about 1300−1550 cm^{-1}. To provide further perspective, at ambient conditions the nitrogen triple-bond has a cohesive energy of 942 kJ/mol while it is of 418 kJ/mol for a double-bond. Thus, the N_2 bond in $Xe(N_2)_2$ (or the S_{Xe} alloy, for that matter) is by no means *weak* and while it is indeed *weakened*, the energy required to break it is still significant. Indeed, the formation of the polymeric Xe-N solid occurs at pressures higher than that of cg-N. As such, the effect of chemical precompression by an element with a

[1] In the previous sections, the formula $\omega_r = \frac{1}{2\pi}\sqrt{\frac{K}{\delta}}$ was introduced, where ω_r is the Raman frequency, K is the spring constant (related to the bond strength) and δ is the effective mass of the system.

large atomic radii, while it negligibly weakens the N-N triple bond, does not seem to be the most efficient route for obtained polynitrogen compounds.

On the other hand, the results obtained with the Li-N_2 system tell us a completely different story on the effect of chemical precompression. In that case however, the chemical precompression effect is achieved through an electronic density transfer. This methods appears unquestionably more efficient as for a Li/N ratio of 3 (Li_3N), the N_2 molecule is completely broken up at ambient pressure, as well as for a Li/N ratio of 1 and 0.5 (LiN and LiN_2) low bond order pernitrides are formed. Even in the case of LiN_5, with a Li/N ratio of only 0.2, a pentazolate anion is formed, albeit at 45 GPa. What would happen if molecular nitrogen were to be mixed with an element that can provide not one, but two electrons, like alkaline earth metals? Moreover, what of transition metals, such as iron, since they are known to have a wide range of oxidation states, reaching even 7+ [268]? Preliminary answers to these questions will be given below.

The chemical change in the N_2-H_2 mixture, although at lower pressure than in pure N_2, is not due to chemical pre-compression but probably to the quantum effect of the hydrogen. Indeed, the nitrogen molecules appear unperturbed (i.e. not chemically interacting) up to about 50 GPa as their vibrational modes were not observed to be redshifted. Nonetheless, a chemical reaction spontaneously occurs, without even the need for laser-heating to cross an energy barrier, and a variety of azanes (with mainly NH_3) are determined to be produced. Hydrogen is one of the few elements for which quantum tunneling was observed to play an active role in solid state transformations at ambient or near ambient temperatures [269,270]. This is explained by its small mass, making hydrogen more mobile than other atoms in the solid. As such, it can more easily explore the energy landscape around a given structural arrangement. Having in mind the structure of the $N_2(H_2)_2$ compound (as well as the $(N_2)_6(H_2)_7$), it is possible that a combination of sample topology and proton tunneling promotes a chemical reaction. With increasing pressure changing the energy landscape, as soon as the energy barrier is low and thin enough, the hydrogen atoms would shifts towards this (local) minima – of lower energy than the van der Waals compounds – and induce a chemical transformation of the whole sample. This type of local diffusion and transformation could explain the variety of azanes, as each segment of the $N_2(H_2)_2$ molecular nitrogen sublattice would be more favorable for forming either an NH_3 or a longer azane. An investigation of N_2-D_2 mixtures seems to validate this theory as no chemical reaction was reported up to 70 GPa, which could thus be attributed to the mass of deuterium which makes quantum tunneling less probable and pushes back the pressure of chemical reaction [271]. It has to be considered that perhaps a global energy minimum for the system could be obtained through laser-heating. Theoretical simulations provide

further weight to this hypothesis as they predict compounds that were not experimentally observed, such as ones containing the energetic N_5^-.

FROM THEORETICAL PREDICTIONS TO EXPERIMENTS

Theoretical calculations, and especially enthalpy convex hulls, are a great help to guide experimentalists towards the most profitable systems to investigate, the concentration and pressure range under which these systems should be studied and the compounds that can be expected. Additionally, the X-ray diffraction data quality is often far from optimal for solids synthesized under high pressure and high temperature, as discussed above, and while their lattices may reliably be determined, their full structural resolution is often difficult. In these circumstances, calculations are of further utility. Indeed, with the insight provided by the theoretical calculations, the structure of N_{32}, *Cmcm* LiN and LiN_2 (along with those of FeN and FeN_2 presented in the Annex) could be fully solved.

However, these calculations have a few shortcomings and still are a ways off from removing the need to perform experiments. A problematic assumption for high pressure-high temperature syntheses is that the calculations are performed at the temperature of absolute zero, henceforth removing the temperature-entropy (-TS) term from the Gibbs free energy equation. For systems in which a small enthalpy gaps exists between two structures, accounting for this extra term can shift the presumed stable compound to unstable. This is especially concerning as significant laser-heating is typically needed to cross activation barriers between two compounds.

Of related nature, enthalpy-based theoretical calculations usually fail at predicting the van der Waals compounds' stability. This is the case for both the N_2-H_2 and the Xe-N_2 systems, where the $(N_2)_6(H_2)_7$, $N_2(H_2)_2$ as well as the $Xe(N_2)_2$ compounds were not expected by the calculations, despite investigating the pressure domain at which they are experimentally shown to be stable [18,21,23]. Such van der Waals compounds were previously demonstrated to be largely stabilized due to entropy considerations [190]. The entropic term's importance is further exacerbated in the case of $N_2(H_2)_2$ and $Xe(N_2)_2$ where the nitrogen molecules are rotationally disordered. The presence of the van der Waals compound provides an explanation as to why, in the case of N_2-H_2 mixtures, the experimental results are so far off the theoretical calculations.

Of course, other issues may prevent accurate theoretical calculations such as the limitations on the unit cell lattice size, unaccounted compound stoichiometries,

inadequate functionals, quantum contributions (especially in the case of hydrogen), a complex Gibbs free energy landscape (polymorphism), etc. This sort of complications could justify the discrepancies between two sets of calculations performed at zero kelvin and with different codes as well as with experiments – as in the case of the structure prediction for the LiN_5 compound and the high pressure polymeric phases of pure nitrogen [12,28,29].

Thus, to improve both experimental efficiency and the theoretical calculations' reliability, a close interaction between the two disciplines is essential.

HIGH PRESSURE SYNTHESIS OF POLYNITROGEN COMPOUNDS: THE NEXT STEPS.

In this thesis, we have successfully demonstrated that the pressure parameter is an efficient tool for discovering new forms of polynitrogen. While the LiN_5 solid is a promising first step, where should we go from there in order to produce even better poly-N solids? Given the current state of research, suggestions will be made. However, hurdles are currently impeding the applicability of high pressure syntheses for real-world applications. Notably, these are metastability issues as well as very high pressure of syntheses; accurate and large throughput compound prediction; and the experimental characterization of the produced solids. Hereafter, we will also describe recent and upcoming advancements that allow to overcome these obstacles and that could help propel high pressure chemistry at the forefront of industrial applications.

Polynitrogen compounds: where to now?

Based on the success obtained by mixing lithium and molecular nitrogen, it would seem that the reduction of N_2 is the most efficient pathway to the low pressure synthesis of a high energy density polynitrogen solid. This begs the question: would mixing nitrogen with elements having even higher oxidation state than lithium yield longer anionic single-bonded N-N chains obtainable at still moderate pressures? Theoretical calculations on alkaline earth-nitrogen mixtures indicate the answer to this question to be a resounding yes. At only 40 GPa, a BeN_4 solid containing a charged 3D puckered $[N_{10}]^{1.7-}$ with single-bonded N-N atoms is predicted to be stable [52,272]. Similarly anionic polynitrogen arrangements are also expected from high density Mg-N_2 and Ca-N_2 mixtures [49,273]. What then of transition metals, which have a wide range of oxidation states? The answer here is not as clear. While charged N_2 dimers have been

observed to form in many N_2-transition metal mixtures (Fe, Ti, Cu, Pt, Ir, Os) up to pressures of about 70 GPa [123,161,274–276], there is only one reported case of longer-than two single-bonded nitrogen chains: the $ReN_8 \cdot xN_2$ inclusion compound [267]. However, that solid was produced at pressures over 100 GPa; similar to that of cg-N. This indicates that while they can reach high oxidation states, they are not sufficiently reactive (i.e. willing to part with a fraction of their electronic density) to promote at moderate pressures single-bonded N-N forms.

While the mixtures described above aimed at stabilizing anionic polynitrogen arrangements, cationic geometries are also predicted to be stable, such as N_4^+, N_5^+ N_9^+ [35,36]. In particular, N_5^+ was synthesized in the N_5AsF_6 and N_5SbF_6 compounds and the latter was even determined as stable at ambient conditions [38]. So far, the N_2-halogens binary phase diagram is completely uncharted at high pressures, with the exception of the fluorine-rich side of the N_2-F binary phase diagram, which was investigated by theoretical calculations up to 300 GPa [277]. The high pressure oxidization of molecule N_2 could prove to be an interesting pathway for novel polynitrogens.

Last but not least, further experiments could be performed on pure molecular nitrogen. As previously described, cg-N is calculated to be stable above 50 GPa but a very large activation barrier needs to be crossed to observe its transformation from its molecular form. Moreover, laser-heating fails at polymerizing nitrogen since entropy favors the molecular phases [135]. Mechanochemistry and photochemistry – by employing a rotational diamond anvil cell and exciting molecular N_2 with extreme ultraviolet photons, respectively – can both provide additional energy to the system without heating it. As such, both methods could potentially enable the moderate pressure synthesis of cg-N.

All of the aforementioned experiments can be performed with the current technical capabilities. In the next sections, we will discuss the future developments that will largely shape the future of polynitrogen syntheses.

Producing high pressure phases at "ambient conditions"

Diamond, which is a high pressure phase of carbon (> 10 GPa), is routinely produced at near ambient pressure [278]. These synthetic diamonds are grown by chemical vapor deposition (CVD) through the exposition a 1% CH_4-99% H_2 mixture to a hot filament (1200 K) in a reactor at a pressure of 2700 Pa [279]. In a similar fashion, in 2017 a team claimed to have grown thin rods (few nanometers) of cg-N. Radio-frequency plasma enhanced CVD was successfully employed by flowing a mixture of 1:1 molecular nitrogen and argon over bulk β-sodium azide [280]. As such, it is

demonstrated that this method can allow the ambient conditions productions of metastable high pressure phases. While it can not yet be applied to all compounds, the rapid development of this field is undoubtedly promising.

Chemical vapor deposition is not the only method permitting this. Indeed, another technique was also demonstrated to be able to produce high pressure polymorphs. In 2011, a phase of aluminum predicted stable above 380 GPa was obtained by an ultrafast laser-induced microexplosion confined inside the bulk of a sapphire (α-Al_2O_3) [281]. This is explained by the fact that the laser pulse causes the solid to superheat and form a plasma. The confined plasma then explodes and generates a powerful shock wave that expands and compresses the surrounding material. The transformed material is preserved on account of the compressed sapphire surrounding it. This is all performed using a tabletop apparatus. According to other reports, this shock wave can generate pressures of over 10 TPa [282]. With this in mind, not only could static high pressure phases be produced at "ambient conditions", but this could be extended to phases synthesized in the terapascal regime.

Machine learning

The CAS (Chemical Abstract Service) registry contains more than 142 million unique organic and inorganic chemical substances (alloys, minerals, mixtures, polymers, salts) [283]. On average, 15000 compounds are added *daily*. What kind of method, technique or person could go through all of these compounds and extract correlation and trends? Data mining and machine learning are the key to this challenge. Through data mining, huge amount information can be gathered, processed and analyzed by a computer, after which with machine learning, it is able to make predictions. For example, as discussed in the introduction of this thesis, the conditions for the metastability of a compound were provided based on a data mining study that looked at 29902 compounds, including 15097 ambient conditions metastable compounds [46]. The trends observed matched common physico-chemistry notions (for example, that there is a strong link between metastability and the cohesion energy of a material) but it also allowed to find that while polymorphs with a larger amount of components have both a lower activation barrier and a lower propensity to form, compounds resulting from a phase separation have a much higher activation barrier and higher probability to be produced.

The same team then used machine learning to predict novel metastable nitrogen-rich nitrides [51]. To do so, it fed the data mined nitrides compounds (both stable and metastable) to a computer which, through statistical methods, was trained to

search for the metastable phases. Afterwards, it was able to predict a multitude of nitrogen-rich compounds, including the FeN_2 pernitride (which we experimentally obtained, as detailed in the Annex). What's important to understand is that the training data set based on which the computer later makes his predictions critically needs to have "good" and "bad" data. When the researchers wanted to determine novel metastable nitrogen-rich nitrides, they also provided in the training data set nitrogen-poor stable compounds. Basically, machine learning allows us to learn from our mistakes as much as from our successes.

In the end, data mining and machine learning are very promising tools for an accurate, very high throughput prediction of compounds with specific properties, whether its metastability, precise band gap value, high superconductivity, high energy density or a combination of characteristics. Henceforth, this will contribute to a much faster convergence towards the most appropriate material for given circumstances as well as permit more complex systems (multi-elements) to be investigated.

Development of experimental techniques

With high predictability and ambient conditions production, all that is left is the step in between: the high pressure synthesis and characterization, validating the compound's stability, structure and properties. In that regard as well, critical advancements are taking place which will allow for higher pressures, more accurate structural determinations and the high pressure implementation of new characterization methods.

First on the list is the improvement of synchrotron-generated light. For example, with the upcoming fourth generation synchrotrons, large gains in X-ray spot size (from a few micrometers down to a few hundred of nanometers) along with an increase in brilliance are expected. This will drastically augment the spatial resolution – which will definitely in obtaining single phase diffraction images of an inhomogeneous laser-heated sample – as well as permit the study of smaller samples sizes. The latter is particularly helpful since as of now, new diamond anvil geometries (described in the *Experimental Techniques in High Pressure Physics* section) have been developed but the very tiny sample sizes were prohibitive for their X-ray diffraction characterization [79,80].

Still on the subject of X-ray diffraction characterization, the conjunction of improved single crystal data analysis software and an elaborate data post-treatment now enables the single crystal X-ray diffraction structural resolving of novel high

pressure phases produced by short burst laser-heating [115]. Indeed, this technique is highly advantageous due to the intrinsic precision of single crystal X-ray diffraction and since a compound transformed by brief laser-heating typically forms multiple nanocrystals discernable from the powdery untransformed solid. This method was recently validated by fully resolving the structure of a $ReN_8 \cdot xN_2$ inclusion compound above 100 GPa and 2300K, without the support of theoretical calculations [267]. As the experimental high pressure structure solving has become more and more reliant on theory, this approach critically allows for experiments to regain their self-sufficiency.

In a similar line of thought, novel laser-heating anvil geometries are also under development. The boron-doped diamond disks acting as laser absorbers described earlier are being improved such as a pure diamond disk with a thin metal absorbing layer protected by a thin diamond coating is underway. The advantage over the boron-doped diamond disks is that those disks' exterior will be exclusively constituted of diamond, which is highly chemically inert. This means that it will be possible to uniformly heat non-absorbing samples – hence enabling homogenous samples in their thermodynamic global minima – without being concerned of inducing a parasitic chemical reaction.

With the ever progressing technological developments, the future of high pressure chemistry – and in particular of polynitrogen syntheses – is just in its infancy. Eventually, it is bound to become as versatile and accomplished as conventional ambient conditions chemistry.

ANNEX

I. *HIGH PRESSURE INVESTIGATION OF IRON AND NITROGEN: THE SEARCH FOR AN IRON PERNITRIDE*

In parallel with the investigations performed in the context of my thesis, a study on the high pressure and high temperature behavior of iron and nitrogen mixtures was also completed. This research was motivated by the fact that transition metal nitrides have been known for a while to be a large group of industrially relevant compounds with outstanding physical properties: hardness, high bulk modulus and high melting point [283,284]. For example, steel nitrides form at the surface of steels through a high temperature reaction with a nitrogen-rich gas; this layer improves the fatigue and corrosion resistance of the material. These solids typically have a metal-nitrogen ratio greater than one [274]. Moreover, these studies undertaken on the Fe-N system were also motivated by recent studies which have shown that a new class of compounds can be formed by the application of extreme pressures and temperatures: transition metal pernitrides.

The transition metal pernitrides are particularly interesting as the pernitrides – charged nitrogen dimmers – are known to lead to a high bulk modulus, leading in some cases to ultrahigh incompressibilities [124,161,285–288]. The unique characteristic of nitrogen pernitrides is attributed to the significant transition metal-nitrogen charge transfer and the lower than three bonding order of the N-N dimer [124,161,274]. In turn, this leads to the filling of N-N antibonding molecular orbitals ($1\pi_g$*) concomitantly with the progressive transfer of electronic density from the transition-metal element to the N_2 dimer. Filled molecular antibonding states result in an increased repulsion between the two N atoms, thus leading to the higher bulk modulus [56,289]. The most famous among them, as well as the very first to be synthesized, is PtN_2 which as a bulk modulus of K_0 = 372 GPa [124,285]. Since, many others were discovered including IrN_2, with a bulk modulus of 428 GPa [161] – the highest after diamond's – as well as the Os, Pd, Rh and Ru pernitrides. Most of these compounds were retrieved and found

metastable at ambient conditions [161,285,287,288,290]. Moreover, the recent synthesis of TiN_2 and subsequently CoN_2, the first pernitrides with a transition metal in the fourth row of the periodic table, evidenced the possibility for these lower electron elements to produce similar nitrogen compounds as the heavier transition metals [274,275].

Along with titanium and cobalt, iron also sits in the fourth row of the periodic table. Even before the start of our investigation, the chemistry of iron and nitrogen had already been established to be rich as six stoichiometries of Fe-N compounds were demonstrated to exist in the bulk: α''-$Fe_{16}N_2$, α'-Fe_8N, γ'-Fe_4N, ε-$Fe_3N_{1\pm x}$, Fe_7N_3 and Fe_2N [291,292]. In all of these compounds, the Fe/N ratio is greater than one. However, theoretical calculations have recently predicted the stability of the iron pernitride FeN_2, which would be the first nitrogen-rich Fe-N compound. That compound is expected to have a hexagonal (*R*-3*m*) lattice and to be stable above 17 GPa at 1000 K. At 34 GPa, a structural phase transition towards a marcasite-type (hexagonal *Pnnm*) phase was calculated. In the marcasite-type FeN_2 a high bulk modulus (385 GPa at 25 GPa, corresponding to about 289 GPa at ambient pressure) as well as a charge analysis suggests that the structure bears double-bonded N_2^{2-} pernitrides [48,293,294].

The objective of our investigation was to explore the nitrogen-rich side of the Fe-N binary phase diagram at high pressures and temperatures and form the first iron-nitrogen compounds with a majority of N atoms.

II. *ARTICLES*

These studies were published as two articles, titled "*Study of the iron nitride FeN into the megabar regime"* and *"High pressure and high temperature synthesis of the iron pernitride FeN_2*" in the Journal of Alloys and Compounds and Inorganic Chemistry, respectively. The article published in Inorganic Chemistry was chosen for the journal's cover for the issue of June 4th 2018. Simultaneously to our publication on the FeN compound, two other groups reported similar observations [275,295].

Analogously to the investigation of the Li-N_2 system, a small piece of iron was loaded along with a much greater quantity of molecular nitrogen. This allowed to synthesize the nitrogen-richest Fe-N solids stable a given pressure. As schematized in Figure 1, the Fe_2N compound is the first obtained upon laser-heating pure Fe embedded in N_2. This compound, which had previously been reported in the literature, adopts an orthorhombic lattice (*Pbcn*) in which the nitrogen molecule is dissociated (the closest N-N distance being of 2.83 Å) [291]. Its structure is drawn in Figure 2. Above 17 GPa and 1500 K, another chemical reaction occurs. The pressure of transition matching that

of the theoretically predicted FeN_2, the latter was thought to have been synthesized. The diffraction lines of this new compound, however, did not correspond those of the hexagonal (*R*-3*m*) FeN_2 lattice. Instead, a hexagonal unit cell with the $P6_3/mmc$ space group was resolved and the solid could be retained back down to ambient conditions. To determine its stoichiometry, energy-dispersive X-ray spectroscopy was performed. This technique allows measuring the amount of an atomic specie present in a solid. Indeed, through bombarding the solid with highly energetic electrons, core electrons are removed from the solid's atoms. These ejected electrons are then replaced by other electrons in an outer, higher-energy shell of the same atom and in doing so, produce a photon of energy equivalent to the difference between its initial and final energy levels. The energy levels being unique to an element, a solid's atomic mapping can thus be done. As demonstrated in the paper, a Fe/N ratio of 0.96(9) was measured on the sample, and the compound's stoichiometry was assumed to be of FeN. Using this information, a Rietveld refinement was performed to resolve the atomic positions (see article). Similarly to Fe_2N, the closest N-N distance is 2.92 Å (at 16.5 GPa).

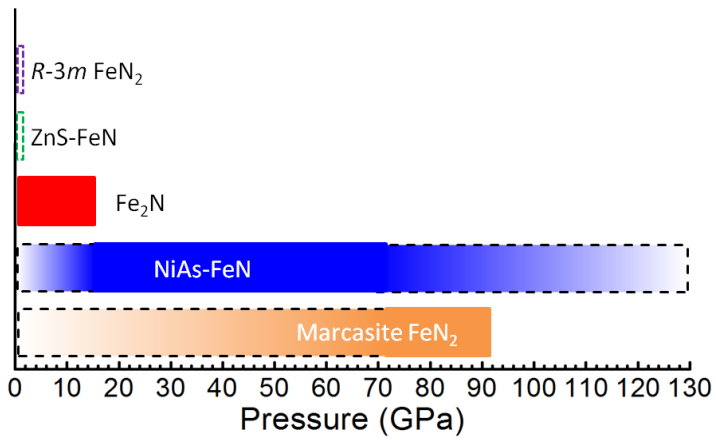

Figure 1: Pressure stability domains of the five iron nitrides observed when in an excess of molecular nitrogen. The full rectangles represent pressure range at which a given compound is obtained after laser-heating whereas the shaded sections with a dashed outline mark the compound is stable (was observed) but is not the preferred solid during laser-heating. ZnS-FeN and R3m FeN_2 are only observed during pressure release of NiAs-FeN and marcasite FeN_2, respectively, to ambient conditions.

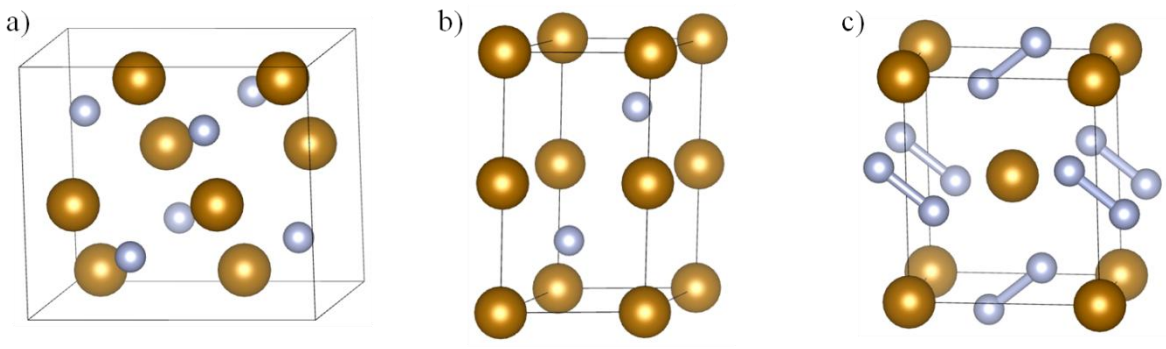

Figure 2: Structure of the Fe-N compound. a) Structure of Fe_2N. b) Structure of FeN. c) Structure of FeN_2, containing pernitrides. The pale blue and gold spheres represent N and Fe atoms, respectively.

The equation of state of FeN was measured from ambient pressure up to 128 GPa. A K_0 = 200(5) GPa and K_0' = 5.3(2) was obtained. The bulk modulus for FeN is slightly higher than what was found in nitrogen-poor iron nitrides, such as Fe_4N (155 GPa), Fe_7N_3 (168 GPa), Fe_2N (190 (9) GPa as well as pure hcp iron (165 GPa).[291,292,296] This follows the trend of an increasing bulk modulus along with nitrogen concentration due to an increase in the crystals' covalency. As seen below, this tendency is further confirmed with the high bulk modulus of FeN_2. Up to the maximum pressure reached on FeN, the solid was laser-heated up to 2000 K at regular pressure intervals and no phase transition was observed. These experiments were performed in the context of the testing of the laser-heating setup at the I15 beamline of the Diamond synchrotron (United Kingdom) where reaching higher temperatures proved to be difficult.

However, on a sample studied at a later date at the ID27 beamline of the ESRF synchrotron, it was found that above 72 GPa and 2200 K, FeN chemically reacts. The new diffraction peaks this time closely matched the orthorhombic (*Pnnm*) FeN_2 structure predicted by the theoretical calculations [52,293,294]. As drawn in Figure 2, the structure contains N_2 dimers with an intramolecular distance of 1.32 Å. This distance, determined from the Rietveld refinement of an integrated X-ray diffraction pattern is not that reliable because of the gap in atomic scattering power between Fe (Z = 26) and N (N = 7). As such, the intensities measured from the X-ray diffraction pattern are much more dependent of the iron atoms than of the nitrogen atoms, as demonstrated in the article. The accurate determination of the N-N bond length is important to then be able to infer the electronic charge density transferred from the iron atoms to those of nitrogen. Luckily, Raman modes could be measured off of the FeN_2 solid, further suggesting a high iono-covalency provided by the N_2 dimer. The main Raman mode of FeN_2 was detected at a frequency of 1056 cm^{-1} at ambient pressure.

Based on this frequency, a N-N bond order close to 1.5 is expected, implying a charge of 3- for the N_2 pernitride. The bulk modulus of FeN_2 – extracted from fitting the pressure-volume data between ambient pressure and 91 GPa by a second order Birch-Murnaghan equation of state – was found to be of K_0 = 344 GPa. As a testament to the low N-N bond order (and thus the filling of the N-N antibonding states), FeN_2 has an ultrahigh incompressibility compared to the previous nitrogen-poor Fe-N solids. Moreover, it represents an astounding increase of about 208% from pure iron and exhibits largest increase in bulk modulus of any other pernitrides over the pure transition metal. Owing to its high bulk modulus and its ambient conditions metastability, FeN_2 could be an attractive solid for the industry.

Both the FeN_2 and FeN solids, while metastable to ambient conditions, were found to partially transform into another structure of the same stoichiometry upon the release of the molecular N_2 gas. Indeed, FeN_2 partly becomes a hexagonal (R-3m) solid while a cubic (F-43m) FeN structure is detected. This is interesting since neither of these phase are the thermodynamically stable Fe-N solid at ambient conditions and in air. This attests to the fact that the activation barrier for a change of structure *and* stoichiometry is greater than the energy needed to undergo a simple structural transformation.

Journal of Alloys and Compounds 733 (2018) 53–58

Contents lists available at ScienceDirect

Journal of Alloys and Compounds

journal homepage: http://www.elsevier.com/locate/jalcom

Study of the iron nitride FeN into the megabar regime

Dominique Laniel [a, *], Agnès Dewaele [a], Simone Anzellini [b], Nicolas Guignot [c]

[a] CEA, DAM, DIF, F-91297 Arpajon, France
[b] Diamond Light Source Ltd, Harwell Science and Innovation Campus, Didcot, Oxfordshire OX11 0DE, UK
[c] Synchrotron SOLEIL, St-Aubin 91192, France

ARTICLE INFO

Article history:
Received 12 July 2017
Received in revised form
5 October 2017
Accepted 29 October 2017
Available online 31 October 2017

Keywords:
High pressure
Chemical synthesis
X-ray diffraction
Synchrotron radiation
Crystal structure and symmetry

ABSTRACT

In this work, the nitrogen-rich portion of the Fe-N binary phase diagram is investigated up to 128 GPa. The samples, largely in excess of nitrogen, were laser-heated in diamond anvil cells to temperatures up to 2000 K at regular pressure intervals to help in crossing possible activation barriers towards the more stable phase. Three Fe-N compounds: ZnS-type FeN, Fe_2N and NiAs-type FeN, are characterized by powder X-ray diffraction and their observed stability domain reported. Below 12.5 GPa, orthorhombic Fe_2N is found to be the energetically-favored compound while NiAs-FeN becomes stable above 17.7 GPa. Energy-dispersive X-ray spectroscopy measurements and a Rietveld refinement confirmed the stoichiometry and structure of the recovered NiAs-FeN sample. A precise determination of its bulk modulus ($K_0 = 200(5)$ GPa) as well as its pressure derivative ($K_0' = 5.3(2)$) is obtained and, based on its unit cell axial ratio evolution, the NiAs-FeN compound appears to decrease in ionicity concomitantly with pressure. Within the pressure-temperature conditions reached here, the predicted iron pernitride FeN_2 is not observed.

© 2017 Elsevier B.V. All rights reserved.

1. Introduction

Transition metal nitrides are known to be a large group of industrially relevant compounds with outstanding physical properties, specifically regarding their high hardness, high bulk modulus and refractory, superconducting as well as catalytic properties [1,2]. Of particular interest are the nitrogen-rich metal pernitrides, composed of charged single-bonded N-N dimers [3]. Their unique mechanical and electronic properties are thought to originate from the significant transition metal-nitrogen charge transfer and the nature of the N-N bond [4–6]. With the notable exception of TiN_2 [6], synthesized transition metal pernitrides (OsN_2, IrN_2, PtN_2, RuN_2, RhN_2, PdN_2) [4,5,7–10] form N-N connected MN_6 octahedrons (M standing for metal) and exhibit a variety of electronic structures corresponding to that of a metal, semiconductor and insulator. Furthermore, they are known for their ultrahigh-incompressibility, similar to that of cubic boron nitride [11].

Recent theoretical studies have predicted the existence of the iron pernitride FeN_2 and calculated its properties [3,12,13]. Anticipated to be a stable compound from 17 GPa at 1000 K (9 GPa at 0 K) [3], *R-3m* hexagonal FeN_2 is expected to undergo a phase transition into the well-known marcasite structure (*Pnnm*) at 22 GPa [12]. Furthermore, convex hull calculations forecast marcasite FeN_2 to be the lowest enthalpy Fe-N compound at 50 GPa [12]. While a rich Fe-N chemistry exists, most synthesized compounds have a Fe/N ratio higher than unity, such as α''-$Fe_{16}N_2$, α'-Fe_8N, γ'-Fe_4N, ε-$Fe_3N_{1\pm x}$, Fe_7N_3, and Fe_2N [14,15]. Being the exception, FeN is most nitrogen-rich iron nitride reported thus far. First found in thin films [16] with the ZnS structure [17], a new phase of Fe-N, presumably NiAs-FeN ($P6_3/mmc$), has very recently been synthesized in a high pressure apparatus by two independent groups [18,19]. However, in these studies some doubt remains regarding the structure, stoichiometry and stability domain of that compound. Indeed, Niwa et al. [19] proposed a 1:1 stoichiometry, supposed the NiAs structure without performing a Rietveld refinement and reported the phase to be stable only above 30 GPa. Diffraction data on the compound was shown up to 40 GPa. On the other hand, Clark et al. [18] reports the synthesis of a compound with the NiAs-type structure from 13 GPa and performs a Rietveld refinement indicating a stoichiometry of Fe_xN, with x between 0.60(5) and 1.0(1). Furthermore, they estimated the NiAs-FeN bulk modulus based on crystallographic information collected at three pressures: 0.1 MPa, 4.4 GPa and 13.3 GPa, obtaining a value of

* Corresponding author.
E-mail address: dominique.laniel@cea.fr (D. Laniel).

https://doi.org/10.1016/j.jallcom.2017.10.267
0925-8388/© 2017 Elsevier B.V. All rights reserved.

K_0 = 198(8) GPa. NiAs-FeN's magnetic properties and enthalpy-based stability were also investigated at low pressures through calculations. Although Ref. [19] suggests that FeN_2 might have been obtained at 59.8 GPa, no experimental evidence confirming its existence was provided.

In this paper, we report a thorough study of NiAs-FeN characterized from ambient conditions to 128 GPa by powder X-ray diffraction. The ambiguities regarding its structure and stoichiometry are resolved with energy-dispersive X-ray spectroscopy and a Rietveld refinement. With the large pressure range under which NiAs-FeN was studied, its equation of state is unequivocally determined. In order to check for the stability of FeN and obtain a new phase richer in nitrogen, i.e. FeN_2, *in-situ* laser-heating of our sample while in excess of N_2 was repeatedly performed up to the maximum reported pressure. The predicted iron pernitride FeN_2 was not observed.

2. Experimental method

A total of seven Fe-N_2 samples were studied in membrane diamond anvil cells (DACs). Five DACs were equipped with anvils of culets larger or equal to 300 μm in diameter, designed to explore the Fe-N system below 70 GPa, while the two others were used to investigate the megabar regime, employing diamond anvil culets of 150 and 100 μm in diameter. Iron powder grains were compressed into a thin foil of about 3 μm in thickness. To ensure chemical and thermal insulation from the diamond anvils, the Fe sample was positioned on top of c-BN micrograins or a thin salt (KCl or NaCl) layer. Nitrogen, acting as both a reactant and a pressure transmitting medium, was loaded with the Fe foil at 150 MPa in the DAC using a high-pressure vessel. Nitrogen was always largely in excess with respect to iron. Gold micrograins and/or a ruby microsphere were also put into the DAC and utilized as pressure calibrants [20]. After sample loading, Raman spectroscopy was performed to ensure that the iron foil was not in contact with the anvils and that molecular nitrogen completely surrounded it.

Samples were characterized by X-ray diffraction at PSICHÉ (SOLEIL) and I15 (Diamond) synchrotron beamlines, using a monochromatic beam with a wavelength of 0.3738 Å and 0.4246 Å, respectively. Both beamlines are equipped with image plate detectors calibrated using a CeO_2 reference sample and an on-line YAG laser-heating setup. In order to overcome possible activation barriers towards the most stable phases, laser-heating was performed at regular pressure intervals. Samples were moved under the YAG laser beam in an attempt to heat the whole sample in a similar fashion and, when occurring, to have a homogeneously transformed sample (a single phase). X-ray diffraction mappings were performed to ensure this. Still, as in some cases discussed below, multiple phases were observed. Temperatures during laser-heating were estimated from the sample's blackbody radiation to be below 2000 K. Electron scanning microscopy (ESM) and energy-dispersive X-ray spectroscopy (EDS) measurements were performed on the synthesized compounds recovered at ambient conditions.

3. Results and discussion

3.1. Stability domain of nitrogen-rich iron nitrides

The large number of Fe-N_2 samples, all in excess of molecular nitrogen, permitted an investigation of the nitrogen-rich side of the binary phase diagram. A total of three previously reported compounds were observed, namely Fe_2N, ZnS-FeN and NiAs-FeN, and their stability domain was finely determined. X-ray diffraction patterns obtained during one run are shown in Fig. 1.

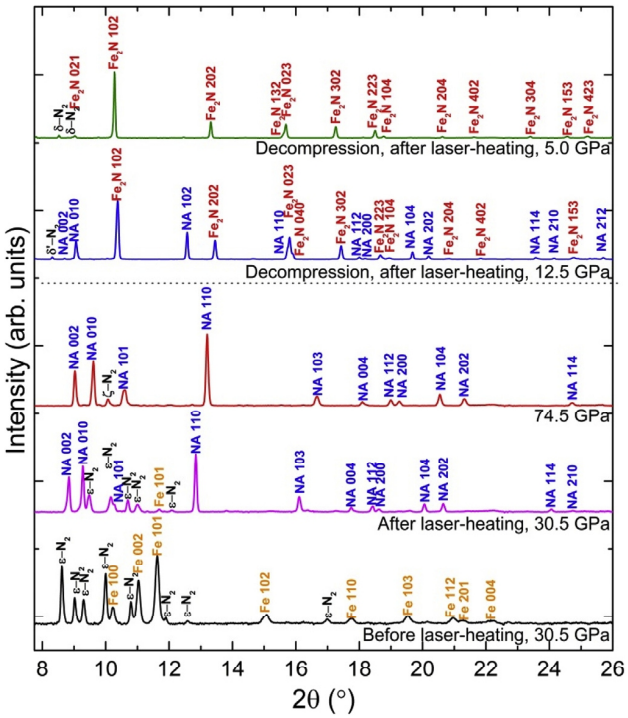

Fig. 1. Integrated X-ray diffraction patterns obtained from a Fe-N_2 sample using a wavelength of λ = 0.3738 Å. Gentle laser-heating of the Fe foil embedded in molecular nitrogen (black pattern) at 30.5 GPa results in the synthesis of NiAs-FeN (pink pattern), which peaks are labeled as NA. Laser-heated at three different pressures during the sample's following compression up 74.5 GPa, NiAs-FeN was still observed. Decompression of the same sample and laser-heating it at 12.5 GPa produced Fe_2N (see blue pattern), although the transformation is not complete due to inhomogeneous heating. Further heating at lower pressure yields pure Fe_2N. (For interpretation of the references to colour in this figure legend, the reader is referred to the web version of this article.)

In that run, the iron foil embedded in molecular nitrogen was laser-heated at 30.5 GPa which resulted in the synthesis of NiAs-FeN (pink diffraction pattern in Fig. 1). While small amounts of pure iron are still observed, subsequent laser-heating produced a complete transformation of the iron foil. Compressed up to 74.5 GPa and further heated without observing a phase transition, the pressure on this sample was then decreased down to 12.5 GPa. This time, laser-heating of the sample induced the partial formation of orthorhombic Fe_2N, with the entire sample reaction obtained at still lower pressures. Through other samples, the stability domain of these two phases, NiAs-FeN and Fe_2N, was further narrowed down. Fe_2N was found to be the most stable compound at least above a few GPa and below 12.5 GPa while beyond 17.7 GPa NiAs-FeN is the observed solid. This was determined by detecting a conversion of Fe_2N into NiAs-FeN during compression at 17.7 GPa and a transformation of NiAs-FeN into Fe_2N during decompression at 12.5 GPa. In between these two threshold pressures, both compounds seem to be very close in their Gibbs free energy: laser-heating unreacted Fe and N_2 resulted in a mixture of both phases. Synthesis of NiAs-FeN was also obtained at 35.0 GPa by laser-heating the pure species, the highest pressure at which a first laser-heating was performed. The observed stability domain of each phase is schematically represented in Fig. 2.

Although Fe_2N and NiAs-FeN have well-defined stability domains, they were found to be very resilient during isothermic decompression. Indeed, both could be retrieved down to ambient conditions, as shown in Fig. 3. However, in the case of NiAs-FeN,

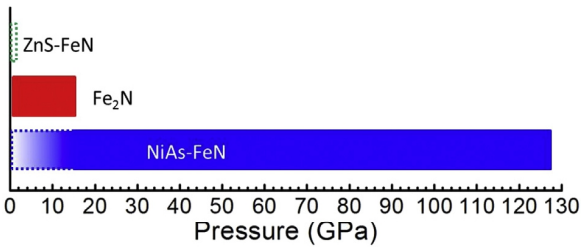

Fig. 2. Pressure stability domains of the three iron nitrides observed when in excess of molecular nitrogen, with the exception of ambient pressure where gaseous N_2 escapes the DAC. The full rectangles represent the experimentally-measured stability domains while the shaded sections with a dashed outline mark the metastability pressure domains. ZnS-FeN is observed only during pressure release of NiAs-FeN to ambient conditions.

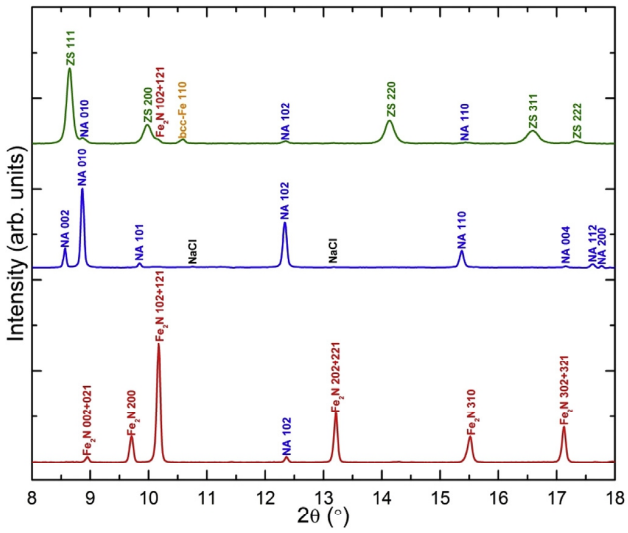

Fig. 3. Integrated X-ray diffraction patterns of samples decompressed down to ambient conditions, obtained using a wavelength of $\lambda = 0.3738$ Å. The Fe_2N sample (red pattern) was obtained by laser-heating the sample successively at 12.5 and 5.0 GPa; pressures below the stability domain of NiAs-FeN. The NiAs-FeN (labeled as NA) diffraction pattern, shown in blue, was obtained by heating the atomic Fe as well as molecular N_2 at 20.0 GPa and then decompressing the sample. The pattern showing mostly ZnS-FeN peaks (labeled as ZS) was acquired from an incompletely transformed sample, previously composed of NiAs-FeN as well as pure Fe and Fe_2N. The ZnS-FeN phase was obtained from the spontaneous phase transition of NiAs-FeN when the DAC was opened up. The lattice parameters of all three phases are given in Table 1. (For interpretation of the references to colour in this figure legend, the reader is referred to the web version of this article.)

either immediately after opening the DAC or over time, ZnS-FeN was detected and eventually became the prominent phase. Based on our observations, a sample with a mixture of phases was prone to a more rapid transformation into ZnS-FeN, which can be understood by instabilities at the phase boundaries. For instance, a sample composed of NiAs-FeN as well as pure Fe and Fe_2N was found to immediately undergo the NiAs-FeN to ZnS-FeN transformation at ambient conditions, as determined from its ambient conditions X-ray diffraction pattern shown in green in Fig. 3. In contrast, a pure FeN sample was found to preserve its NiAs structure immediately after cell opening.

In ZnS-FeN, Fe (or N) has four N (or Fe) nearest neighbors, forming a compositionally ordered version of the diamond structure. This lower coordination number does suggest a stability domain at lower pressure than NiAs-FeN where both Fe and N atoms are hexacoordinated, as further described in the next section. Indeed, a pressure-induced ZnS-type to NiAs-type phase transition has been observed in compounds such as AlAs and AlP [21,22]. At ambient conditions, the volume per formula unit of ZnS-FeN and NiAs-FeN is, respectively, 19.82(2) $Å^3$ and 16.87(2) $Å^3$, which corresponds to a volume difference of almost 15%, very close to that measured for an identical phase transition in AlAs [21]. This structural phase transition is diffusionless and can be described by a distortion of the base angle of the ZnS structure from 90° to 60° along with an increase in its c/a ratio, which requires a fairly low activation energy [23]. This is consistent with our observation of a transition at ambient conditions. In any case, it was found that the higher stability of Fe_2N hinders the formation of ZnS-FeN at all pressures but ambient conditions. The lattice parameters of all three phases at ambient conditions are given in Table 1. The obtained values closely match those reported in the literature [14,18,19].

3.2. Crystalline structure and high pressure behavior of NiAs-FeN

Although its hexagonal lattice is unquestionable, some doubt remains regarding the Wyckoff position occupied by the atoms in NiAs-FeN and its stoichiometry [18,19]. Fully transformed into NiAs-FeN above 20 GPa and its structural integrity verified back at ambient conditions, this sample was later on studied by ESM and EDS. Previously to those measurements, the EDS apparatus had been calibrated against an iron nitride of known stoichiometry, Fe_2N. Illustrated in Fig. 4 a), a Fe/N ratio of 0.96 ± 0.09 was measured on the FeN sample. Since NiAs-FeN transforms progressively into ZnS-FeN, some ambiguity exists on the structural nature of the compound at the time of the EDS measurements. In the case where a significant fraction of the sample underwent the phase transition, a partial decomposition of the sample and loss of gaseous N_2 is possible and would affect the measured Fe/N ratio. Thus, the obtained value provides an upper bound on the atomic species' ratio.

With the stoichiometry determined, a Rietveld refinement was performed on a pure NiAs-FeN sample at 1.7 GPa (Fig. 4 b)). This pressure is below pure molecular nitrogen's melting point and thus its diffraction lines are avoided. Since the NiAs-FeN diffraction rings are formed from hundreds of diffraction spots, their integrated intensity is suitable for such an analysis. The Rietveld refinement was done with a Fe/N stoichiometry ratio of 0.96, but it is worth noting that a 1:1 Fe:N ratio, which is still within uncertainty, actually yielded a marginally better fit (a χ^2 of 7.02 and 6.97, respectively). The quality of the refinement, seen in Fig. 4 b), verifies that FeN crystallizes into the NiAs structure (Fig. 4 c)) at pressures above ambient. All atoms in the NiAs structure have a sixfold coordination but only the iron atoms are in an octahedral site; the nitrogen atoms are in a trigonal prismatic coordination resulting from the hcp packing. This structural arrangement is typically observed in ionic compounds with anions of groups IV, V as well as VI [22], and differs only slightly from the well-known NaCl structure (viewed along its (111) axis) by its stacking arrangement for the special case of $c/a = 1.633$. When c/a differs from 1.633, this distorts the octahedrons and results in shorter

Table 1
Space group, number of formula units per unit cell (Z), lattice parameters and volume of ZnS-FeN, NiAs-FeN and Fe_2N at ambient conditions.

	a (Å)	b (Å)	c (Å)	V ($Å^3$)	Z	Space group
ZnS-FeN	4.296(1)			79.26(2)	4	*F-43m*
NiAs-FeN	2.791(1)		5.002(1)	33.74(2)	2	*$P6_3/mmc$*
Fe_2N	4.418(1)	5.527(1)	4.802(1)	117.26(2)	4	*Pbcn*

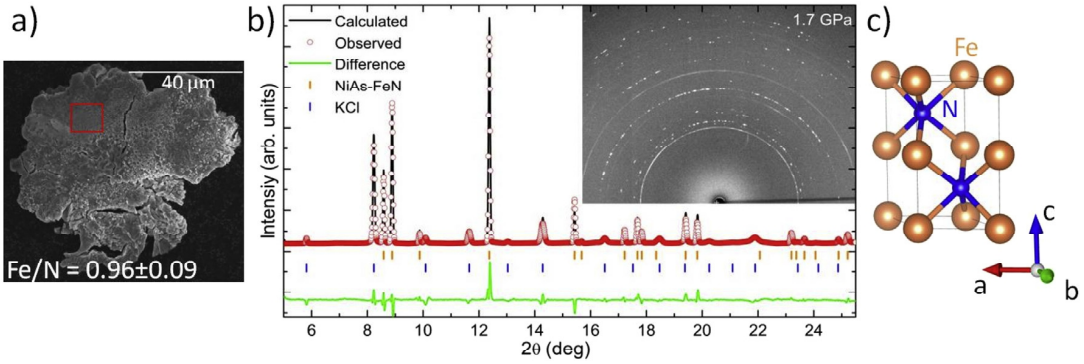

Fig. 4. a) Scanning electron microscope imaging of the FeN sample recovered back to ambient conditions. The section marked by the red square is where the EDS measurements were performed and, because of its flatness, gives the most accurate results. b) Rietveld refinement of NiAs-FeN at 1.7 GPa, with $a = 2.784(1)$ Å and $c = 4.993(1)$ Å. The orange and blue ticks indicate diffraction lines from NiAs-FeN and KCl, respectively. This phase was synthesized at 20 GPa and the pressure was subsequently decreased down to 1.7 GPa, below molecular nitrogen's melting point. This diffraction data was obtained with a wavelength of $\lambda = 0.3738$ Å. (Inset) The image plate corresponding to the refined diffraction pattern. The perfectly homogeneous diffraction rings belong to KCl while the slightly spotty ones are from the NiAs-FeN phase. c) The NiAs-FeN crystallographic structure obtained from the Rietveld refinement, where the orange spheres represent the Fe atoms and the blue spheres the N atoms. The shortest Fe-N and Fe-Fe distances are 2.04 Å and 2.50 Å, respectively. (For interpretation of the references to colour in this figure legend, the reader is referred to the web version of this article.)

cation-cation distances, assuming a fixed cation-anion distance. In this fashion, the NiAs structure can accommodate a higher covalency and metallicity than the NaCl structure [22,24]. A NaCl → NiAs transition, observed in the similar iron-based compound FeO [24,25], is obtained through a diffusionless shuffle of the dense (111) planes of the NaCl structure. The NiAs structure has also been observed in other iron-based compounds, including FeSe [26], FeS [27] and FeSb [28]. Furthermore, while FeN is the only 3d transition-metal nitride with the NiAs structure, niobium nitride (ε-NbN) [29] and tantalum nitride (TaN) [30] were also found to crystallise in this structural arrangement. Tungsten nitride WN was predicted to adopt the NiAs structure [31] but later experiments unveiled a compound with the W_2N_3 stoichiometry [32]. Also, δ-MoN was found to favor a slightly distorted NiAs structure that doubles its unit cell volume [2,33].

As seen in Fig. 5, NiAs-FeN was studied up to 128 GPa with laser-heating performed at regular pressure intervals. The smooth evolution of the *d*-spacings of NiAs-FeN clearly establishes the lack of a chemical reaction or phase transition. Twelve diffraction lines were followed up to the maximum pressure and used to accurately determine the unit cell volume of NiAs-FeN. The volume-pressure data was fitted with a third order Birch-Murnaghan equation of state. Values of the bulk modulus (K_0) and its derivative (K_0') were determined to be 200 (5) GPa and 5.3(2), respectively, while the V_0 was set to the measured volume of 33.74(2) Å^3 at ambient conditions. Albeit of slightly higher value, the obtained bulk modulus agrees well with the one previously reported, which was determined to be of $K_0 = 198(8)$ GPa (with its derivative K_0' set to 4) [18]. The bulk modulus for NiAs-FeN is slightly higher than what was found in nitrogen-poor iron nitrides, such as Fe_4N (155 GPa), Fe_7N_3 (168 GPa), Fe_2N (190 (9) GPa, see Fig. 5 b) for details) as well as pure hcp iron (165 GPa) [14,15,34]. This agrees with the trend that the

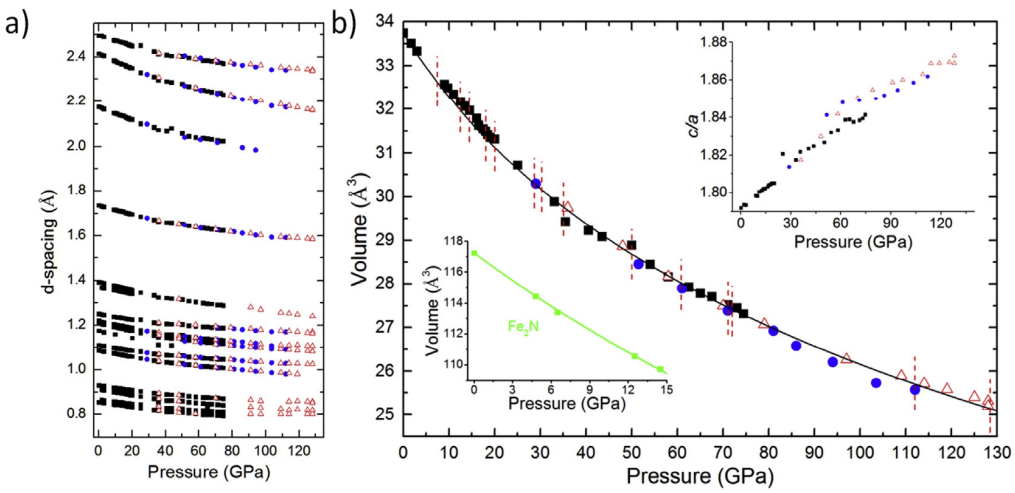

Fig. 5. a) *d*-spacing evolution of NiAs-FeN diffraction lines with pressure. The various symbols represent different experimental runs. Up to 128 GPa, the *d*-spacings decrease smoothly with pressure, showcasing the compound's structural stability. b) Unit cell volume of NiAs-FeN in function of pressure, containing two formula units. The data points were fitted with a third order Birch-Murnaghan equation of state using the $V_0 = 33.744$ Å^3 (fixed), $K_0 = 200(5)$ GPa and $K_0' = 5.3(2)$ values, drawn as a full black line. The vertical red lines mark the pressures at which NiAs-FeN was laser-heated. The various symbols represent different experimental runs. (Upper inset) The *c*/*a* evolution of the NiAs-FeN lattice with pressure. The *c*-axis is found to be less compressible than the *a*-axis. (Lower inset) Evolution with pressure of Fe_2N orthorhombic lattice volume. The datapoints are fitted with a third order Birch-Murnaghan equation of state which yielded a $K_0 = 190$ (9) GPa with $K_0' = 4$ (fixed) and $V_0 = 117.26(2)$ Å^3(fixed). (For interpretation of the references to colour in this figure legend, the reader is referred to the web version of this article.)

Table 2
Unit cell lattice parameters and volume of NiAs-FeN measured up to 128 GPa.

Pressure (GPa)	*a* (Å)	*c* (Å)	V (Å^3)
16.5	2.726(1)	4.918(1)	31.64(2)
33.1	2.667(1)	4.848(1)	29.88(2)
50.0	2.633(1)	4.811(1)	28.88(2)
67.5	2.592(1)	4.763(1)	27.71(2)
81.3	2.562(1)	4.739(1)	26.92(2)
103.5	2.520(1)	4.683(1)	25.73(2)
128.2	2.497(1)	4.667(1)	25.20(2)

addition of nitrogen atoms strengthens the crystalline structure by increasing the crystal's overall covalency. The lattice parameters of NiAs-FeN at various pressures between 16.5 and 128.2 GPa are given in Table 2. Parameters at ambient conditions are given in Table 1.

The c/a ratio measured from NiAs-FeN is shown in the inset of Fig. 5 b). It is significantly higher than the ideal value of 1.633, contrarily to most compounds adopting the NiAs-type structure at ambient conditions [22], and similar in that sense to FeO ($c/a = 2.01$ at 96 GPa and 800 K) [24]. Onodera et al. [35] have shown a correlation in several materials with the NiAs-type structure between their c/a ratio at ambient conditions and its evolution with pressure: a compound with an ambient conditions c/a value above (below) the ideal value of 1.633 would see that same ratio increase (decrease) with pressure. This trend allows a decrease of the packing index $\alpha = V/d$ [3], where V is the volume per formula unit and d the shortest cation-anion distance. NiAs-FeN follows nicely that trend, with a c/a of 1.79 at ambient conditions that progressively increases along with pressure to reach 1.87 at 128 GPa. With the a-axis being the most compressible, the six second-neighbors of Fe atoms surrounding a given Fe atom have their interatomic distances shortened the most compared to the first Fe-Fe neighbors and the shortest Fe-N distance (see Fig. 6). This interaction is interpreted as due to a weakening of the compound's ionicity.

Raman spectroscopy was performed on NiAs-FeN but the signal was too weak to be detected. This is probably due to the metallic nature of this compound [36].

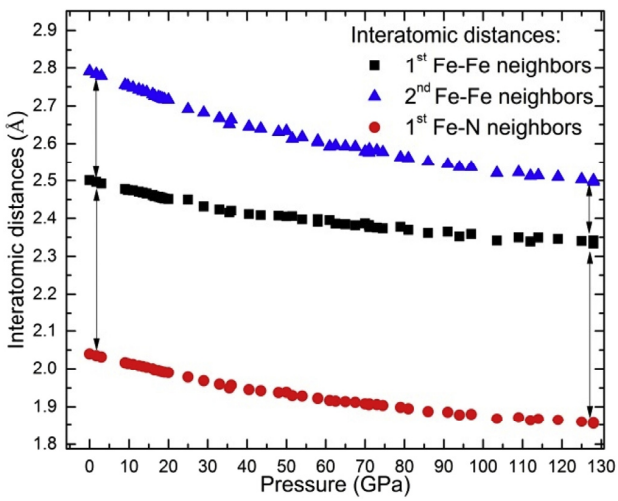

Fig. 6. Evolution of the interatomic distances in NiAs-FeN with pressure. As seen, the interatomic distances that are most reduced with pressure are Fe-Fe second-neighbors, followed by Fe-N first-neighbors and then the Fe-Fe first-neighbors. At the maximum pressure, the first and second shells of Fe-Fe have similar interatomic distances (6.8% difference).

3.3. Comparison between experimental data and ab initio calculations

In this work, NiAs-FeN was characterized up to 128 GPa and frequently laser-heated while in excess of pure nitrogen. This vastly exceeds the conditions under which theoretical studies predicted the synthesis of an iron pernitride (17 GPa at 1000 K, 9 GPa at 0 K) [3,13] or even iron nitrides with a lower Fe/N ratio (FeN_4 is calculated stable around 50 GPa) [12]. Our measurements revealed no such compounds but instead NiAs-FeN was observed over a wide range of pressures and temperatures. This compound, which seems to be partially responsible for the misprediction, had not been foreseen by any of the *ab initio* studies, including those using structure searching methods [12]. Most enthalpy comparisons were therefore performed against the ZnS-FeN compound so as to determine whether or not an iron pernitride would be energetically favorable.

The synthesis of NiAs-FeN in excess of nitrogen is not explained by recent density functional calculations on this system as the enthalpy of FeN_2 is estimated to be lower than ZnS-FeN+1/2 N_2 above 9 GPa (0 K) [3]. At pressures larger than 22.6 GPa, NiAs-FeN is calculated to be more stable than ZnS-FeN [18], but should remain higher in enthalpy than FeN_2. Tentative interpretations of this discrepancy are listed below. First, a temperature increase was shown to produce a destabilizing effect on FeN_2 [3], which could reduce its stability domain. Second, very large activation barriers for the NiAs-FeN + 1/2 $N_2 \rightarrow FeN_2$ reaction, unsurmounted by the laser-heating performed here, could impede a possible chemical transformation. Third, errors in the calculated enthalpy of NiAs-FeN, FeN_2 or even pure N_2, within the density functional theory can be not excluded, especially due to the demonstrated importance (and difficulty) of correctly accounting for magnetic ordering and electronic correlations in iron nitrides [18,37].

Equipped with the structure and equation of state parameters of Fe_2N and NiAs-FeN, comprehensive calculations can be done and provide an updated estimate on the stability of the iron pernitride. Moreover, the NiAs-FeN compound needs to be further studied under greater pressure and/or temperature conditions to perhaps produce nitrogen-richer iron nitrides.

4. Conclusions

In this work, we have explored the nitrogen-rich portion of the Fe-N binary phase diagram up to 128 GPa and 2000 K. Laser-heating of the samples at regular pressure intervals helped to overcome activation barriers towards the most stable phase. Below 12.5 GPa, orthorhombic Fe_2N is the energetically-favorable compound while above 17.7 GPa and up to at least 128 GPa, NiAs-FeN was observed. With the very large pressure range under which NiAs-FeN was characterized by X-ray diffraction, an accurate determination of its bulk modulus as well as its derivative could be obtained. Based on its axial ratio evolution, NiAs-FeN appears to decrease in ionicity concomitantly with pressure. Contrary to recent numerical simulations based on density functional theory, the iron pernitride FeN_2 was not observed even at pressures and temperatures above its predicted synthesis conditions. With the data provided in this paper on ZnS-FeN, NiAs-FeN and Fe_2N, undoubtedly more accurate numerical simulations can be made and give insight on the stability domain of FeN_2.

Acknowledgements

The authors gratefully acknowledge the Centre National d'Etudes Spatiales (CNES) and the Natural Sciences and Engineering Research Council of Canada (NSERC) for financially supporting the

Ph.D. of D.L. The authors acknowledge the SOLEIL synchrotron and the DIAMOND light source for the provision of beamtime under proposals 20160261 and NT18126, respectively. We also wish to thank Olivier Marie for performing the EDS measurements.

References

[1] A. Salamat, A.L. Hector, P. Kroll, P.F. McMillan, Coord. Chem. Rev. 257 (2013) 2063.
[2] A. Friedrich, B. Winkler, E.A. Juarez-Arellano, L. Bayarjargal, Materials (Basel) 4 (2011) 1648.
[3] M. Wessel, R. Dronskowski, Chem. Eur. J. 17 (2011) 2598.
[4] A.F. Young, J.A. Montoya, C. Sanloup, M. Lazzeri, E. Gregoryanz, S. Scandolo, Phys. Rev. B 73 (2006) 2.
[5] A.F. Young, C. Sanloup, E. Gregoryanz, S. Scandolo, R.J. Hemley, H.K. Mao, Phys. Rev. Lett. 96 (2006).
[6] V.S. Bhadram, D.Y. Kim, T.A. Strobel, Chem. Mater. 28 (2016) 1616.
[7] J.C. Crowhurst, A.F. Goncharov, B. Sadigh, C.L. Evans, P.G. Morrall, J.L. Ferreira, A.J. Nelson, Science 311 (2006).
[8] R. Yu, Q. Zhan, L.C. De Jonghe, Angew. Chem. Int. Ed. 46 (2007) 1136.
[9] K. Niwa, D. Dzivenko, K. Suzuki, R. Riedel, I. Troyan, M. Eremets, M. Hasegawa, Inorg. Chem. 53 (2014) 697.
[10] K. Niwa, K. Suzuki, S. Muto, K. Tatsumi, K. Soda, T. Kikegawa, M. Hasegawa, Chem. Eur. J. 20 (2014) 13885.
[11] E.V. Yakovenko, I.V. Aleksandrov, A.F. Goncharov, S.M. Stishov, Sov. Phys. JETP 68 (1989) 1213.
[12] Z. Wang, Y. Li, H. Li, I. Harran, M. Jia, H. Wang, Y. Chen, H. Wang, N. Wu, J. Alloys Compd. 702 (2017) 132.
[13] S.D. Gupta, S.K. Gupta, P.K. Jha, Eur. Phys. J. B 86 (2013).
[14] M. Hasegawa, T. Yagi, J. Alloys Compd. 403 (2005) 131.
[15] H.A. Wriedt, N.A. Gokcen, R.H. Nafziger, Bull. Alloy Phase Diagr. 8 (1987) 355.
[16] K. Suzuki, H. Morita, T. Kaneko, H. Yoshida, H. Fujimori, J. Alloys Compd. 201 (1993) 11.
[17] I. Jouanny, P. Weisbecker, V. Demange, M. Grafouté, O. Peña, E. Bauer-Grosse, Thin Solid Films 518 (2010) 1883.
[18] W.P. Clark, S. Steinberg, R. Dronskowski, C. McCammon, I. Kupenko, M. Bykov, L. Dubrovinsky, L.G. Akselrud, U. Schwarz, R. Niewa, Angew. Chem. Int. Ed. 56 (2017) 7302.
[19] K. Niwa, T. Terabe, D. Kato, S. Takayama, M. Kato, K. Soda, M. Hasegawa, Inorg. Chem. 56 (2017) 6410.
[20] A. Dewaele, M. Torrent, P. Loubeyre, M. Mezouar, Phys. Rev. B 78 (2008) 104102.
[21] R.G. Greene, H. Luo, T. Li, A.L. Ruoff, Phys. Rev. Lett. 72 (1994) 2045.
[22] A. Mujica, A. Rubio, A. Muñoz, R.J. Needs, Rev. Mod. Phys. 75 (2003) 863.
[23] J. Cai, N. Chen, Phys. Rev. B 75 (2007) 174116.
[24] Y. Fei, H.K. Mao, Science 266 (1994) 1678.
[25] H. Ozawa, K. Hirose, K. Ohta, H. Ishii, N. Hiraoka, Y. Ohishi, Y. Seto, Phys. Rev. B 84 (2011) 134417.
[26] G. Song, H. Matsui, H. Akai, H. Tabata, J. Vac. Sci. Technol. B 31 (2013) 42801.
[27] A. Kavner, T.S. Duffy, G. Shen, Earth Planet. Sci. Lett. 185 (2001) 25.
[28] P. Feschotte, D. Lorin, J. Less-Common Met. 155 (1989) 255.
[29] N. Terao, Jpn. J. Appl. Phys. 4 (1965) 353.
[30] A. Fontbonne, J.C. Gilles, Rev. Int. Des. Hautes Temp. Des. Refract. 6 (1969) 181.
[31] P. Kroll, T. Schröter, M. Peters, Angew. Chem. Int. Ed. 44 (2005) 4249.
[32] S.M. Wang, X.H. Yu, Z.J. Lin, R.F. Zhang, D.W. He, J.Q. Qin, J.L. Zhu, J. Han, L. Wang, H.K. Mao, J.Z. Zhang, Y.S. Zhao, Chem. Mater. 24 (2012) 3023.
[33] C.L. Bull, P.F. McMillan, E. Soignard, K. Leinenweber, J. Solid State Chem. 177 (2004) 1488.
[34] A. Dewaele, P. Loubeyre, F. Occelli, M. Mezouar, P.I. Dorogokupets, M. Torrent, Phys. Rev. Lett. 97 (2006) 29.
[35] A. Onodera, M. Mimasaka, I. Sakamoto, J. Okumura, K. Sakamoto, S. Uehara, K. Takemura, O. Shimomura, T. Ohtani, Y. Fujii, J. Phys. Chem. Solids 60 (1999) 167.
[36] A.F. Goncharov, V.V. Struzhkin, J. Raman Spectrosc. 34 (2003) 532.
[37] Z. Zhao, K. Bao, D. Duan, F. Tian, B. Liu, T. Cui, RSC Adv. 5 (2015) 31270.

Inorganic Chemistry
Cite This: Inorg. Chem. 2018, 57, 6245−6251
Article
pubs.acs.org/IC

High Pressure and High Temperature Synthesis of the Iron Pernitride FeN_2

Dominique Laniel,*[,†] Agnès Dewaele,[†] and Gaston Garbarino[‡]

[†]CEA, DAM, DIF, F-91297 Arpajon, France
[‡]European Synchrotron Radiation Facility, 6 Rue Jules Horowitz BP220, F-38043 Grenoble CEDEX, France

ABSTRACT: The high pressure chemistry of transition metals and nitrogen was recently discovered to be richer than previously thought, due to the synthesis of several transition metal pernitrides. Here, we explore the pressure-temperature domain of iron with an excess of nitrogen up to 91 GPa and 2200 K. Above 72 GPa and 2200 K, the iron pernitride FeN_2 is produced in a laser-heated diamond anvil cell. This iron-nitrogen compound is the first with a N/Fe ratio greater than 1. The FeN_2 samples were characterized from the maximum observed pressure down to ambient conditions by powder X-ray diffraction and Raman spectroscopy measurements. The crystal structure of FeN_2 is resolved to be a *Pnnm* marcasite structure, analogously to other transition metal pernitrides. On the basis of the lattice's axial ratios and the recorded N-N vibrational modes of FeN_2, a bond order of 1.5 for the nitrogen dimer is suggested. The bulk modulus of the iron pernitride is determined to be of K_0 = 344(13) GPa, corresponding to an astounding increase of about 208% from pure iron. Upon decompression to ambient conditions, a partial structural phase transition to the theoretically predicted $R\bar{3}m$ FeN_2 is detected.

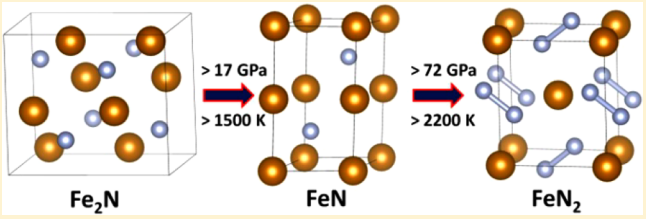

INTRODUCTION

The chemistry of nitrogen-based compounds is a rich research field due to their potential as high-energy density materials,[1−7] their refractory, superconducting as well as catalytic properties,[8,9] their applications for planetary sciences[10−14] and even for hydrogen storage.[15] Transition metal pernitrides recently found significant interest in the field of material sciences as ultrahard solids.[16,17] In 2004, platinum pernitride was obtained by a direct reaction between elements in a laser-heated diamond anvil cell.[18] This first study assigned the stoichiometry PtN to this compound, but it was later correctly identified as PtN_2 with a pyrite structure.[19−22] It was determined to possess an extremely high bulk modulus (K_0 = 372 GPa), explained by its single-bonded nitrogen dimer, as well as to be recoverable to ambient conditions.[19,20] Since this first synthesis, a large variety of theoretical and experimental works have been performed and lead to the discovery of several other transition metal pernitrides, such as IrN_2, with a bulk modulus of 428 GPa[23]—the highest bulk modulus after diamond's—as well as the Os, Pd, Rh, and Ru pernitrides. Most of these compounds were retrieved and found metastable at ambient conditions.[20,23−26] The recent synthesis of TiN_2 and subsequently CoN_2, the first pernitrides with a transition metal in the fourth row of the periodic table, evidenced the possibility for these lower electron elements to produce nitrogen compounds similar to those formed with heavier transition metals.[27,28]

Iron is one of the elements sharing the fourth row of the periodic table with titanium and cobalt. Unlike for these, a large variety of iron nitrides exists, totaling seven stoichiometries: α''-$Fe_{16}N_2$, α'-Fe_8N, γ'-Fe_4N, ε-$Fe_3N_{1\pm x}$, Fe_7N_3, Fe_2N, and, more recently discovered, FeN.[28−32] Interestingly, the bulk modulus of these compounds was observed to steadily increase with nitrogen content, reaching 200 GPa for NiAs-FeN.[32] Recent theoretical calculations have predicted that new iron-nitrogen compounds with a never seen before N/Fe ratio greater than 1 are stable under pressure. The iron pernitride FeN_2 is one of them. A hexagonal ($R\bar{3}m$) phase was anticipated stable above 17 GPa at 1000 K while a marcasite-type phase was determined favored from 34 GPa at the same temperature. Marcasite FeN_2 was calculated to have a high bulk modulus, and charge analysis suggests that the structure bears double-bonded N_2^{2-} dimers.[33−35] While the NiAs-FeN compound was observed to be stable up to 128 GPa and 2000 K,[32] we have extended the scanned temperature range in the search for iron-nitrogen compounds with a higher N/Fe ratio. Indeed, high temperatures can be necessary to cross possible large activation barriers impeding the synthesis of compounds with new stoichiometries.

Here, we report the synthesis of the first iron-nitrogen compound with the N/Fe ratio greater than 1, FeN_2, obtained above 72 GPa and 2200 K. This new pernitride was characterized by powder X-ray diffraction and Raman spectroscopy down to ambient conditions. The structure of FeN_2 is resolved and insight on the nature of the N-N dimer is obtained through the measurement of FeN_2 vibrational modes as well as upon comparison of its lattice axial ratios, previously shown as representative of the dimer's valence state. Furthermore, the bulk modulus of the iron pernitride is determined during

Received: January 6, 2018
Published: March 5, 2018

© 2018 American Chemical Society

DOI: 10.1021/acs.inorgchem.7b03272
Inorg. Chem. 2018, 57, 6245−6251

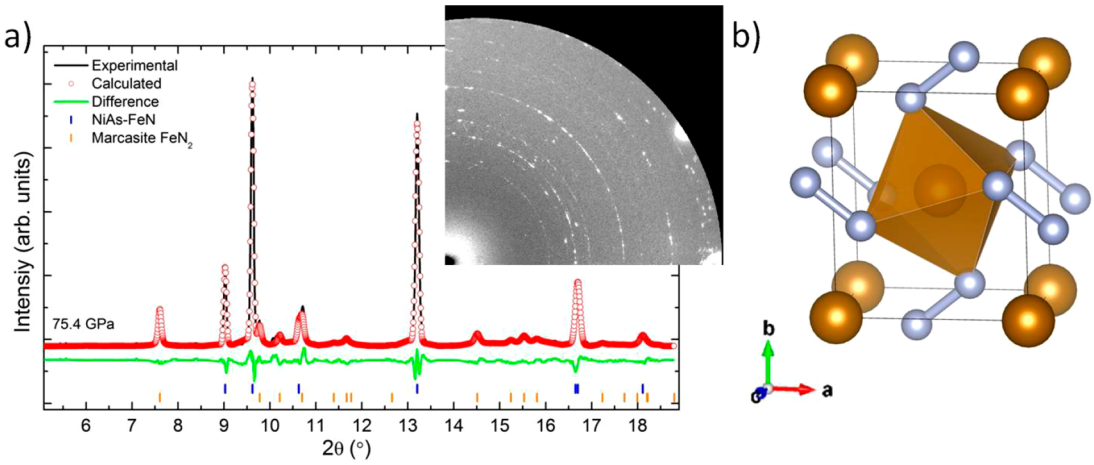

Figure 1. (a) Rietveld refinement of a powder X-ray diffraction pattern obtained at 75.4 GPa. Lattice parameters of FeN_2 at this pressure can be found in Table 2. (Inset) The diffraction pattern's corresponding image plate, showing the fairly homogeneous powder diffraction rings. (b) Marcasite type structure of FeN_2, where the pale blue and orange spheres represent the nitrogen and iron atoms, respectively.

Table 1. Comparison between Experimental and Theoretical Structural Parameters of Marcasite FeN_2[a]

structure	a (Å)	b (Å)	c (Å)	V (Å^3)	N 4g (x,y,0)	
marcasite FeN_2 (28 GPa) (exp.)	3.722(1)	4.427(1)	2.430(1)	40.04(2)	0.141(1)	0.406(1)
marcasite FeN_2 (25 GPa) (theo.)[33]	3.8015	4.5258	2.4840	42.73	0.13016	0.40322
difference (%)	−2.1	−2.2	−2.2	−6.3		

[a]The predicted pseudo-marcasite structure was transformed into a regular marcasite structure.

sample decompression and found to be extremely large. An explanation based on previous theoretical calculations is provided. Finally, upon the complete release of pressure, a partial phase transition in FeN_2 is detected and verified to match the predicted low pressure phase of FeN_2.

EXPERIMENTAL METHOD

Iron and nitrogen were studied in membrane diamond anvil cells (DACs) equipped with anvil's culet of 150 or 100 μm in diameter, designed to explore the Fe-N system beyond 70 GPa. Iron powder grains were compressed into a thin foil of about 1.5 μm in thickness. To ensure chemical and thermal insulation from the diamond anvils, the Fe foils were positioned on top of c-BN micrograins. Nitrogen, acting as both a reactant and a pressure transmitting medium, was loaded with the Fe at 1400 bar in the DACs. With respect to iron, nitrogen was always largely in excess. Gold micrograins and a ruby microsphere were also put into the DAC and utilized as pressure calibrants.[36]

Confocal Raman spectroscopy was performed using an Alpha300M+ instrument (WITec). Immediately after sample loading, Raman measurements were done to ensure that the iron foil was not in contact with the anvils and that molecular nitrogen completely surrounded it. Characterization of the reacted sample during its decompression was also achieved by Raman spectroscopy. Sample excitation was accomplished with a continuous Ar-Kr laser using the 647.1 nm line with a focused laser spot of less than 1 μm. The Stokes Raman signal was collected in a backscattering geometry by a CCD coupled to a 600 l/mm grating, allowing a spectral resolution of approximately 6 cm^{-1}. Automated motorized sample positioning with piezo-driven scan stages of submicron accuracy allowed for precise Raman spectral imaging of the samples.

The X-ray diffraction characterization was performed at the ID27 beamline of the European Synchrotron Radiation Facility (ESRF) in angular-dispersive mode. The X-ray beam, with λ = 0.3738 Å, was focused by two Kirkpatrick−Baez mirrors and cleaned by one pinhole to an ~3 × 3 μm^2 spot on the sample. The beamline is equipped with an online YAG laser-heating setup and bidimensional detectors, calibrated using a CeO_2 reference sample. In order to overcome possible activation barriers, laser-heating was performed through both openings of the DACs, achieving temperatures over 2200 K in the bulk of the sample. Temperatures during laser-heating were accurately measured from the sample's blackbody radiation.[37]

RESULTS AND DISCUSSION

The pure iron flake surrounded by molecular nitrogen was compressed to 75.4 GPa, a pressure at which the sample was moderately laser-heated (below 1200 K), resulting in the synthesis of the well-known NiAs-FeN.[28,31,32] A second round of laser-heating, this time above 2200 K, resulted in the detection of new diffraction lines that could not be attributed to any established Fe-N phase or the pure elements (see Figure 1). The same sample was heated once more at 2200 K and 91.3 GPa, resulting in the observation of the same diffraction lines. A second sample also heated at 2200 K and 72.5 GPa produced a similar X-ray diffraction pattern to the one presented in Figure 1. Through a Rietveld refinement (shown in Figure 1) done at 75.4 GPa, these new peaks were found to be perfectly fitted by a marcasite ($Pnnm$) orthorhombic structure (a = 3.722(1) Å, b = 4.427(1) Å, and c = 2.430(1) Å), with the Fe and N atoms on the 2a (0, 0, 0) and 4g (0.141, 0.406, 0) Wyckoff positions. The N/Fe ratio of 2 corresponds to the FeN_2 stoichiometry, expected to be stable under high pressure in excess nitrogen by theoretical calculations.[33−35] The proposed marcasite structure is isostructural to the theoretically predicted pseudo-marcasite structure of FeN_2, and the transformation from the latter to the former is done through a simple change of the y parameter ($y \rightarrow 0.5 - y$) of the Wyckoff positions.[33] The measured lattice parameters and Wyckoff positions closely match the forecasted structure,[33] as compared in Table 1. The marcasite structure is commonly observed in other transition metal pernitrides, such as OsN_2 and RuN_2,[23,26] whose metallic elements are just below Fe in the periodic table, as well as CoN_2 and RhN_2.[25,28] This atomic arrangement contains FeN_6 octahedrons with a slight

DOI: 10.1021/acs.inorgchem.7b03272
Inorg. Chem. 2018, 57, 6245−6251

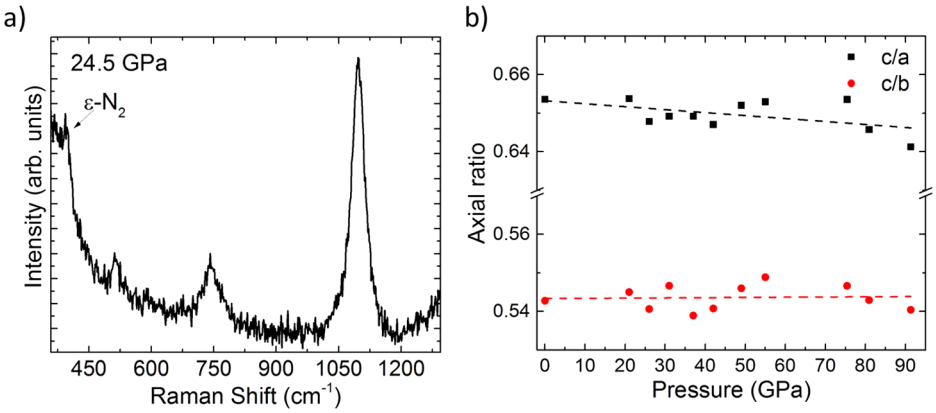

Figure 2. (a) Representative Raman spectrum of the marcasite FeN_2 at 24.5 GPa. The most intense Raman mode, centered at 1097 cm^{-1}, corresponds to the A_g symmetric stretching mode of the nitrogen dimer. (b) Evolution of the FeN_2 lattice axial ratios with pressure. While the c/b is almost constant, the c/a ratio slightly decreases with pressure, indicating a softer c (and b) axis.

distortion and rotation, allowing the N−N bonds (see Figure 1).

Further laser-heating of the sample did not allow a more complete transformation into marcasite FeN_2, which could be attributed to its formation at the iron−nitrogen interface and acting as a diffusion barrier to nitrogen into the bulk of the iron flake. This is a common occurrence in pernitrides as PtN_2, IrN_2, CoN_2, and others were also synthesized in DACs as a minority phase mixed with the unreacted reagents.[20,23−28]

On the basis of the refined atomic positions, the covalently bonded nitrogen dimers have an intramolecular distance of 1.32 Å in marcasite FeN_2, which is closer to the expected length of a double bond (∼1.2−1.3 Å)[38−40] rather than a triple (∼1.1 Å)[41] or a single bond (∼1.4 Å).[41] However, due to the large electron number difference between Fe (Z = 26) and N (Z = 7), the performed Rietveld refinement is not very sensitive to the nitrogen atom's position (nor its partial occupancy). Indeed, manually changing its position to (0.15, 0.1, 0), yielding a N−N distance of 1.41 Å that matches that of a single bond, results in a χ^2 difference of only 0.4%, imperceptibly changing the quality of the fit to the eyes. A similar result regarding the atomic partial occupancies was obtained, with variations up to 14% for N, producing a 1% variation of χ^2. Further insight on the nature of the N_2 dimer covalent bond could be obtained based on the empirical relationship found between lattice axial ratios and the transition metal valence state in marcasite-type $M^{+y}(X_2)^{-y}$ pnictides and chalcogenides (where M is a transition metal, the X is a pnictide or a chalcogenide, and y is the valence state).[42] Indeed, these compounds were observed to have the transition metal valence state decrease concomitantly with increasing c/a and c/b ratios, ranging from 4+ (lower axial ratios) to 2+ (higher axial ratios). Rhodium pernitride has an axial ratio in between compounds with a transition metal valence state of 2+ and 4+ which suggests, according to this relationship, a valence state closer to 3+ for Rh and thus a N−N bond order of about 1.5. Raman spectroscopy measurements validated the proposed bond order in RhN_2.[42] Analogously, the c/a and c/b ratios for marcasite FeN_2, plotted in Figure 2b, average 0.650 and 0.542, respectively, over pressure and fall close to that of RhN_2 (c/a = 0.685, c/b = 0.568), thus advocating for a $\sim(N_2)^{3-}$ dimer with a bonding order of ∼1.5.[42]

Further insight into the nature of the N−N bond could also be obtained by Raman spectroscopy measurements (see Figure 2). The spectra reveal three vibrational modes belonging to FeN_2, all at frequencies below 1200 cm^{-1}. That amount of measured modes is within prediction based on group theory analysis, since the $M^{+y}(X_2)^{-y}$-type marcasite structure with X-X dumbbells allows six Raman active modes ($\Gamma = 2A_g + 2B_1 + B_{2g} + B_{3g}$). The symmetric stretching mode (A_g), typically the most intense, provides insight into the nature of the N−N covalent bond as its frequency strongly depends on the bonding order. A triple-, double-, and single-bonded nitrogen dimer has a typical frequency of 2400, 1300−1550, and 700−850 cm^{-1}, respectively, at ambient conditions.[19,24,38−40,43−45] In our case, the measured value of the A_g mode is of 1056 cm^{-1} at ambient pressure, which sits in between that of a single and double bond. This observation, along with the extremely high bulk modulus of marcasite FeN_2 (see below), further suggests a bond order of about 1.5. This analysis falls in line with results on RhN_2 which has a very similar A_g mode frequency (about 1010 cm^{-1} near 12 GPa) and an assigned bond order of 1.5.[25] Moreover, a $(N_2)^{3-}$ radical formed at ambient conditions in yttrium complexes was determined to have its vibrational mode at 989 cm^{-1}.[46] However, as thoroughly demonstrated in the study of the $Li_2Ca_3[N_2]_3$ compound, multiple techniques, such as electron spin resonance and magnetic measurements, are vital to conclusively assert a N_2 dimer's bond order.[47] These measurements would be very difficult to perform on the small amount of sample synthesized here especially due to its coexistence with magnetic NiAs-FeN.[31]

The measurement of Raman modes from marcasite FeN_2 suggests the compound's nonmetallicity. The IrN_2, PtN_2 as well as RhN_2 pernitrides were also deemed nonmetallic based on the observation of Raman modes.[19,20,23,25]

Interestingly, our experimental results regarding the $(N_2)^{3-}$ dimer with a bond order of about 1.5 and the sample nonmetallic nature contrast with conclusions based on *ab initio* calculations. Bader charge analysis previously performed on FeN_2[33] showed the Fe atom to transfer 1.6 electrons to the N dimer. Due to the known underestimation of these types of calculations (finding a charge of +0.85 for the Na cation in the NaCl salt, for example),[48] N_2^{-2} units, corresponding to a N═N double bond, were expected and deemed reasonable. The discrepancy between theoretical and experimental results regarding the compound's metallic or nonmetallic nature could be explained by the larger than anticipated electron transfer from the Fe atom to the N dimer (closer to 3 instead of

DOI: 10.1021/acs.inorgchem.7b03272
Inorg. Chem. 2018, 57, 6245−6251

1.6) which, in turn, could substantially modify the electron density of state computation and thus the compound's band gap calculations. The known underestimation of the density functional theory gradient-corrected approximation (DFT-GGA) calculations of a material's band gap, along with the misleading Bader charge calculations, could also be at play.[49,50]

The high pressure and high temperature synthesized FeN_2 samples were decompressed back to ambient pressure and characterized by Raman spectroscopy and X-ray diffraction (Figure 3). Table 2 provides the measured lattice parameters of

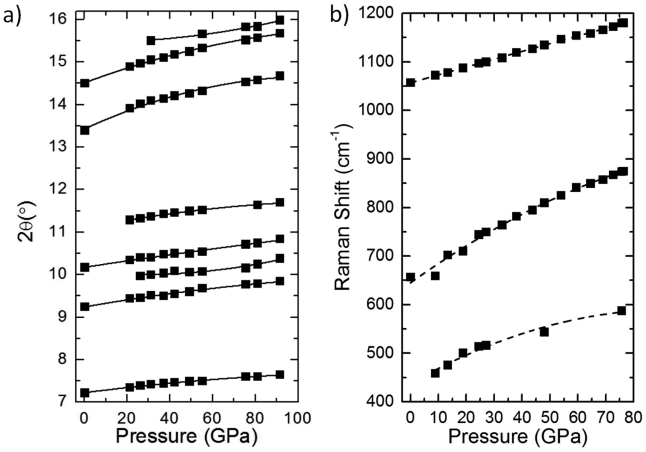

Figure 3. Characterization of marcasite FeN_2 upon its decompression to ambient condition. (a) X-ray diffraction lines' and (b) vibrational modes' evolution with pressure.

Table 2. Unit Cell Parameters and Volume of Marcasite FeN_2 Measured up to 91 GPa

P (GPa)	a (Å)	b (Å)	c (Å)	V (Å^3)
0	3.850(1)	4.636(1)	2.516(1)	44.91(2)
21.3	3.797(1)	4.554(1)	2.482(1)	42.93(2)
37.8	3.749(1)	4.516(1)	2.434(1)	41.20(2)
55.2	3.722(1)	4.427(1)	2.430(1)	40.04(2)
75.4	3.667(1)	4.384(1)	2.396(1)	38.52(2)
91.3	3.662(1)	4.345(1)	2.348(1)	37.37(2)

FeN_2 at various pressures. The smooth evolution of the X-ray diffraction lines as well as of the vibrational modes reveals no phase transition in marcasite FeN_2 along with its retrievability down to ambient conditions.

The volume−pressure data of marcasite FeN_2 shown in Figure 4, obtained with gold as a pressure calibrant, was fitted with a third-order Birch−Murnaghan equation of state. The compound was determined to have an extremely high bulk modulus of 344(13) GPa, with its pressure derivative fixed at $K_0' = 4$ and a refined $V_0 = 45.1(2)$ Å^3. Even though the unit cell volume was experimentally determined at ambient pressure, the low number of diffraction lines used to calculate it yields a lower accuracy. It is for this reason that the fitted value of V_0 was retained instead of the measured one. This fitted value provides a more conservative K_0, which would otherwise have been of $K_0 = 360(5)$ GPa (with V_0 fixed to 45.91 Å^3). These parameters could be tweaked by performing further experiments.

The bulk modulus of FeN_2 is by far the largest of any other Fe-N compound: Fe_4N (155 GPa), Fe_7N_3 (168 GPa), Fe_2N (190 GPa), and NiAs-FeN (200 GPa) as well as pure iron (165

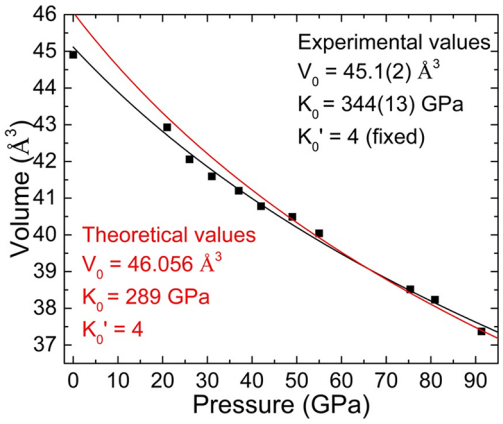

Figure 4. Volume of the marcasite FeN_2 lattice with respect to pressure. The black squares represent the measured V−P data, fitted with a third-order Birch−Murnaghan equation of state. The theoretically calculated values result in an overestimation the compound's volume at low pressure as well as an underestimation at pressures beyond 65 GPa, as shown with the red curve.

GPa).[29,30,32,51] Compared to other transition metal pernitrides, FeN_2 has the third largest, only behind IrN_2 (428 GPa) and OsN_2 (358 GPa),[23] which values are not too far from the K_0 of their pure metallic element Ir (365 GPa, 17% increase) and Os (395 GPa, 9% decrease), respectively. In comparison, the addition of N dimers to pure Fe provides marcasite FeN_2 with the largest increase in bulk modulus (about 208%). While pernitrides are known to have a large K_0, especially when single-bonded N-N dimers are formed, such a dramatic increase from the pure transition metal element was never previously observed.

Theoretical calculations forecasted a bulk modulus of 385 at 25 GPa, with $V_{25\ GPa} = 42.75$ Å^3.[33] In order for an adequate comparison with the experimental results to be possible, the corresponding bulk modulus and volume values were extrapolated from 25 GPa to ambient pressure. Using $K_0' = 4$, a $K_0 = 289$ GPa and $V_0 = 46.056$ Å^3 are obtained (see Figure 4). The discrepancy between calculated and experimental bulk modulus values is in part due to the volume overestimation of the calculations at a given pressure. Indeed, if the equilibrium volume is overestimated by *ab initio* calculations, the bulk modulus is also underestimated.[36] This can be corrected by utilizing the calculated bulk modulus at experimental equilibrium value (45.1(2) Å^3), here yielding 314 GPa. Thus, only a 9% discrepancy exists between the experimental and the corrected theoretical predictions. This difference could be attributed to errors in the DFT.

Theoretical calculations are insightful with regards to explaining a pernitrides' low compressibility in relation with the N dimer; directly linked to the filling of N-N antibonding molecular orbitals ($1\pi_g^*$) and the metal's valence state, which can be modeled using crystal orbital Hamilton population (COHP) computations.[45,52] These antibonding states are progressively filled as the metallic element transfers to the N dimer more electrons, i.e., as its valence state is higher. Filled molecular antibonding states result in an increased repulsion between the two N atoms, leading to a higher bulk modulus. With this approach, the low bulk modulus of BaN_2 and the high bulk modulus of TiN_2 and PtN_2 are well understood.[16,45] The COHP of the N-N dimer in marcasite FeN_2 was calculated in ref 33, and the N-N antibonding states are seen to be almost

DOI: 10.1021/acs.inorgchem.7b03272
Inorg. Chem. 2018, 57, 6245−6251

completely filled, similarly to what is observed in PtN_2.[45] This leads to believe that these filled states are responsible for the extremely high bulk modulus of marcasite FeN_2. Additionally, this further underlines the plausibility of a bond order of 1.5 (over one of greater value) as it suggests a significant filling of the antibonding orbitals. Of course, as demonstrated in $PtAs_2$, other parameters such as the structure and charge transfer behavior with pressure can also have an effect, although here deemed minor, on a solid's compressibility.[53]

Upon reaching ambient pressure during the sample decompression, new low intensity X-ray diffraction lines were detected, adding to those belonging to marcasite FeN_2 and NiAs-FeN. These diffraction lines were unambiguously determined to match a hexagonal ($R\bar{3}m$) structure with a = 2.855(1) Å and c = 10.605(1) Å, as shown through a Le Bail refinement (Figure 5). The powder's significant texture did not allow for a Rietveld refinement. The proposed unit cell—both its lattice parameters and its determined space group—agrees very well with the theoretically predicted $R\bar{3}m$ FeN_2 phase (see Table 3).[34] Thus, a phase transition from marcasite FeN_2 to $R\bar{3}m$ FeN_2 is concluded to have occurred. This observation is in line with the enthalpies of $R\bar{3}m$ FeN_2 and marcasite FeN_2 calculated within DFT: at 0 K, the $R\bar{3}m$ phase has a lower enthalpy than the marcasite phase below 11−22 GPa, depending on the details of the calculation.[33,34]

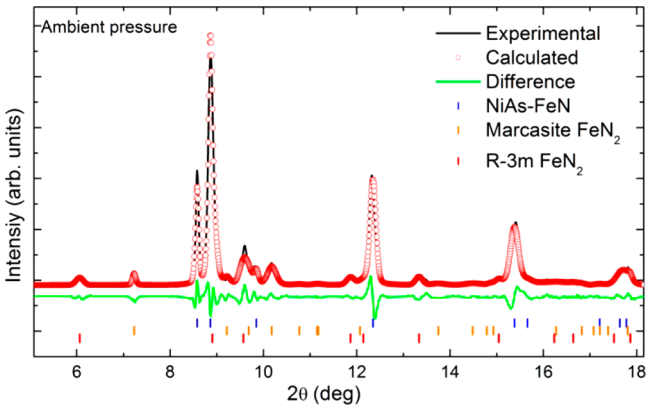

Figure 5. Le Bail refinement at ambient conditions of a decompressed marcasite FeN_2 sample. New low intensity diffraction lines are displayed to be properly fitted by the theoretically predicted $R\bar{3}m$ FeN_2 compound.

Table 3. Comparison between Experimental and Theoretical Structural Parameters of $R\bar{3}m$ FeN_2

structure	a (Å)	b (Å)	c (Å)	V (Å^3)
$R\bar{3}m$ FeN_2 (0 GPa) (exp.)	2.855(1)	2.855(1)	10.605(1)	64.62(2)
$R\bar{3}m$ FeN_2 (0 GPa) (theo.)[34]	2.835	2.835	10.624	63.83
difference (%)	0.7	0.7	0.2	1.2

Below 12.5 GPa, it was previously evidenced that Fe_2N is the stable phase as it is produced directly from pure iron and excess nitrogen upon laser-heating.[29,32] However here, it is observed that while it is energetically unfavorable, marcasite FeN_2 prefers to transform into the metastable $R\bar{3}m$ FeN_2 under 10 GPa rather than decomposing into $^1/_2(Fe_2N + 3/2N_2)$. This observation emphasizes that chemical reactions have non-negligible energy barriers unlike martensitic phase transformations which are typically athermal and thus do not require heating to proceed. It also underlines that the thermodynamical pathway can be critical in synthesizing a given phase; as shown here, the only approach producing $R\bar{3}m$ FeN_2 is the decompression of same-stoichiometry marcasite FeN_2. A similar observation was made for NiAs-type FeN and CoN compounds: upon decompression to ambient conditions, the NiAs structure spontaneously transforms to the ZnS structure, instead of chemically reacting into the stable phases under these conditions.[28,32]

In the current work, laser-heating above 2200 K was performed between 72 and 91 GPa and marcasite FeN_2 was always observed. In our previous experiments, iron samples were heated in an excess of N_2 up to 130 GPa.[32] Combining the results presented in this work with those reported in previous studies allows an updated plot of the experimentally determined pressure stability domain of each known iron nitrides produced in excess of nitrogen, drawn in Figure 6. The stability domain of marcasite FeN_2 is tentatively set at 72.5 GPa, while it could be lower as Niwa et al.[28] reported a new phase appearing after laser-heating NiAs-FeN in an excess of N_2 at about 60 GPa. While the high pressure stability limit of marcasite FeN_2 is not known, theoretical simulations predict nitrogen-richer Fe_xN_y compounds, i.e., FeN_4.[33] This phase might have been synthesized as part of our experiments on laser-heated FeN_2 at 91 GPa and above 2200 K as new faint diffraction lines were observed, but the related phase could not be sufficiently well characterized.

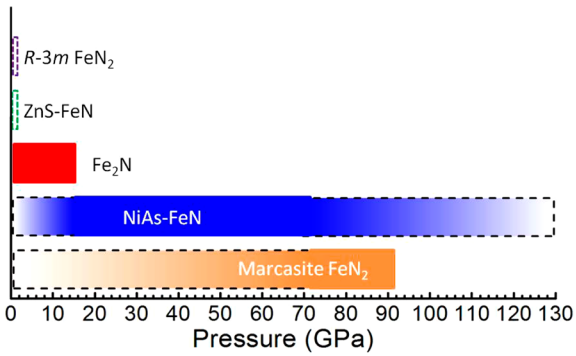

Figure 6. Pressure stability domains of the five iron nitrides observed when in an excess of molecular nitrogen, with the exception of ambient pressure where gaseous N_2 escapes the DAC. The full rectangles represent the experimentally measured stability domains while the shaded sections with a dashed outline mark the metastability pressure domains. ZnS-FeN and $R\bar{3}m$ FeN_2 are only observed during pressure release of NiAs-FeN and marcasite FeN_2, respectively, to ambient conditions. The stability domain of Fe_2N has been determined in our previous work.[32] The pressure which delimits the stability domains of NiAs-FeN and marcasite-FeN_2 has been tentatively set to 72 GPa (see text).

■ CONCLUSION

In this work, iron and nitrogen were compressed to 72.5 GPa and laser-heated above 2200 K, temperature allowing to overcome the energy barrier toward the formation of the more stable compound FeN_2. This is the first synthesis of an iron-nitrogen compound with a N/Fe ratio greater than 1. The iron pernitride was structurally resolved and determined to adopt the common marcasite structure, matching the

DOI: 10.1021/acs.inorgchem.7b03272
Inorg. Chem. 2018, 57, 6245−6251

theoretically predicted structure.[33] Through lattice parameters length ratio considerations as well as the measurement of its Raman vibrational frequencies, the bond order of the nitrogen dimer was determined to be of approximately 1.5, which is analogous to that of rhodium pernitride.[25,42] The detection of these Raman modes suggests marcasite FeN_2 to be nonmetallic, differing from the theoretical prediction.[33] The characterization of marcasite FeN_2 down to ambient conditions revealed an astoundingly large bulk modulus of 344(13) GPa, representing a 208% increase over pure iron's bulk modulus. While this makes FeN_2 the iron nitride with the highest K_0 value, it is also third compared to other transition metal pernitrides, only behind IrN_2 and OsN_2. A better theoretical understanding of the drastic gain in hardness discovered in marcasite FeN_2 might uncover new methods to produce high bulk modulus materials. Finally, at ambient pressure, a partial transition to $R\bar{3}m$ FeN_2 is detected, implying this low pressure phase to be metastable and only found through the decompression of marcasite FeN_2. The X-ray diffraction and Raman data indicate that marcasite FeN_2 is partially retained after complete decompression. The determination of its metastability lifetime would provide an understanding of its decomposition pathway and eventually allow blocking this transformation. Only then could this possible ultrahard compound be fully characterized and contemplated for eventual industrial applications. Moreover, the synthesis of ternary compounds under pressure, for instance in the Fe-C-N system, is another possibility that needs extensive experimental studies and that could also result in compounds relevant for the industry.

■ AUTHOR INFORMATION

Corresponding Author

*E-mail: dominique.laniel@cea.fr.

ORCID

Dominique Laniel: 0000-0002-6889-9820

Notes

The authors declare no competing financial interest.

■ ACKNOWLEDGMENTS

The authors gratefully acknowledge the Centre National d'Études Spatiales (CNES) and the Natural Sciences and Engineering Research Council of Canada (NSERC) for financially supporting the Ph.D. of D.L. The authors also acknowledge the European Synchrotron Radiation Facility (ESRF) for provision of beamtime at the ID27 beamline under proposal CH-5255.

■ REFERENCES

(1) Peng, F.; Yao, Y.; Liu, H.; Ma, Y. Crystalline LiN_5 Predicted from First-Principles as a Possible High-Energy Material. *J. Phys. Chem. Lett.* **2015**, *6*, 2363−2366.

(2) Steele, B. A.; Stavrou, E.; Crowhurst, J. C.; Zaug, J. M.; Prakapenka, V. B.; Oleynik, I. I. High-Pressure Synthesis of a Pentazolate Salt. *Chem. Mater.* **2017**, *29* (2), 735−741.

(3) Laniel, D.; Sebastiao, E.; Cook, C.; Murugesu, M.; Hu, A.; Zhang, F.; Desgreniers, S. Dense Nitrogen-Rich Energetic Materials: A Study of 5,5′-bis(1H-Tetrazolyl)amine. *J. Chem. Phys.* **2014**, *140*, 184701.

(4) Peng, F.; Wang, Y.; Wang, H.; Zhang, Y.; Ma, Y. Stable Xenon Nitride at High Pressures. *Phys. Rev. B: Condens. Matter Mater. Phys.* **2015**, *92*, 094104.

(5) Vaitheeswaran, G.; Babu, K. R. Metal Azides under Pressure : An Emerging Class of High Energy. *J. Chem. Sci.* **2012**, *124* (6), 1391−1398.

(6) Ciezak, J. A.; Rice, B. M. *Polymeric Nitrogen: The Ultimate, Green High Performing Energetic Material*; U.S. Army Research Laboratory: Aberdeen Proving Ground, Maryland, 2006.

(7) Zhang, L.; Wang, Y.; Lv, J.; Ma, Y. Materials Discovery at High Pressures. *Nat. Rev. Mater.* **2017**, *2*, 17005.

(8) Salamat, A.; Hector, A. L.; Kroll, P.; McMillan, P. F. Nitrogen-Rich Transition Metal Nitrides. *Coord. Chem. Rev.* **2013**, *257* (13−14), 2063−2072.

(9) Friedrich, A.; Winkler, B.; Juarez-Arellano, E. A.; Bayarjargal, L. Synthesis of Binary Transition Metal Nitrides, Carbides and Borides from the Elements in the Laser-Heated Diamond Anvil Cell and Their Structure-Property Relations. *Materials* **2011**, *4* (10), 1648−1692.

(10) Qian, G.-R.; Hu, C.-H.; Oganov, A. R.; Zeng, Q.; Zhou, H.-Y.; Niu, H. Diverse Chemistry of Stable Hydronitrogens, and Implications for Planetary and Materials Sciences. *Sci. Rep.* **2016**, *6*, 25947.

(11) Chidester, B. A.; Strobel, T. A. The Ammonia-Hydrogen System under Pressure. *J. Phys. Chem. A* **2011**, *115* (38), 10433−10437.

(12) Goncharov, A. F.; Holtgrewe, N.; Qian, G.; Hu, C.; Oganov, A. R.; Somayazulu, M.; Stavrou, E.; Pickard, C. J.; Berlie, A.; Yen, F.; et al. Backbone N X H Compounds at High Pressures. *J. Chem. Phys.* **2015**, *142*, 214308.

(13) Palasyuk, T.; Troyan, I.; Eremets, M.; Drozd, V.; Medvedev, S.; Zaleski-Ejgierd, P.; Magos-Palasyuk, E.; Wang, H.; Bonev, S. a.; Dudenko, D.; et al. Ammonia as a Case Study for the Spontaneous Ionization of a Simple Hydrogen-Bonded Compound. *Nat. Commun.* **2014**, *5*, 3460.

(14) Ninet, S.; Datchi, F.; Dumas, P.; Mezouar, M.; Garbarino, G.; Mafety, A.; Pickard, C. J.; Needs, R. J.; Saitta, A. M. Experimental and Theoretical Evidence for an Ionic Crystal of Ammonia at High Pressure. *Phys. Rev. B: Condens. Matter Mater. Phys.* **2014**, *89* (17), 174103.

(15) Nakamori, Y.; Orimo, S. Li−N Based Hydrogen Storage Materials. *Mater. Sci. Eng., B* **2004**, *108* (1−2), 48−50.

(16) Zhang, M.; Cheng, K.; Yan, H.; Wei, Q.; Zheng, B. Electronic Bonding Analyses and Mechanical Strengths of Incompressible Tetragonal Transition Metal Dinitrides TMN 2 (TM = Ti, Zr, and Hf). *Sci. Rep.* **2016**, *6*, 36911.

(17) Soto, G. Computational Study of Hf, Ta, W, Re, Ir, Os and Pt Pernitrides. *Comput. Mater. Sci.* **2012**, *61*, 1−5.

(18) Gregoryanz, E.; Sanloup, C.; Somayazulu, M.; Badro, J.; Fiquet, G.; Mao, H.; Hemley, R. J. Synthesis and Characterization of a Binary Noble Metal Nitride. *Nat. Mater.* **2004**, *3* (5), 294−297.

(19) Young, A. F.; Montoya, J. A.; Sanloup, C.; Lazzeri, M.; Gregoryanz, E.; Scandolo, S. Interstitial Dinitrogen Makes PtN_2 an Insulating Hard Solid. *Phys. Rev. B: Condens. Matter Mater. Phys.* **2006**, *73* (15), 153102.

(20) Crowhurst, J. C.; Goncharov, A. F.; Sadigh, B.; Evans, C. L.; Morrall, P. G.; Ferreira, J. L.; Nelson, A. J. Synthesis and Characterization of the Nitrides of Platinum and Iridium. *Science* **2006**, *311*, 1275.

(21) Yu, R.; Zhang, X. F. Platinum Nitride with Fluorite Structure. *Appl. Phys. Lett.* **2005**, *86* (12), 121913.

(22) Yu, R.; Zhang, X. F. Family of Noble Metal Nitrides: First Principles Calculations of the Elastic Stability. *Phys. Rev. B: Condens. Matter Mater. Phys.* **2005**, *72* (5), 054103.

(23) Young, A. F.; Sanloup, C.; Gregoryanz, E.; Scandolo, S.; Hemley, R. J.; Mao, H. K. Synthesis of Novel Transition Metal Nitrides IrN2 and OsN2. *Phys. Rev. Lett.* **2006**, *96*, 155501.

(24) Crowhurst, J. C.; Goncharov, A. F.; Sadigh, B.; Zaug, J. M.; Aberg, D.; Meng, Y.; Prakapenka, V. B. Synthesis and Characterization of Nitrides of Iridium and Palladium. *J. Mater. Res.* **2008**, *23* (1), 1−5.

(25) Niwa, K.; Dzivenko, D.; Suzuki, K.; Riedel, R.; Troyan, I.; Eremets, M.; Hasegawa, M. High Pressure Synthesis of Marcasite-Type Rhodium Pernitride. *Inorg. Chem.* **2014**, *53* (2), 697−699.

(26) Niwa, K.; Suzuki, K.; Muto, S.; Tatsumi, K.; Soda, K.; Kikegawa, T.; Hasegawa, M. Discovery of the Last Remaining Binary Platinum-Group Pernitride RuN2. *Chem. - Eur. J.* **2014**, *20* (43), 13885−13888.

DOI: 10.1021/acs.inorgchem.7b03272
Inorg. Chem. 2018, 57, 6245−6251

(27) Bhadram, V. S.; Kim, D. Y.; Strobel, T. A. High-Pressure Synthesis and Characterization of Incompressible Titanium Pernitride. *Chem. Mater.* **2016**, *28* (6), 1616−1620.
(28) Niwa, K.; Terabe, T.; Kato, D.; Takayama, S.; Kato, M.; Soda, K.; Hasegawa, M. Highly Coordinated Iron and Cobalt Nitrides Synthesized at High Pressures and High Temperatures. *Inorg. Chem.* **2017**, *56*, 6410−6418.
(29) Hasegawa, M.; Yagi, T. Systematic Study of Formation and Crystal Structure of 3d-Transition Metal Nitrides Synthesized in a Supercritical Nitrogen Fluid under 10 GPa and 1800 K Using Diamond Anvil Cell and YAG Laser Heating. *J. Alloys Compd.* **2005**, *403* (1−2), 131−142.
(30) Wriedt, H. A.; Gokcen, N. A.; Nafziger, R. H. The Fe−N (Iron−Nitrogen) System. *Bull. Alloy Phase Diagrams* **1987**, *8*, 355.
(31) Clark, W. P.; Steinberg, S.; Dronskowski, R.; McCammon, C.; Kupenko, I.; Bykov, M.; Dubrovinsky, L.; Akselrud, L. G.; Schwarz, U.; Niewa, R. High-Pressure NiAs-Type Modification of FeN. *Angew. Chem., Int. Ed.* **2017**, *56*, 7302−7306.
(32) Laniel, D.; Dewaele, A.; Anzellini, S.; Guignot, N. Study of the Iron Nitride FeN into the Megabar Regime. *J. Alloys Compd.* **2018**, *733*, 53−58.
(33) Wang, Z.; Li, Y.; Li, H.; Harran, I.; Jia, M.; Wang, H.; Chen, Y.; Wang, H.; Wu, N. Prediction and Characterization of the Marcasite Phase of Iron Pernitride under High Pressure. *J. Alloys Compd.* **2017**, *702*, 132−137.
(34) Wessel, M.; Dronskowski, R. A New Phase in the Binary Iron Nitrogen System?-The Prediction of Iron Pernitride, FeN2. *Chem. - Eur. J.* **2011**, *17* (9), 2598−2603.
(35) Gupta, S. D.; Gupta, S. K.; Jha, P. K. Structural, Electronic and Dynamical Stability of Heavy Metal Iron Pernitride: A Spin Polarized First-Principles Study. *Eur. Phys. J. B* **2013**, *86*, 8.
(36) Dewaele, A.; Torrent, M.; Loubeyre, P.; Mezouar, M. Compression Curves of Transition Metals in the Mbar Range: Experiments and Projector Augmented-Wave Calculations. *Phys. Rev. B: Condens. Matter Mater. Phys.* **2008**, *78* (10), 104102.
(37) Mezouar, M.; Giampaoli, R.; Garbarino, G.; Kantor, I.; Dewaele, A.; Weck, G.; Boccato, S.; Svitlyk, V.; Rosa, A. D.; Torchio, R.; et al. Methodology for in Situ Synchrotron X-Ray Studies in the Laser-Heated Diamond Anvil Cell. *High Pressure Res.* **2017**, *37* (2), 170−180.
(38) Schneider, S. B.; Frankovsky, R.; Schnick, W. Lithium Diazenide High-Pressure Synthesis and Characterization of the Alkali Diazenide Li2N2. *Angew. Chem., Int. Ed.* **2012**, *51*, 1873−1875.
(39) Schneider, S. B.; Frankovsky, R.; Schnick, W. Synthesis of Alkaline Earth Diazenides MAEN2 (MAE = Ca, Sr, Ba) by Controlled Thermal Decomposition of Azides under High Pressure. *Inorg. Chem.* **2012**, *51* (4), 2366−2373.
(40) Auffermann, G.; Prots, Y.; Kniep, R. SrN and SrN 2 : Diazenides by Synthesis under. *Angew. Chem., Int. Ed.* **2001**, *40* (3), 547−549.
(41) Eremets, M. I.; Gavriliuk, A. G.; Serebryanaya, N. R.; Trojan, I. A.; Dzivenko, D. A.; Boehler, R.; Mao, H. K.; Hemley, R. J. Structural Transformation of Molecular Nitrogen to a Single-Bonded Atomic State at High Pressures. *J. Chem. Phys.* **2004**, *121* (22), 11296−11300.
(42) Niwa, K.; Terabe, T.; Suzuki, K.; Shirako, Y.; Hasegawa, M. High-Pressure Stability and Ambient Metastability of Marcasite-Type Rhodium Pernitride. *J. Appl. Phys.* **2016**, *119* (6), 065901.
(43) Eremets, M. I.; Gavriliuk, A. G.; Trojan, I. A.; Dzivenko, D. A.; Boehler, R. Single-Bonded Cubic Form of Nitrogen. *Nat. Mater.* **2004**, *3*, 558−563.
(44) Schneider, H.; Häfner, W.; Wokaun, A.; Olijnyk, H. Room Temperature Raman Scattering Studies of External and Internal Modes of Solid Nitrogen at Pressures $8 \leq P \leq 54$ GPa. *J. Chem. Phys.* **1992**, *96* (11), 8046.
(45) Wessel, M.; Dronskowski, R. Nature of N-N Bonding within High-Pressure Noble-Metal Pernitrides and the Prediction of Lanthanum Pernitride. *J. Am. Chem. Soc.* **2010**, *132*, 2421−2429.
(46) Evans, W. J.; Fang, M.; Zucchi, G.; Furche, F.; Ziller, J. W.; Hoekstra, R. M.; Zink, J. I. Isolation of Dysprosium and Yttrium Complexes of a Three-Electron Reduction Product in the Activation of Dinitrogen, the (N2)-3 Radical. *J. Am. Chem. Soc.* **2009**, *131*, 11195−11202.
(47) Schneider, S. B.; Seibald, M.; Deringer, V. L.; Stoffel, R. P.; Frankovsky, R.; Friederichs, G. M.; Laqua, H.; Duppel, V.; Jeschke, G.; Dronskowski, R.; et al. High-Pressure Synthesis and Characterization of Li2Ca 3[N2]3-An Uncommon Metallic Diazenide with [N2]2-Ions. *J. Am. Chem. Soc.* **2013**, *135* (44), 16668−16679.
(48) Henkelman, G.; Arnaldsson, A.; Jónsson, H. A Fast and Robust Algorithm for Bader Decomposition of Charge Density. *Comput. Mater. Sci.* **2006**, *36* (3), 354−360.
(49) Hasnip, P. J.; Refson, K.; Probert, M. I. J.; Yates, J. R.; Clark, S. J.; Pickard, C. J. Density Functional Theory in the Solid State. *Philos. Trans. R. Soc., A* **2014**, *372*, 20130270.
(50) Perdew, J. P. Density Functional Theory and the Band Gap Problem. *Int. J. Quantum Chem.* **1985**, *28* (S19), 497−523.
(51) Dewaele, A.; Loubeyre, P.; Occelli, F.; Mezouar, M.; Dorogokupets, P. I.; Torrent, M. Quasihydrostatic Equation of State of Iron above 2 Mbar. *Phys. Rev. Lett.* **2006**, *97* (21), 215504.
(52) Dronskowski, R.; Blöchl, P. E. Crystal Orbital Hamilton Populations (COHP). Energy-Resolved Visualization of Chemical Bonding in Solids Based on Density-Functional Calculations. *J. Phys. Chem.* **1993**, *97*, 8617−8624.
(53) Tschauner, O.; Kiefer, B.; Tetard, F.; Tait, K.; Bourguille, J.; Zerr, A.; Dera, P.; McDowell, A.; Knight, J.; Clark, S. Elastic Moduli and Hardness of Highly Incompressible Platinum Perpnictide PtAs2. *Appl. Phys. Lett.* **2013**, *103* (10), 101901.

DOI: 10.1021/acs.inorgchem.7b03272
Inorg. Chem. 2018, 57, 6245−6251

III. *DATA ON THE XE-N SOLID*

Table 2: Measured X-ray diffraction peaks of the Xe-N solid from 170 GPa down to 74 GPa. The X-ray wavelength is λ = 0.3738 Å.

Pressure (GPa)	2θ (°)	d-spacing (Å)
170	2.76591	7.74402
170	4.99457	4.28944
170	5.77514	3.71008
170	6.6653	3.21505
170	8.30955	2.57968
170	8.64833	2.4788
170	8.79456	2.43767
170	9.10664	2.35429
170	9.19623	2.33141
167	2.76559	7.74491
167	8.35247	2.56644
167	8.82081	2.43043
155	2.73396	7.8345
155	3.96294	5.40544
155	4.95608	4.32274
155	5.80311	3.69221
155	6.70324	3.19687
155	8.29095	2.58545
155	8.70617	2.46237
155	8.57995	2.49852
155	9.07816	2.36166
146	2.72277	7.86668
146	3.93847	5.43901
146	4.94154	4.33545
146	5.78857	3.70148
146	6.66547	3.21496
146	8.23326	2.60354
146	8.54545	2.50859
146	8.67168	2.47214
146	9.08357	2.36026
137	2.71823	7.87982
137	3.88707	5.5109
137	3.91402	5.47297
137	4.94365	4.33361
137	5.76078	3.71932
137	6.64103	3.22678
137	8.13862	2.63376

137	8.19883	2.61445
137	8.46787	2.53153
137	8.6306	2.48388
137	9.04576	2.37011
126	2.69344	7.95232
126	3.90254	5.48907
126	4.87236	4.39697
126	5.71935	3.74624
126	6.57637	3.25847
126	8.14078	2.63306
126	8.41314	2.54797
126	8.55597	2.50551
126	8.98783	2.38535
116	2.67208	8.0159
116	3.87453	5.52874
116	4.86437	4.40419
116	4.87375	4.39571
116	5.64495	3.79557
116	6.55835	3.26742
116	8.09624	2.64752
116	8.36529	2.56252
116	8.52803	2.51371
116	8.92329	2.40257
105	3.83979	5.57874
105	5.61351	3.81682
105	8.0183	2.67322
105	8.32719	2.57422
105	8.46674	2.53187
105	8.88527	2.41283
105	3.83979	5.57874
85	2.61798	8.18152
85	3.80384	5.63144
85	5.53767	3.86904
85	7.90925	2.71001
85	8.34108	2.56994
85	8.34109	2.56994
85	8.68651	2.46793
74	5.46303	3.92187
74	8.10702	2.64401
74	8.47899	2.52822

REFERENCES

[1] R. J. Hemley, Annu. Rev. Phys. Chem **51**, 763 (2000).

[2] C. S. Yoo, AIP Conf. Proc. **1195**, 11 (2009).

[3] J. A. Ciezak and B. M. Rice, *Polymeric Nitrogen: The Ultimate, Green High Performing Energetic Material* (2006).

[4] C. Mailhiot, L. Yang, and A. McMahan, Phys. Rev. B **46**, 14419 (1992).

[5] A. F. Goncharov, E. Gregoryanz, H. Mao, and R. J. Hemley, Low Temp. Phys. **27**, 866 (2001).

[6] E. Gregoryanz, A. Goncharov, R. Hemley, and H. Mao, Phys. Rev. B **64**, 052103 (2001).

[7] E. Gregoryanz, A. Goncharov, R. Hemley, H. Mao, M. Somayazulu, and G. Shen, Phys. Rev. B **66**, 224108 (2002).

[8] M. I. Eremets, R. J. Hemley, H. Mao, and E. Gregoryanz, Nature **411**, 170 (2001).

[9] A. F. Goncharov, E. Gregoryanz, H. K. Mao, Z. Liu, and R. J. Hemley, Phys. Rev. Lett. **85**, 1262 (2000).

[10] M. I. Eremets, A. G. Gavriliuk, I. A. Trojan, D. A. Dzivenko, and R. Boehler, Nat. Mater. **3**, 558 (2004).

[11] N. W. Ashcroft, Phys. Rev. Lett. **92**, 187002 (2004).

[12] X. Wang, Y. Wang, M. Miao, X. Zhong, J. Lv, T. Cui, J. Li, L. Chen, C. J. Pickard, and Y. Ma, Phys. Rev. Lett. **109**, 175502 (2012).

[13] C. J. Pickard and R. J. Needs, Phys. Rev. Lett. **102**, 1 (2009).

[14] Y. Ma, A. Oganov, Z. Li, Y. Xie, and J. Kotakoski, Phys. Rev. Lett. **102**, 065501 (2009).

[15] W. Li, X. Huang, K. Bao, Z. Zhao, Y. Huang, L. Wang, G. Wu, B. Zhou, D. Duan, F. Li, Q. Zhou, B. Liu, and T. Cui, Sci. Rep. **7**, 39249 (2016).

[16] X. Wang, F. Tian, L. Wang, X. Jin, D. Duan, X. Huang, B. Liu, and T. Cui, New J. Phys. **15**, 013010 (2013).

[17] D. Tomasino, M. Kim, J. Smith, and C.-S. Yoo, Phys. Rev. Lett. **113**, 205502 (2014).

[18] F. Peng, Y. Wang, H. Wang, Y. Zhang, and Y. Ma, Phys. Rev. B **92**, 094104 (2015).

[19] Q. J. Liu, W. Zeng, F. S. Liu, and Z. T. Liu, Comput. Theor. Chem. **1014**, 37 (2013).

[20] A. Hu and F. Zhang, J. Phys. Condens. Matter **23**, 22203 (2011).

[21] G.-R. Qian, C.-H. Hu, A. R. Oganov, Q. Zeng, and H.-Y. Zhou, Sci. Rep. **6**, 25947 (2014).

[22] K. Yin, Y. Wang, H. Liu, F. Peng, and L. Zhang, J. Mater. Chem. A **3**, 4188 (2015).

[23] B. A. Steele and I. I. Oleynik, J. Phys. Chem. A **121**, 1808 (2017).

[24] D. K. Spaulding, G. Weck, P. Loubeyre, F. Datchi, P. Dumas, and M. Hanfland, Nat. Commun. **5**, 5739 (2014).

[25] A. F. Goncharov, N. Holtgrewe, G. Qian, C. Hu, A. R. Oganov, M. Somayazulu, E. Stavrou, C. J. Pickard, A. Berlie, F. Yen, M. Mahmood, S. S. Lobanov, Z. Konôpkova, and V. B. Prakapenka, J. Chem. Phys. **142**, 214308 (2015).

[26] H. Wang, M. I. Eremets, I. Troyan, H. Liu, Y. Ma, and L. Vereecken, Sci. Rep. **5**, 13239 (2015).

[27] D. Dirtu, L. Odochian, A. Pui, and I. Humelnicu, Cent. Eur. J. Chem. **4**, 666 (2006).

[28] F. Peng, Y. Yao, H. Liu, and Y. Ma, J. Phys. Chem. Lett. **6**, 2363 (2015).

[29] Y. Shen, A. R. Oganov, G. Qian, H. Dong, Q. Zhu, and Z. Zhou, Sci. Rep. **5**, 1 (2015).

[30] D. L. V. K. Prasad, N. W. Ashcroft, and R. Hoffmann, J. Phys. Chem. C **117**, 20838 (2013).

[31] M. Zhang, H. Yan, Q. Wei, H. Wang, and Z. Wu, EPL **101**, 26004 (2013).

[32] C. Zhang, C. Yang, B. Hu, C. Yu, Z. Zheng, and C. Sun, Angew. Chemie - Int. Ed. **56**, 4512 (2017).

[33] Y. Xu, Q. Wang, C. Shen, Q. Lin, P. Wang, and M. Lu, Nature **549**, 78 (2017).

[34] C. Zhang, C. Sun, B. Hu, C. Yu, and M. Lu, Science **355**, 374 (2017).

[35] P. C. Samartzis and A. M. Wodtke, Int. Rev. Phys. Chem. **25**, 527 (2006).

[36] F. Cacace, G. de Petris, and A. Troiani, Science **295**, 480 (2002).

[37] A. Vij, J. G. Pavlovich, W. W. Wilson, V. Vij, and K. O. Christe, Angew. Chemie - Int. Ed. **41**, 3051 (2002).

[38] K. O. Christe, W. W. Wilson, J. A. Sheehy, and J. A. Boatz, Angew. Chemie Int. Ed. **38**, 2004 (1999).

[39] T. Hager, *The Alchemy of Air* (Broadway Books, New York, 2008).

[40] P. M. Bell, H. K. Mao, and R. J. Hemley, Phys. B+C **139–140**, 16 (1986).

[41] T. Zhang, S. Zhang, Q. Chen, and L.-M. Peng, Phys. Rev. B **73**, 094105 (2006).

[42] V. E. Zarko, Combust. Explos. Shock Waves **46**, 121 (2010).

[43] C. Pooley and E. LeBouthillier, *Orbital Aspirations* (CreateSpace Independent Publishing Platform, Washington, 2013).

[44] K. O. Christe, Propellants, Explos. Pyrotech. **32**, 194 (2007).

[45] V. Ozolinš and A. Zunger, Phys. Rev. Lett. **82**, 767 (1999).

[46] W. Sun, S. T. Dacek, S. P. Ong, G. Hautier, A. Jain, W. D. Richards, A. C. Gamst, K. A. Persson, and G. Ceder, Sci. Adv. **2**, 1 (2016).

[47] B. A. Steele and I. I. Oleynik, Chem. Phys. Lett. **643**, 21 (2016).

[48] Z. Wang, Y. Li, H. Li, I. Harran, M. Jia, H. Wang, Y. Chen, H. Wang, and N. Wu, J. Alloys Compd. **702**, 132 (2017).

[49] B. A. Steele, E. Stavrou, J. C. Crowhurst, J. M. Zaug, V. B. Prakapenka, and I. I. Oleynik, Chem. Mater. **29**, 735 (2017).

[50] S. Yu, B. Huang, Q. Zeng, A. R. Oganov, L. Zhang, and G. Frapper, J. Phys. Chem. C **121**, 11037 (2017).

[51] S. Wei, D. Li, Z. Liu, X. Li, F. Tian, D. Duan, B. Liu, and T. Cui, J. Phys. Chem. Chem. Phys. **19**, 9246 (2017).

[52] W. Sun, A. Holder, B. Orvañanos, E. Arca, A. Zakutayev, S. Lany, and G. Ceder, Chem. Mater. **29**, 6936 (2017).

[53] S. Zhang, Z. Zhao, L. Liu, and G. Yang, J. Power Sources **365**, 155 (2017).

[54] G. Soto, Comput. Mater. Sci. **61**, 1 (2012).

[55] J. Zhang, A. R. Oganov, X. Li, and H. Niu, Phys. Rev. B **95**, 020103 (2017).

[56] M. Wessel and R. Dronskowski, J. Am. Chem. Soc. **132**, 2421 (2010).

[57] M. I. Eremets, A. G. Gavriliuk, N. R. Serebryanaya, I. A. Trojan, D. A. Dzivenko, R. Boehler, H. K. Mao, and R. J. Hemley, J. Chem. Phys. **121**, 11296 (2004).

[58] D. Li, P. Zhu, J. Jiang, D. Xu, R. Liu, X. Wang, and Q. Cui, J. Phys. Commun. **1**, 025002 (2017).

[59] D. Li, P. Zhu, J. Jiang, M. Li, Y. Chen, B. Liu, X. Wang, Q. Cui, and H. Zhu, J. Phys. Chem. C **120**, 27013 (2016).

[60] M. Pravica, D. Sneed, Q. Smith, B. Billinghurst, T. May, M. White, and K. Dziubek, Cogent Phys. **3**, 1169880 (2016).

[61] M. Pravica, D. Sneed, M. White, and Y. Wang, Cit. Rev. Sci. Instruments Chem. Phys **85**, 086110 (2014).

[62] D. Sihachakr and P. Loubeyre, Phys. Rev. B **74**, 064113 (2006).

[63] V. I. Levitas, Phys. Rev. B - Condens. Matter Mater. Phys. **70**, 184118 (2004).

[64] V. I. Levitas and L. K. Shvedov, Phys. Rev. B - Condens. Matter Mater. Phys. **65**, 104109 (2002).

[65] R. Bini and V. Schettino, *Materials under Extreme Conditions* (Imperial College Press , London, 2014).

[66] H.-K. Mao, B. Chen, J. Chen, K. Li, J.-F. Lin, W. Yang, and H. Zheng, Matter Radiat. Extrem. **1**, 59 (2016).

[67] C. H. Polsky and E. Van Valkenburg, in *Handb. Vib. Spectrosc.* (John Wiley & Sons, Ltd, 2006), pp. 1352–1360.

[68] C. E. Weir, E. R. Lippincott, and N. E. Bunting, J. Res. Natl. Bur. Stand. - A. Phys. Chem. **63**, 55 (1959).

[69] J. C. Jamieson, A. W. Lawson, and N. D. Nachtrier, Rev. Sci. Instrum. **30**, 1016 (1959).

[70] R. Letoullec, J. P. Pinceaux, and P. Loubeyre, High Press. Res. **1**, 77 (1988).

[71] W. B. Daniels and M. G. Ryschkewitsch, Rev. Sci. Instrum. **54**, 115 (1983).

[72] R. Boehler and K. De Hantsetters, High Press. Res. **24**, 391 (2004).

[73] A. Y. Liu and M. L. Cohen, Science **245**, 841 (1989).

[74] J. E. Graebner, in *Diam. Electron. Prop. Appl.*, edited by L. S. Pan and D. R. Kania (Springer US, Boston, 1995), pp. 285–318.

[75] A. Jayaraman, Rev. Mod. Phys. **55**, 65 (1983).

[76] A. L. Ruoff, H. Xia, H. Luo, and Y. K. Vohra, Rev. Sci. Instrum. **61**, 3830 (1990).

[77] B. Li, C. Ji, W. Yang, J. Wang, K. Yang, R. Xu, W. Liu, Z. Cai, J. Chen, and H. Mao, Proc. Natl. Acad. Sci. **115**, 1713 (2018).

[78] H. W. Hayden, W. G. Moffat, and J. Wulff, *The Structure and Properties of Materials* (Wiley, New York, 1965).

[79] A. Dewaele, F. Occelli, and P. Loubeyre, ESRF Exp. Rep. (2015).

[80] N. Dubrovinskaia, L. Dubrovinsky, N. A. Solopova, A. Abakumov, S. Turner, M. Hanfland, E. Bykova, M. Bykov, C. Prescher, V. B. Prakapenka, S. Petitgirard, I. Chuvashova, B. Gasharova, Y.-L. Mathis, P. Ershov, I. Snigireva, and A. Snigirev, Sci. Adv. **2**, e1600341 (2016).

[81] P. Loubeyre, R. Letoullec, and J. P. Pinceaux, **71**, 12 (1993).

[82] J.-P. Pinceaux, J.-P. Maury, and J.-M. Besson, J. Phys. Lettres **40**, 307 (1979).

[83] H. Olijnyk, J. Chem. Phys. **93**, 8968 (1990).

[84] F. Schwabl, in *Stat. Mech.*, 3rd ed. (Springer Science & Business Media, Berlin, 2002), pp. 231–236.

[85] A. White, *Intermolecular Potentials of Mixed Systems: Testing the Lorentz-Berthelot Mixing Rules with Ab Initio Calculations* (2000).

[86] J. O. Hischefelder, C. F. Curtiss, and R. B. Bird, *Molecular Theory of Gases and Liquids* (John Wiley and Sons Ltd, New York, 1964).

[87] Z. M. Geballe and R. Jeanloz, J. Appl. Phys. **111**, 123518 (2012).

[88] R. Reichlin, K. E. Brister, A. K. McMahan, M. Ross, S. Martin, Y. K. Vohra, and A. L. Ruoff, Phys. Rev. Lett. **62**, 669 (1989).

[89] M. Krisch, J. Raman Spectrosc. **34**, 628 (2003).

[90] A. Polian, J. Raman Spectrosc. **34**, 633 (2003).

[91] Y. Bi, H. Zhou, Z. Huang, H. Zhou, and X. Yang, Rev. Sci. Instrum. **85**, 125002 (2014).

[92] C.-S. Zha, H. Mao, and R. J. Hemley, Proc. Natl. Acad. Sci. U. S. A. **97**, 13494 (2000).

[93] K. K. Zhuravlev, A. F. Goncharov, S. N. Tkachev, P. Dera, and V. B. Prakapenka, J.

Appl. Phys. **113**, 113503 (2013).

[94] J.-P. Poirier, *Introduction to the Physics of the Earth's Interior* (Cambridge University Press, Cambridge, 1991).

[95] H. Takeuchi and H. Kanamori, J. Geophys. Res. **71**, 3985 (1966).

[96] A. Dewaele, M. Torrent, P. Loubeyre, and M. Mezouar, Phys. Rev. B **78**, 104102 (2008).

[97] H. K. Mao, P. M. Bell, J. W. Shaner, and D. J. Steinberg, J. Appl. Phys. **49**, 3276 (1978).

[98] K. Takemura and A. Dewaele, Phys. Rev. B **78**, 104119 (2008).

[99] S. Anzellini, A. Dewaele, F. Occelli, P. Loubeyre, and M. Mezouar, J. Appl. Phys. **115**, 043511 (2014).

[100] Y. Akahama and H. Kawamura, J. Phys. Conf. Ser. **215**, 012195 (2010).

[101] J. Als-Nielsen and D. McMorrow, in *Elem. Mod. X-Ray Phys.*, Second Edi (John Wiley & Sons, Ltd, 2011), pp. 29–68.

[102] M. Mezouar, W. A. Crichton, S. Bauchau, F. Thurel, H. Witsch, F. Torrecillas, G. Blattmann, P. Marion, Y. Dabin, J. Chavanne, O. Hignette, C. Morawe, and C. Borel, J. Synchrotron Radiat. **12**, 659 (2005).

[103] M. Mezouar, R. Giampaoli, G. Garbarino, I. Kantor, A. Dewaele, G. Weck, S. Boccato, V. Svitlyk, A. D. Rosa, R. Torchio, O. Mathon, O. Hignette, and S. Bauchau, High Press. Res. **37**, 170 (2017).

[104] C. Prescher and V. B. Prakapenka, High Press. Res. **35**, 223 (2015).

[105] A. Boultif and D. Louër, J. Appl. Crystallogr. **24**, 987 (1991).

[106] J. Laugier and B. Bochu, Checkcell, LMGP-Suite of Programs for the Interpretation of X-Ray Experiments. Laboratoire des Materiaux et du Génie Physique de l'Ecole Supérieure de Physique de Grenoble, Laboratoire des Materiaux et du Genie, Saint Martind'Heres. http://www.ccp14.ac.in/tutorial/lmgp/ (2004).

[107] V. Favre-Nicolin and R. Černý, J. Appl. Crystallogr. **35**, 734 (2002).

[108] A. Altomare, C. Cuocci, C. Giacovazzo, A. Moliterni, R. Rizzi, N. Corriero, and A. Falcicchio, J. Appl. Crystallogr. **46**, 1231 (2013).

[109] J. Rodriguez-Carvajal, Phys. B Condens. Matter **192**, 55 (1993).

[110] J. I. Langford and D. Lou, Reports Prog. Phys. **59**, 131 (1996).

[111] A. Le Bail, H. Duroy, and J. L. Fourquet, Mater. Res. Bull. **23**, 447 (1988).

[112] S. Desgreniers and K. Lagarec, J. Appl. Crystallogr. **27**, 432 (1994).

[113] T. B. Ballaran, A. Kurnosov, and D. Trots, High Press. Res. **33**, 453 (2013).

[114] D. F. Datchi and D. G. Weck, Zeitschrift Für Krist. – Cryst. Mater. **229**, 135 (2014).

[115] E. Bykova, Single-Crystal X-Ray Diffraction at Extreme Conditions in Mineral Physics and Material Sciences, University of Bayreuth, 2015.

[116] CrysAlisPRO, Oxford Diffraction /Agilent Technologies UK Ltd, Yarnton, England. (2015).

[117] V. Petrícek, M. Dušek, and L. Palatinus, Zeitschrift Fur Krist. **229**, 345 (2014).

[118] L. Palatinus and G. Chapuis, J. Appl. Crystallogr. **40**, 786 (2007).

[119] M. C. Burla, R. Caliandro, M. Camalli, B. Carrozzini, G. L. Cascarano, L. De Caro, C. Giacovazzo, G. Polidori, and R. Spagna, J. Appl. Crystallogr. **38**, 381 (2005).

[120] F. Birch, Phys. Rev. B **71**, 809 (1947).

[121] P. Vinet, J. Ferrante, J. H. Rose, and J. R. Smith, J. Geophys. Res. **92**, 9319 (1987).

[122] R. E. Cohen, O. Gülseren, and R. J. Hemley, Am. Mineral. **85**, 338 (2000).

[123] E. Gregoryanz, C. Sanloup, M. Somayazulu, J. Badro, G. Fiquet, H. Mao, and R. J. Hemley, Nat. Mater. **3**, 294 (2004).

[124] A. F. Young, J. A. Montoya, C. Sanloup, M. Lazzeri, E. Gregoryanz, and S. Scandolo, Phys. Rev. B **73**, 2 (2006).

[125] G. W. Stinton, I. Loa, L. F. Lundegaard, and M. I. McMahon, J. Chem. Phys. **131**, 104511 (2009).

[126] D. Laniel, V. Svitlyk, G. Weck, and P. Loubeyre, Phys. Chem. Chem. Phys. **20**, 4050 (2018).

[127] D. Laniel, G. Weck, and P. Loubeyre, Phys. Rev. B **94**, 174109 (2016).

[128] P. Chemistry, Methods Phys. Chem. (2012).

[129] B. Dietzek, D. Cialla, M. Schmitt, and J. Popp, in *Confocal Raman Microsc.*, edited by T. Dieing, O. Hollricher, and J. Toporski (Springer, Berlin, 2010), pp. 21–27.

[130] A. F. Goncharov, Int. J. Spectrosc. **2012**, 1 (2012).

[131] J. H. Eggert, K. A. Goettel, and I. F. Silvera, Appl. Phys. Lett. **53**, 2489 (1988).

[132] A. D. Buckingham, C. Graham, and J. H. Williams, An Int. J. Interface Between Chem. Phys. Mol. Phys. **493**, 703 (1983).

[133] P. Bündgen, F. Grein, and A. J. Thakkar, J. Mol. Struct. THEOCHEM **334**, 7 (1995).

[134] A. Mulder, J. P. J. Michels, and J. A. Schouten, J. Chem. Phys. **105**, 3235 (1996).

[135] A. Erba, L. Maschio, C. Pisani, and S. Casassa, Phys. Rev. B **84**, 012101 (2011).

[136] G. Weck, F. Datchi, G. Garbarino, S. Ninet, J.-A. Queyroux, T. Plisson, M. Mezouar, and P. Loubeyre, Phys. Rev. Lett. **119**, 235701 (2017).

[137] E. Gregoryanz, A. F. Goncharov, C. Sanloup, M. Somayazulu, H. K. Mao, and R. J. Hemley, J. Chem. Phys. **126**, 184505 (2007).

[138] M. Frost, R. T. Howie, P. Dalladay-Simpson, A. F. Goncharov, and E. Gregoryanz, Phys. Rev. B **93**, 024113 (2016).

[139] D. Schiferl, D. T. Cromer, R. R. Ryan, A. C. Larson, R. LeSar, and R. L. Mills, Acta Crystallogr. C **39**, 1151 (1983).

[140] R. L. Mills, B. Olinger, and D. T. Cromer, J. Chem. Phys. **84**, 2837 (1986).

[141] M. I. M. Scheerboom and J. A. Schouten, J. Chem. Phys. **105**, 2553 (1996).

[142] H. Schneider, W. Häfner, A. Wokaun, and H. Olijnyk, J. Chem. Phys. **96**, 8046 (1992).

[143] H. Olijnyk and A. P. Jephcoat, Phys. Rev. Lett. **83**, 332 (1999).

[144] D. T. Cromer, R. L. Mills, D. Schiferi, and L. A. Schwalbe, Acta Crystallogr. Sect. B Struct. Crystallogr. Cryst. Chem. **B37**, 8 (1981).

[145] M. I. M. Scheerboom and J. A. Schouten, Phys. Rev. Lett. **71**, 2252 (1993).

[146] M. Hanfland, M. Lorenzen, C. Wassilew-Reul, and F. Zontone, Rev. High Press. Sci. Technol. **7**, 787 (1998).

[147] R. Bini, M. Jordan, L. Ulivi, and H. J. Jodl, J. Chem. Phys. **108**, 6849 (1998).

[148] R. Bini, L. Ulivi, J. Kreutz, and H. J. Jodl, J. Chem. Phys. **112**, 8522 (2000).

[149] L. Mederos, E. Chacn, and P. Tarazona, Phys. Rev. B **42**, 8571 (1990).

[150] S. Ninet, G. Weck, P. Loubeyre, and F. Datchi, Phys. Rev. B **83**, 7 (2011).

[151] J. Hooper, A. Hu, F. Zhang, and T. K. Woo, Phys. Rev. B **80**, 104117 (2009).

[152] T. W. Barbee III, Phys. Rev. B **48**, 9327 (1993).

[153] R. Caracas, J. Chem. Phys. **1271**, 144510 (2007).

[154] D. Tomasino, Z. Jenei, W. Evans, and C.-S. Yoo, J. Chem. Phys. **140**, 244510 (2014).

[155] A. F. Goncharov, J. C. Crowhurst, V. V. Struzhkin, and R. J. Hemley, Phys. Rev. Lett. **101**, 095502 (2008).

[156] A. R. Oganov and C. W. Glass, J. Chem. Phys. **124**, 244704 (2006).

[157] G. D. Mukherjee and R. Boehler, Phys. Rev. Lett. **99**, 225701 (2007).

[158] D. Donadio, L. Spanu, I. Duchemin, F. Gygi, and G. Galli, Phys. Rev. B - Condens. Matter Mater. Phys. **82**, 1 (2010).

[159] P. Zaleski-Ejgierd, V. Labet, T. A. Strobel, R. Hoffmann, and N. W. Ashcroft, J. Phys. Condens. Matter **24**, 155701 (2012).

[160] S. Jiang, X. Huang, D. Duan, S. Zheng, F. Li, X. Yang, Q. Zhou, B. Liu, and T. Cui, J. Phys. Chem. C **118**, 3236 (2014).

[161] A. F. Young, C. Sanloup, E. Gregoryanz, S. Scandolo, R. J. Hemley, and H. K. Mao, Phys. Rev. Lett. **96**, 155501 (2006).

[162] N. Bartlett and F. O. Sladky, in *Chem. Monatomic Gases* (Pergamon Press, New York, 1973), pp. 213–330.

[163] N. Bartlett, Proc. Chem. Soc. 218 (1960).

[164] H. H. Claassen, H. Selig, and J. G. Malm, J. Am. Chem. Soc. **84**, 3593 (1962).

[165] J. Haner and G. J. Schrobilgen, Chem. Rev. **115**, 1255 (2015).

[166] J. H. Burns, P. A. Agron, and H. A. Levy, Science **139**, 1208 (1963).

[167] J. A. Ibers and W. C. Hamilton, Science **139**, 1 (1963).

[168] J. G. Malm, C. L. Chernick, and S. M. Williamson, in *Inorg. Synth.*, edited by H. F. Holtzlaw (John Wiley & Sons, Inc., Hoboken, 1966).

[169] J. G. Malm, I. Sheft, and C. L. Chernick, J. Am. Chem. Soc. **85**, 110 (1963).

[170] R. Hoppe, W. Dabne, H. Mattauch, and K. Rodder, Angew. Chemie Int. Ed. English **1**, 599 (1962).

[171] S. Hoyer, T. Emmler, and K. Seppelt, J. Fluor. Chem. **127**, 1415 (2006).

[172] D. S. Brock, G. J. Schrobilgen, and B. Zemva, in *Compr. Inorg. Chem.*, edited by J. Reedijk and K. Poeppelmeier, 1st ed. (Elsevier, Oxford, UK, 2013), p. 755.

[173] M. Ross, J. Chem. Phys. **56**, 4651 (1972).

[174] H. Chacham, X. Zhu, and S. G. Louie, Europhys. Lett. **14**, 65 (1991).

[175] M. Ross and A. K. McMahan, Phys. Rev. B **21**, 1658 (1980).

[176] D. A. Nelson and A. L. Ruoff, Phys. Rev. Lett. **42**, 383 (1979).

[177] K. Syassen, Phys. Rev. B **2**, 6548 (1982).

[178] I. Makarenko, G. Weill, J. P. Itié, and J. M. Besson, Phys. Rev. B **26**, 7113 (1982).

[179] A. N. Zisman, I. V. Aleksendrov, and S. M. Stishov, Pis'ma Zh. Eksp. Teor. Fiz. **40**, 253 (1984).

[180] D. Schiferl, R. L. Mills, and L. E. Trimmer, Solid State Commun. **46**, 783 (1983).

[181] A. P. Jephcoat, H.-K. Mao, L. W. Finger, D. E. Cox, R. J. Hemley, and C.-S. Zha, Phys. Rev. Lett. **59**, 2670 (1987).

[182] M. Eremets, E. Gregoryanz, V. Struzhkin, H.-K. Mao, R. Hemley, N. Mulders, and N. Zimmerman, Phys. Rev. Lett. **85**, 2797 (2000).

[183] H. Cynn, C. S. Yoo, B. Baer, V. Iota-Herbei, A. K. McMahan, M. Nicol, and S. Carlson, Phys. Rev. Lett. **86**, 4552 (2001).

[184] S. Sasaki, N. Wada, T. Kume, and H. Shimizu, J. Raman Spectrosc. **40**, 121 (2009).

[185] K. A. Goettel, J. H. Eggert, I. F. Silvera, and W. C. Moss, Phys. Rev. Lett. **62**, 665 (1989).

[186] P. H. Lahr and W. G. Eversole, J. Chem. Eng. Data **7**, 42 (1962).

[187] A. Dewaele, P. Loubeyre, P. Dumas, and M. Mezouar, Phys. Rev. B **86**, 014103 (2012).

[188] W. Hume-Rothery, G. W. Mabbott, and C. Evans, R. Trans. Philos. Soc. Ser. A **233**, 1 (1934).

[189] X. Cottin and P. A. Monson, J. Chem. Phys. **102**, 3354 (1993).

[190] A.-P. Hynninen, L. Filion, and M. Dijkstra, J. Chem. Phys. **131**, 064902 (2009).

[191] J. Zhu, C. Liu, L. Pike, and P. Liaw, Metall. Mater. Trans. A **30A**, 1449 (1999).

[192] C. Sanloup, S. A. Bonev, M. Hochlaf, and H. E. Maynard-Casely, Phys. Rev. Lett. **110**, 1 (2013).

[193] M. Somayazulu, P. Dera, A. F. Goncharov, S. A. Gramsch, P. Liermann, W. Yang, Z. Liu, H.-K. Mao, and R. J. Hemley, Nat. Chem. **2**, 50 (2010).

[194] G. Weck, A. Dewaele, and P. Loubeyre, Phys. Rev. B **82**, 014112 (2010).

[195] R. O. Pepin and D. Porcelli, Rev. Mineral. Geochemistry **47**, 191 (2002).

[196] S. S. Shcheka and H. Keppler, Nature **490**, 531 (2012).

[197] L. Zhu, H. Liu, C. J. Pickard, G. Zou, and Y. Ma, Nat. Chem. **6**, 644 (2014).

[198] Q. Zhu, D. Y. Jung, A. R. Oganov, C. W. Glass, C. Gatti, and A. O. Lyakhov, Nat. Chem. **5**, 61 (2013).

[199] A. Hermann and P. Schwerdtfeger, J. Phys. Chem. Lett. **5**, 4336 (2014).

[200] A. Dewaele, N. Worth, C. J. Pickard, R. J. Needs, S. Pascarelli, O. Mathon, M. Mezouar, and T. Irifune, Nat. Chem. **8**, 784 (2016).

[201] A. Dewaele, C. M. Pépin, G. Geneste, and G. Garbarino, High Press. Res. **37**, 137 (2017).

[202] E. Stavrou, Y. Yao, A. F. Goncharov, S. Lobanov, J. M. Zaug, H. Liu, E. Greenberg, and V. B. Prakapenka, Phys. Rev. Lett. **120**, 96001 (2018).

[203] Y. Wang, J. Lv, L. Zhu, and Y. Ma, Phys. Rev. B - Condens. Matter Mater. Phys. **82**, 1 (2010).

[204] W. J. Evans, M. J. Lipp, C. S. Yoo, H. Cynn, J. L. Herberg, R. S. Maxwell, and M. F. Nicol, Chem. Mater. **18**, 2520 (2006).

[205] R. T. Howie, R. Turnbull, J. Binns, M. Frost, P. Dalladay-Simpson, and E. Gregoryanz, Sci. Rep. **6**, 34896 (2016).

[206] K. Niwa, F. Matsuzaki, and M. Hasegawa, Phys. Chem. Chem. Phys. **19**, 59 (2017).

[207] J. Lin, O. Degtyareva, C. Prewitt, P. Dera, N. Sata, E. Gregoryanz, H. Mao, and R. Hemley, Nat. Mater. **3**, 389 (2004).

[208] M. Pravica, L. Bai, and Y. Liu, Chem. Phys. Lett. **555**, 115 (2013).

[209] E. Wigner and H. B. Huntington, J. Chem. Phys. **3**, 764 (1935).

[210] J. McMinis, R. C. Clay, D. Lee, and M. A. Morales, Phys. Rev. Lett. **114**, 1 (2015).

[211] E. G. Brovman, Y. Kagan, and A. Kholas, Zh. Eksp. Tear. Fiz **35**, 1492 (1972).

[212] R. P. Dias and I. F. Silvera, Science **355**, 715 (2017).

[213] M. I. Eremets and I. A. Troyan, Nat. Mater. **10**, 927 (2011).

[214] H. Mao, R. Hemley, and M. Hanfland, Phys. Rev. Lett. **65**, 484 (1990).

[215] N. K. Mao and R. J. Hemley, Science **244**, 1462 (1989).

[216] I. F. Silvera and J. W. Cole, J. Phys. Conf. Ser. **215**, 012194 (2010).

[217] N. Wibert, in *Inorg. Chem.*, edited by N. Wiberg (Academic Press, New York, 2001), pp. 598–777.

[218] J. E. Troyan, Eng. Process Dev. **45**, 2608 (1953).

[219] 1N Hydrazine Thruster, ArianeGroup, http://www.space-propulsion.com/spacecraft-propulsion/hydrazine-thrusters/1n-hydrazine-thruster.html (2018).

[220] D. S. Moore and S. D. Robinson, in *Adv. Inorg. Chem. Radiochem.*, edited by H. J. Emeléus and A. G. Sharpe (Academic Press, London, 1986), pp. 1–68.

[221] M. Gauthier, P. Pruzan, J. C. Chervin, and J. M. Besson, Phys. Rev. B **37**, (1988).

[222] S. Ninet, F. Datchi, A. M. Saitta, M. Lazzeri, and B. Canny, Phys. Rev. B - Condens. Matter Mater. Phys. **74**, 1 (2006).

[223] B. A. Chidester and T. A. Strobel, J. Phys. Chem. A **115**, 10433 (2011).

[224] J. G. O. Ojwang, R. S. McWilliams, X. Ke, and A. F. Goncharov, J. Chem. Phys. **137**, 064507 (2012).

[225] S. Ninet, F. Datchi, P. Dumas, M. Mezouar, G. Garbarino, A. Mafety, C. J. Pickard, R. J. Needs, and A. M. Saitta, Phys. Rev. B **89**, 174103 (2014).

[226] T. Kume, S. Sasaki, and H. Shimizu, J. Raman Spectrosc. **32**, 383 (2001).

[227] J. Ciezak, T. Jenkins, and R. Hemley, AIP Conf. Proc. **1195**, 1291 (2009).

[228] R. Chellappa, D. Dattelbaum, L. Daemen, and Z. Liu, J. Phys. Conf. Ser. **500**, 052008 (2014).

[229] S. Ninet and F. Datchi, J. Chem. Phys. **128**, 154508 (2008).

[230] T. Palasyuk, I. Troyan, M. Eremets, V. Drozd, S. Medvedev, P. Zaleski-Ejgierd, E. Magos-Palasyuk, H. Wang, S. a. Bonev, D. Dudenko, and P. Naumov, Nat. Commun. **5**, 3460 (2014).

[231] C. J. Pickard and R. J. Needs, Nat. Mater. **7**, 775 (2008).

[232] A. S. Williams, B. A. Steele, and I. I. Oleynik, J. Chem. Phys. **147**, 234701 (2017).

[233] D. Laniel, G. Weck, G. Gaiffe, G. Garbarino, and P. Loubeyre, J. Phys. Chem. Lett. **9**, 1600 (2018).

[234] J. C. Crowhurst, J. M. Zaug, H. B. Radousky, B. a Steele, A. C. Landerville, and I. I. Oleynik, J. Phys. Chem. A **118**, 8695 (2014).

[235] S. A. Medvedev, M. I. Eremets, J. Evers, T. M. Klapötke, T. Palasyuk, and I. A. Trojan, Chem. Phys. **386**, 41 (2011).

[236] S. A. Medvedev, T. Palasyuk, I. A. Trojan, P. G. Naumov, J. Evers, T. M. Klapötke, and M. I. Eremets, Vib. Spectrosc. **58**, 188 (2012).

[237] P. Loubeyre, F. Occelli, and R. LeToullec, Nature **416**, 613 (2002).

[238] M. Hanfland, I. Loa, K. Syassen, U. Schwarz, and K. Takemura, Solid State Commun. **112**, 123 (1999).

[239] M. Hanfland, K. Syassen, N. E. Christensen, and D. L. Novikov, Nat. Lett. **408**, 174 (2000).

[240] C. L. Guillaume, E. Gregoryanz, O. Degtyareva, M. I. Mcmahon, M. Hanfland, S. Evans, M. Guthrie, S. V Sinogeikin, and H.-K. Mao, Nat. Phys. **7**, 211 (2011).

[241] T. Matsuoka and K. Shimizu, Nature **458**, 186 (2009).

[242] J. B. Neaton and N. W. Ashcroft, Nature **400**, 141 (1999).

[243] Z. Yu, H. Y. Geng, Y. Sun, and Y. Chen, Sci. Rep. **8**, 3868 (2018).

[244] M. S. Miao and R. Hoffmann, Acc. Chem. Res. **47**, 1311 (2014).

[245] A. M. J. Schaeffer, W. B. Talmadge, S. R. Temple, and S. Deemyad, Phys. Rev. Lett. **109**, 185702 (2012).

[246] S. Deemyad and R. Zhang, Phys. C Supercond. Its Appl. **548**, 68 (2018).

[247] F. A. Gorelli, S. F. Elatresh, C. L. Guillaume, M. Marqués, G. J. Ackland, M. Santoro, S. A. Bonev, and E. Gregoryanz, Phys. Rev. Lett. **108**, 055501 (2012).

[248] Y. Feng, J. Chen, D. Alfè, X. Z. Li, and E. Wang, J. Chem. Phys. **142**, 064506 (2015).

[249] E. Dönges, in *Handb. Prep. Inorgative Chem.*, edited by G. Brauer, Second Edi (Academic Press, London, 1963), p. 984.

[250] A. Rabenau, Solid State Ionics **6**, 277 (1982).

[251] T. Shodai, S. Okada, S. Tobishima, and J. Yamaki, J. Power Sources **68**, 515 (1997).

[252] Y. Sun, Y. Li, J. Sun, Y. Li, A. Pei, and Y. Cui, Energy Storage Mater. **6**, 119 (2017).

[253] P. Chen, Z. Xiong, J. Luo, J. Lin, and K. Lee Tan, Nature **420**, 302 (2002).

[254] J. L. O'Loughlin, C. H. Wallace, M. S. Knox, and R. B. Kaner, Inorg. Chem. **40**, 2240 (2001).

[255] H. D. Fair and R. F. Walker, *Energetic Materials* (Plenum Press, New York, 1977).

[256] H. Beister, S. Haag, R. Kniep, K. Strössner, and K. Syassen, Angew. Chem. Int. Ed. Engl. **27**, 1101 (1988).

[257] A. Lazicki, B. Maddox, W. J. Evans, C. S. Yoo, A. K. McMahan, W. E. Pickett, R. T. Scalettar, M. Y. Hu, and P. Chow, Phys. Rev. Lett. **95**, 165503 (2005).

[258] S. A. Medvedev, I. A. Trojan, M. I. Eremets, T. Palasyuk, T. M. Klapötke, and J. Evers, J. Phys. Condens. Matter **21**, 195404 (2009).

[259] S. B. Schneider, R. Frankovsky, and W. Schnick, Angew. Chem. Int. Ed. **51**, 1873 (2012).

[260] R. Huisgen and I. Ugi, Angew. Chemie **68**, 96 (1956).

[261] B. Bazanov, U. Geiger, R. Carmieli, D. Grinstein, S. Welner, and Y. Haas, Angew. Chemie - Int. Ed. **55**, 13233 (2016).

[262] L. Zhang, Y. Wang, J. Lv, and Y. Ma, Nat. Publ. Gr. **2**, 1 (2017).

[263] R. Dronskowski and P. E. Blöchl, J. Phys. Chem. **97**, 8617 (1993).

[264] A. C. Ho, M. K. Granger, A. L. Ruoff, P. E. Van Camp, and V. E. Van Doren, Phys. Rev. B **59**, 6083 (1999).

[265] S. Duwal, Y.-J. Ryu, M. Kim, C.-S. Yoo, S. Bang, K. Kim, and N. H. Hur, J. Chem. Phys. **148**, 134310 (2018).

[266] M. Bykov, E. Bykova, E. Koemets, T. Fedotenko, G. Aprilis, K. Glazyrin, H.-P. Liermann, A. V Ponomareva, J. Tidholm, F. Tasnádi, I. A. Abrikosov, N. Dubrovinskaia, and L. Dubrovinsky, Angew. Chemie Int. Ed. **10**, (2018).

[267] Y. D. Perfiliev and V. K. Sharma, in *ACS Symp. Ser.* (American Chemical Society, Washington, DC, 2008), pp. 112–123.

[268] M. Benolt, D. Marx, and M. Parrinello, Nature **392**, 258 (1998).

[269] R. T. Howie, T. Scheler, C. L. Guillaume, and E. Gregoryanz, Phys. Rev. B - Condens. Matter Mater. Phys. **86**, 3 (2012).

[270] M. Kim and C. S. Yoo, J. Chem. Phys. **134**, 044519 (2011).

[271] S. Wei, D. Li, Z. Liu, W. Wang, F. Tian, K. Bao, D. Duan, B. Liu, and T. Cui, J. Phys. Chem. C **121**, 9766 (2017).

[272] S. Zhu, F. Peng, H. Liu, A. Majumdar, T. Gao, and Y. Yao, Inorg. Chem. **55**, 7550 (2016).

[273] D. Laniel, A. Dewaele, and G. Garbarino, Inorg. Chem. **57**, 6245 (2018).

[274] V. S. Bhadram, D. Y. Kim, and T. A. Strobel, Chem. Mater. **28**, 1616 (2016).

[275] K. Niwa, T. Terabe, D. Kato, S. Takayama, M. Kato, K. Soda, and M. Hasegawa, Inorg. Chem. **56**, 6410 (2017).

[276] D. Kurzydłowski and P. Zaleski-Ejgierd, Sci. Rep. **6**, 1 (2016).

[277] T. Irifune, A. Kurio, S. Sakamoto, T. Inoue, H. Sumiya, and K. ichi Funakoshi, Phys. Earth Planet. Inter. **143**, 593 (2004).

[278] N. M. Hwang, *Non-Classical Crystallization of Thin Films and Nanostructures in CVD and PVD Processes* (Springer Netherlands, Dordrecht, 2016).

[279] E. M. Benchafia, Z. Yao, G. Yuan, T. Chou, H. Piao, X. Wang, and Z. Iqbal, Nat. Commun. **8**, 1 (2017).

[280] A. Vailionis, E. G. Gamaly, V. Mizeikis, W. Yang, A. V. Rode, and S. Juodkazis, Nat. Commun. **2**, 445 (2011).

[281] S. Juodkazis, K. Nishimura, S. Tanaka, H. Misawa, E. G. Gamaly, B. Luther-Davies, L. Hallo, P. Nicolai, and V. T. Tikhonchuk, Phys. Rev. Lett. **96**, 1 (2006).

[282] Chemical Abstracts Service (CAS) REGISTRY system, https://www.cas.org/support/documentation/chemical-substances (2018).

[283] A. Salamat, A. L. Hector, P. Kroll, and P. F. McMillan, Coord. Chem. Rev. **257**, 2063 (2013).

[284] A. Friedrich, B. Winkler, E. A. Juarez-Arellano, and L. Bayarjargal, Materials (Basel). **4**, 1648 (2011).

[285] J. C. Crowhurst, A. F. Goncharov, B. Sadigh, C. L. Evans, P. G. Morrall, J. L. Ferreira, and A. J. Nelson, Science **311**, (2006).

[286] R. Yu, Q. Zhan, and L. C. De Jonghe, Angew. Chemie - Int. Ed. **46**, 1136 (2007).

[287] K. Niwa, D. Dzivenko, K. Suzuki, R. Riedel, I. Troyan, M. Eremets, and M. Hasegawa, Inorg. Chem. **53**, 697 (2014).

[288] K. Niwa, K. Suzuki, S. Muto, K. Tatsumi, K. Soda, T. Kikegawa, and M. Hasegawa, Chem. Eur. J. **20**, 13885 (2014).

[289] M. Zhang, K. Cheng, H. Yan, Q. Wei, and B. Zheng, Sci. Rep. **6**, 36911 (2016).

[290] J. C. Crowhurst, A. F. Goncharov, B. Sadigh, J. M. Zaug, D. Aberg, Y. Meng, and V. B. Prakapenka, J. Mater. Res. **23**, 1 (2008).

[291] M. Hasegawa and T. Yagi, J. Alloys Compd. **403**, 131 (2005).

[292] H. A. Wriedt, N. A. Gokcen, and R. H. Nafziger, Bull. Alloy Phase Diagr. **8**, 355 (1987).

[293] M. Wessel and R. Dronskowski, Chem. Eur. J. **17**, 2598 (2011).

[294] S. D. Gupta, S. K. Gupta, and P. K. Jha, Eur. Phys. J. B **86**, 1 (2013).

[295] W. P. Clark, S. Steinberg, R. Dronskowski, C. McCammon, I. Kupenko, M. Bykov, L.

Dubrovinsky, L. G. Akselrud, U. Schwarz, and R. Niewa, Angew. Chemie - Int. Ed. **56**, 7302 (2017).

[296] A. Dewaele, P. Loubeyre, F. Occelli, M. Mezouar, P. I. Dorogokupets, and M. Torrent, Phys. Rev. Lett. **97**, 29 (2006).